Experimental Investigation and Numerical Simulation of Fiber Laser Welding of Ti-6Al-4V Alloy and SS-316L

A thesis submitted
in partial fulfillment of the requirements
for the degree of

Doctor of Philosophy

By

Chandan Kumar
Roll No.-126103018

Department of Mechanical Engineering

Indian Institute of Technology Guwahati

Guwahati, India

July, 2018

Declaration

I declare that this written submission represents my ideas in my own words and where others' ideas or words have been included, I have adequately cited and referenced the original sources. I also declare that I have adhered to all principles of academic honesty and integrity and have not misrepresented or fabricated or falsified any idea/data/fact/source in my submission. I understand that any violation of the above will be cause for disciplinary action by the Institute and can also evoke penal action from the sources which have thus not been properly cited or from whom proper permission has not been taken when needed.

Date:

Chandan Kumar

Roll No. 126103018

Department of Mechanical Engineering
Indian Institute of Technology Guwahati
Guwahati-781039
INDIA

CERTIFICATE

It is certified that the work contained in the thesis entitled "**Experimental Investigation and Numerical Simulation of Fiber Laser Welding of Ti-6Al-4V Alloy and SS-316L**", submitted by **Chandan Kumar**, Roll No. 126103018 to the Indian Institute of Technology Guwahati, Assam for the degree of Doctor of Philosophy has been carried out under my supervision in the Department of Mechanical Engineering, Indian Institute of Technology Guwahati. This work has not been submitted elsewhere for a degree.

Date:

Dr. Manas Das
(Assistant Professor)
Department of Mechanical Engineering
Indian Institute of Technology Guwahati
Guwahati- 781039, Assam, India

Dedicated to

My family

THESIS APPROVAL SHEET

The thesis titled

Experimental Investigation and Numerical Simulation of Fiber Laser Welding of Ti-6Al-4V Alloy and SS-316L

by

Chandan Kumar

is approved for the degree of Doctor of Philosophy.

Examiners

_____

Supervisor

_____

Chairman

_____

Date:

Place: IIT Guwahati

Acknowledgement

This thesis is the result of five years of work at IIT Guwahati whereby I have been accompanied and supported by many people. First and foremost, I would like to take this opportunity to pay my deep sense of respect and sincere gratitude to my supervisor, Dr. Manas Das, Department of Mechanical Engineering, Indian Institute of Technology Guwahati, Assam-781039 for his invaluable advice, resourceful guidance, inspiring instructions, active supervision and constant encouragement without which it would not have been possible for me to reach to this point.

I would like to convey my deep regards to my doctoral committee members, Professor P. S. Robi, Dr. Swarup Bag and Dr. Koustava Dasgupta for his valuable support and suggestions from time to time to carry out my research work which incented me to widen my research from various perspectives. I must not miss the opportunity to thank all the Professors of Mechanical Engineering Department, Indian Institute of Technology Guwahati, whose motivation and timely help molded me in all possible forms. I would also like to thanks Mr. Saiffuddin Ahmed, Mr. Jiten Basumatary, Mr. Sanjib Sarma, Mr. N. K. Das and workshop technicians Mr. Dilip Chetri, for their support in carrying out the research work. I would like to acknowledge central instrument facility of IIT Guwahati for kind assistance for metallurgical characterization. I also gratefully acknowledge the technical support of Dr. C. P Paul, Mr. Upendra Kumar and other team members of Laser Additive Manufacturing Laboratory, Raja Ramanna Centre for Advanced Technology, Indore, India to carry out my research work.

I am deeply indebted to my parents for the sacrifices they have borne to ensure the fulfillment of my dreams for his love, prayers, care and support for educating and preparing me for my future. Also, I express my thanks to my sister and brother their support and valuable prayers. My special thanks go to my wife Kumari Rachna for their mental support and keen interest shown to complete this thesis successfully. Last, but not least, the time I spent with all my friends at IIT Guwahati, Anwesa Barman, Anupam Alok and Kelli Durgaprasad, who made my life enjoyable and memorable on the campus.

And finally I would thank the Almighty God for his showers of blessings throughout my life and during period of research work to complete the research successfully.

Date: ----------

TH-2032_126103018 CHANDAN KUMAR

Abstract

The full form of Laser is '**L**ight **A**mplification by **S**timulated **E**mission of **R**adiation'. The most attractive and important properties of laser beam which are significant in material processing are high power, low divergence, directional, coherent and monochromatic beam. One of the most important characteristics of laser beam is its high energy density due to which it is widely used in welding of materials having high melting point. Titanium and its alloys serve as a bridge between the ideal properties of aluminum and steel. It is recognized as a workhorse for aerospace and automotive industries and is widely used in many areas such as aerospace, medicinal, chemical and aviation industries etc. due to its excellent combination of both high strength and ductility, low density, better corrosion resistance and excellent biocompatibility. The main goal of ongoing research work is to investigate the weldability of similar materials of Ti-6Al-4V alloy having thicknesses of 5, 2 and 1.5 mm and austenitic stainless steel of grade 316L (SS-316L) having thickness of 3 mm using fiber laser autogenously.

In the present study, a 2 kW solid state ytterbium doped fiber laser having wavelength of 1.08 µm combined with a computer numerical control worktable is used for welding experiments. A specially designed workpiece fixture with shielding gas delivery system is fabricated to reduce distortion and displacement of workpieces and to protect bead contamination from environment during welding. Three main process parameters which are considered are beam power, welding speed and defocused position of laser beam. The effect of process parameters on weld bead features like fusion zone width and area, size of heat affected zone at different locations in weld bead, bead shape, bead microstructure, weld defects and mechanical properties of the weldments are studied. The quality of the weldments is investigated via bead appearance under optical microscope, energy dispersive X-ray spectroscopy analysis, metallographic characterization of weld bead and testing of mechanical properties using Vickers microhardness tester and universal tensile testing machine. The weld bead microstructure is observed under optical microscope and their morphologies are compared using field emission scanning electron microscope. Further, the fractured surfaces are analyzed using FESEM images to confirm different modes of fracture failure i.e. ductile or brittle fracture. Further welding experiments are extended to optimize the process parameters using response surface methodology of statistical design of experiments for achieving satisfactory weld quality. Analysis of variance (ANOVA) is carried out to identify the most significant process parameters during welding for both Ti-

6Al-4V and SS-316L workpieces and their percentage contribution on output responses are calculated. After that regression analysis is carried out. The effect of individual process parameters and their combined effect are studied using 2D and 3D response plots obtained from regression equations. Further, a three-dimensional finite element based model is developed using ANSYS®14.5 to determine transient temperature profile around weld pool.

Experimentally it is observed that penetration depth in the base plate is primarily controlled by beam power density on workpiece surface. However, width of fusion zone and size of heat affected zone depend on line energy. In the present study, almost linear relationship between width of FZ and line energy is observed irrespective of penetration depth in the base plate. Smooth, uniform, acceptable size of micro pores, shiny bead with no spatters and crack free weld bead is formed. Welding power shows positive effect on bead features whereas welding speed shows negative impact. However, defocused position of the laser beam shows diverse effect on bead geometry. The weld bead is almost symmetrical about the centre line of fusion zone. Moreover, lack of symmetricity is only observed at higher beam power on root side of weld bead. Presence of α′ martensitic phase having needle shaped structure in the fusion zone reflects high self-quenching characteristics of laser beam welding process. In the present study, most of the welded samples are defects free. Although, in few welded samples small amount of underfill defect, excess penetration and porosity are observed in the weld bead. However, the size of the porosities is within acceptable range (< 0.4 mm) as per BS EN: 4678:2011 European standard. Maximum hardness value is observed in the fusion zone for both Ti-6Al-4V and SS-316L and its value continuously decreases towards BMZ. The percentage elongation of the welded specimens is found lower than base metal due to the presence of brittle α′ martensitic phase in the FZ which possess high tensile strength at the expense of ductility. Ductile mode of fracture failure is observed in both base metal as well as in welded specimen of Ti-6Al-4V and SS-316L. A FEM based numerical simulation of laser welding process is developed for transient thermal analysis of Ti-6Al-4V workpiece by employing double ellipsoidal and 3-D cone-shaped volumetric heat source models. A non-linear relationship between peak temperature and beam power is noticed possibly due to the variation of Ti-6Al-4V alloy's absorption coefficient with temperature. The present model can be useful to reduce the number of trial experiments before performing the actual experiment which helps in reducing experimental cost.

Table of Contents

List of Figures

List of Tables

Nomenclature

Symbol

λ	Wavelength
α	Alpha
β	Beta
M_s	Martensitic transformation start temperature
M_f	Martensitic transformation finished temperature
P	Beam power
V	Welding speed
d	Defocused position of laser beam
d_p	Penetration depth
Ar	Argon
κ	Thermal conductivity
t	Material thickness
ρ	Density of material
c	Specific heat
q	Heat flux
T_m	Melting temperature
σ	Stefan-Boltzmann constant
ε	Emissivity
h	Heat transfer coefficient
h_{lump}	Lumped heat transfer coefficient
T_o	Initial ambient temperature
T_c	Temperature of interest
E	Enthalpy
τ	Relative plate thickness
Q_{avg}	Average power density
H_{net}	Total heat input
A	Area of laser beam spot
T_i	Interaction time
η	Welding efficiency
T_β	β transus temperature

T_L	Liquidus temperature
T_S	Solidus temperature

Acronym

LBW	Laser beam welding
GMAW	Gas metal arc welding
SMAW	Shield metal arc welding
SAW	Submerged arc welding
GTAW	Gas tungsten arc welding
EBW	Electron beam welding
CW	Continuous wave
TIG	Tungsten inert gas
Ar	Argon
BCC	Body centered cubic
HCP	Hexagonal closed packed
CNC	Computer numerical control
BPP	Beam product parameter
SOD	Standoff distance
BM	Base metal
BMZ	Base metal zone
FZ	Fusion zone
HAZ	Heat affected zone
BOP	Beads on plate
HV	Vickers microhardness
EDS	Energy dispersive X-ray spectroscopy
FESEM	Field emission scanning electron microscope
OM	Optical microscope
CR	Cooling rate
LE	Line energy
DP	Depth of penetration
DOE	Design of experiment
RSM	Response surface methodology
CCRD	Central composite rotatable design
ANOVA	Analysis of variance

CCT	Continuous cooling transformation curve
SW	Successful weld
USW	Unsuccessful weld
EP	Excess penetration
FP	Full penetration
PP	Partial penetration
US	Uneven surface
SF	Smooth surface
HR	High roughness
ME	Metal evaporation
NC	No crack
LEUF	Line energy utilization factor
YS	Yield strength
UTS	Ultimate tensile strength
El	Elongation
FEM	Finite element method

Chapter 1

Introduction

1.0 Material processing with laser beam

Light is a form of electromagnetic radiation of energy. It exhibits different kinds of wavelengths and frequencies. On the basis of wave-particle duality concept, it is considered as an energy wave with distinct quantized energy levels. Laser beam is also a light source and from 1960 onward it has been extensively used as a heat source for material processing. The full form of Laser is '**L**ight **A**mplification by **S**timulated **E**mission of **R**adiation'. Laser delivers a parallel beam which has different properties than normal light source. The most attractive and important laser properties which are significant in material processing are high power, monochromatic beam, low divergence, directional and coherent beam. The monochromatic light is important for focusing laser beam into a small spot area providing maximum power density. These properties of laser light can be utilized in many applications such as welding, cutting, drilling and surface treatment of a wide range of engineering materials. One of the most important characteristics of laser beam is its high energy density due to which it is widely used in welding of materials having high melting point (Ready, 2001). There is no requirement of filler materials in laser beam welding (LBW) and the high cooling rate favours the formation of fine microstructure in the fusion zone which enhances material's strength without undergoing further heat treatment. The high welding speed contributes high solidification and cooling rates and it results in a narrow fusion and heat affected zones. Due to low heat input, deformation of parts is minimal and at the same time there is no direct contact between workpiece and heat source. In addition, there is a short interaction time between laser beam and workpiece material due to less start and stop time. Both precision and speed of welding can be significantly enhanced by delivering laser beam through fiber optics. However, a small spot diameter is essential for precise part fit-up. Misalignment of workpieces is a critical issue during laser beam welding process. The laser welding system is more expensive than traditional fusion welding systems. Whenever there is a necessity of high quality weldments, LBW is an attractive and cost effective way of welding technique (Asibu, 2009 and Jin et al., 2004). Nowadays, the newly developed solid-state fiber laser is extensively used in many fields of material processing.

1.1 Laser material interaction

The generation of a laser beam is essentially a three step process that occurs instantaneously i.e. atomic excitation by the process of energy absorption, spontaneous and stimulated emission and population inversion. A laser made of three components are

- A lasing medium or "gain medium"−it may be a solid (crystals, glasses etc.), liquid (dyes or organic solvents), gas (helium, CO_2 etc.) or semiconductors.
- An energy source or "pump"−may be a high voltage discharge, a chemical reaction, diode, flash lamp or another laser source.
- An optical resonator or "optical cavity"−consists of a cavity containing the lasing medium with two parallel mirrors on either side. One mirror is highly reflective and the other mirror is partially reflective, allowing some of the light to leave the cavity to produce the laser beam.

When sufficient amount of energy is supplied to the atom, electrons may jump from low-energy orbitals (ground state, near the nucleus) to high-energy orbitals, leading to atomic excitation by the process of energy absorption. Some of the electrons in the high-energy orbit spontaneously return to the ground state, releasing the difference in energy in the form of a photon, with a wavelength which depends exactly upon the difference in energy of the two energy states having a random phase and direction. This process is called spontaneous emission and the photons produced by this method are the seed for laser generation.

The photons emitted by spontaneous emission eventually strike other electrons in the higher energy states. "Eventually" in a very short time due to the speed of light and density of excited atoms. The incoming photon "knocks" the electron from the excited state to a lower energy level creating another photon. These two photons are coherent meaning they are in phase of the same wavelength and traveling in the same direction. This is called stimulated emission. The photons are emitted in all directions, however some of the photons travel along the laser medium to strike the resonator mirrors to be reflected back through the medium. The resonator mirrors define the preferential amplification direction for stimulated emission. For the amplification to occur there must be a greater percentage of atoms in the excited state than the lower energy levels. This "population inversion" of more atoms in the excited state leads to the conditions required for laser generation.

1.1.1 Optical absorption

When a light beam in impinged on a material surface, portion of the incident beam that is not reflected by the material is either absorbed or transmitted through the material. Metal's absorptivity to incident laser irradiation depends on the following parameters.

- **Wavelength** − At shorter wavelength, more energetic photons can be absorbed by a greater number of bound electrons. Hence, at shorter wavelength, reflectivity falls down and consequently absorptivity of the surface increases. Generally, laser energy is highly absorbed by metals for shorter wavelength as compared to longer wavelength.

- **Temperature** − As the temperature of the structure rises there will be an increase in the phonon population causing more phonon-electron energy exchanges. Thus the electrons are more likely to interact with the structure rather than oscillate and re-radiate. Therefore, there is a decrease in reflectivity and an increase in the absorptivity with increased temperature.

- **Surface roughness** – Surface roughness shows a great effect on absorption due to multiple reflections in the undulations. There also may be some stimulated absorption due to beam interference with sideways reflected beams. When the roughness is less than the beam wavelength, the radiation will not suffer these events.

1.1.1.1 Beer-Lambert's law

It states that the intensity of light decreases exponentially with the depth in the material.

$$I = \mathrm{I}_0 \exp\left(\frac{-4\pi\alpha \mathrm{d}}{\lambda}\right) \tag{1.1}$$

Where I is the intensity at depth d, I_0 is the intensity of light on the surface, λ is the wavelength of light and α is the extinction coefficient.

1.2 Welding process

Joining of metal pieces was started more than 2000 years back. In late 1800's, welding process was emerged as a joining process and had been undergone with many inventions and discoveries. Welding is one of the most versatile joining processes applicable for the fabrication of several products used in many industries like automotive, aerospace, medical, aviation and chemical. In welding process, two pieces of material are joined together. First, the material absorbs some part of applied energy and the material melts down locally. Afterward, it quickly comes back to the solid phase after removal of the energy source. Joining of metallic components is required whenever the required components cannot be produced by simple manufacturing processes like casting, forging, rolling, extrusion, etc. Joining of components by using nut and bolt is commonly used in industries. However, it increases the weight of an assembly unlike in welding process where it may reduce (Kou, 2002). Following parameters are considered while designing a joint.

- Properties of the materials to be joined
- Joint efficiency
- Environmental condition where the joint will be placed
- Load condition on the joint

Welding process can be performed in different environments including open air, under water and may be inside closed chamber. Different types of energy sources are commonly used for welding such as gas flame, electric arc, laser beam, electron beam, frictional force and ultrasound. The welding process is necessary for product development. However, welding process is a potentially hazardous and requires precautions to avoid burns, electric shock, inhalation of poisonous gases and fumes and exposure to highly intensive ultraviolet radiation.

1.3 Classification of welding processes

The classification of welding processes is shown in Fig. 1.1.

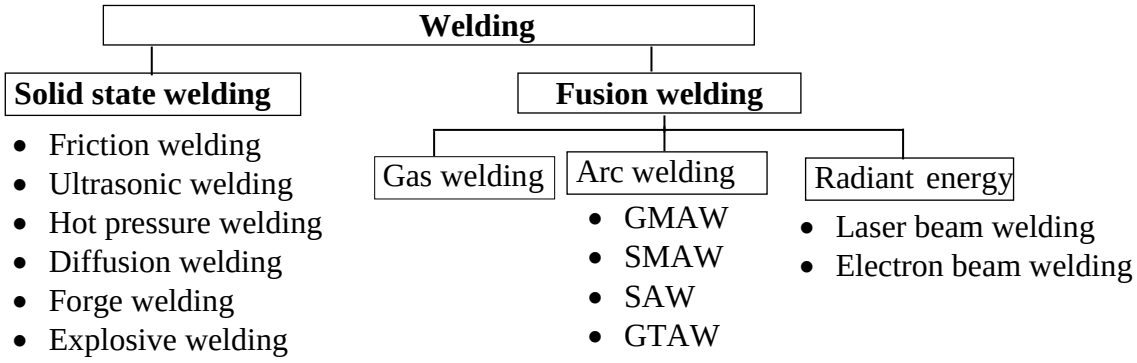

Fig. 1.1 Classification of welding processes

1.4 Radiant energy welding

In this process, radiant energy like laser and electron beam is utilized for welding purpose. Low carbon steel, HSLA steel, alloy steel, stainless steel, Ni alloys and titanium and its alloys can be easily welded by using this process.

1.4.1 Laser beam welding (LBW)

The theoretical and experimental studies on laser beam were started in 1962. However, the use of laser beam in welding purpose was reported in 1971 using CO_2 laser heat source (Banas, 1971). Since then the use of laser beam in welding purpose had grown rapidly in manufacturing industries. A wide range of similar, dissimilar materials and non-metals can be joined by means of laser heat source (Dowden et al., 1983). Various kind of intricate shapes, weld geometries and configurations can be produced with high level of productivity, quality and flexibility in case of laser beam welding (LBW). Nowadays, a variety of laser systems are developed for making micro weld in electronic circuit inside vacuum tubes and in other specialized applications where conventional technology is unable to provide reliable joint. Present days the demand for joining engineering materials are continuously increasing using laser heat source due to their various attractive advantages like capable of joining very thin to thick plates, producing very narrow heat affected and fusion zones, low residual stress and minimal weld defects (Sakagawa et al., 2011 and Behler et al., 1998).

LBW is one of the most important types of non-conventional, non-traditional and advanced welding technique for joining similar or dissimilar materials. LBW has many benefits as compared to traditional fusion welding techniques. The primary features of LBW process are its high efficiency, excellent controllability and its ability to focus into a very small area which yields high intensity of beam energy on the workpiece surface (Wu et al., 2002). The LBW process is completed in three main consecutive processes i.e. energy

absorption, melting and cooling. Initially, laser beam impinges on the workpiece surface. Large percentage of the beam energy is reflected back from the material surface depending on the absorptivity of the material. Some portion of the beam energy is absorbed to heat up the material surface. When the temperature of the surface is increased, the laser absorption is also increased forming melting pool. Further, the melt pool transforms into solid state due to rapid cooling (Steen, 2003 and Suder and Williams, 2014). The laser radiation on the workpiece material is often interrupted due to the evolution of hot gases formed on the irradiated material. Under certain conditions, this hot gas may turn into plasma via metal vaporization that can severely attenuate the laser beam due to absorption, defocusing and scattering. Therefore, the weld depth is shallow. To eliminate the plasma, the shielding gas is applied. Laser beam can weld a variety of metals or plastics ranging from thin sheets of about 0.01 mm thickness to thick plates of about 50 mm in the presence of shielding gas such as helium, argon or sometimes nitrogen under atmospheric condition. It gains great popularity among all welding processes having high beam quality, high precision, high performance, high speed, good flexibility and low deformation. This process can be robotized and can be made fully automated which reduces manpower requirement (Hongping et al., 2011 and Chen et al., 2009). The LBW process can be carried out either in pulsed mode or in continuous wave (CW) mode. Knowledge regarding the specifications and the capability of laser apparatuses, factors affecting weld penetration, weld defects and the mechanical properties of welded joints are required to decide the mode of operation. The comparisons of LBW process with other welding processes are shown in Table 1.1.

Table 1.1 Comparison of laser welding with other welding processes (Kou, 2002)

Parameter	**LBW**	**EBW***	**GTAW**	**GMAW**	**Resistance welding**
Joining efficiency	0	0	-	-	+
High aspect ratio	+	+	-	-	-
Small HAZ	+	+	-	-	0
High processing speed	+	+	-	+	-
Bead profile	+	+	0	0	0
Welding at atmospheric Pr.	+	-	+	+	+
Reflectivity of metals	-	+	+	+	+
Combine with filler	0	-	+	+	-
Automatic process	+	-	+	+	+
Capital cost	-	-	+	+	+
Operating cost	0	0	+	+	+
Reliability cost	+	-	+	+	+

*+Advantage; - Disadvantage; 0neutral; *EBW: Electron beam welding, GTAW: Gas tungsten arc welding, GMAW: Gas metal arc welding*

1.4.2 Advantages

There are several advantages of LBW process. These are as follows:

- Laser beam has high energy density. Hence, it provides high welding speed.
- Unlike electron beam welding (EBW) process, LBW does not require vacuum environment. It is mostly carried out in atmospheric condition.
- Magnetic materials can also be welded by LBW process which is not possible in EBW process.
- Being non-contact type process, welded workpiece does not require further cleaning unlike submerged arc welding (SMAW) or tungsten inert gas (TIG) welding.
- Inaccessible areas can be welded by passing laser beam through optical fiber.
- Laser beam is having high power density, high heating and cooling rate which helps to reduce heat affected zone (HAZ) size.
- LBW can be carried out at higher operating temperature than other welding processes.
- The power density of laser beam is equivalent to electron beam and is much higher than arc or plasma.
- LBW can be carried out at higher welding speed than arc and plasma welding processes.
- LBW joint possess higher reliability than other welding processes.
- LBW can be executed autogenously having accurate control over penetration and weld bead with excellent repeatability.

1.4.3 Limitations

There are several limitations associated with the LBW process (Wang et al., 2009 and Chen et al., 2011a). These are listed as follows:

- Welding equipment is expensive and initial investment and maintenance costs are higher than traditional welding processes.
- Due to smaller spot diameter and narrower weld bead, high precision of joining edges of samples is required. Hence, the tolerance available for the joint fit up and workpiece alignment is very less.
- Laser weld conversion efficiency is generally very low, typically 5~30%.
- In some cases undercut and underfill weld defects are observed.
- High reflectivity and high conductivity of some materials can affect laser weldability.
- Maximum joint thickness is limited in case of LBW process as compared to EBW.

1.5 Welding mode

Depending on the availability of the input energy, two different modes of LBW process are mentioned in the literature (Nath et al., 2002). These are conduction and keyhole modes of welding as shown in Figs. 1.2(a) and 1.2(b), respectively. Both types of welding modes can be performed autogenously i.e. filler material is not required during welding.

1.5.1 Conduction mode

Conduction mode of welding is a low energy input process having laser beam power density below 10^3 W/cm^2. In this mode of welding, the laser energy is absorbed at the material surface and it is distributed to the bulk material by conduction only. Here, the bead depth to width ratio is less than keyhole mode. The profile generated by the conduction mode of welding is shallow in nature and is bowl shaped as shown in Fig. 1.2(a). In conduction mode, most of the energy is reflected away. Hence, conduction mode has lower efficiency than keyhole mode of welding. Different properties of conduction mode of welding are low penetration depth, small aspect ratio, low coupling efficiency, very smooth and highly aesthetic weld bead, large heat affected zone (HAZ) as compared to key hole mode of welding (Chen et al., 2009).

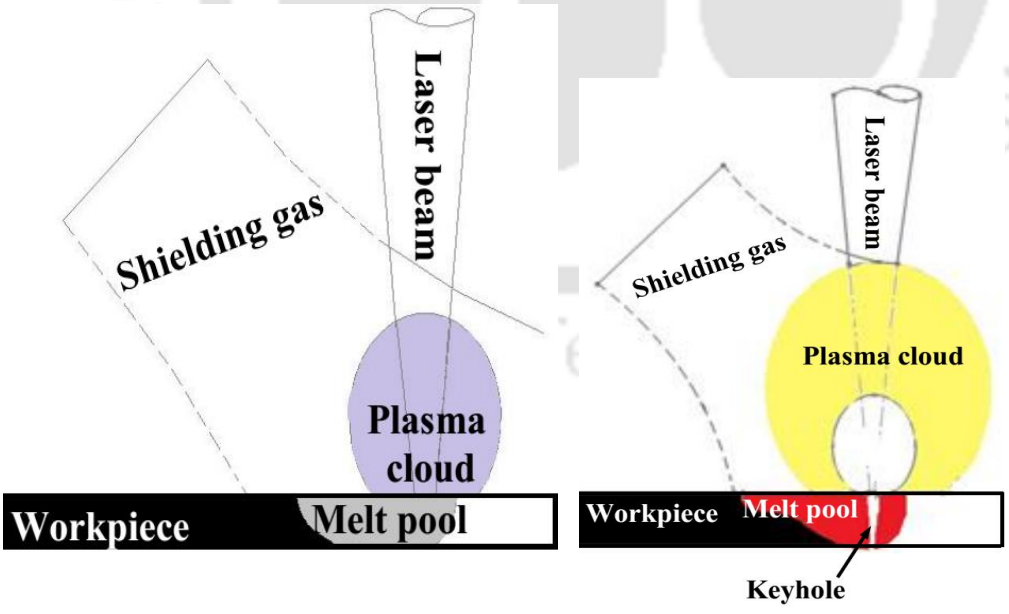

(a) (b)

Fig. 1.2 Schematic diagram of (a) conduction and (b) keyhole mode of welding

1.5.2 Keyhole mode

In keyhole mode of welding (Fig. 1.2(b)), the laser beam is focused at the workpiece surface so that it can generate power density in the range of 10^5-10^7 W/cm^2. At the center of the focused laser beam, vaporization of metal takes place which creates a hole into the molten pool i.e. a keyhole is generated. Vapor pressure holds surrounding molten metal and keeps the hole open during the process. This metal vapor also re-radiates laser energy into the molten metal along the sidewall of the keyhole. The keyhole allows the laser beam energy to reach deeper into the fusion zone and produce a deeper weld. Hence, the energy is transferred through the entire depth of the keyhole and a high aspect ratio hole is produced. The energy is absorbed by inverse bremsstrahlung in ionized plasma above the keyhole and by Fresnel absorption with reflections on the walls of the keyhole (Ki et al., 2002). In this mode of welding, the bead depth to width ratio is generally more than conduction mode of welding process. The small size of keyhole is responsible for producing relatively small fusion and heat affected zones. Due to the generation of the highly localized heat on the workpiece surface, simultaneous heating up and cooling down of both fusion and heat affected zones occur rapidly leading to the reduction of grain growth in the welded region. Keyhole mode of welding is applied for joining intricate and thick materials, joining of automobile bodies and aerospace parts. Different properties of keyhole mode of welding are high penetration depth, high aspect ratio, high coupling efficiency, smooth and highly aesthetic bead appearance and narrow HAZ (Manonmani et al., 2007).

1.6 Classification of laser heat sources

Different types of laser heat sources are available for welding purpose. These are

- Gas laser: CO_2 laser, Helium-neon laser, Argon laser and Nitrogen laser etc.
- Solid state laser: Fiber laser, Nd: YAG, Er: YAG laser etc.
- Diode laser
- Disk laser

The comparison between different laser heat sources in terms of wavelength and beam quality are presented in Table 1.2.

Table 1.2 Comparison between different laser heat sources (Duley, 1998)

Laser type	Wavelength (μm)	Avg. power (kW)	Beam quality
CO_2	10.6	50 (Max.)	Good
Nd:YAG	1.06	10−15	Poor
Diode	0.98	10−15	Poor
Disk	1.03	16	Good
Fiber	1.08	100	Good

1.6.1 Fiber laser

The solid state lasers operating at wavelength close to 1 μm have a benefit that the laser beam can be delivered through optical fiber which makes the laser system more flexible. The high-power solid state lasers like Nd: YAG lasers have relatively poor beam quality and electrical efficiency. One of the main workhorses of laser material processing is fiber laser. It operates at near infrared wavelength region (just outside the visible wavelength region) and it is invisible to the human eye. The development of fiber laser has improved the beam quality and electrical efficiency significantly. These lasers can be used in a diversity of materials since its low wavelength allows absorption by almost all metals and alloys. The use of fiber laser is started in 2000 with 100 W and later in 2005 maximum 17 kW fiber laser is produced. Also, the newer technologies are coming up to produce high power fiber lasers. It is a promising alternative to the conventional solid state laser systems.

The fiber laser is widely used in commercial industries and different areas of science and technology. Fiber laser is preferred while welding thick plates at high speed where conventional welding technique cannot be applied. In case of fiber laser, the active gain medium is optical fiber. The gain medium is doped with rare earth elements such as erbium, neodymium, dysprosium, ytterbium etc. It is excited by a diode laser. The outer cladding is covered with glass or polymeric material having low refraction coefficient to prevent signal attenuation. It has high beam quality and high output efficiency of about 50% compared to about 10-30% for CO_2 laser and 2% for Nd: YAG laser. The ytterbium doped fiber laser has a wall plug efficiency of 16-20%. Erbium and thulium based fiber lasers have lower wall plug efficiency however, more efficient than Nd: YAG laser (Quintino et al., 2007).

1.6.1.1 Advantages of fiber laser

The fiber laser offers several advantages as compared to other solid state lasers **(**Kawahito et al., 2007a and Kawahito et al., 2007b). These are as follows:

- **Light coupled into a flexible fiber –** Fiber laser generates beam inside the fibers, so the delivery of the beam doesn't require any optical medium. This makes it very stable and easy to use.
- **Higher efficiency –** Fiber laser offers higher efficiency than other lasers used for similar applications like Nd: YAG and CO_2 lasers.
- **High output power –** Fiber lasers can have active regions several kilometers long. Hence, it provides very high optical gain. It can produce kilo Watt level of continuous output power. Fiber lasers can be coiled easily within a small volume. In continuous wave multimode operation, 50 kW mean power and in pulse mode, peak power in mega Watt range can be obtained.
- **High optical beam quality –** In fiber laser, the beam is generated inside small core of the fiber. Hence, a high quality straight optical beam with less diffraction can be produced.
- **Low operating costs –** Fiber laser consumes less power and requires less maintenance leading to lesser operating cost than other lasers.
- **Low maintenance cost –** No periodic maintenance like mirror adjustment or its replacement are required for fiber laser set up. There is no blower or moving parts in fiber laser unlike CO_2 laser. Hence, no extra maintenance is required for fiber laser.
- **Long life time –** The operating lifetime of a fiber laser is determined by the lifetime of its diode laser pump which is estimated as 100,000 hours. This is much greater than the lifetime of Nd: YAG and CO_2 lasers.

1.7 Laser beam welding process parameters

The successful joining of materials strictly depends on the selection of laser beam welding process parameters. In LBW, the main process parameters which affect the quality and geometry of the welded joints are laser beam welding power, welding speed, defocused position of laser beam, offset distance and type and flow rate of shielding gas (Brock et al., 2014, Kuryntsev et al., 2017 and Tenner, 2015). Apart from these main parameters, there are many other parameters which affect weld qualities. These are shown in the fishbone diagram in Fig. 1.3.

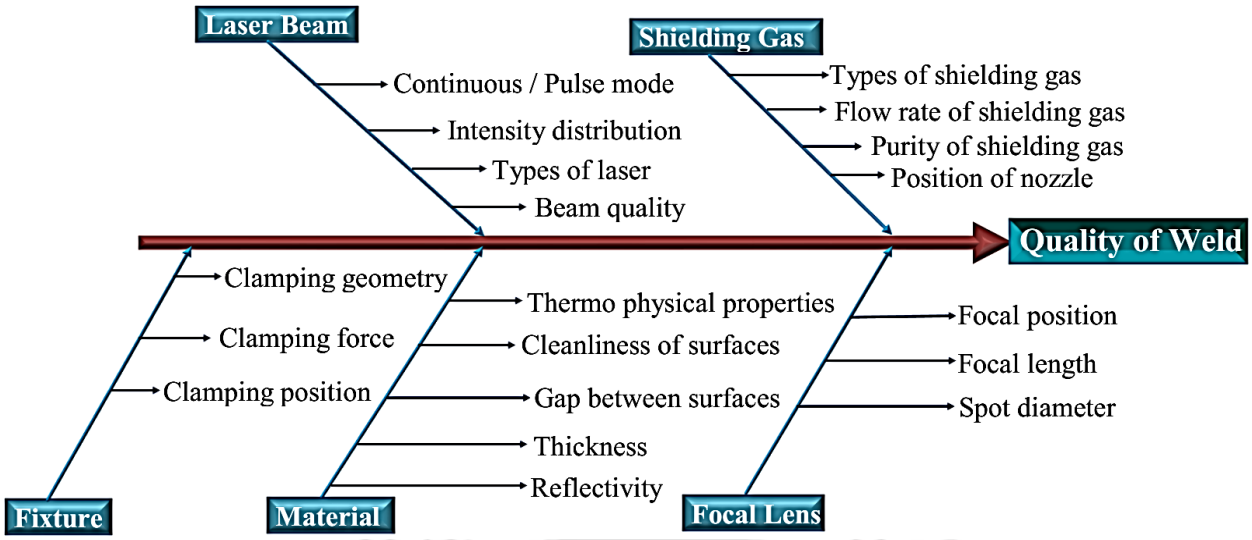

Fig. 1.3 Fishbone diagram of laser beam welding process parameters

By controlling these parameters, high quality weld having satisfactory mechanical properties can be achieved. The laser power and welding speed are the main process parameters as they affect bead shape and quality of the weldments. Hence, mostly these two parameters are adjusted to achieve optimum welding condition (Ayoola et al., 2017). The total energy per unit length is determined by the laser power and welding speed. When the welding speed is too high, lack of penetration occurs in the base plate. While at low welding speed, excessive drop out and porosity are observed. The main LBW process parameters are discussed below.

- **LBW power –** The laser power is a basic parameter in laser welding process. Power is defined as the rate of energy flow from the heat source. The power density of the laser is calculated from laser power and spot diameter of laser beam. The penetration depth in the base plate during laser welding is directly related to power density of the laser beam. Higher laser power generates bigger sized weld bead features.

- **Welding speed/traverse speed –** Traverse speed denotes the speed at which either laser beam or workpiece moves with respect to other. The penetration depth in the base plate increases with lower welding speed due to increased heat input per unit length.

- **Spot size –** The diameter of the focused laser beam at the workpiece surface is commonly known as spot size. The laser power density can be raised with a smaller spot diameter and it generates deeper penetration.

- **Power density or irradiance –** The laser beam power per unit area of the workpiece surface is commonly known as power density or irradiance.

- **Heat input per unit length/line energy –** The ability of the laser beam to melt a volume of material depends on the energy delivered per unit length of the weld. It is commonly referred as heat input per unit length. The heat input per unit length is calculated by dividing laser power with welding speed.

- **Defocused position of laser beam –** Location of focal point relative to the sample surface determines the beam size and it affects depth of penetration and bead width. The optimum value of defocused position produces maximum penetration depth and minimum bead width. The laser energy density is maximum at the focal point and its value decreases along the direction of beam axis away from the focal point. Defocusing distance is defined as the distance of the focal spot position from the workpiece top surface. Figure 1.4 shows the different defocusing distances in laser beam welding process. When the focal spot position is above the top surface of the workpiece, it is called positive defocusing (Fig.1.4 (a)). When the focal spot is just on the top surface of the workpiece, it is called zero defocusing distance (Fig.1.4 (b)).

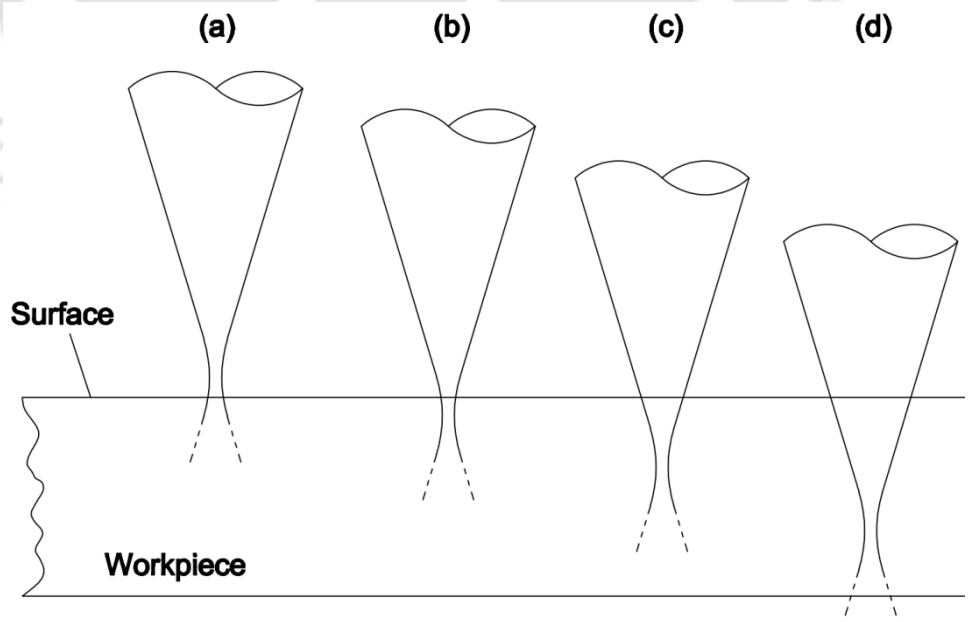

Fig. 1.4 Different defocusing positions in laser beam welding process

On the other hand, when the focal spot position is below the surface of the workpiece, it is called negative defocusing (Fig.1.4 (c) and (d)). The focal spot should be positioned

to a place with respect to workpiece surface so that it gives maximum penetration depth (Dawes, 1992). It is found that focal position below workpiece surface increases penetration depth for titanium alloys due to the enhancement of multiple internal reflections.

- **Shielding gas –** The shielding gas plays the most vital role during LBW process. The main role of shielding gas is to prevent oxidation of the weld zone and to reduce the chances of oxide inclusions in the weld pool. The next role is to suppress plasma formation over the weld zone and to escape out the formed plasma that may be created during LBW process. It also ensures the laser beam to reach the weld zone with minimal interruption thus improving weld quality and increasing penetration depth. Also, the shielding gas protects the optics from metal slag. During welding, the weld pool is created by imposing high intensity laser beam. The atmospheric gases, especially oxygen, can diffuse into the melt pool forming brittle material. Before welding, the shielding gas is initially applied to expel the oxygen from the workpiece surface. The oxygen from the workpiece surrounding can be mostly eliminated with proper supply of shielding gas flow rate. As laser power density exceeds 10^6 W/cm^2, the molten metal from workpiece surface is vaporized, ejected and it forms a cloud over the workpiece. This hot cloud is called plasma. Plasma can absorb beam energy resulting reduced laser intensity on workpiece surface. Moreover, the plasma can scatter the laser beam as studied by different researchers (Ducharme et al., 1992, Heidecker et al., 1988, Matsunawa, 1990). The scattering of laser beam is inversely proportional to λ^4 (Hansen and Duley, 1994) where λ is laser beam wave length. Therefore, Nd: YAG laser (wavelength 1.06 µm) shows more scattering effect than CO_2 laser (wavelength 10.6 µm) and fiber laser (wavelength 1.08 µm). Over the workpiece surface, there are two gases namely, plasma and air having different reflective indices. At the boundary of these two gases there is a discontinuity due to the difference in their reflective indices. Due to this, laser beam is distorted and hence power density is reduced at the workpiece surface. In order to overcome the plasma effect, shielding gas is used (Duley, 1998). Shielding gas expels and blows away the plasma from the workpiece surfaces. The main parameters in shielding gas delivery system are type of shielding gas and its flow rate. The selection of type of shielding gas and its flow rate are very important for successful completion of welding process. The gases with higher ionization potential have lower atomic number and hence lighter in weight. The lighter gases are less

effective in displacing air from melt pool area in a short period of time in laser welding. Heavier gases have better performance during LBW process (Chung et al., 1999 and Wang et al., 2007). The gas flow rate is also an important parameter for efficient shielding of weld bead. With appropriate gas flow rate, oxygen can be almost completely expelled and plasma can be suppressed at a faster rate. At very low flow rate, plasma becomes highly absorbent and the interaction of the laser beam with the materials decreases. Also, at a high flow rate of shielding gas, molten pool is blown out from the joints region resulting poor weld quality. Hence, it is very important to select appropriate flow rate for maximum welding efficiency and excellent weld quality (Tani et al., 2007).

1.8 Titanium and its alloys

Titanium is discovered in 1791 by British mineralogist and chemist "William Gregor" and it was purified in early 1900s. It is 9th most copious element on the earth planet and 4th most structural material. The word titanium originates from "Titan". According to Greek methodology "Titan" was a powerful son of earth. The physical and metallurgical characteristics of titanium and its alloys are very interesting and complex. Pure titanium exists in two crystal forms i.e. alpha (α) phase and beta (β) phase. At room temperature, pure titanium has a hexagonal close packed (HCP) crystal structure which is referred as alpha (α) phase. The α phase is stable at lower temperature, whereas β phase is stable at higher temperature (above transition temperature). The transition temperature of unalloyed titanium is 882 ± 20 ºC. Above this transition temperature, the allotropic transformation from HCP (α) phase to BCC (β) phase in pure titanium takes place. The exact transformation temperature mainly depends on the purity of the metal. The transformation temperature of pure titanium is affected by the presence of interstitial and substitutional elements. Alloying elements of titanium can be either α stabilizers which increases β transus temperature or β stabilizers which lowers down β transus temperature or it may act as a solid-solution-strengtheners without affecting transition temperature. The substitutional element like Al and the interstitial elements like O, N and C are strong in α stabilizer and V, Mo, Nb, Ta, Fe, Mn, Cr, Ni, Co, Cu and H are β stabilizing elements. Zr and Sn are neutral alloying elements which do not change the β transition temperature. The increase in amount of α stabilizers i.e. O, N and C leads to significant increase in strength at the expense of ductility. Titanium has high chemical affinity to these elements especially at elevated temperature that is why inert atmospheric environment is essential while processing titanium at high temperature (Leyens

and Peters, 2003). Titanium is nonmagnetic in nature having excellent heat-transfer properties. The coefficient of thermal expansion of pure titanium is lower than steel and approximately half of pure aluminium. Low density, excellent mechanical properties at high temperature and good corrosion resistance are the attractive properties of titanium. When temperature exceeds 130 ºC, aluminium-based materials can be replaced with titanium alloys in applications such as external shells of turbines, power generation units (Lima, 2005) etc. Moreover, titanium possesses very low corrosion rate in human body. Hence, it is used in medical industry for making prosthetic devices such as artificial heart pumps, pacemaker case, heart valve parts as well as hip bone replacement. Also, it is used in healthcare instruments such as in wheelchairs, equipment for handicapped persons such as artificial limbs and artificial legs etc. Titanium alloys are mainly divided into three categories (Donachie, 2000).

- Alpha alloy (α)
- Alpha and beta (α+β) alloy
- Beta alloy (β)

In recent years, various types of titanium based alloys are developed for wide range of applications. The use of titanium based alloys is increasing day by day in several industries to develop large variety of components due to their excellent combination of mechanical as well as chemical properties. Table 1.3 shows the year of introduction and maximum working temperature of different titanium alloys. Table 1.4 shows qualitative comparison of different types of titanium alloy. Alpha alloys show higher ductility but lower strength. On the other hand, β alloys exhibit higher strength but lower ductility and poor weldability. In contrast, α+β titanium alloy (Ti-6Al-4V) shows a good balance between strength and ductility.

Table 1.3 Composition and properties of different titanium alloys (Donachie, 2000)

Ti Alloy	Composition (wt.%)	Year introduced	Max. Working Temp.
Ti-6Al-4V	6Al,4V	1954	300
IMI-550	4Al,2Sn,4Mo, 0.5Si	1956	425
Ti-811	8Al,1Mo,1V	1961	400
IMI-679	8Al,1Mo,1V	1961	450
Ti-6246	2Al,11Sn,5Zr,1Mo,0.2Si	1966	450
Ti-6242	6Al,2Sn,4Zr,6Mo	1967	450
IMI-685	6Al,5Zr,0.5Mo,0.25Si	1969	520
Ti-11	6Al,2Sn,1.5Zr,1Mo, 0.1Si,0.3Bi	1972	540
Ti-17	5Al,2Sn,2Zr,4Mo,4Cr	1973	350
Ti-6242S	6Al,2Sn,4Zr,2Mo,0.1Si	1974	520

Table 1.4 Characteristic comparison of α, α+β and β titanium alloys (Leyens and Peters, 2003)

Mechanical properties	α	α+β	β
Strength	−	+	++
Ductility	++	+	−−
Weldability	++	+	−

$^{+}$High, $^{++}$very high, $^{-}$low, $^{--}$very low

1.8.1 Ti-6Al-4V alloy

In last few years, the demand for lightweight materials is increased extensively in many industries where fuel consumption and resistance to severe working circumstances are critical issue. To resolve these issues, use of titanium and its alloys are spreading rapidly in aerospace, automotive, medical and aviation industries. The biocompatibility of titanium makes it attractive for medical industry, resistance to corrosion makes its appealing for petrochemical and marine applications. Aerospace industry is one of the largest users of titanium alloys where they are used as material for compressor, structures in jet engines, airframe structures and landing gear structural components in aircrafts, space rockets and satellites (Brewer et al., 1998). The main reason for large use of titanium alloys in aerospace industry is their excellent strength-to-weight ratio and lower density. The two-phase (α+β) alloys are currently most popular among all titanium alloys. It is possible to vary the mechanical as well as physical properties of titanium alloys by either varying percentage of alloying elements or controlling the microstructural evolution and phase estimation during thermo-mechanical processing. Titanium and its alloys serve as a bridge between the ideal properties of aluminium and steel (Gaspar, 2012 and Caiazzo et al., 2017).

Ti-6Al-4V is a (α+β) phase titanium alloy where aluminium (6 wt. %) stabilizes α phase and vanadium (4 wt. %) stabilizes β phase. It is a very important structural material. In the midst of entire α+β titanium alloys, Ti-6Al-4V alloy is highly attractive material for aerospace and automotive industries. The aerospace industries are the biggest consumer (more than 80 %) of Ti-6Al-4V alloy as it possesses excellent combination of toughness, ductility, moderate strength along with excellent corrosion resistance. However, it has poor forming and shaping properties with respect to steel and aluminium at room temperature. Ti-6Al-4V alloy has lower hardenability and it is mostly used in annealed condition. These alloys can be deformed only at high temperature (Donachie, 2000). Ti-6Al-4V alloy possesses lower value of thermal conductivity (about one-fourth of iron and one-third of aluminium). However, its heat of fusion and heat of vaporization are almost double of iron. It is stronger than pure titanium having same stiffness and thermal properties except thermal

conductivity which is around 60% lower than pure titanium (Richter et al., 2007). Generally, Ti-6Al-4V alloy is thermo-mechanically treated to produce desired amount of equi-axed α phase and inter-granular β phase having fine grain for achieving optimum mechanical properties. The β transition temperature for Ti-6Al-4V alloy is approximately 995° ± 20 °C. It varies with its composition, presence of interstitial element and cooling rate. At room temperature, the microstructure mainly consists of two phases i.e. inter-granular β phase and globular α/ equi-axed α phase. The β phase is dispersed in the dominant matrix of elongated α phase. The microstructure of titanium alloys is generally described by the size and arrangement of α and β phases in the matrix (Joshi, 2006). The two types of phase arrangements are lamellar microstructure (with higher α/β surface area and more oriented colonies) which is generated upon cooling from β phase field and equi-axed microstructure (uniform structure composed of α-grains and grain boundaries of β) which is formed during recrystallization and globularization process. Lamellar microstructure is formed at slow cooling rate when deformation or heat treatment of single-phase β-field takes place at a temperature above beta-transus temperature, T_β. It consists of colonies of α-phase lamellae within grains of β phase having diameter of several hundred microns. Lamellar microstructure is characterized by its relatively low ductility, moderate fatigue properties and good creep and crack growth resistance (Kuhlman et al., 1987). The equiaxed microstructure has better balance between strength and ductility at room temperature. Its fatigue property depends on crystallographic texture of α-phase. The effect of microstructure on mechanical properties of Ti-6Al-4V alloy is presented in Table 1.5.

Table 1.5 Effect of microstructure on mechanical properties of Ti-6Al-4V alloy (Leyens and Peters, 2003)

Fine	Coarse	Mechanical property	Lamellar	Equiaxed
○	○	Elastic modulus	○	↑
↑	↓	Strength	↓	↑
↑	↓	% elongation	↓	↑
↓	↑	Fracture toughness	↑	↓
↑	↓	Creep strength	↑	↓
↑	↓	Oxidation behaviour	↑	↓

○ no effect, ↑ increase, ↓ decrease

Depending on cooling rate and prior heat treatment, the micro-constituents and microstructures are divided into several types, namely grain boundary allotriomorph α, globular or primary α (called bi-modal microstructure when the globular α is surrounded by Widmanstatten platelets), Widmanstatten, basketweave and martensitic structure are shown in Fig. 1.4 (Donachie, 2000). A recently described microstructure is bi-lamellar in which retained β phase lies between α platelets in a Widmanstatten structure (Suryanarayana et al., 1998). At very slow cooling rate, cooled from above β-transus temperature, the β-phase mainly transforms into globular α-phase. Increasing cooling rate enhances α nucleation rate in the β grain boundaries. The length and width of these α platelets depend on the cooling rate. An increase in cooling rate increases nucleation rate but decreases growth rate, reducing length and width of the platelets. If quenched, the β grain fully or partially transforms into martensitic α, denoted as α′. Ahmed and Rack (1998) reported that minimum cooling rate necessary for full martensite structure is 410 °C/s for Ti-6Al-4V. A trace amount of β is always present in the martensite. The reason for the presence of β-phase is vanadium as a β stabilizer and 4% V is sufficient enough to drop the temperature for the end of martensitic transformation (M_f) below room temperature (Boyer et al., 1994).

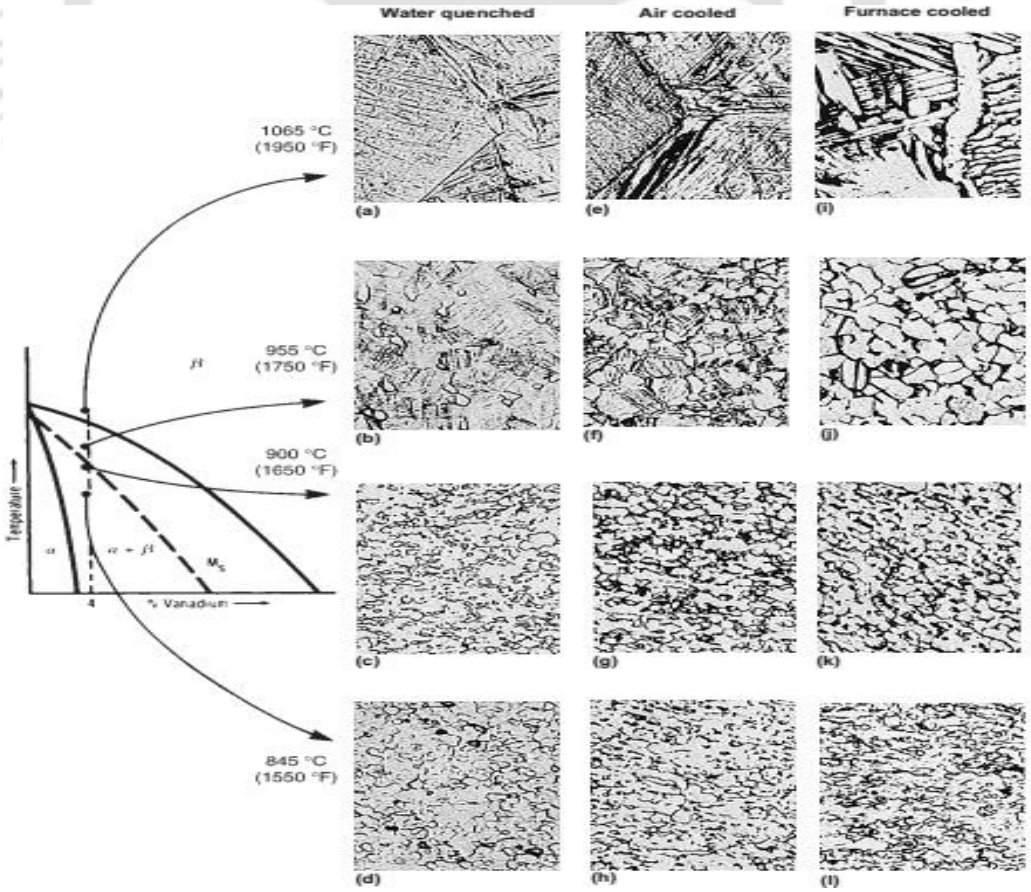

Fig. 1.5 Typical microstructures for Ti-6Al-4V at different cooling rates (Donachie, 2000)

1.8.2 Laser weldability of Ti-6Al-4V alloy

The weldability of a material is defined as the ability to yield a good quality joint at a specific process parameter condition. Alloy compositions, welding procedures and subsequent heat treatments are very much important in determining final properties of the welded joints. Ti-6Al-4V has been reported as the best weldable among all α+β alloys. Ti-6Al-4V is prone to change in strength, ductility and toughness due to thermal cycle exposed during welding. Proper joining process can make the joint ductile and corrosion resistant like base metal while improper joining process may lead to embrittlement of weldments with less corrosion resistance. The main difficulty while welding Ti-6Al-4V alloy is its high reactivity with atmospheric gases above 550 ºC temperature especially in liquid state which causes weld embrittlement and rapid grain growth (Li et al., 2009). Because of the high welding speed and fast thermal cycle during LBW, material gets short period of exposure at elevated temperature which leads to narrow fusion and heat-affected zones suppressing grain growth.

Different types of weld defects are found during LBW of Ti-6Al-4V alloy such as misalignment, distortion, undercuts/underfill, excessive penetration, weld cracks, contamination cracking and porosity (Lisiecki, A, 2012a, and Richter et al., 1997). Misalignment defects appear mostly due to improper fixing of the sheets using clamp and thermal distortion that arises during movement of heat source. In order to minimize it, two welding spots at both edges of the specimen are made before welding. Distortion is a common problem encountered in LBW process. It occurs due to continuous expansion and contraction of the specimen during heating and cooling cycles of LBW process. Distortion causes degradation of the specimen performance which needs to be eliminated or minimized below a critical level. Factors on which weld distortion depends are identified as specimen thickness, welding speed and power, specimen edge preparation and material properties. Specimen thickness and material properties cannot be changed since these are fixed for a given material. However, the weld distortion can be minimized using low heat input and high welding speed.

The most visible weld defect found by visual inspection is underfill. The main reasons for underfill defects are evaporation and expulsion of molten material from the melt pool. At higher beam power or lower welding speed material may evaporate causing underfill defects. Spatters may form at higher laser power which is also a reason for underfill formation. At higher welding speed, cooling rate is faster, so the fusion zone has shorter time to solidify causing underfill. The increase in gas pressure may also account for the expulsion of liquid metal resulting underfill. Underfill may be avoided by reducing welding speed, in other

words by lowering rate of solidification. Generally, crack initiation starts from underfill position of joint and it degrades tensile strength of the weldments and fatigue properties. Underfill reduces cross-sectional thickness of the weld and hence, reduces the strength of the weld. Wang et al. (2003) suggested that underfill can be reduced by slightly re-melting weld surface at increased focal length and lower laser power.

Spatter produces when the molten metal is expelled during welding and it adheres to the surface of the joint. The spherical shape of the spatters indicates metal solidified from small droplets of molten metal without restraint resulting loss of liquid metal. Volatility of the alloying elements and instabilities of the keyhole may be the reasons of spatter. Ti-6Al-4V alloys are generally not considered susceptible to solidification cracking like other structural alloys, such as aluminum alloys and many austenitic stainless steel. However, under severe condition, solidification cracking along columnar beta grain boundaries is reported by Baeslack (1981). Again titanium alloys are also very resistant to HAZ liquation cracking due to the absence of second phase dispersoids or precipitate particles or impurities at the grain boundaries.

Porosity is one of the most common and an undesirable welding defect which severely degrades joint performance. There are many reasons for porosity formation during welding such as physical trapping of shielding gas, chemical reaction at the welding pool, keyhole phenomenon and evaporation of low boiling point elements (Khaled, 1994 and Akman et al., 2009). Generally, two kinds of welding porosities i.e. metallurgical and characteristic pores are observed during deep penetration LBW of Ti-6Al-4V alloy. The pores can appear at various locations in the weld bead such as near centerline of FZ, at the interface between FZ and HAZ or arbitrarily distributed in the FZ. The formation of the pores due to the trapped gases within solidifying weld pool of Ti-6Al-4V alloy is reported in various literatures (Kabir et al., 2010, Gao et al., 2014a and Karimzadeh et al., 2005). The formation of porosity in keyhole mode of LBW is still not well understood. There is a discrepancy in the understanding of actual reason for the formation of porosity in the weld bead. During experimentations, it is not possible to fully eliminate porosity formation during LBW (Panwisawas et al., 2017). However, its number and size of pores can be controlled. The propensity of porosity formation during welding can be minimized under proper shielding gas environment. Titanium has high absorption in laser. Therefore, laser welding can efficiently apply to titanium and its alloys. Due to high absorptivity of titanium alloy by laser, low power density input is required during LBW resulting low heat damage area. Fiber laser having lesser wavelength with higher absorptivity is suitable to weld titanium and its alloys.

The comparison between different welding techniques for welding Ti-6Al-4V alloy is presented in Table 1.6.

Table 1.6 Comparison between different welding processes for welding Ti-6Al-4V (Steen, 2003)

Quality	**LBW**	**EBW**	**TIG**
Welding rate	High	High	Low
Heat input	Low	Low	Large
HAZ	Narrow	Narrow	Large
Bead appearance	Better	Excellent	Good
Fixture	Required	No	No
Welding in air	Yes	No	Yes
Noise and fume	Low	No	High

1.9 Austenitic stainless steel of grade 316L

Normally stainless steels are iron alloy which contains at least 12% (by weight) chromium. During starting of 20th century, it was found that by adding Cr at least 12% in stainless steel, its corrosion resistance dramatically increases. Stainless steels are classified into several subcategories such as martensitic, ferritic, duplex and austenitic stainless steel. Austenitic stainless steel has high level of nickel as well as chromium. Austenitic stainless steel of grade 316L is considered to be more resistant to corrosion due to its high concentration of chromium and nickel typically ranges between 18–20 % and 8–12 %, respectively. It is non-magnetic material. Austenitic stainless steel has good ductility and strength which is maintained also at lower temperature (Mukherjee et al. 2015 and Hao et al., 2015). Austenitic steel can be hardened by plastic deformation without embrittlement. The chemical composition and microstructure of austenitic steel governs its mechanical properties. At ambient temperature, austenitic steel contains a mixture of austenite-ferrite structure (Alcock et al., 2017). Among all types of austenitic stainless steels, grade 316L (i.e. SS-316L) is mostly used in petrochemical, nuclear, marine, architectural applications, heat exchanger tubes, corrosive chemical environments, aerospace and automotive industries. The automotive parts and structure of aircraft are very complex having intricate shapes and design (Gu et al., 2011). In aerospace application, the materials are chosen based on their mechanical properties such as strength, operating temperature range and corrosion resistance. Therefore, Ti-6Al-4V and SS-316L are highly recommended. SS-316L can be welded using laser heat source without using filler material. SS-316L possesses good weldability, high formability, excellent toughness at lower temperature and higher tensile strength. It is more durable and corrosion resistant than ferritic steel. It is not susceptible to solidification cracking during

high speed laser beam welding process. Also, SS-316L is not susceptible to martensitic transformation which forms brittle structure. No preheating and post heating treatment is necessary in LBW of SS-316L. In SS-316L, carbon percentage is very low and hence the carbide which may form in both fusion and heat affected zones during welding may precipitate during cooling stage. The precipitation of chromium carbides occurs at the edge of the austenitic grains. The thermal conductivity of SS-316L is one-third of carbon steels and it has higher absorption coefficient. Hence, higher depth of penetration is achieved in case SS-316L than carbon steel for the same experimental condition (Rahman et al., 2015). The thermal expansion coefficient of SS-316L is generally 50% higher than carbon steel. These factors together with low thermal conductivity cause non-uniform expansion and distortion of the weldments while the material is welded by employing high energy welding techniques. Lasers are highly suitable for welding SS-316L due to their low heat input and high welding speed which reduces metallurgical defects enhancing strength of weldments.

1.10 Organization of the thesis

The present thesis is organized into nine chapters. **Chapter 1** deals with theoretical review of the laser beam welding which is extensively adopted by manufacturing industries. It starts with laser beam properties which are utilized into welding. The laser welding process parameters like laser power, welding speed, shielding gas and joint configuration etc. are presented. The theoretical review and weldability of titanium and its alloy followed by austenitic stainless steel of grade 316L are also discussed. **Chapter 2** deals with literature survey on experimental investigation of laser beam welding of engineering materials specifically titanium and its alloys followed by different grades of austenitic stainless steel. Also, literature survey related to numerical simulation of laser beam welding process is provided at the end. In this chapter the significance of literature survey, scope and objectives of the present research work are described. In **Chapter 3**, experimental setup, design and fabrication of workpiece fixture with shielding gas delivery system, workpiece materials and measurement methodologies are described. **Chapter 4** deals with preliminary as well statistical design of experiments of 5 mm thick Ti-6Al-4V alloy plates and its metallurgical characterization. In **chapter 5,** experimental investigation and bead characterization of 2 mm thick Ti-6Al-4V alloy plates along with bead shape comparison and their metallurgical as well as mechanical properties are discussed briefly. Experimental investigation of 1.5 mm thick Ti-6Al-4V alloy plates and its metallurgical characterization and mechanical properties with respect to line energy are discussed in **chapter 6**. **Chapter 7** deals with experimental

investigation of 3 mm thick austenitic stainless steel plates and its metallurgical characterization based on response surface method. In **chapter 8**, numerical simulation of LBW process for Ti-6Al-4V alloy using double ellipsoidal and cone shaped volumetric heat source models are discussed. **Chapter 9** demonstrates summary and conclusions observed in the present study. Further, the scopes for future work are documented in this chapter. The references are provided at the end.

Chapter 2

Literature survey

2.0 General background

Over last decade, a large number of researchers are working in the area of materials' joining by means of high energy density laser beam welding (LBW) process. There are various research articles concerning experimental investigations and numerical simulations which deal with temperature distribution around melt pool, bead shape and microstructural characterization in the weld bead and variation in mechanical properties with welding process parameters for different kind of engineering materials. The design of weld joint is very complex as the welding area is considered as geometrical discontinuity which creates large stress distribution in the weldments. The interactions between different factors like geometry of weld bead, microstructural modifications assisted by thermal cycle, distortion and misalignment are caused by simultaneous material heating and cooling. Therefore, the weld quality is highly affected. Due to the involvement of huge number of influencing process parameters, the prediction of quality of weldment is a very complicated task (Ayoola et al., 2017 and Ahn et al., 2016). No standard guidelines are available for achieving satisfactory weld quality in laser welding of titanium and its alloys.

During LBW process a non-uniform temperature distribution occurs throughout welded samples. The temperature distribution depends on several factors in the fusion zone such as heat input, temperature-depended material properties, latent heat of fusion and rate of convective and radiative heat transfer (Rai et al., 2007 and Elmer et al., 2004). The acceptance of the specific welding method for product development depends on set of weld quality acceptance criteria which can be attained only by rigorous testing of weldments. The use of laser welding process in manufacturing processes is increasing day by day to improve productivity and quality of the products. Due to the involvement of large number of process parameters, determination of optimum value of process parameters experimentally is very difficult for achieving certain welding performance (Casalino et al., 2005, Ai et al., 2017 and Filip et al., 2003). The literatures related to weldability aspects of pure titanium and its alloys like Ti-6Al-4V and different grades of austenitic stainless steel such as SS-316L grade in terms of microstructural characterization at different locations in the weld bead, bead features such as penetration depth, fusion zone width, fusion zone area, size of heat affected zone, various weld defects and mechanical properties variation with respect to welding process

parameters are documented in this chapter. The present literature survey intends to highlight the contribution of various researchers' in the field of LBW of above mentioned materials. Fusion welding process is a complicated joining technique and it comprises various interacting physical phenomena simultaneously. The flow behaviour of molten metal and heat flux significantly influences temperature gradient, cooling rate and solidification phenomena. Sometime the vaporization of the alloying elements also occurs depending on the imposed energy level on the workpiece surface.

The fiber LBW is a newly developed welding technique. As joining technology advances, the need for joining high melting point materials, intricate shape and miniaturized components is rapidly increasing. Laser welding is a very challenging area and most critical. However, limited work is carried out in this field as compared to conventional fusion welding techniques like gas welding and different kind of arc welding processes. Therefore, definite scope is available to study LBW process of engineering materials. Several experimental and computational investigations on laser beam welding process are carried out by various researchers. Some of the important literatures are presented in this chapter to find out the scopes for present research work.

2.1 Literature survey on titanium and its alloys

Li et al. (1997) reported that LBW comes under the category of fusion welding process. It is most appropriate and non-traditional welding technique to join similar as well as dissimilar materials of titanium and its alloys. Assuncao et al. (2010) reported that fiber LBW offers extremely high welding speed and low operating cost per hour as compared to CO_2 and Nd: YAG laser. The main LBW process parameters are laser beam spot diameter, beam power, welding speed and flow rate of shielding gas (Chen et al., 2013, Costa et al., 2007). Tobar et al. (2010) reported two different welding modes i.e. conduction and keyhole modes of LBW process. Conduction mode of welding occurs at low heat input having LBW power density less than 10^3 W/cm^2. The power density in keyhole mode of welding is in the range of 10^5–10^7 W/cm^2 (Torkamany et al., 2016). Akman et al. (2009) studied microstructural and mechanical properties in Nd-YAG laser beam welded Ti-6Al-4V alloy at different welding conditions. They observed that acicular α′martensite is formed from columnar α and β grains in the FZ and a mixture of α′martensite, acicular α and primary α is formed in the HAZ. It is also observed that grain size increases in the FZ with increased beam power. Mohandas et al. (1999) did microstructural characterization of Ti-6Al-4V alloy in the FZ for electron beam welding process. They concluded that at lower welding speed lesser amount of porosity is

formed. Also, welding speed influences the formation of martensitic lath in FZ. Caiazzo et al. (2013) investigated the disk laser beam welded butt joint of 3 mm thick Ti-6Al-4V alloy plates. They developed special kind of nozzle and workpiece fixture to protect the melt pool from environmental contamination. They reported that α′ acicular martensitic microstructure is developed in the FZ. Also, they reported that the area of FZ is unaffected by defocusing distance although bead profile is affected by defocused position of the laser beam. However, tensile properties of the welded samples are degraded after welding. Bhargava et al. (2014) investigated the effect of different process parameters on penetration depth, bead profile and angular distortion during fiber LBW of 6 mm thick SS 304 stainless steel. They reported that by providing chamfered edges in the base plate, the convexity of the bead geometry and angular distortion can be minimized.

Ahn et al. (2016) investigated the continuous wave (CW) fiber LBW of 2 mm thick Ti-6Al-4V plate at different beam power, welding speed and defocusing distance. The joint quality was characterized in terms of weld geometry, microstructure, weld bead defects and hardness. They reported that spatter and undercut are the main welding defects which appear at high LBW power whereas incomplete penetration occurs at low LBW power and high welding speed. Micropores are also detected in the weld bead and their sizes are in the acceptable range. Caiazzo et al. (2004) investigated CO_2 laser beam welded Ti-6Al-4V alloy having thickness of 1, 1.5, 2.5 and 2.85 mm. They observed that melting of fusion zone area is directly proportional to the specific thermal energy. The value of micro hardness in FZ is slightly increased in the weldments. They also reported that due to the misalignment of the specimens and excessive gap between the sheets, the ultimate tensile strength (UTS) of the welded specimens are degraded. Huiqiang et al. (2004) investigated the microstructural evaluation in FZ and fracture behavior of electron beam welding of Ti-6Al-4V alloy. They reported that disordered and short needle type martensitic microstructures are formed in the FZ and it is responsible for the ductile mode of fracture failure similar to base metal as shown in Fig. 2.1(a) having fine dimples in fractured area. The fracture occurs completely in transgranular manner as shown in Fig 2.1(b). Kabir et al. (2010) investigated the continuous wave Nd: YAG LBW of 5.1 mm thick Ti-6Al-4V plates at different welding speeds and defocusing distances. They reported that crack free weld can be achieved using high power Nd: YAG laser. However, the welding defects like underfill and porosity are also observed in the weld bead. Higher hardness is reported in the FZ and near boundary between FZ and HAZ due to the formation of α′ martensitic phase. They did not found significant differences

in bead geometry, hardness, underfill defects and microstructures in the FZ at different defocusing distances.

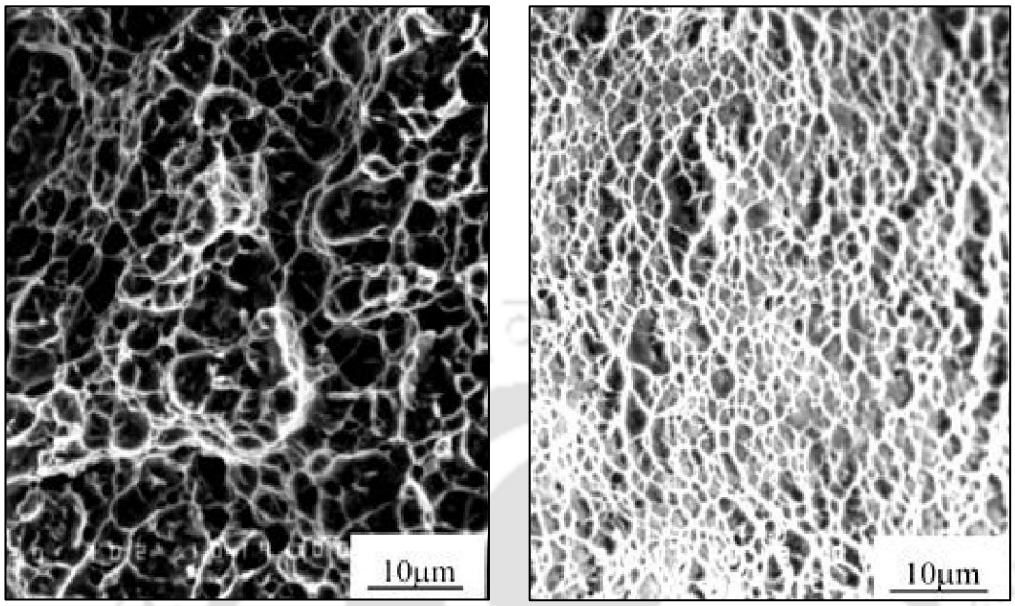

(a) (b)

Fig. 2.1 SEM fractographs of tensile specimens of (a) base metal and (b) weldment (Huiqiang et al. (2004). Copyright (2018) Authors. Open access under a Creative Common License (License No. 4391730733562) from Springer Nature.

Squillace et al. (2012) investigated the effect of welding speed and laser beam power on the weld quality of 1.6 mm thick Ti-6Al-4V plate using Nd: YAG laser. The joint quality was characterized in terms of weld morphology, microstructure and mechanical properties. They reported that during LBW, the joint region (i.e. from FZ to the base metal) undergoes through a large thermal gradient. This spatial distribution of temperature produces a non-uniform microstructure. The microstructure development in the FZ and HAZ depends on specific heat input depending on welding speed and beam power. Zhou et al. (2003) joined Ti-6Al-4V alloy using GTAW process and studied microstructure in the FZ. They reported that the impact toughness of the welded metal is 50 % higher than the base metal.

Mohandas et al. (1998) did microstructural characterization and porosity study in the FZ of Ti-6Al-4V alloy for electron beam welding process. They concluded that at low welding speed less porosity is formed and the formation of martensitic lath depends on welding speed. It is most probably due to the presence of fine acicular martensitic microstructure in these zones. Also, they reported that the welded specimens exhibit lower value of impact toughness in both FZ and HAZ than in the base metal. Rao et al. (2008) investigated electron beam welding of Ti-6Al-4V alloy. They reported that using bead-over-bead welding technique, the notch toughness as well as fracture toughness of the welded

sample improve. They did hardness test and microstructural study in support of their results. The hardness in the FZ is found to be higher than the base metal zone (BMZ). Higher fracture toughness in the FZ is due to the formation of basket-weave microstructure while equi-axed microstructure is formed in the BMZ resulting lower fracture toughness. Lisiecki (2012b) did a comparative study between diode and disk lasers during welding two different thicknesses of Ti-6Al-4V alloys (i.e. 1.5 and 2.0 mm). They reported that better weld quality is achieved by diode laser compared to the disk laser. However, the plasma plume over the melt pool disrupts the flow of shielding gas and it considerably reduces the effectiveness of the shielding gas from environmental contamination. Gao et al. (2014b) investigated the effect of heat input on bead geometry, microstructural features and mechanical properties of Nd: YAG welded Ti-6Al-4V alloy. They reported that V-shaped weld bead is formed at lower heat input whereas at higher heat input, H-shaped bead is formed. Maximum hardness is reported in the FZ due to the formation of fine acicular martensitic structure in both V-shaped and H-shaped weld bead as shown in Fig. 2.2(a) and 2.2(b), respectively. The H-shaped bead shows higher tensile strength than V-shaped bead. However, for both bead profiles fracture occurs in BMZ.

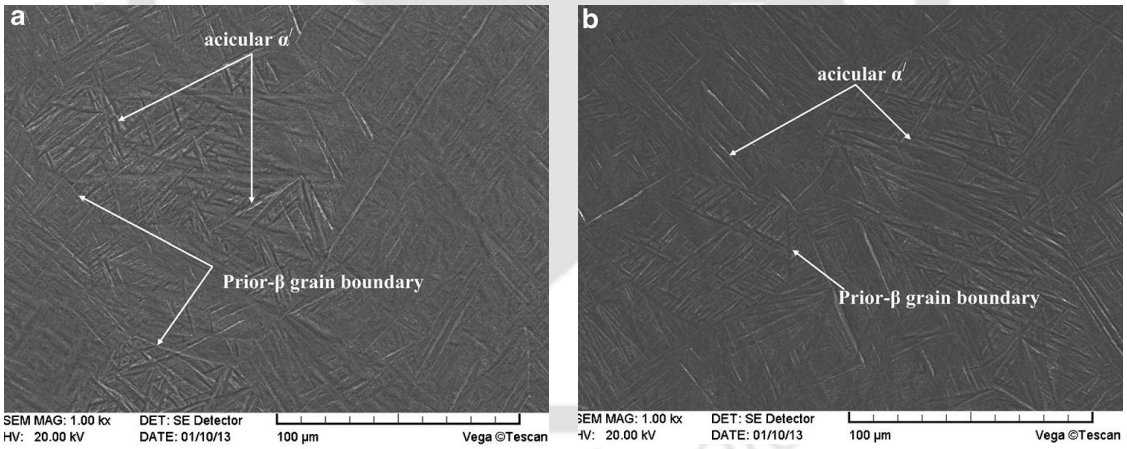

(a) (b)

Fig. 2.2 Microstructures of FZ for two different bead shape (a) V-shaped and (b) H-shaped Gao et al. (2014a). Copyright (2018) Authors. Open access under a Creative Common License (License No. 4387550196951) from Springer Nature.

Campanelli et al. (2015) investigated the fiber laser beam welded Ti-6Al-4V alloy and reported that weld bead geometry is changed from nail head to V shaped with increased LBW speed from 2 to 2.5 m/min. Also, they reported that oxidation of melt pool can be prevented by employing suitable gas delivery system. The tensile properties of the welded specimens are reduced as compared to base metal. Sun et al. (2002) compared the weld quality of TIG, plasma and CO_2 laser beam welded specimens of 5 mm thick Ti-6Al-4V alloy sheets. They

reported that sufficient amount of shielding gas is necessary for achieving successful joints. Also, smallest grains are observed in the laser welded sample than TIG or plasma. Aleksander (2012) reported the effect of disk LBW parameters on weld quality and mechanical properties in terms of tensile and bending strength, bulk and micro hardness while welding Ti-6Al-4V alloy. He found that both FZ and HAZ sizes increase with increasing heat input. There is a slight increase in hardness and tensile strength in the FZ. Cao and Jahazi (2009) joined Ti-6Al-4V plates having thickness of 1 and 2 mm using Nd: YAG laser. They investigated the effect of welding speed on surface morphology, bead shape, welding defects, microstructure, hardness at different regions of weld bead and tensile properties of weldments. It is reported that the microstructure in HAZ consists of a mixture of α′ martensite and primary α phase. Near fusion zone, large amount of α′ martensite along with some amount of primary α are observed whereas far away from the fusion zone a relative increase in primary α is observed because of lower cooling rate. The fusion zone area and its width decreases with increasing welding speed. The HAZ becomes narrow and underfill depth decreases with increasing welding speed. No solidification cracks were observed in the fusion zone. They compared the joint strength and its ductility with the parent material and found slightly higher value. However, the ductility of the joint is reduced due to the presence of micro pores.

Casalino et al. (2015) found fully martensitic microstructure in the FZ and a combination of primary α, blocky α and martensitic α′ in the HAZ during fiber LBW of Ti-6Al-4V alloy. They also reported that welding defects can be minimized by adopting a reliable nozzle design and employing sufficient amount of shielding gas. However, ultimate tensile strength and % elongation of the samples are degraded after welding. Nirsanametla et al. (2014) conducted fiber LBW experiments on 3 mm thick SS 316 work piece and validated their numerical heat transfer model. Tobar et al. (2010) observed that lesser welding defects occur in conduction mode due to the stability of the melt pool as compared to keyhole mode. However, maximum penetration depth is achieved in keyhole mode of welding due to the transfer of more beam energy into the keyhole bottom rather than onto the surface. Zhang et al. (2011) reported that laser beam reaches to the bottom of the keyhole through multiple reflections with the keyhole wall. As a result, energy transfer inside keyhole is increased. Gao et al. (2014a) studied the weld quality of Nd: YAG laser beam welded 0.8 mm thin Ti-6Al-4V alloy sheets. They reported that at higher overlapping factor, coarser grain is formed in the FZ. They also reported that there is a critical value of overlapping factor above which the porosities are reduced extensively.

Costa et al. (2007) used newly developed fiber LBW technique to join 6.5 mm thick Ti-6Al-4V alloy sheets at various welding power and speed at constant defocused position. They showed that full penetration, narrower weld width and minimal weld defects can be achieved at higher LBW power and speed. They also reported that the microstructure in the fusion zone depends on both cooling rate and heat input. Kashaev et al. (2016) reported that bead features such as FZ width and HAZ size depend on heat input during LBW of Ti-6Al-4V alloy using 3.3 kW Nd: YAG laser. Pan et al. (2007) reported similar or slightly higher joint strength of weldments of Ti-6Al-4V alloy as compared to the base metal with reduced ductility. The decrease in ductility is due to the presence of micro pores and inclusions of aluminum oxide in the weld bead. Wang et al. (2003) analyzed the effect of temperature (up to 450^0 C) on tensile properties of Ti-6Al-4V after LBW. They observed that ultimate tensile strength (UTS) of the weldment is slightly higher than the base metal. However, yield stress is lower than base metal especially above 150^0C. The weld bead elongation was about 5% lower than the base metal within 300^OC. Chen et al. (2011b) investigated the effect of process parameters like laser power, welding speed and offset distance of the laser beam from interface of dissimilar material of Ti-6Al-4V with Inconel 718 on joint efficiency during fiber LBW process. Crack free weld is observed at higher laser power and welding speed while joining 2 mm thick sheets of Ti-6Al-4V and Inconel 718 using 1kW fiber laser.

Katayama et al. (2009) investigated the effect of various welding parameters on weld penetration and welding defects in fiber laser beam welding of various aluminum alloys of different thickness. They reported that with increasing laser power, weld beads become deeper. Full penetration into the base plate was obtained at power density of 640 kW/mm^2 and welding speed of 10 m/min. However, the surface in the welded region becomes a combination of both convex and concave profiles. In case of high power density with high welding speed, porosity was not observed although many pores were found at low welding speed. At ultra-high power density, fewer pores were formed at high welding speed. Also, it was reported that nitrogen gas is more effective than argon to prevent the formation of porosity in FZ. Li et al. (2010) introduced fiber laser-gas metal arc hybrid welding process for joining pure titanium plate having 1.5 mm thickness. The effect of welding parameters on weld bead shape, hardness, tensile strength and microstructure of hybrid welding process were investigated and compared with LBW process. It was observed that hybrid welded joints possess better combination of strength and ductility. Weld bead geometry plays a vital role in determining mechanical properties of the welded joints. Also, weld quality strongly depends on it. Hence, the selection of optimum welding process parameters is very crucial for

achieving optimal weld bead geometry. Following conventional method of one variable at a time experiment requires large number of experiments to be carried out which is costly and time consuming. Hence, various soft computing techniques like genetic algorithm (GA), artificial neural network (ANN) and statistical design of experiments (DOE) such as factorial design, Taguchi method and response surface methodology (RSM) are extensively used to find out most significant process parameters and their optimum value for achieving better weld quality and also to predict weld bead geometry, size of the heat affected zone and fusion zone area. Optimization of the process parameters is a key step in RSM. The optimum process parameters obtained from central composite rotatable design (CCRD) of RSM are insensitive to the variation in the environmental conditions and other noise factors. Basically DOE using full factorial method is cumbersome especially when numbers of process parameters are more which leads to a large number of experiments. To solve this problem, now-a-days CCRD approach is extensively followed by the researchers to study entire space of process parameters with less number of experiments. Acherjee et al. (2012) employed RSM to conduct welding experiments on PMMA sheets considering LBW power, travel speed, standoff distance and clamp pressure as input parameters. Their analysis shows that interaction effect of LBW power, welding speed and stand-off distance are higher on weld strength and its width. Further, it was reported that optimum welding parameters can be successfully determined using numerical optimization technique.

Khorram et al. (2010) investigated butt-welded specimens of 1.7 mm thick Ti-6Al-4V alloy plates by means of a 2.2 kW CO_2 laser. Experiments are designed using five level of RSM. Effect of process parameters including laser power, welding speed and focal position on bead features such as FZ width, width of HAZ and penetration depth are investigated using ANN. Their results indicate that welding speed and laser power are the most significant process parameters whereas focal position is found to be insignificant. The multi-response optimization techniques are used to optimize the process parameters. The validation results show that the developed model matches well with the experimental results with an error of 12.5%. Rajakumar and Balasubramanian (2012) derived a relationship to predict the grain size, ultimate tensile strength, corrosion rates and hardness of friction stir welded aluminum alloys using RSM. The developed relationship can be effectively used to predict weld nugget grain size and joint tensile strength. Caiazzo et al. (2013) used CCRD of RSM to conduct fiber LBW experiment on 3 mm thick Ti-6Al-4V alloy. The pores and spatters are not observed within the range of process parameters. Their analysis shows that LBW power produces direct effect and welding speed produces inverse effect on root width and fusion

zone area. However, the defocused position of the laser beam does not affect the area of the fusion zone significantly. Benyounis et al. (2005) employed three levels Box-Behnken design for conducting laser welding experiments. The effect of welding parameters on output responses are investigated by response surface methodology. The results indicate that the developed model predict responses adequately within selected range of experimental plan. Sathiya et al. (2012) used genetic algorithm to relate LBW input parameters i.e. beam power, travel speed and focal position to three responses i.e. depth of penetration, bead width and tensile strength and to determine the optimal welding process parameters. They reported that LBW power is the most significant process parameter followed by interaction effect of power and welding speed. Further, optimization of the process parameters was carried out considering multiple output variables simultaneously.

Anawa and Olabi (2008a) employed Taguchi approach to optimize welding parameters for reducing fusion zone size. Their results indicate that laser beam power and speed have strong effect on fusion zone area. However, focal position is not significant for total weld pool size. Pal et al. (2008) performed welding experiments using RSM in pulsed MIG welding process. They developed a multilayer neural network model for predicting ultimate tensile stress (UTS) of welded plates. Pulse voltage, back-ground voltage, pulse duration, pulse frequency, wire feed rate, welding speed, root mean square (RMS) values of welding current and voltage were used as input variables of the model. UTS of welded plate are considered as the output response. Further responses obtained from multiple regression analysis were compared with the responses obtained from ANN model. They concluded that welding strength predicted by ANN model is much better than that multiple regression analysis. The experimental data was interpolated by Casalino et al. (2005) by means of ANN and it is most important for confirming statistical significance of some parameters. The result of ANOVA analysis was matched with their published literature. The Taguchi method has been applied on high power diode LBW of Ti-6Al-4V alloy to find out the optimum welding parameters such as welding speed, shielding gas etc. that produces lower level of defects. To obtain the lower value of defects in smaller thickness, higher welding speed and helium gas were suggested. Finally, the output of the investigation is validated using ANOVA and Taguchi approaches.

2.2 Literature survey on austenitic stainless steel

Benjamin et al. (2012) did weld bead characterization of 8 mm thick 316L stainless steel by electron beam welding process by varying laser power. It was found that material hardness decreases with increasing Q/V ratio due to the variation in cooling rate. Q is heat energy and V is welding speed. Further, they found that material toughness is decreased by increasing Q/V ratio due to reduced grain size which depends on FZ cooling rate. Also, they found that ferrite concentration in FZ highly depends on cooling rate. Tadamalle et al. (2014) reported that welding efficiency of Nd: YAG welded stainless steel of AISI 304L grade depends mostly on welding speed. Defect free weld can be obtained at optimum welding speed. Sun et al. (2014) did comparative study between LBW process and arc welding process of 2.3 mm thick low carbon steel plate. They reported that LBW process induces lesser distortion and longitudinal residual stress in the welded specimens compared to arc welding process. Nirsanametla et al. (2015) investigated the effect of controlled welding environment during fiber LBW of 5 and 3 mm thick stainless steel plates of SS-304 and SS-316. They reported that weld quality is improved by conducting welding experiments under argon gas atmosphere. A set of experiments were designed by Quintino et al. (2007) while joining 19 mm thick low carbon steel used for pipe line application using a high power fiber laser. The experiments were carried out using four levels of beam power and six levels of welding speed. The beam focal point was fixed at workpiece surface. It was reported that conduction mode of welding is prevailed at low heat input having lesser penetration depth which is increased significantly at higher heat input with keyhole mode of welding. The weld depth decreases exponentially by increasing welding speed and it shows almost linear relationship with laser beam welding power.

Miranda et al. (2009) compared microstructures of 19 mm thick low carbon steel plate welded using fiber laser and TIG. It was observed that the microstructure in the base metal is changed from fine-grain-ferrite and pearlite to fine-structure martensite after welding. With increased heat input, the microstructure in the fusion zone becomes coarser with Widmanstatten morphology with decreased hardness value. Fine microstructure was observed in TIG welding with lower hardness value than fiber laser in the fusion zone. Narrow and deep penetrations of weld bead, fine grain structure were observed in fiber laser than TIG welding of same material. Zhang et al. (2014) conducted deep penetration LBW of 12 mm thick stainless steel with a 10 kW fiber laser. The effect of process parameters on weld bead, microstructure and mechanical properties of the joints were investigated. Results revealed that focal position plays an important role for welding thick plates. There exists a certain

range of power which produces full penetration in the joint. The weld depth was also influenced by the top shielding gas. The bottom shielding gas affects the stability of the entire welding process and is responsible for the weld appearances for both top and bottom surfaces of the joint. Kaflan et al. (2009) used 15 kW fiber laser for joining 8 and 16 mm thick stainless steel plates. Full penetration was achieved at 7 and 3 m/min welding speeds for both 8 and 16 mm thick plates, respectively. Rayleigh length and beam diameter were critical although narrow sound welds can be achieved; heavy spatter ejection along with underfill can take place at the top and root side, particularly at high power density and low line energy. Spatter was observed by using high speed imaging of the weld pool surface and keyhole. An illustrative theoretical description and the formulation of a standard documentation methodology were developed for generalization and transferring the knowledge as a guideline to incorporate spatter suppression in LBW processes.

Yousuke et al. (2007) investigated the bead-on-plate welding of SS 304 steel plate using 6 kW fiber laser. The effect of laser power, power density and welding speed on weld quality were investigated at four laser beam spot diameters of 130, 200, 360 and 560 μm. The welding phenomena were observed using a high-speed video camera having X-ray transmission imaging system. The keyhole type of penetrations was observed at all spot diameters and maximum depth of penetration of 11 mm was observed at 130 μm spot diameter at 0.6 m/min welding speed. It is also observed that a sound weld bead is formed at 6 m/min welding speed with 360 μm spot diameter. Lifang et al. (2013) did a comparative study of overlap welding on auto-body-galvanized steel and cold rolled steel using fiber and CO_2 lasers. They studied bead shape and mechanical properties of the weldments. They found that the shape of fusion zones are ‘I’ and ‘Y’ shaped while welding using fiber and CO_2 laser, respectively. Better mechanical properties and more uniform crystalline grains of the welded plates were observed in fiber laser than CO_2 laser. Kumar et al. (2017a) investigated laser welding of 1.5 mm thick austenitic stainless steel by varying incident angle of pulsed laser beam. It is reported that beam power is most significant parameter which greatly affects ultimate tensile strength of the weldments followed by incident angle and welding speed. Tan and Shin (2015) studied multi-scale modeling of solidification behaviour and microstructure development in keyhole mode laser welding of austenitic stainless steel. The developed model is validated with the experimental results and the effect of welding parameters on dendrites’ growth rate are reported. Baghjari and Mousavi (2013) studied the effect of process parameters and post-weld heat treatment on microstructure and hardness of laser beam welded AISI 420 stainless steel. Shanmugarajan et al. (2013) studied the influence of

various process parameters such as beam power, welding speed, flow rate of shielding gas and laser beam mode on developed microstructure in FZ and mechanical properties of weldments for 304B4 borated stainless steel. Kumar et al. (2017b) did the comparative analysis between pulsed Nd:YAG laser welding of AISI 304 and AISI 316 stainless steels. They reported that higher line energy is required for SS-304 as compared to SS-316 to achieve higher ultimate tensile strength and minimum weld width. Also, they reported that lower line energy yields fine grain structure along with higher δ-ferrite fraction as compared to higher line energy irrespective of base metals of SS-304 and SS-316 as shown in SEM image in Fig. 2.3.

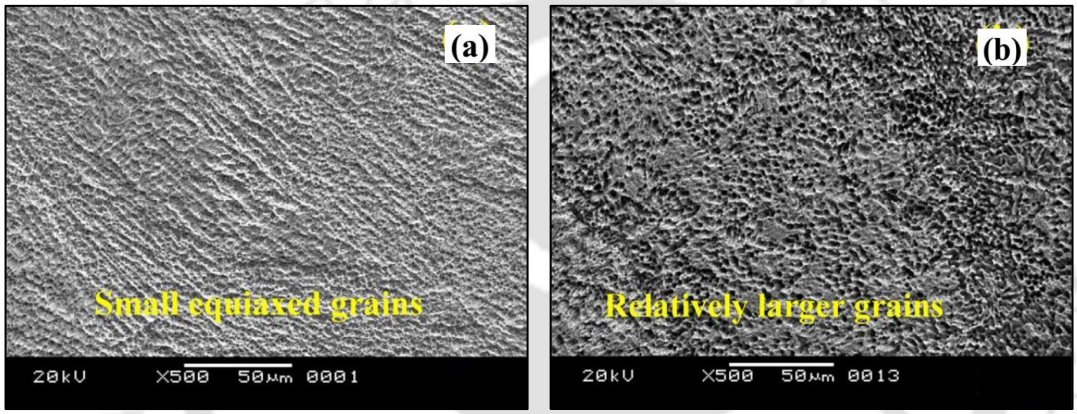

(a) (b)

Fig. 2.3 Microstructures at (a) lower and (b) higher line energies Kumar et al. (2017b). Copyright (2018) Authors. Open access under a Creative Common License (License No. 4387540301519) from Elsevier.

Balasubramanian et al. (2007) investigated LBW of austenitic stainless steel of 3 mm thick plates using 2kW Nd: YAG laser. The effect of laser power, welding speed and flow rate of the shielding gas on weld bead geometry was investigated. ANN and multiple regression analysis techniques were used for the modeling purposes which are further used for the prediction of output parameters. Olabi et al. (2007) developed regression model by employing statistical DOE techniques for minimization of residual stress in laser beam welded components of AISI 304 steel. They reported that residual stresses are not strongly affected by focus position. However, it is strongly influenced by welding speed. Anawa and Olabi (2008b) employed Taguchi method using L25 orthogonal array for conducting LBW experiments on 2 mm thick AISI 316L stainless steel. Their developed model adequately predicts the output responses within the selected range of process parameters. Also, they reported that tensile strength of weldments is not affected by focus position. However, the responses are strongly influenced by laser beam welding power along with welding speed.

A mathematical model is developed by Zhou et al. (2005) to study the behaviour of fluid flow in the melt pool, heat transfer and keyhole dynamics during keyhole mode of pulse laser welding. The effect of laser power, scanning speed, defocus distance, beam incident angle and line energy on weld bead geometry of laser welded samples of dissimilar material of AISI 304L and AISI 430 stainless steel are investigated by Khan et al. (2012). Matsunawa et al. (1998) studied weld pool dynamics to reveal the mechanism of porosity formation and its suppression methods. A numerical model is developed by Cho et al. (2012) to study the temperature profile in the weld bead and molten pool dynamics for high power disk laser welding of structural carbon steel. Balasubramaniam et al. (2008) conducted welding experiments using three level of Box Behnken's method to analyse transient temperature profiles, weld pool geometry, bead width using SYSWELD software for SS 304 sheets and optimized weld parameters such as LBW power, welding speed and beam angle for deep penetration. Masoumi et al. (2010) investigated the effect of pulse frequency, laser energy and weld speed on mechanical and metallurgical characterization of low carbon steels and found that effective pulse energy is the most controlling factor to determine joint strength. The quality of the fiber LBW specimens of SS-316L is investigated by Rong et al. (2017) in terms of microstructure, hardness, distortion and residual stress. They reported that large amount of austenite with insignificant amount of ferrite is formed in FZ as shown in Fig. 2.4 at different magnifications.

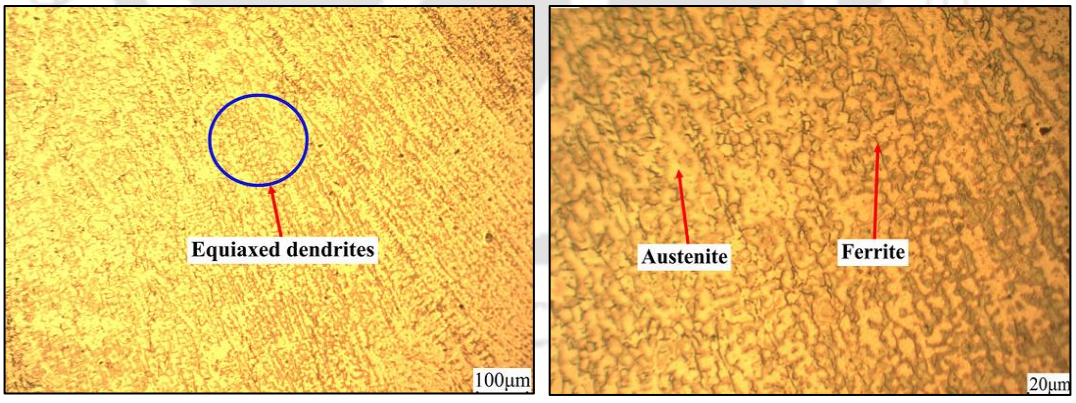

(a) (b)

Fig. 2.4 Microstructure of fusion zone for SS-316L at (a) 100X (b) 500X Rong et al. (2017). Copyright (2018) Authors. Open access under a Creative Common License (License No. 4391740066410) from Springer Nature.

Nath et al. (2002) investigated the amount of heat energy required to melt a substrate in welding process using experimental results, dimensionless parameter model and energy balance model. Hayajneh et al. (2018) conducted DOE to weld stainless steel. They successfully identified the most significant process parameters affecting output responses like

bending distortion using analysis of variance (ANOVA) technique. Sathiya et al. (2011) employed Taguchi approach to find out optimal welding condition. They developed a relationship between process parameters i.e. welding power, welding speed and defocusing distance with output responses such as penetration depth, FZ width and tensile strength. Katayama et al. (2010) studied fiber laser welding process and reported that at high welding speed spatter is generated which enhances underfill and undercut weld defects at the top of the weld bead while at lower welding speed porosity is formed at the keyhole tip. Kawahito et al. (2009) observed that spatter in molten pool is generated by shear force which is accompanied by vapour plume inside melt pool. Wang et al. (2012) reported that periodic oscillation of vapour plume is responsible for oscillation of keyhole during high power fiber LBW process. Benyounis et al. (2005) adopted Box–Behnken design matrix of RSM for conducting welding experiments. They reported that welding speed provides inverse effect on bead features whereas welding power shows direct effect on it.

2.3 Literature survey on numerical simulation

Presently, welding has become most important material processing technology in manufacturing processes. At the same time stress is given on reduction of cost and the simplest possible way to develop a new product quickly. The dynamical development of computer technology in the last few years has markedly contributed to the development of numerical analysis. This is also true for the welding area, where numerical simulations can solve even more complex tasks by shorter computation time. With the help of numerical analysis, it is possible to simulate welding process on the basis of obtained results. Now-a-days, modelling and simulation has become a powerful tool for welding research and development. After combining software based simulation approaches with less experimental validations, welding technology can be transformed from earlier mode of “theory-experiment-production” to the newer mode “theory-computer-simulation-production” mode. During last two decades many of the existing welding processes have been simulated by numerical methods, especially by finite element methods.

The numerical simulation of a welding process is a complex process involving interaction of thermal, mechanical, electrical and metallurgical phenomena. Due to the involvement of large number of variables, the experimental determination of all input parameters is very difficult for achieving higher welding performance. Hence, the demand of finite element method (FEM) based numerical simulation technique is progressively increasing. The use of FEM in product development is now well established and became a

part of the manufacturing industries. Its use in manufacturing industries is increasing day-by-day to improve the quality of the products. It is also useful for better understanding of the effect of different process parameters on the quality of the products (Yang et. al., 2010). In mathematical aspect, FEM approach is used for getting solution of partial differential and integral equations (Tsirkas et. al., 2003). The thermal cycle in welding is studied by analytical and numerical methods by many researchers. The most popular analytical model for predicting transient temperature profile during welding is developed by Rosenthal in 1946 for moving heat source considering quasi-stationary state where heat source is concentrated at a point. The temperature dependent material properties are not included in his model. This point heat source model was insufficient to explain transient temperature profile (Rosenthal, 1946). Goldak et al. (1984) considered a 3-D non-axisymmetric double-ellipsoidal heat source model in order to simulate welding phenomena. Na and Lee (1987) analyzed transient temperature distribution in GTAW (gas tungsten arc welding) process by using a 3-D FEM model. The combination of convection and boundary conditions were varied during simulation. Frewin and Scott (1999) developed a 3-D FE model to calculate transient temperature history at the fusion zone and HAZ considering Gaussian energy distribution of laser beam. The simulated result was in close agreement with the experimental data. Tsirkas et al. (2003) developed a finite element based SYSWELD code to simulate LBW process using non-linear heat transfer analysis. This model is used for coupled transient thermo-mechanical analysis considering temperature dependent material properties of AH36 shipbuilding steel plates. Nguyen et al. (2004) derived an analytical solution for double ellipsoidal heat source model for finite thick plate. Their solution can be used effectively to predict the thermal history of a thick welded plate and also the shape of weld pool. Zhu and Chao (2004) developed an inverse analysis method to determine transient temperature history of friction stir welded 304L stainless steel based on experimental data of transient temperature history at several specific locations. After transient temperature field is determined, the residual stresses in the welded plate are then calculated using a three-dimensional elastic–plastic thermo-mechanical simulation.

Deng and Murakawa (2006) developed both 2-D and 3-D FE codes to measure transient temperature and residual stress in multi-pass welding of 304 stainless steel pipe. The simulated results show that 2-D model saves large amount of computational time and it can be effectively used to simulate temperature fields and residual stresses for SS-304 pipe. Experiments are carried out to verify simulated results and both 3-D and 2-D models are in good agreement with the experimental results. Spina et al. (2007) developed a 3D finite

element model to predict the displacement of AA5083 thin sheets during LBW process at different welding speeds. Yang et al. (2010) developed a finite element model to measure the size of heat affected zone in laser heating of Ti-6Al-4V plate and concluded that the size of HAZ decreases with increasing laser scan speed. Biswas et al. (2010) developed a 3-D FEM model for double-sided fillet submerge arc welding (SAW) process and successfully compared the simulated results with the experimental results. The temperature distribution obtained from both FEM analysis and experimental measurements fairly compared well with a variation of 8% for peak temperature. Shanmugam et al. (2010) employed a FEM code to determine thermal field and bead shape during LBW of T-joint. Proper fusion of base material (horizontal and vertical sheets) is achieved when the laser system is operated at 60° beam incident angle irrespective of the beam power and welding speed. A weld defect is found in the macro-graph at 30° beam angle. Comparison between experimental and simulation results reveals a very good correlation between depth of penetration and bead width with an error of 2.78% and 1.9%, respectively. Pengfei et al. (2011) developed a 3D FEM model using ANSYS® to simulate heat transfer phenomena. It is observed that the distribution of temperature gradient and the change in depth-to-width ratio in the weld pool have corresponding relationship with the generation of undercut. Ranjbarnodeh (2011) developed a 3-D FEM model to predict temperature profile during welding of dissimilar materials (CK4 and AISI 409) using automatic TIG welding process. Also, experimental measurements were performed to assess the effect of welding parameters on grain growth in HAZ. It was concluded that the grain size and its distribution were strongly dependent on heat input during welding. The sample with highest welding heat input (i.e. 583 J/mm) showed larger grain size (250 μm), more homogenous grain size distribution in the HAZ for AISI 409. Double-ellipsoidal volumetric heat source with Gaussian distribution of heat intensity is most popular, which is used for the modeling of fusion welding process. Yadaiah and Bag (2012) suggested an optimum value of ratio of front and rear length of double ellipsoidal heat source model.

Shanmugam et al. (2009) developed a 3-D FE model using ANSYS® to obtain transient temperature profile and melt pool shape. They considered a 3-D conical Gaussian heat source distribution for performing non-linear transient thermal analysis. Thermo physical material properties of AISI 304 stainless steel were also included in the model. Good agreement between simulation and experimental results were observed. Moreover, only conduction based heat transfer models are not sufficient for an accurate assessment of thermal cycles and weld bead dimensions. Transport phenomena based on heat transfer and fluid

models are also required for an exact estimation of transient thermal history in molten weld pool (Bag and De, 2010, Yadaiah and Bag, 2013). Yadaiah and Bag (2014) proposed a new 'egg' configuration heat source model for simulation of linear GTA and LBW process to measure transient temperature history and predict weld pool size. The advantage of this model is less number of parameters as compared to double ellipsoidal heat source model. Akbari et al. (2014) developed a 3-D FEM model for the prediction of transient temperature profile of laser welded Ti-6-Al-4V alloy considering Gaussian energy distribution of laser beam. The average absorptivity of Ti64 alloy was considered as 0.34. The thermo physical property of Ti-6-Al-4V alloy was also incorporated in the model. The model prediction error was found in the range of 2-17%.

2.4 Significance of literature survey

From literature survey it is observed that successful joining of Ti-6Al-4V alloy using LBW process is strictly dependent on the keyhole behavior whose stability depends on the balance between recoil pressure and surface tension of the surrounding keyhole walls. If keyhole collapses, penetration depth becomes lower and gas bubbles get trapped in the weld pool leading to porosities. High beam power density at the workpiece surface is crucial to achieve and to maintain keyhole mode of welding. Too high power density can result in spatter, undercut, underfill and dropout. For a given laser power, smallest focal spot gives maximum power density. High power density is not always desirable during welding as it may cause extensive evaporation of materials from the workpiece surface resulting underfill defect. It is also observed from the survey that suitable welding technique for titanium and its alloys are not yet fully established. However, laser welding is one of the most efficient welding techniques which is confirmed by laser processing industries market value in billion dollars' business. Other welding methods, like gas and arc welding are not suitable for titanium and its alloys as they yield poor weld quality. However, laser has prominent properties which can provide a good weld quality for titanium and its alloys. Laser beam welding process is a complex process having many control parameters. However, this process is stochastic in nature. Due to this, achieving optimum process parameters just by trial-and-error method is very difficult. For successful welding of Ti-6Al-4V alloy, some factors need to be considered.

To achieve high weld quality in Ti-6Al-4V alloy by employing traditional fusion welding techniques is very challenging because of its extremely high affinity towards atmospheric gases such as H_2, O_2 and N_2 beyond 500–650°C temperature which leads to

welding defects. Small concentration of these elements strengthens titanium at the expense of ductility and toughness. Therefore, hydrogen and oxygen pickup tendency of the melt pool should be minimized by supplying sufficient amount of inert gas like argon or helium during LBW process. Moreover, the shielding gas flow rate is maneuvered during LBW to suppress oxidation and plasma for improving weld quality and weld appearance simultaneously. The simultaneous heating and cooling cycles are involved in welding processes which affect mechanical properties of Ti-6Al-4V alloy. Hence, it needs to be considered while welding in progress. It is found that weld quality is highly susceptible to welding techniques, variation in material thickness, types of shielding gas, laser heat source, joint design, design of workpiece fixture, welding modes, nozzle design and selected welding process parameters. Still now, LBW experiments on Ti-6Al-4V alloy are mainly carried out by CO_2 laser and low power of Nd: YAG laser. However, limited experimental research work concerning weldability of Ti-6Al-4V alloy using fiber laser is available in the literature. The understanding of the influence of LBW process parameters on bead features, metallurgical characterization, weld defects and porosity formation and its minimization techniques are still lagging in case of continuous wave fiber LBW process of similar material of Ti-6Al-4V alloy and austenitic stainless steel of grade 316L.

2.5 Scope and objectives of present research work

The goal of this ongoing research work is to investigate the fiber laser weldability of similar joint of Ti-6Al-4V alloy and stainless steel of grade-316L without using filler material. The fiber laser weldability of Ti-6Al-4V alloy and SS-316L are studied by analyzing the effect of laser welding process parameters on weld bead geometry, microstructure and weld defects. The mechanical properties are measured using Vickers microhardness and tensile test. Ti-6Al-4V alloy is welded with three aspects: different laser power, welding speed and defocused position of laser beam. The quality of the welding is investigated via metallography and mechanical properties. The surface appearance is observed by an optical microscope. The microstructure is observed using optical microscope and their morphologies are compared using field emission transmission electron microscope (FESEM). Further, the fractured surfaces are analyzed using FESEM to confirm different modes of fracture failure i.e. ductile or brittle fracture mode. The objectives of the present work are as follows.

- To design and fabricate a special types of workpiece fixture having shielding gas delivery system which is efficiently protect the melt pool and to reduce weld bead

contamination from atmospheric air and to minimize distortion and movement of workpieces during welding of similar material of Ti-6Al-4V and SS 316L alloy. To confirm shielding gas effectiveness, the weld bead appearance is investigated under naked eye as well as under optical microscope. Further, EDS analysis is performed for measuring chemical compositions to confirm any oxide formation during welding.

- To investigate the feasibility study of LBW process by conducting preliminary bead-on-plate experiments at various welding conditions. Ti-6Al-4V plates having thickness of 5 mm, 2 mm and 1.5 mm, also SS-316L plates having thickness of 3 mm are considered as workpiece materials.
- To carry out statistical DOE to find out optimum process parameters window and feasible welding conditions to generate deep penetration in keyhole mode of welding, narrow FZ width and small HAZ. To study the effect of different process parameters such as welding power, welding speed, defocused position of laser beam on bead appearances, bead features (such penetration depth, width and area of FZ and size of HAZ) and mechanical properties of weldments.
- Microstructural characterization in the fusion zone (FZ), at different locations within heat affected zones (HAZ) and base metal zone (BMZ) and to study their variations at different welding conditions at all three zones. Further, their morphologies are compared with FESEM images. To find out correlation between developed microstructures in the weld bead and variation in mechanical properties of weldments such as Vickers microhardness and tensile properties at different welding conditions are investigated.
- To investigate different weld defects like underfill, porosity that appear in the weldments at different welding conditions and to study their minimization techniques.
- To study the size and distribution of micro-pores in both T and X-shaped beads and their effect on mechanical properties of the joints.
- To investigate different modes of fracture failure, the fractured surfaces are analyzed in FESEM. During tensile tests, the fracture in the specimens may be occurring in two different modes i.e. either in ductile or brittle mode. The fracture surfaces after tensile tests are investigated using FESEM images and the surface topography is compared with base metal. At the microscopic level, ductile fracture is characterized by a uniform or elongated dimple structure, tearing ridges with large plastic deformation. Whereas, brittle fracture is low energy fracture and it occurs with no or minor plastic deformation and it is characterized by unstable crack growth.

- During LBW, a non-uniform temperature distribution takes place throughout the workpiece. The temperature distribution depends on several factors such as heat input, temperature depended material properties, latent heat of fusion and rate of convective heat flow in fusion zone. The heat loss to the surrounding takes place by convection and radiation. Due to these large numbers of variables, the experimental determination of all input parameters is very difficult for achieving higher welding performance. Hence, a three-dimensional FEM model using ANSYS®14.5 is carried out by employing both double ellipsoidal and 3-D cone-shaped volumetric heat source models to study the effect of laser beam power and welding speed on temperature profile of weldment in the FZ and away from the FZ. The temperature dependent material properties (i.e. thermal conductivity, enthalpy, density, specific heat and emissivity) of Ti-6Al-4V alloy are also incorporated in the FEM model.

Chapter 3
Experimental setup, workpiece materials and measurement methodology

3.0 Experimental setup

In the present study, a 2 kW solid state ytterbium doped fiber laser having wavelength of 1.08 µm combined with computer numerical control (CNC) worktable is used. The welding system mainly comprises of laser generation unit, CNC controlled work station having resolution of 100 µm for linear axis and 0.01 degree for rotary axis, laser column, laser beam delivery system and welding nozzle. The fiber laser beam welding machine used in the present study is shown in Fig. 3.1. The laser head is attached vertically and it is moved using a CNC controller. The worktable is kept stationary during welding process and heat source is moved along the length direction of the workpieces. The fiber laser beam welding machine configurations and the parameters which are kept fixed during experiments are provided in Table 3.1. During most of the experiments, the laser head is tilted by an angle of 5° with vertical axis to prevent the focusing lens getting damaged from back reflection of laser beam. The welding experiments are carried out at "Laser Design and Industrial Applications Division," Raja Ramanna Center for Advanced Technology (RRCAT), Indore.

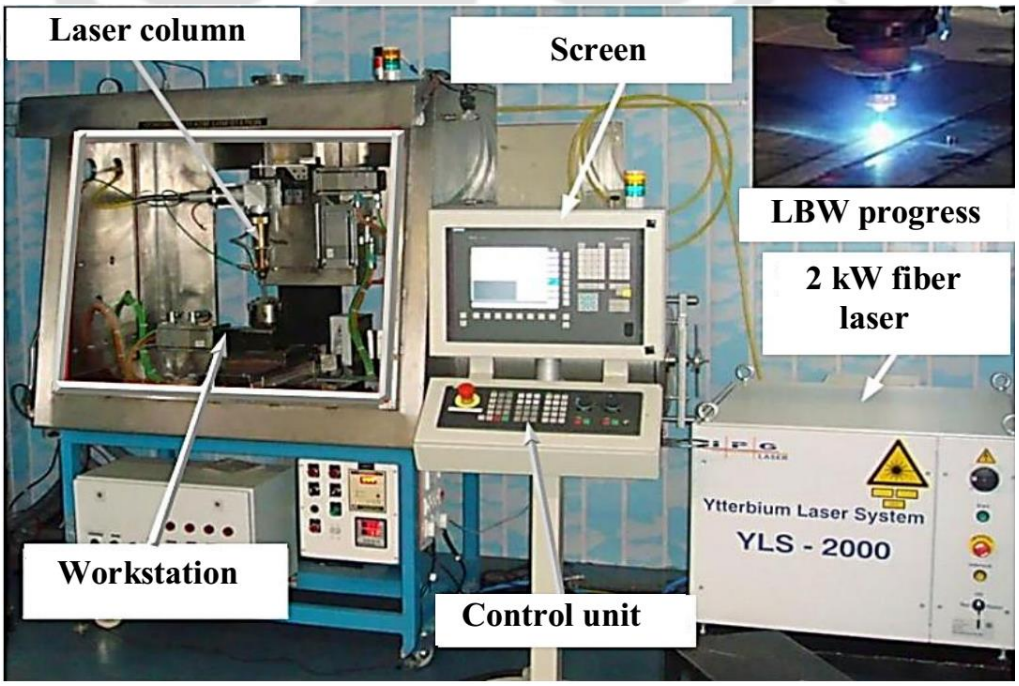

Fig. 3.1 Photograph of fiber laser beam welding experimental set up

Table 3.1 Fiber laser machine configurations and fixed parameters during welding

1.	Power delivering mode	Continuous wave (CW)
2.	Laser beam spot diameter	200 µm (at processing point)
3.	Emission wavelength	1.08 µm
4.	Incidence angle of laser beam	85°
5.	Type of shielding gas	Argon (99.99% purity level)
6.	Beam product parameter (BPP)	Less than 2.5 mm mrad
7.	Standoff distance (SOD)	10 mm fixed from workpiece surface. In some cases varied.
8.	Beam mode	Multimode, 40% TEM_{00} and 60% TEM_{01}
9.	Shielding gas flow rate	(i) 10 liter per minute (from both sides of a specially designed workpiece fixture Fig. 3.2). (ii) 5 liter per minute (surrounding laser beam nozzle and with another nozzle at an angle 45° with laser column on top surface of workpiece).
10.	Fiber core diameter	50 µm

3.1 Workpiece fixture

From literature survey, it is observed that bead shielding is necessary to minimize oxidization and atmospheric contaminations in order to achieve satisfactory weld quality. To reduce bead contamination from atmospheric air and weld distortion during welding of Ti-6Al-4V alloy, a workpiece fixture with shielding gas delivery system must be suitably designed. In the present study, a specially designed shielding gas delivery system in the workpiece fixture is fabricated as shown in Fig. 3.2. The workpieces are kept within fixture and it is properly fixed using clamping device to minimize distortion and displacement of workpieces during welding. The direction of heat source movement during welding is also presented in Fig. 3.2.

3.2 Workpiece materials

In the present study, titanium alloy (Ti-6Al-4V) of grade-5 (AMS4911) plates in annealed condition with three different thicknesses of 5 mm, 2 mm and 1.5 mm are used for experimentations along with 3 mm thick plates of stainless steel grade 316L (SS-316L). The workpiece dimension is 100 × 70 × t mm^3 (material thickness (t) = 5, 2 and 1.5 mm) for Ti-6Al-4V alloy and 120 × 120 × 3 mm^3 for SS-316L. All samples are welded in butt configuration. The cleanness of specimen surface shows great impact on weld quality for both Ti-6Al-4V and SS-316L due to their higher susceptibility towards environmental contaminants. Hence, the specimen surfaces are cleaned using wire brush and acetone, respectively before welding. The standard concentration (wt. %) of alloying elements in base

metal (BM) of Ti-6Al-4V and SS-316L are measured using energy dispersive X-ray spectroscopy (EDS). These results are presented in Table 3.2 for Ti-6Al-4V and in Table 3.3 for SS-316L.

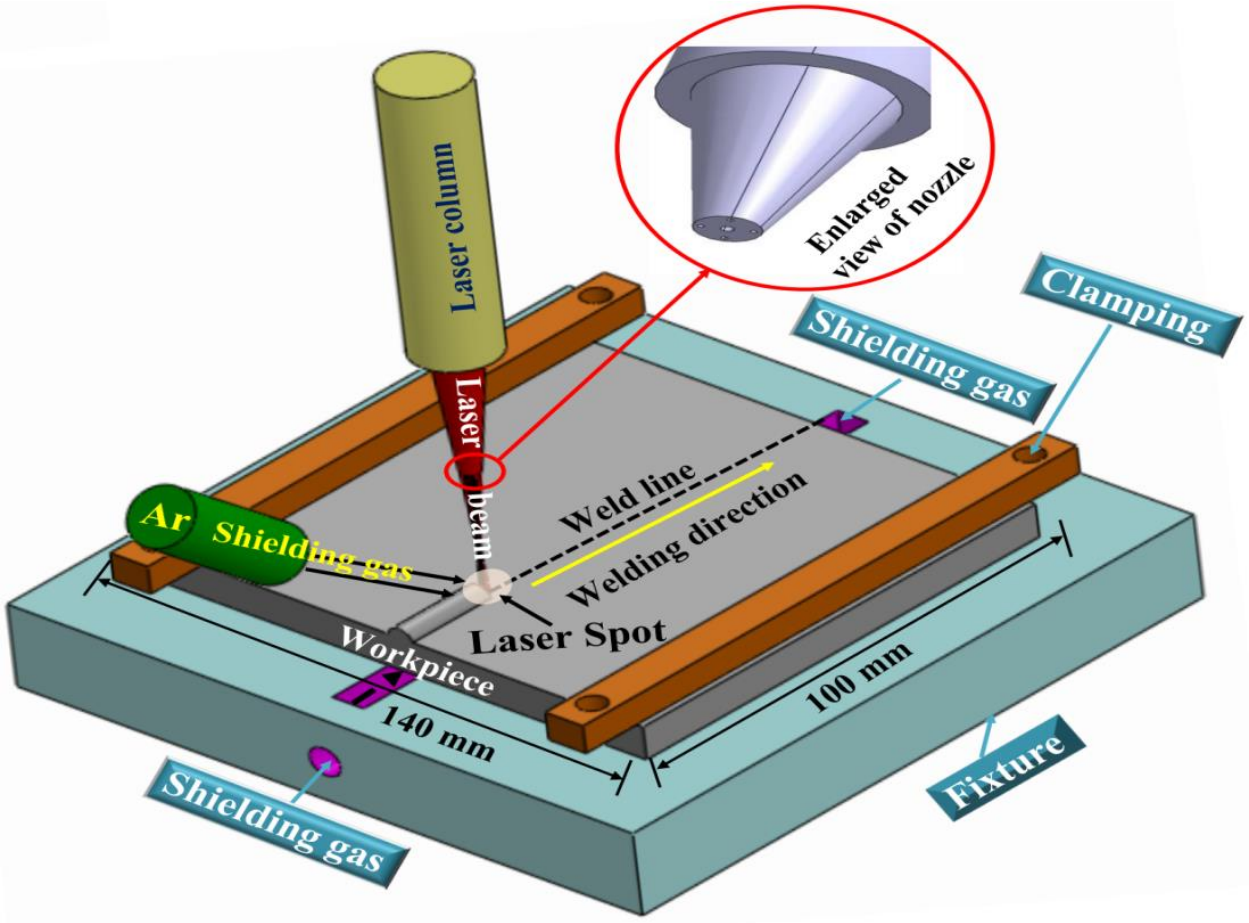

Fig. 3.2 Schematic diagram of laser beam welding setup, welding direction and specially designed workpiece fixture with shielding gas delivery system

Table 3.2 Chemical compositions of Ti-6Al-4V alloy base metal

Element	C	Al	V	Fe	H	N	O
Wt.%	<0.08	5.5-6.75	3.5-4.5	<0.30	<0.015	<0.03	<0.25

Table 3.3 Chemical compositions of SS-316L base metal

Element	C	Mn	P	S	Si	Cr	Ni	Mo	N	Fe
Wt.%	0.03	0.9	0.1	0.3	1.7	17.3	9.5	1.6	0.1	Balance

3.3 Joint configuration

The joints which are widely used for laser welding are butt joint, lap joint, spot weld, flank weld etc. The butt joint has simple geometry and filler metal is not necessary for this of joint configuration. Therefore, titanium alloy and SS-316L are welded in butt configuration only in the present study without using any filler material. In butt configuration, maintaining

gap between two plates is a critical issue due to small laser beam spot diameter (Sokolov et al., 2012). Therefore, the specimens' edges are suitably prepared maintaining surface roughness, R_a in the range of 1.5 – 2.1 µm to achieve close fit up gap between two specimens so that laser beam doesn't pass through it without heating the material. The face gap tolerances are kept within 15% of the thickness of the material.

3.4 Shielding gas and its flow rate

In laser welding of Ti-6Al-4V, few undesirable phenomena like oxidation of base metal and plasma effect occur. Shielding gas helps in improving quality, appearance and mechanical properties of the weld. The parameters of the shielding gas are type of gas and its flow rate. Selection of proper shielding gas is very important. The shielding gas is especially used to control the plasma. Hence, ionization potential of shielding gas must be considered while selecting. The value of the ionization potential is decreased as the molecular weight decreases. The low ionization potential can easily transform the gas into ions. Therefore, it is not much effective for shielding purpose. Hence, shielding gas having high ionization potential such as helium or argon should be selected. The ionization potential of shielding gases is provided in Table 3.4.

Table 3.4 Ionization potential of shielding gases (Larson and Meredish, 1990)

Shielding gas	Symbol	Molecular weight	Ionization potential (eV)
Argon	Ar	39.95	15.7
Helium	He	4	24.5

From Table 3.4, it is observed that helium possesses higher ionization potential than argon. However, the advantage of using argon is due to its higher density than air. When atmospheric gas is ejected, argon quickly falls down to the weld area as compared to helium. The other advantage of argon is its cost. Helium is expensive than argon. So for long term use like in welding industry, argon is a saver. Hence, in the present study argon gas is selected as shielding gas for all experiments.

Gas flow rate is an important parameter for efficient shielding of weld bead from environmental contamination. With appropriate gas flow rate, oxygen can be completely expelled and also the plasma can be quickly suppressed when it is created. The excessive flow rate of shielding gas can attenuate the incident laser beam. In high speed welding, gas flow rate is more crucial for producing successful joints. The shielding gas is supplied to protect both top and underside of the weld. In the present study, argon gas is supplied at a

flow rate of 10 liter per minute from both sides of the fixture and at 5 liter per minute through laser beam nozzle on the top surface of the workpiece (Fig. 3.2). Argon gas is also supplied through another nozzle at an angle 45° with the laser column (Fig. 3.2) at 5 liter per minute on the top surface of the workpiece. These informations are provided in Table 3.1.

3.5 Measurement methodology

The following measurement methodologies are considered to verify the quality of the welded samples and these are discussed in the following subsections.

3.5.1 Bead on plate experiments

In laser beam welding process, the laser beam power and welding speed are primary and important factors as it determines the rate of heat energy applied on the workpiece surface. In addition, for successful laser welding, optimization of other process parameters such as spot size and location of focal spot i.e. defocused position of laser beam are also required. Therefore, a change in focal position with respect to workpiece surface is also considered during experimental investigations. At first, beads-on-plate experiments are conducted on each thickness (5 mm, 2 mm and 1.5 mm) of Ti-6Al-4V alloy plates and 3 mm thick SS-316L plates for identification of gross processing parameters for laser welding. For a fixed beam power and defocused position of laser beam, bead-on-plate experiments are conducted at different welding speeds so that the specific threshold irradiance for conduction to keyhole transition would overcome even in negative defocussed position. The critical range of laser beam power are found by conducting bead on plate tests aiming to yield no significant drop-out of molten metal at the lower side of the plates. Negative defocused positions of laser beam i.e. focal point kept beneath the metal surfaces are considered for higher thickness (5 mm thick plate of Ti-6Al-4V alloy and 3 mm thick SS-316L) of the plates as it reduces the grain size in the fusion zone as reported by Mastrocinque et al. (2012). Otherwise, the increase in grain size may decrease the tensile properties of the weldments. Further, the welded plates are cut transverse to the direction of the weld line and the bead cross-sections are examined under optical microscope. The aspect ratio i.e. weld depth to bead width of the weld bead cross-section is used to select the window of the range of process parameters on the basis of penetration depth with minimal weld bead convexity / concavity.

3.5.2 Macro and microstructural analysis

During LBW process, heat source interacts with certain areas of the workpiece material. Hence, the welded region undergoes to an excessive thermal gradient starting from weld pool to towards base metal. During LBW, three distinct regions in the weldment namely FZ, HAZ and unaffected BMZ are generated. Due to this spatial and temporal distribution of temperature, a non-uniform microstructure in the weldment is formed from FZ to BMZ. Among all three zones, HAZ experiences a temperature which is sufficient enough to produce only solid-state micro-structural changes without melting. The FZ experiences both melting and solidification. The microstructural development in the FZ depends on the solidification behavior of the weld pool which controls the shape and size of the grains. It affects mechanical properties of the welded joint. Hence, after welding, the specimens are prepared according to ASTM: E3 and BSEN:1321 standards for metallographic characterization.

All samples are prepared from the cross section perpendicular to the welding direction and are cold mounted using epoxy resin. The surface of metallographic specimens is prepared by grinding, polishing and etching simultaneously. Initially, the scratches are removed from the sample surface by polishing successively using 80, 120, 220, 320, 400, 600, 800, 1000, 1200, 1600 and 2000 grade emery papers. After that, each sample is polished on a velvet cloth using 1 and 0.5 µm diamond paste successively to achieve mirror finish.

After that the polished sections are dipped in Kroll's reagent for 30 seconds. The compositions of the etchant are 92 % distilled water, 6 % HNO_3 and 2 % HF. This 30s time duration is found suitable for etching Ti-6Al-4V base metal only. However, longer etching time between 30− 60 s is required depending on the welded specimens until their microstructures are revealed. The SS-316L samples are etched using aqueous solution of glyceregia for 60 s. Further, the etched samples are examined under both optical microscopy (OM) and field emission scanning electron microscopy (FESEM) for metallographic study.

3.5.3 Vickers micro-hardness test

The goal of any weld is to create a structure that can meet all demands for its service environment. In many cases, the best way of assessing the performance of a weld or weld quality is to establish its mechanical properties. Hence, Vickers microhardness (HV) and tensile properties of the welded specimens are measured in the present study. Hardness value of a material is not a unique property, however, a difference in hardness between two materials indicates that the materials are not alike. Among various mechanical and optical

tests performed to determine the characteristics of a material to determine its suitability for a given application, hardness testing is one of the most critical one. Hardness testing is often the best way of establishing component's survival and performance in their specific applications. The hardness value of the welded samples depends on the presence of different phases of the materials and their developed microstructure during welding. The hardness value in the HAZ gives indications of its susceptibility to crack. Also, the hardness value in FZ is commonly used to find out less ductile phases in the FZ which may be prone to cracking. In the present study, Vickers micro hardness is measured for base metal as well as across the weld line at different locations of the weldment. The hardness test is performed at room temperature under a constant load of 500 g for 5 mm thick plate and 200 gm for 2 and 1.5 mm thick Ti-6Al-4V and also for 3 mm thick SS-316L plates for a dwell time of 15 s at different locations from the center of the fusion zone to the base metal zone. Each hardness value is calculated from the average of three indentations. The minimum spacing between two indentations which is followed here is based on ASTM standard. Also, the hardness value is measured at seven different points on the base material under same loading and environmental conditions. The largest and smallest values are discarded and an average of five remaining readings is considered. For different thickness of the workpieces, different loads are selected to generate sufficiently large and visible impression of the indenter as it is easy to measure diagonal of the indentation. However, a higher load may produce an oversized impression, where the diagonal may be larger than the micrometer scale attached to the Vickers microhardness tester. Hence, an optimum value of the load as mentioned above is selected.

3.5.4 Tensile test

A tensile test is a fundamental material testing method in which a specimen is pulled out by uniaxial tension until failure. Properties which are measured from tensile test are ultimate tensile strength, maximum elongation, yield strength, maximum force and area reduction. Table 3.5 shows specimen dimensions and tolerances as per ASTM E-8 standard. The tensile testing specimens of the base metal and welded samples are prepared using wire electro discharge machine. The specimens are polished using SiC abrasive paper up to 800 grit size. Tensile tests of the samples are carried out using Instron model machine at room temperature with a maximum load of 10 kN at a constant cross head speed of 0.5 mm/min for Ti-6Al-4V and 1 mm/min for SS-316L. The dimensions of the tensile test specimens are considered as per ASTM E-8 sub-standard (standard size B, Table 3.5) for Ti-6Al-4V as

shown in Fig. 3.3 and for SS-316L as per standard size A in Table 3.5. During tensile testing, the load is measured using load cells attached to the machine and strain is measured using an extensometer. Tensile tests are performed on three specimens prepared from each welded sample and an average value is calculated for analyzing the results.

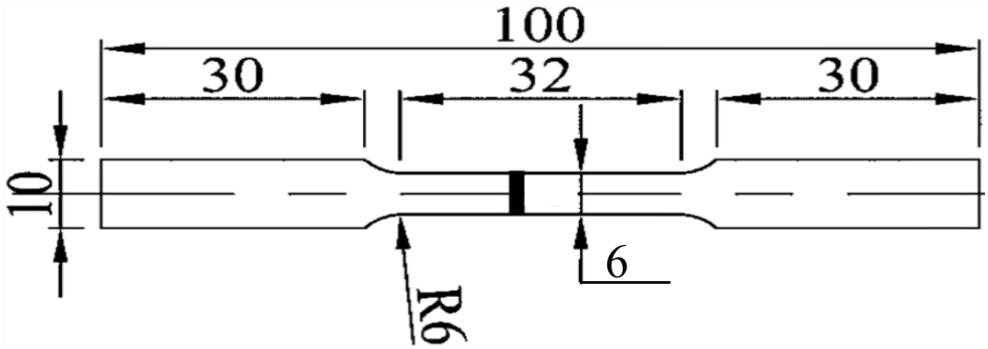

Fig. 3.3 Dimensional specification (in mm) of tensile testing specimen for Ti-6Al-4V alloy As per ASTM E-8 sub-standard

Table 3.5 Dimension (in mm) of tensile testing specimen as per ASTM E-8 standard

	Standard size **A**	Sub-sized **B**	Sub-sized C	Sub-sized D
G- Gauge length	**50±0.1**	**25±0.1**	25±0.1	12.5±0.1
W- Width	**12±0.2**	**6.0±0.1**	4.8±0.1	3.2±0.05
R- Radius of fillet (minimum)	**12.50**	**6**	6	4
L- Overall length	**200**	**100**	100	84
A-Length of reduced section (minimum)	**57**	**32**	32	16
B-Length of reduced section (minimum	**50**	**30**	30	30
C-Width of grip section (approximate)	**20**	**10**	10	10

3.5.5 Estimation of cooling rate for Ti-6Al-4V alloy

From the literature survey it is observed that the mechanical properties of Ti-6Al-4V alloy is highly sensitive to cooling-rate below T_β temperature. The change in microstructure of Ti-6Al-4V depends on cooling rate and its transformation kinetics. The cooling rate (°C/s) of Ti-6Al-4V alloy during LBW in the fusion zone can be calculated theoretically (Adams, 1958) as

$$Cooling\ rate\ (CR) = 2\pi\kappa\rho c\left(\frac{t}{H_{net}}\right)^2 (T_c - T_o)^3 \qquad (3.1)$$

where κ is thermal conductivity of material (J g^{-1} °C^{-1} s^{-1}), ρ is density of material (g mm^{-3}), c is specific heat of solid metal (J g^{-1} °C^{-1}), t is material thickness, T_c is temperature of interest (°C), T_o is initial plate temperature and H_{net} = heat input × heat transfer efficiency. The Thermo-physical material property which is used for cooling rate calculation of Ti-6Al-4V

alloy is taken from the Yang et al. (2010). The heat transfer efficiency for fiber laser is taken constant as 40% at all welding conditions. Adams (1958) reported that Eq. (3.1) can be used to calculate theoretical cooling rate in FZ, if relative plate thickness is less than 0.75. The relative plate thickness (τ) is given by Eq. (3.2) as

$$\text{Relative plate thickness } (\tau) = t\sqrt{\frac{\rho c\left(T_c - T_O\right)}{H_{net}}} \tag{3.2}$$

3.5.6 Grain size measurement

In the present study, the grain size in both FZ and BMZ are measured by line intercept method in optical microscope. A random horizontal or vertical straight line named as test line is drawn through the micrographic image. The number of grains intercepted or the number of grain boundaries intersected with the test line are counted which is further used for grain size measurement as per ASTM E 112-13 standard.

Chapter 4
Experimental investigation of 5 mm thick Ti-6Al-4V plates

4.0 Introduction

In laser beam welding process many process parameters are involved (Fig. 1.3). Hence, the selection of appropriate process parameters along with their optimum values is difficult for achieving high weld quality. Limited experimental studies which focus on the influence of various welding process parameters on weld quality in fibre LBW of Ti-6Al-4V alloy are available in the literature. Also, in most of the published literature, minor variation in the defocused position is reported. The defocused position of laser beam influences both weld bead geometry and mechanical properties of the weldments. Hence, more variations in defocused positions are required to understand its effect properly. To investigate the weldability of 5 mm thick Ti-6Al-4V plates using fiber laser in butt configuration without using filler wire, preliminary beads on plate experiments are carried out to perform feasibility study. From preliminary study, it is observed that Ti-6Al-4V alloy is highly oxidized while welding under atmospheric condition. Hence, experiments are carried out under shielding gas environment as explained in section 3.4. In this chapter, two sets of welding experiments i.e. (a) preliminary welding experiments and further (b) statistical design of experiments (DOE) are conducted for better understanding of beam-material interaction phenomenon.

4.1 Preliminary experiments

In this study, the weldability of 5 mm thick Ti-6Al-4V plate is investigated at a constant welding speed of 300 mm/min and 2 mm defocused position below workpiece surface. The preliminary experiments are carried out in two steps. Initially, beads on plate (BOP) experiments are conducted between 1200− 1500 W beam power (P). After that, preliminary welding experiments in butt configuration are carried out at different beam power (1500 – 1900 W) keeping other parameters fixed. To confirm the effectiveness of shielding gas, energy dispersive X-ray spectroscopy (EDS) analysis along the weld line and weld bead appearance on the top surface of the weldments are conducted. The morphology of the joint is assessed by measuring different weld bead features i.e. penetration depth (d_p) and upper width of fusion zone (FZ_{UP}) as shown in Fig. 4.1 using optical microscope (OM). The

metallographic features of the weld bead are also studied using FESEM and optical micrographs to characterize weld quality in terms of FZ microstructure and hardness of weldments. The chemical composition (in wt. % of alloying elements) of Ti-6Al-4V base metal (BM) is confirmed by EDS analysis as shown in Table 4.1 and their mechanical properties such as tensile properties and hardness are tested at room temperature as listed in Table 4.2.

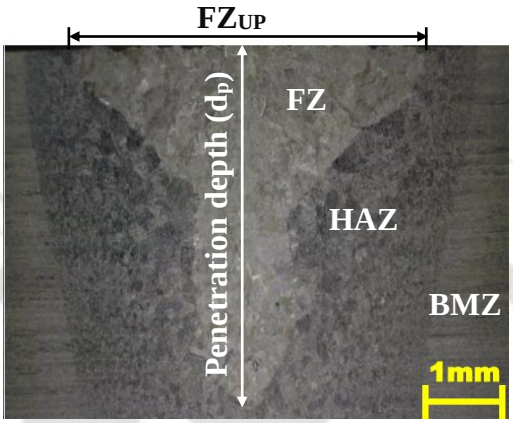

Fig. 4.1 Bead features with different zones

Table 4.1 Chemical composition of 5 mm thick Ti-6Al-4V base metal

Element	Al	V	C	Fe	O	Ti
Wt.%	5.5	3.7	2.9	0.2	0.3	Balance

Table 4.2 Mechanical properties of Ti-6Al-4V base metal at room temperature

Yield strength (MPa)	Ultimate tensile strength (MPa)	Young's Modulus (GPa)	% elongation	Hardness (HV)
850	957	113	11	298-302

4.1.1 Beads on plate (BOP) experiments

The objective of BOP experiments is to find out the minimum value of LBW power to produce at least 80% penetration depth in base plate. Optical macrographs (OM) of the bead on plate experiments at different beam power are presented in Fig. 4.2. It is found that penetration depth increases with increased beam power from 1200 W to 1500 W. It reaches to the 80% of the base plate thickness at 1500 W beam power.

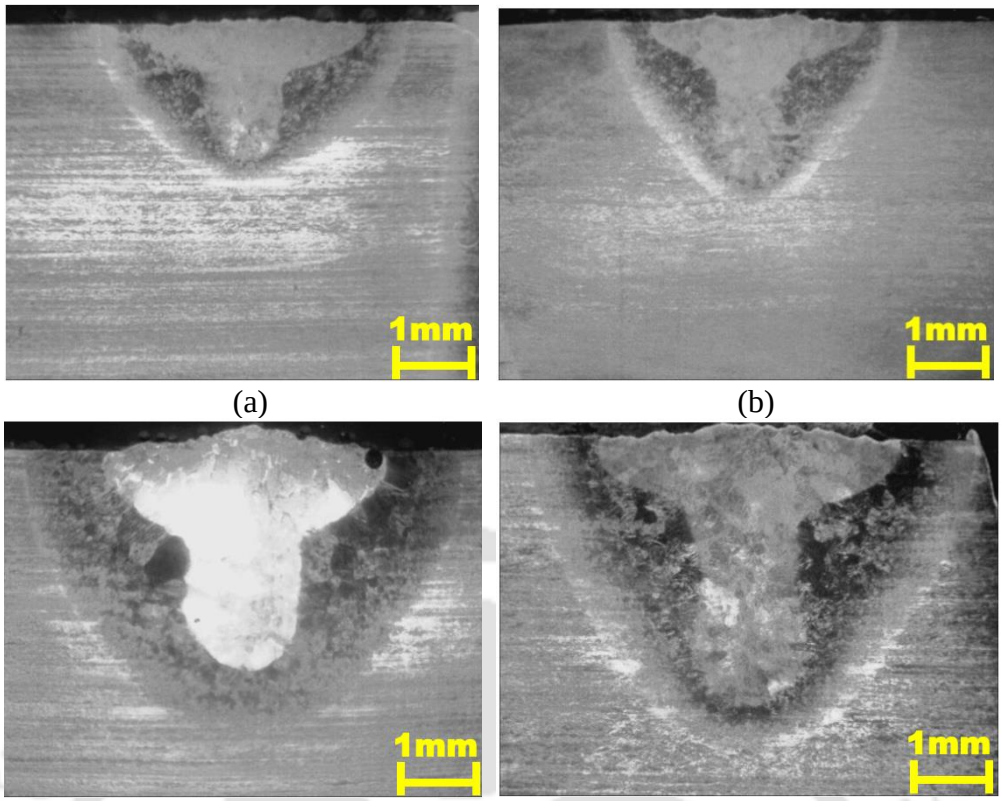

Fig. 4.2 Penetration depth at different beam power (a) 1200 W, (b) 1300 W, (c) 1400 W and (d) 1500 W for preliminary bead on plate experiments

4.1.2 Preliminary welding experiments

In this section, experimental results of preliminary welding experiments at different beam power (1500 – 1900 W) as shown in Table 4.3 are discussed. Also, the significance of EDS analysis, bead appearance and effect of beam power on bead shape, penetration depth (d_p), upper width of fusion zone (FZ_{UP}) and fusion zone area (FZ_{area}) are studied.

Table 4.3 Experimental conditions for LBW process

Exp. No.	P (W)	V (mm/min)	d (mm)
1	1500		
2	1600		
3	1700	300	-2
4	1800		
5	1900		

4.1.2.1 EDS analysis

EDS analysis is conducted before (Fig. 4.3(a)) and after (Fig. 4.3(b)) welding along the weld line to confirm shielding gas effectiveness. From EDS spectra (Fig. 4.3), it is found that there is an insignificant increase in O_2 concentration (wt. %) from 0.30 % in BM (Fig.

4.3(a), Table 4.1) to 1.6 % after welding along the weld line (Fig. 4.3(b), Table 4.4). It is probably due to shielding gas disruption by the plasma plume over melt pool which deteriorates effectiveness of shielding gas forming TiO_2. However, the effectiveness of shielding environment is acceptable and the observations are in line with the work of former researchers. The EDS spectra confirms the presence of carbon in both BM and welded samples as the samples were placed over a carbon tape on sample holder of the machine during EDS analysis (Baruah et al., 2016).

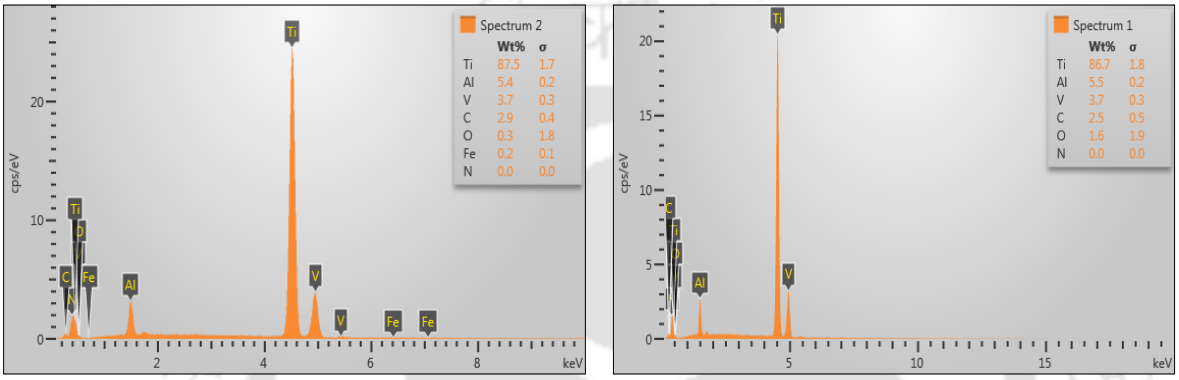

(a) (b)

Fig. 4.3 Chemical composition of Ti-6Al-4V alloy using EDS (a) before and (b) after welding

Table 4.4 Chemical composition of weldment using EDS

Element	Al	V	C	Fe	O	Ti
Wt.%	5.4	3.7	2.5	0	1.6	Balance

4.1.2.2 Bead appearance and its shape

Hong and Shin (2016) reported that, visual assessment of top surface appearance of Ti-6Al-4V weldments can be used for surface imperfections, degree of oxidation as well as shielding gas effectiveness. The change in surface color from silver, light straw through dark straw, light blue, dark blue to grey and in powdery form on the weld surfaces represent increasing order of oxidation and contamination (Wu et al., 2017). Wang et al. (2014a) reported that surface oxidation is highly sensitive to temperature and oxygen concentration.

The appearances of top surface of weldments at different beam power are shown in Fig. 4.4. In the present study, all the welded surfaces (Figs. 4.4(a-e)) are bright, uniform, smooth, silvery and aesthetic in appearance which shows excellent shielding of weld pool from environmental contaminations. Also, the weldments are free from severe weld cracks and also, spatter free weld is formed throughout experimental conditions. It is mostly due to

excellent crack resistance of BM. The bead shapes and penetration depths at different beam power are shown in optical macrographs in Fig. 4.5.

(a) (b) (c) (d) (e)

Fig. 4.4 Weld bead appearances at (a) 1500 W, (b) 1600 W, (c) 1700 W, (d) 1800 W and (e) 1900 W beam power

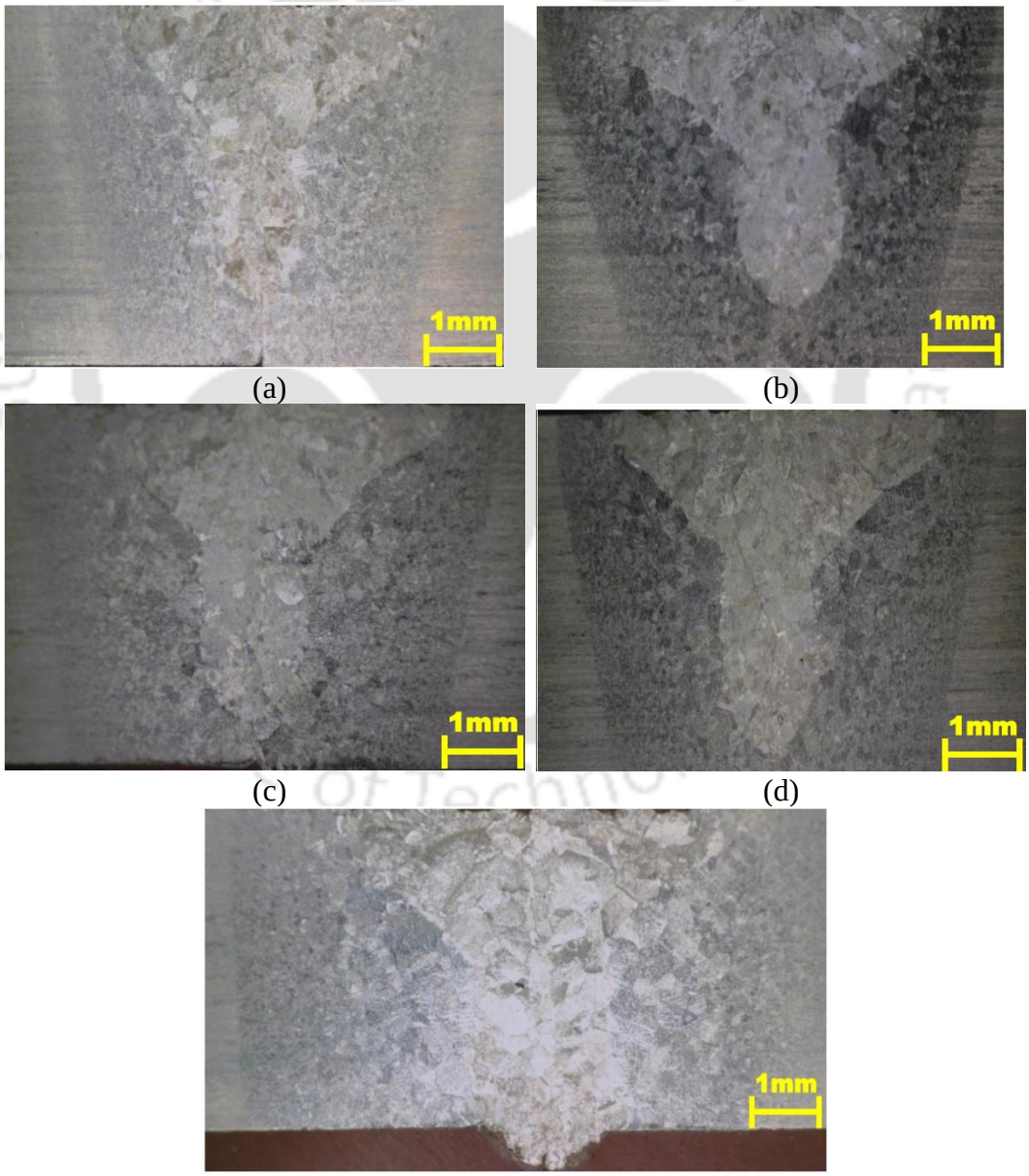

(a) (b) (c) (d) (e)

Fig. 4.5 Weld bead shapes at different beam power (a) 1500 W, (b) 1600 W, (c) 1700 W, (d) 1800 W and (e) 1900 W

The shape of weld bead continuously changes from V shaped to hourly glass shape with elongated top while increasing beam power. The hourly glass shape with elongated top is the characteristics of deep penetration LBW and it is attributed to the flow behaviour of molten metal inside melt pool. The molten metal flows from high temperature to low temperature regions which leads to enlarged top surface of FZ forming hourly glass shape.

It is observed from the macrographs of the weldments (Figs. 4.5(a-e)) that the weld pool is almost symmetrical about the centre line of FZ. However, small amount of lack of symmetricity is observed at the root side of weld bead at higher beam power. It may be due to the combined effect of two opposing forces in the weld pool region i.e. electromagnetic and surface tension forces. It may happen that electromagnetic force dominates surface tension force which affects convective heat transfer. Because of this, flow field of liquid metal in the melt pool is changed dramatically by any local agitation which leads to insignificant amount of local asymmetry in the root side of weld bead.

4.1.2.3 Penetration depth and fusion zone width (FZ_{UP})

The power density is most influencing parameter in LBW process. The mode of welding can be changed from conduction mode to penetration / keyhole mode by changing power density on the workpiece surface. In this experimental study, the laser beam spot diameter is kept constant on the sample surface. The defocused position of laser beam is kept constant at 2 mm below from the top surface of workpiece. Hence, power density depends only on applied beam power. Increasing beam power, increases energy density on the workpiece surface. The relationship between LBW power and power density is expressed as

$$Power\ density\ (Q_{avg}) = \frac{\text{Beam power (P)}}{Area\ of\ laser\ beam\ spot\ (A)} \qquad (4.1)$$

Figures 4.6(a) and (b) represent the effect of beam power on penetration depth (d_p) and upper width of fusion zone (FZ_{UP}), respectively. At lower range of welding power (1500 W- 1700 W), penetration depth increases linearly with increased beam power as observed in Fig. 4.6(a). It is prominent because of imposed higher heat input per unit length (i.e. line energy) along the weld line on workpiece surface which increases with increasing beam power. The relationship between beam power and welding speed with line energy (LE) is expressed as

$$Heat\ input\ per\ unit\ length\ (\text{i.e.}\ Line\ energy, LE) = \frac{Beam\ power\ (P)}{Welding\ speed\ (V)} \quad (4.2)$$

The LE increases with increasing beam power. Hence, more amount of base metal being melt and sometimes it may vaporize. The linear relationship between beam power and depth of penetration changes with further increase in welding power. The depth of penetration sharply increases with further increment of beam power from 1700 W to 1800 W. However, full penetration in the base plate is achieved at 1900 W beam power. It is due to the fact that power density is very high at higher beam power. Also, due to negative defocusing distance (i.e. 2 mm below metal surface), the laser beam converges gradually towards focus point executing high energy density than that of the specimen surface. Consequently, stronger melting and vaporization of molten metal takes place inside keyhole due to multiple reflections of laser beam prompted by Fresnel absorption at the keyhole wall (Kim and Ahn, 2012 and Cheng et al., 2012). From Fig. 4.6(b), it is found that increasing beam power, FZ_{UP} continuously increases due to higher heat input imposed on workpiece surface. At higher LBW power, the plasma cloud is formed at the top surface of the weld bead. The plasma cloud absorbs some part of imposed laser beam energy and it reradiates the heat energy on the top surface of the bead which promotes widening of the bead width. In addition, due to Marangoni effect induced by the surface tension force, the recoil pressure is build up inside keyhole of the melt pool. Hence, very intense flow of molten metal occurs from the bottom of molten weld pool towards its top. As a result, the width of FZ_{UP} becomes enlarged (Kumar et al., 2017c and Zhou and Chew, 2003).

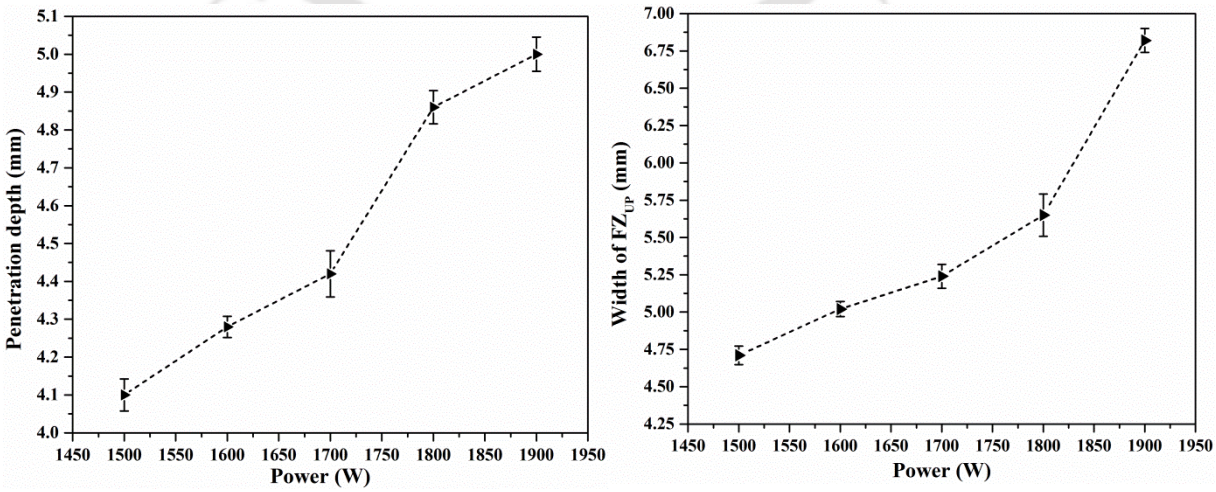

(a) (b)

Fig. 4.6 Effect of beam power on (a) penetration depth and (b) width of FZ_{UP}

4.1.2.4 Microstructural analysis in fusion zone

In LBW process, the weldments experience high temperature gradient starting from FZ to towards BMZ. As a result, three different zones in the weld bead i.e. FZ, HAZ and BMZ appears as clearly observed in Fig. 4.7 for Exp. 5 (Table 4.3). The three-dimensional, chronological temperature gradient yield non-homogeneous microstructure in the weld bead at both sides of weld line from FZ to BMZ. From previous literature, it is observed that both melting and solidification occur in the FZ whereas only solid-state micro-structural changes without melting occur in the HAZ.

Figures 4.8(a) and (b) show microstructural images (i.e. OM and FESEM, respectively) of BM. The base metal microstructure mainly consists of inter-granular β phase in a dominant matrix of equi-axed α phase. The β phase is dispersed along grain boundaries of α phase. The α phase is represented by light areas whereas inter-granular β phase is represented by dark areas. Optical as well as FESEM images of FZ microstructures are shown in Figs. 4.9(a) and (b), respectively for Exp. 5 (Table 4.3). Fully α' martensitic structure along with small amount of grain boundary α are observed in FZ. Presence of α′ martensite in the FZ reflects self-quenching characteristics of LBW process which leads to high cooling rate of weld bead during solidification of melt pool. Higher cooling rate promotes diffusionless transformation in FZ in which most of the β phase transforms into α' martensite. The shape of the α' lamella looks like needle shaped as shown in Fig. 4.9(b). The presence of grain boundary α in a dominant matrix of α′martensitic structure in the FZ signifies that the cooling rate at that welding condition for Exp. 5 (Table 4.3) is slightly above lowest limit i.e. 410°C/s for the formation of α' martensitic phase in the FZ as explained in the continuous cooling transformation (CCT) curve by Ahmed and Rack (1998). Similar microstructure in FZ is observed by Caiazzo et al. (2013) during fiber LBW of Ti-6Al-4V alloy.

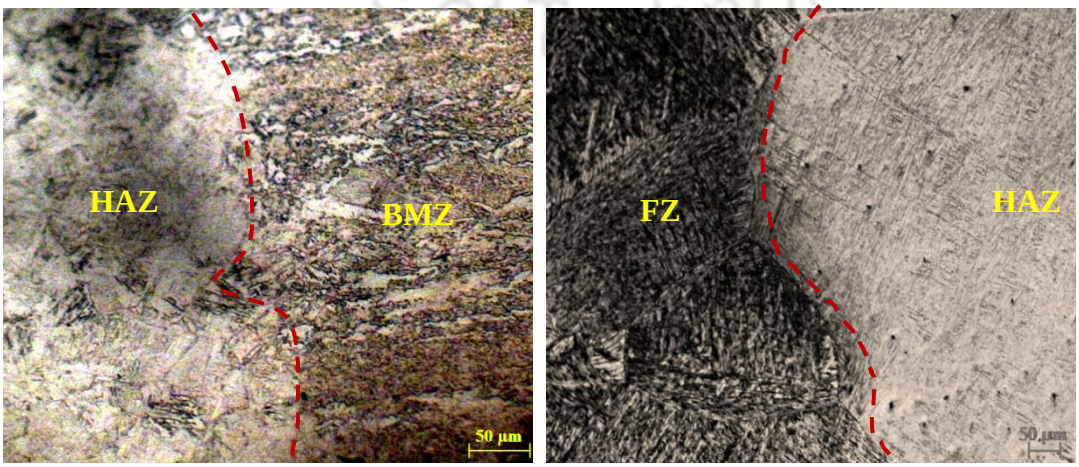

(a) (b)

Fig. 4.7 Optical macrographs showing (a) BMZ and HAZ and (b) FZ and HAZ

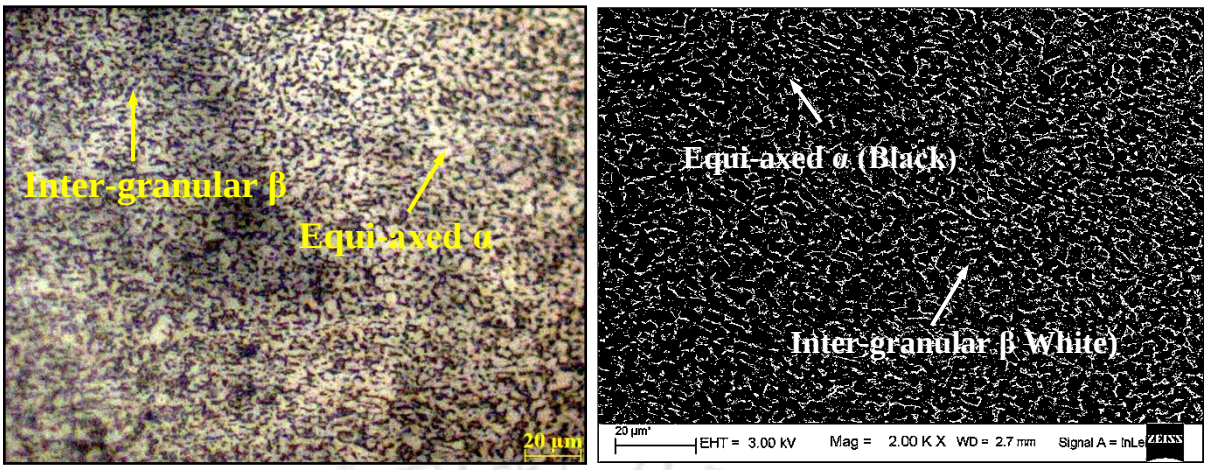

(a) (b)

Fig. 4.8 Microstructure of Ti-6Al-4V base metal using (a) optical microscope and (b) FESEM

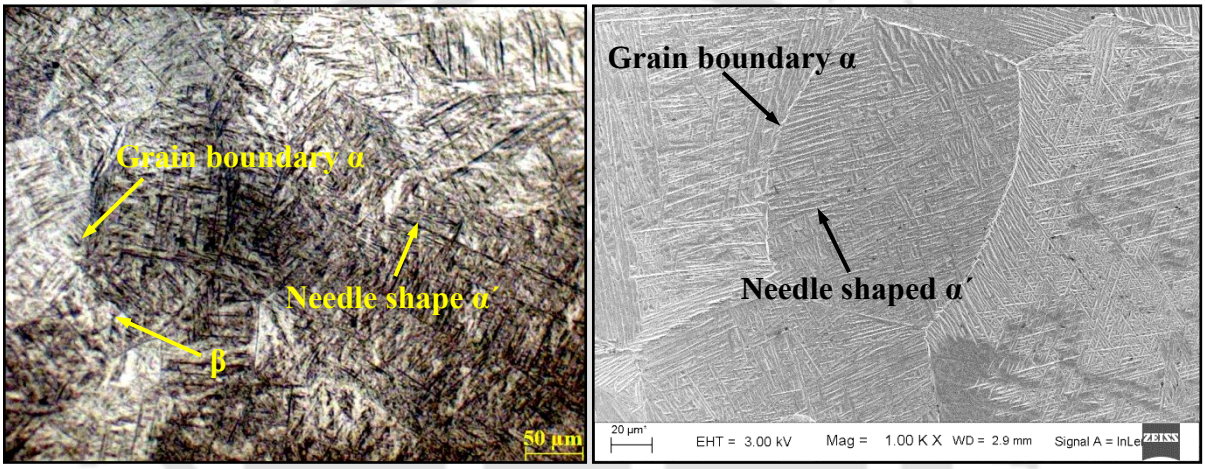

(a) (b)

Fig. 4.9 FZ microstructure for Exp. 5 (Table 4.3) using (a) optical microscope and (b) FESEM

4.1.2.5 Hardness

In the present study, Vickers microhardness is measured at different locations along transverse direction of welding line at top and middle of bead cross-section as shown in Fig. 4.10(a) for Exp. 5 (Table 4.3). The hardness distribution curve is presented in Fig. 4.10(b). The lowest average hardness (310-318 HV) is found in the BMZ and its value continuously increases towards FZ as presented in Fig. 4.10(b). The maximum hardness (350-364 HV) in FZ is mainly due to the existence of large amount of α′ martensite. The development of α′ martensitic structure is promoted by higher cooling rate in the FZ. The α′ martensite possesses high hardness and tensile strength with reduced ductility. Due to the continuously reducing amount of α′ martensite from highest percentage in FZ to nearly zero percent in BMZ, the hardness value is also decreased on both sides of weld line as clearly observed in Fig. 4.10(b). Similar trends are also reported by Akman et al. (2009) and Kabir et al. (2010)

in LBW of Ti-6Al-4V alloy. Higher average hardness is observed at top bead cross-section (Fig. 4.10(b)) as compared to the middle of the weld bead. It is mainly due to higher cooling rate at the top portion of the weld bead than the middle portion.

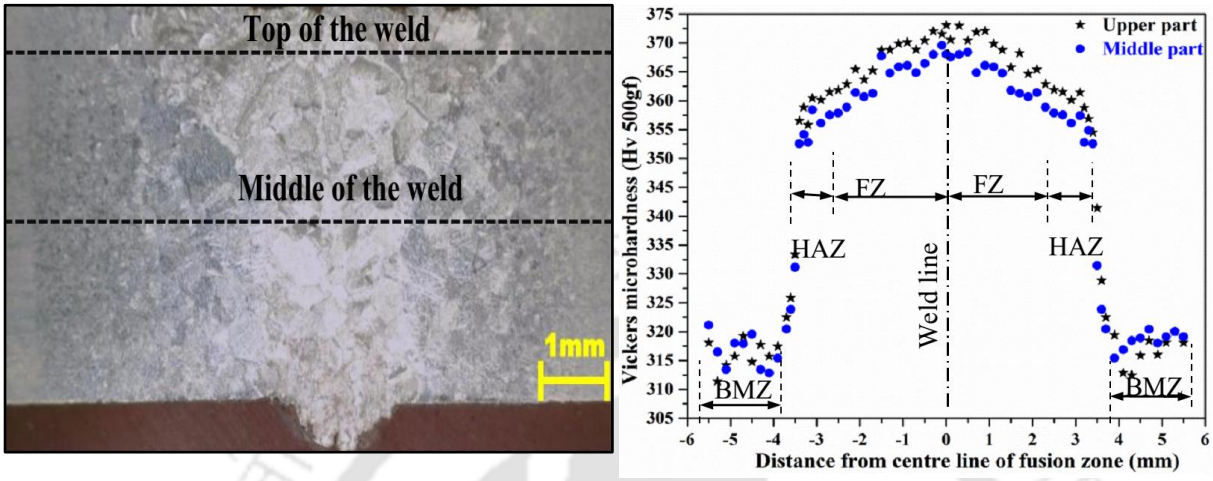

(a) (b)

Fig. 4.10 (a) Different positions of hardness measurement at weld bead cross-section and (b) Vickers microhardness distribution at top and middle positions of weld bead cross-section along transverse direction to weld line

4.1.3 Conclusions from preliminary experiments

Preliminary experimental investigations are carried out on fiber LBW of 5 mm thick Ti-6Al-4V alloy plates. The ranges of welding parameters are selected from results obtained from beads on plate experiments. The welding experiments are conducted at different beam power at constant 2 mm defocused position of laser beam and 300 mm/min welding speed. From EDS analysis along the weld line and top surface bead appearance of weldments, the effectiveness of the shielding gas is confirmed. Smooth, uniform, shiny bead, without spatters and crack free weld is formed. The weld pool is almost symmetrical with respect to the center line of FZ. It is observed that with increased laser beam welding power, both penetration depth and width of fusion zone are increased. From microstructural analysis it is observed that fusion zone microstructure consists of α′ martensite and its structure looks like needle shaped. The maximum value of the Vickers micro hardness is observed in the FZ as compared to HAZ and BMZ due to the formation of α′martensitic structures in the FZ. The hardness value at the top surface of bead cross section is higher than middle of the weld bead due to higher cooling rate at the top. Experimental results obtained from preliminary welding experiments reflect that 5 mm thick Ti-6Al-4V plates can be welded successfully using 2 kW fiber laser. However, the optimum value of the welding process parameters is required to achieve high weld quality. Hence, statistical design of experiments is conducted for

systematic study of parametric effect on bead features and to obtain optimal process parameters window for achieving satisfactory weld quality as discussed below.

4.2 Design of experiments (DOE)

In the present study, experimental investigation of fiber LBW of 5 mm thick Ti-6Al-4V plates is carried out according to central composite rotatable design (CCRD) matrix of response surface method (RSM) at different welding conditions to understand their effect on weld bead geometry and final solidified microstructures of weldments which further influence the hardness and tensile properties of weldments. Analysis of variance (ANOVA) is carried out to identify the most significant process parameters and their percentage contribution on output responses. The effect of individual process parameter and their interactions on output responses are studied and analyzed using regression equations. Further study is extended to optimize the process parameters to achieve satisfactory weld quality. The metallographic features using field emission scanning electron micrographs (FESEM) and optical micrographs of the weld beads are studied to characterize the weld quality. Also, the mechanical properties like hardness and tensile properties of the weldments are tested and discussed.

There are lots of factors involved in LBW process which influence the quality of weldments as shown in fishbone diagram in Fig. 1.3. In this study, three independent LBW input process parameters i.e. laser beam power (P), welding speed (V) and defocused position (d) of laser beam are selected to understand the beam-material interaction phenomena in terms of weld quality. The focal position is varied by varying the stand-off-distance i.e. the distance between the laser nozzle tip and the upper surface of the workpiece. In the present case, negative defocussing position (i.e. focal point of the laser beam is kept below workpiece surface) is considered as it reduces the grain size in the fusion zone which enhances mechanical properties of weldments (Caiazzo et al., 2013). Initially, beads on plate experiments are carried out by varying one parameter at a time while keeping rest of the parameters at a constant value to find out their working ranges. Absence of visible welding defects and at least 80% penetration depth in the base plate are selected as the criteria for choosing the working ranges for each parameter.

DOE using full factorial method is cumbersome when number of process parameters increases which leads to large number of experiments to be conducted. To resolve this issue, CCRD approach of RSM is carried out in the present experimental work to study entire space of process parameters with lesser number of experiments. The selected process parameters

and their ranges are given in Table 4.5. The welding experiments are conducted in random order to avoid any systematic error. The repeatability of the experiments and statistical significance of the measurements are checked by conducting three experiments at each experimental condition. Two transverse specimens are cut from each weldment to measure bead features. The bead features i.e. responses are measured using optical microscope with digital micrometers attached to both X and Y axes with an accuracy of 0.001 mm. The averages of the weld bead features from two samples are recorded for each response. The design matrix and responses at each experimental condition are shown in Table 4.6. Three separate analysis of variance (ANOVA) are carried out considering three responses i.e. upper width of fusion zone (FZ_{UP}), size of upper heat affected zone (HAZ_{UP}) and area of fusion zone (FZ_{area}). The bead profiles i.e. width of FZ_{UP}, size of HAZ_{UP} and FZ_{area} are shown schematically in Fig. 4.11.

Table 4.5 Process parameters and their levels

S. No	Parameters	Unit	Levels		
			-1	**0**	**1**
1	Power (P)	Watt	1800	1900	2000
2	Speed (V)	mm/min	200	300	400
3	Defocused position (d)	mm	-1	-1.5	-2*

* *- means focal position is kept below workpiece surface*

Table 4.6 Experiments as per DOE, responses and observations

Exp. No.	Process parameters			Responses			Observations
	P (W)	V (mm/min)	d (mm)	FZ_{UP} (mm)	HAZ_{UP} (mm)	FZ_{area} (mm)	
1	1800	200	1	6.02	8.87	16.44	Dropout
2	2000	200	1	6.79	10.30	17.93	Dropout
3	1800	400	1	5.21	6.90	9.31	DP* > 80%
4	2000	400	1	5.39	7.25	10.78	Full penetration, SW
5	1800	200	2	5.57	9.46	16.51	DP > 80%
6	2000	200	2	6.44	10.85	18.33	Full penetration, SW
7	1800	400	2	4.62	7.38	8.98	Lack of penetration
8	2000	400	2	4.95	7.57	9.75	Full penetration, SW
9	1750	300	1.5	5.86	7.95	10.24	Lack of penetration
10	2000	300	1.5	6.28	8.41	11.91	Full penetration, SW
11	1900	132	1.5	6.80	11.21	21.49	Dropout
12	1900	468	1.5	4.76	6.34	7.96	Full penetration, SW
13	1900	300	0.7	5.51	8.21	11.31	Full penetration, SW
14	1900	300	2.3	5.08	8.63	10.88	DP > 80%
15	1900	300	1.5	6.31	7.87	10.58	Full penetration, SW
16	1900	300	1.5	6.24	7.68	10.96	Full penetration, SW
17	1900	300	1.5	6.13	7.72	11.36	Full penetration, SW
18	1900	300	1.5	6.18	7.56	11.35	Full penetration, SW
19	1900	300	1.5	6.09	7.79	11.28	Full penetration, SW
20	1900	300	1.5	6.21	7.55	10.38	Full penetration, SW

**SW- Successful weld, DP - depth of penetration*

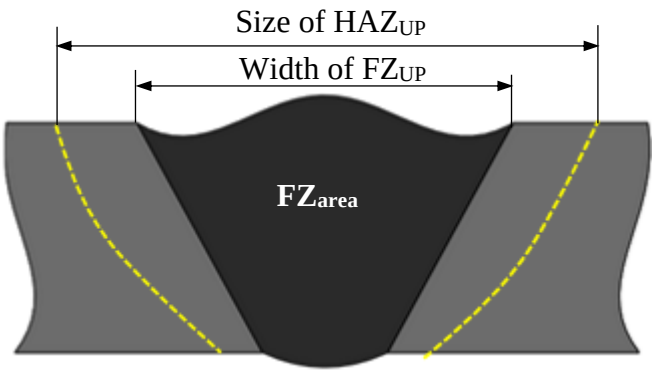

Fig. 4.11 Schematic diagram of weld bead features

4.2.1 Analysis of variance (ANOVA)

ANOVA is carried out to find out the most significant welding process parameters affecting the eminence characteristic of the weld bead. The ANOVA Tables for width of FZ_{UP}, size of HAZ_{UP} and area of FZ_{area} are given in Tables 4.7, 4.8 and 4.9, respectively. Quadratic model is suggested from the fit summaries of the ANOVA for all three responses. In all three cases, the main parameters and some interaction terms are significant and the model is not aliased (p-values < 0.0001). The p-values of less than 0.05 for all three models for 95% confidence level indicate that the model terms are statistically significant. All the adequacy measures R^2, adjusted R^2 and predicted R^2 are in reasonable agreement and are close to 1, which indicates adequacy of the models. The predicted R^2 value indicates how good the model predicts a response value. The adjusted R^2 and predicted R^2 are within approximately 0.20 of each other (Acherjee et al., 2012 and Montgomery, 2012).

The % contribution (F/ΣF) of individual process parameters and their interactions are given in Tables 4.7, 4.8 and 4.9. It is observed that welding speed has most significant contribution on the width of the FZ_{UP} (60%), size of HAZ_{UP} (80.53 %) and FZ_{area} (82.64 %) followed by beam power. However, insignificant effect of defocused position of the laser beam is observed in case of FZ_{area}. The regression equations in terms of actual factor values are given in Eqs. (4.3-4.5) for three different responses.

Table 4.7 ANOVA for width of FZ_{UP}

Source	Sum of Squares	DOF	Mean Square	F-Value	p- value	% Contribution
Model	7.89	9	0.88	89.45	< **0.0001***	
P	0.58	1	0.58	59.32	< **0.0001***	7.30
V	4.78	1	4.78	487.51	< **0.0001***	60
d	0.49	1	0.49	49.72	< **0.0001***	6.12
PV	0.16	1	0.16	16.31	**0.0024***	2
Pd	8.51×10^{-3}	1	8.51×10^{-3}	0.87	0.3733**	0.11
Vd	6.90×10^{-3}	1	6.90×10^{-3}	0.70	0.4210**	0.09
P^2	9.60×10^{-3}	1	9.60×10^{-3}	0.98	0.3457**	0.12
V^2	0.34	1	0.34	34.65	**0.0002***	4.26
d^2	1.59	1	1.59	162.55	< **0.0001***	20
Lack of Fit	0.067	5	0.013	2.17	0.2076**	

**Significant,* ***Non-significant,* $R^2 = 0.9877$, *Adj* $R^2 = 0.9767$, *Predicted* $R^2 = 0.9317$

$$\text{Width of } FZ_{UP} = -20.07 + 0.02P + 0.03V + 2.86d - 1.41\times10^{-5}PV + 6.53\times10^{-4}Pd - 5.88\times10^{-4}Vd - 3.63\times10^{-6}P^2 - 1.53\times10^{-5}V^2 - 1.44d^2 \quad (4.3)$$

Table 4.8 ANOVA for size of HAZ_{UP}

Source	Sum of Squares	DOF	Mean Square	F-Value	p- value	% contribution
Model	31.19	9	3.47	133.07	< **0.0001***	
P	1.62	1	1.62	62.15	< **0.0001***	5.16
V	25.27	1	25.27	970.24	< **0.0001***	80.53
d	0.52	1	0.52	20.07	**0.0012***	1.67
PV	0.66	1	0.66	25.19	**0.0005***	2.09
Pd	5.35×10^{-3}	1	5.35×10^{-3}	0.21	0.6599**	0.02
Vd	0.015	1	0.015	0.57	0.4672**	0.05
P^2	0.66	1	0.66	25.47	**0.0005***	2.11
V^2	1.84	1	1.84	70.82	< **0.0001***	5.88
d^2	0.78	1	0.78	30.06	**0.0003***	2.50
Lack of Fit	0.18	5	0.036	2.27	0.1952**	

**Significant,* ***Non-significant,* $R^2 = 0.9917$, *Adj* $R^2 = 0.9843$, *Predicted* $R^2 = 0.9461$

$$\text{Size of } HAZ_{UP} = 99.92 - 0.10P + 0.02V - 1.38d - 2.86\times10^{-5}PV - 5.17\times10^{-4}Pd - 8.62\times10^{-4}Vd + 3.02\times10^{-5}P^2 + 3.56\times10^{-5}V^2 + 1.01d^2 \quad (4.4)$$

Table 4.9 ANOVA for FZ_{area}

Source	Sum of Square	DOF	Mean Square	F-Value	p- value	% contribution
Model	250.06	9	27.78	82.14	< **0.0001***	
P	6.74	1	6.74	19.92	**0.0012***	2.69
V	206.80	1	206.80	611.35	<**0.0001***	82.64
d	0.19	1	0.19	0.56	0.4702**	0.08
PV	0.14	1	0.14	0.41	0.5341**	0.06
Pd	0.016	1	0.016	0.049	0.8299**	0.01
Vd	0.42	1	0.42	1.23	0.2931**	0.17
P^2	2.64	1	2.64	7.81	**0.0189***	1.06
V^2	32.55	1	32.55	96.22	< **0.0001***	13.01
d^2	0.77	1	0.77	2.27	0.1629**	0.31
Lack of Fit	2.49	5	0.50	2.79	0.1419**	

**Significant,* ***Non-significant,* $R^2 = 0.9867$, *Adj* $R^2 = 0.9746$, *Predicted* $R^2 = 0.9174$

$$FZ_{area} = 228.66 - 0.21P - 0.10V - 0.14d - 1.32\times10^{-5}PV - 9.06\times10^{-4}Pd - 4.56\times10^{-3}Vd + 6.02\times10^{-5}P^2 + 1.50\times10^{-4}V^2 + 0.99d^2 \quad (4.5)$$

4.2.2 Model validation and optimization study

To validate the model developed from the regression analysis, three confirmation tests are carried out at welding conditions chosen randomly within the range of process parameters as presented in Table 4.10.

Table 4.10 Validation tests

Exp. No	P (W)	V (mm/min)	d (mm)
1	1900	300	1.0
2	1800	300	2.0
3	1900	400	1.5

The actual responses are calculated as the average of three measured results for each response. The predicted responses are calculated from the regression equations (Eqs. (4.3-4.5)) for each case. After that percentage error between the actual and predicted results are calculated. The measured and predicted bead features and % error are shown in Fig. 4.12 for three experiments. Good agreements between the experimental and predicted responses with error less than 5% are observed for all three responses.

After completing ANOVA, an optimization study is carried out based on Derringer and Suich (1980) algorithm to find out optimum values of the process parameters to minimize width of FZ_{UP}, size of HAZ_{UP} and FZ_{area}. All independent parameters are varied within their selected experimental ranges. Table 4.11 shows the optimized solutions of the current study

in terms of desirability value. A desirability value of 'one' represents the ideal case. A 'zero' desirability indicates that one or more responses fall outside the desirable limits.

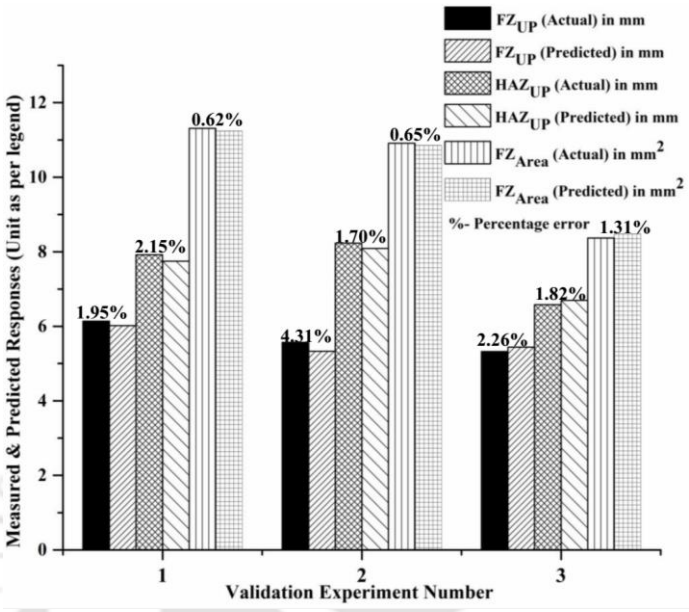

Fig. 4.12 Results of confirmation tests

Table 4.11 Optimum combination of process parameters

Sl. No.	Welding parameters			Desirability
	P (W)	V (mm/min)	d (mm)	
1	1900	400	2	0.922
2	1900	400	1.99	0.921
3	1900	400	1.92	0.911

4.3 Results and discussion

During LBW process, the mode of fluid flow of molten metal and the heat and mass transfer in the fusion zone affect the characteristics and the quality of the welded joints. The measurement of temperature and the velocity field in the weld pool are very difficult due to its small size and the presence of plasma surrounding it. In the present work, experimental analysis is carried out to understand the beam-material interaction during LBW of Ti-6Al-4V alloy.

In the following subsection, the effect of individual process parameters i.e. welding speed, LBW power and defocused position of the laser beam on width of FZ_{UP}, size of HAZ_{UP} and FZ_{area} of the welded specimens are studied and discussed within the range of process parameters. All the graphs are plotted using regression equations (Eqs. (4.3 – 4.5)).

4.3.1 Width of fusion zone i.e. FZ_{UP}

The welding speed, LBW power and defocused position of laser beam are the most important process parameters based on their significance level which affect fusion zone width. The heat input per unit length (i.e. line energy, LE) combines both welding speed (V) and LBW power (P) using a relationship shown in Eq. (4.2) and their effect on the responses are discussed together in the following subsection.

4.3.1.1 Effect of welding power and welding speed

LBW power and welding speed are the most influential factors in LBW process as they affect weld bead geometry, joint dimensions and weld quality. Highest % contribution on the width of the FZ_{UP} is observed by welding speed (60%) followed by LBW power (7.30 %) among all parameters and their interaction terms as shown in Table 4.7. The effect of LBW power on width of FZ_{UP} at different defocused positions and 300 mm/min constant welding speed is shown in Fig. 4.13(a). The width of FZ_{UP} increases with the increase in the LBW power. Higher value of LBW power leads to the more heat input per unit length i.e. line energy (LE) at a fixed welding speed and defocused position. Hence, larger volume of BM is being melted which increases the width of the FZ_{UP}. Nearly linear relationship between the width of FZ_{UP} and LBW power is observed at different defocused positions as shown in Fig. 4.13(a). Figure 4.13(b) shows the effect of LBW power on the width of FZ_{UP} at different welding speeds. In Fig. 4.13(b), the slope of each curve depends on the speed at which laser heat source is moved along the weld line. It is observed that higher value of the welding speed leads to decreased fusion zone width. Welding speed contribute more effect on FZ_{UP} width than beam power as observed in 3D response surface plot (Fig. 4.13(c)) since welding speed influences both size and shape of the weld bead.

Fig. 4.14(a) shows the effect of welding speed on FZ_{UP} width at different LBW power and 1.5 mm constant defocused position. In Fig. 4.14(a), the slope of the curves gradually increases with increased welding speed. The lower value of the slope at lower range of welding speed indicates that welding speed does not have prominent effect on FZ_{UP} width. In this regime, the width of the fusion zone mainly depends on the LBW power. This phenomenon can be explained with the help of plasma absorption characteristics of the laser beam. The plasma is generated due to the electric field of the focused laser beam. Plasma absorption is very high at the top surface of weld bead where energy density is very high. It leads to enlarged fusion zone width. The plasma absorption at the top surface is enhanced further by increasing LBW power as the power density of the laser beam on the top of the

workpiece surface increases with increased LBW power. Hence, widening of the fusion zone at the top surface takes place.

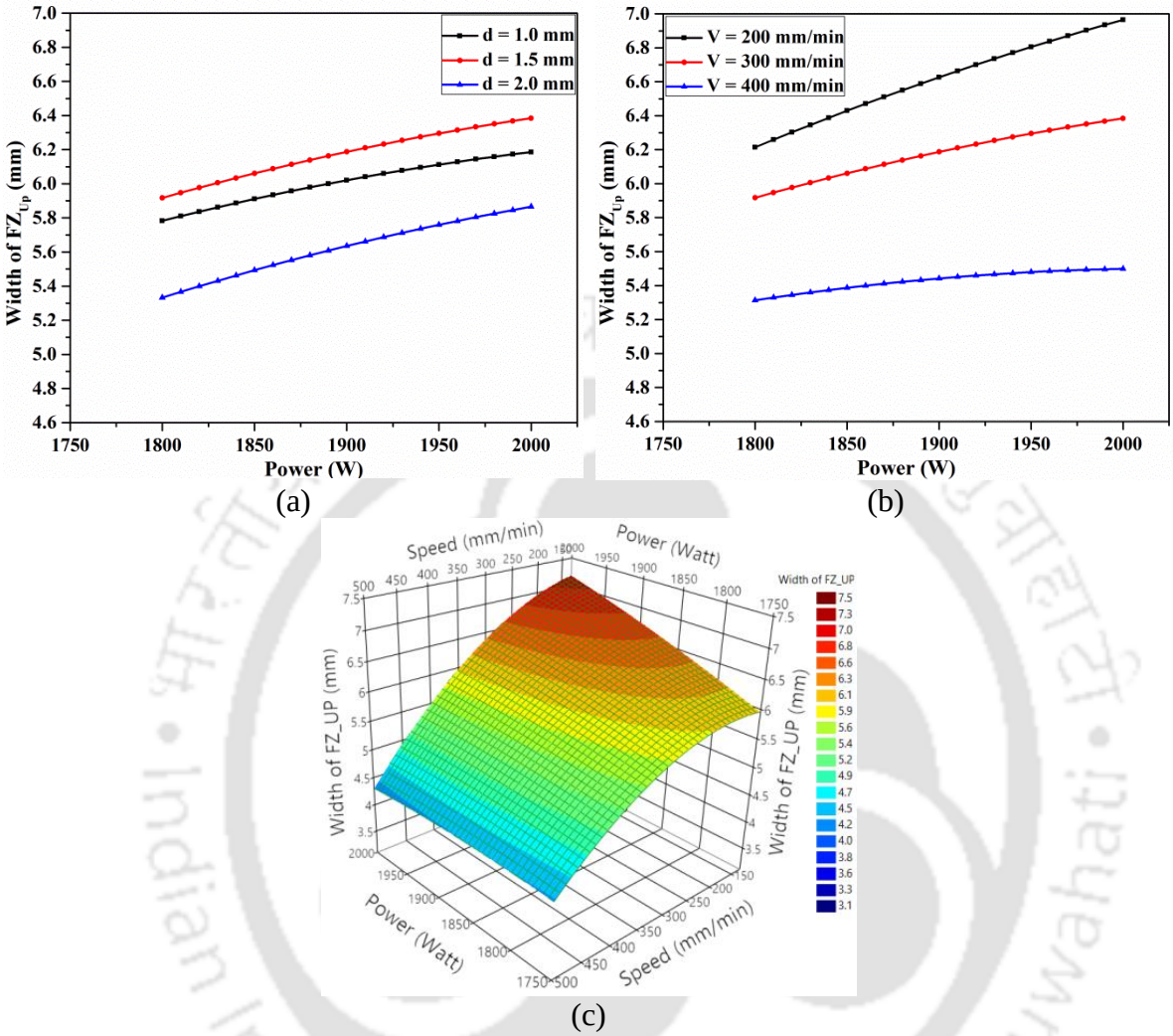

Fig. 4.13 Effect of LBW power on width of FZ_{UP} at different (a) defocused positions and (b) welding speeds; (c) 3D plot showing combined effect of LBW power and welding speed on width of FZ_{UP}

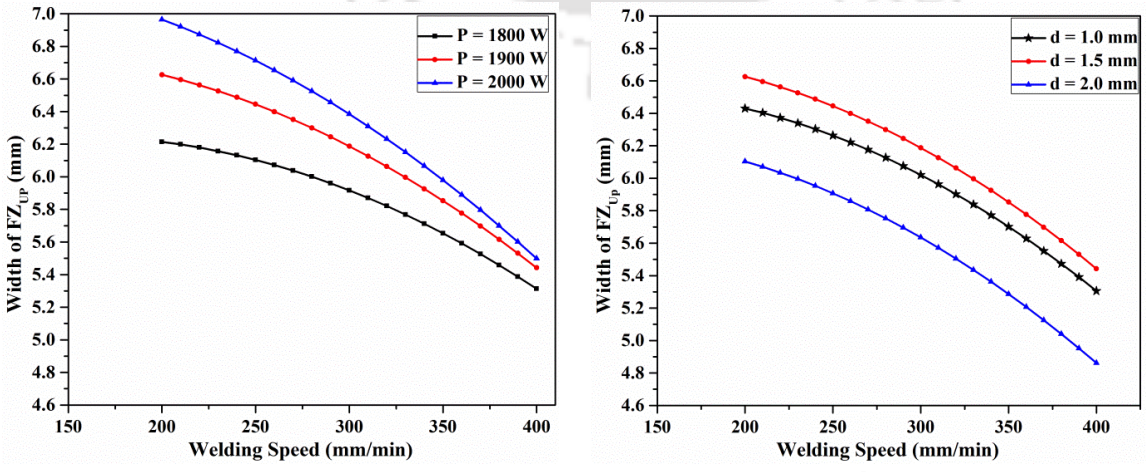

Fig. 4.14 Effect of welding speed on the width of FZ_{UP} at different (a) LBW power and (b) defocused position

Initially, most of the plasma absorption occurs inside the keyhole and hence the size of the keyhole increases with the increased LBW power. With further increase in the LBW power, plasma cloud is generated just above the top surface of the weld bead (Wang et al., 2012a). As a result, extra plasma absorption on the top of the weld surface takes place which increases the width of FZ_{UP}. Similar observations are reported by Weldingh and Kristensen (2001). The slope of curve in Fig. 4.14(a) is reached to its maximum value at 400 mm/min welding speed. It implies that welding speed has more impact on FZ_{UP} width than LBW power within welding speed range of 300 – 400 mm/min. At higher welding speed the process conditions are more likely to be near threshold energy density. The threshold energy density is defined as the minimum energy density required to bring the material to the boiling point and to maintain the vaporization rate to a level sufficient enough to generate a keyhole. Mathematically, it is expressed as a product of power density and interaction time. The interaction time (T_i) defines the time at which a particular point on the workpiece is interacting with the heat source while it is moving with a constant speed. The interaction time (T_i) is expressed as

$$\textit{Interaction time}\ \left(T_i\right) = \frac{\textit{Beam spot}\ \text{diameter}\ (D)}{\textit{Welding}\ \text{speed}\ (V)} \tag{4.6}$$

The power density, Q_{avg} (Eq. (4.1)) and interaction time, T_i (Eq. (4.6)) can be varied by changing laser beam power and welding speed, respectively at a constant beam spot diameter. For a given power density, there is a minimum interaction time at higher welding speed which produces threshold energy density. Thus in this range (i.e. 300 to 400 mm/min) of welding speed, any variation in the LBW power has lesser effect on FZ_{UP} width as compared to welding speed.

The reduction in the width of the FZ_{UP} at higher welding speed can be explained with the help of heat input and interaction time (Suder, 2014). With increased welding speed interaction time decreases. Hence, the heat input exerted on the workpiece surface along the weld line also decreases which results in lesser volume of metal being melted and it produces narrow FZ_{UP} width. Similar trend is observed in the curves between FZ_{UP} width and welding speed at different defocused positions (i.e. 1, 1.5 and 2 mm) as shown in Fig. 4.14(b) for 1900 W constant beam power.

4.3.1.2 Effect of defocused position

The power density exerted on the workpiece surface depends on both laser beam power and the distance between the workpiece surface and the focused plane i.e. defocused distance. The spot diameter of the laser beam is minimum at the focus plane. Hence, power density is maximum at this location. The spot diameter gradually increases by varying defocused position of the laser beam either below or above the workpiece surface. With an increase in the spot diameter, the energy distribution is more drawn out over the workpiece surface, hence the power density decreases resulting in decreased weld penetration. However, larger spot radius generates increased melting area on the top surface of the workpiece which results in wider weld pool. The laser beam progressively diverges away from the focus point. However, the laser beam slightly oscillates in the range of Rayleigh length. When the defocused point is positioned below the surface of the workpiece, the laser beam enters the keyhole and it converges progressively to the focus point and imposes higher power density to the focus point than that of the workpiece surface. It favours stronger melting and vaporization which facilitates the transfer of laser energy to more depth and thus welding depth becomes deeper. However, if negative defocus distance surpasses the laser Rayleigh length significantly, the dimension of the laser spot sharply increases. It changes the space distribution of the laser power density and further bead geometry (Liu et al., 2007 and Wang et al., 2014b).

From Figs. 4.15(a) and (b), it is observed that initially the width of the FZ_{UP} progressively increases with increasing defocused position.

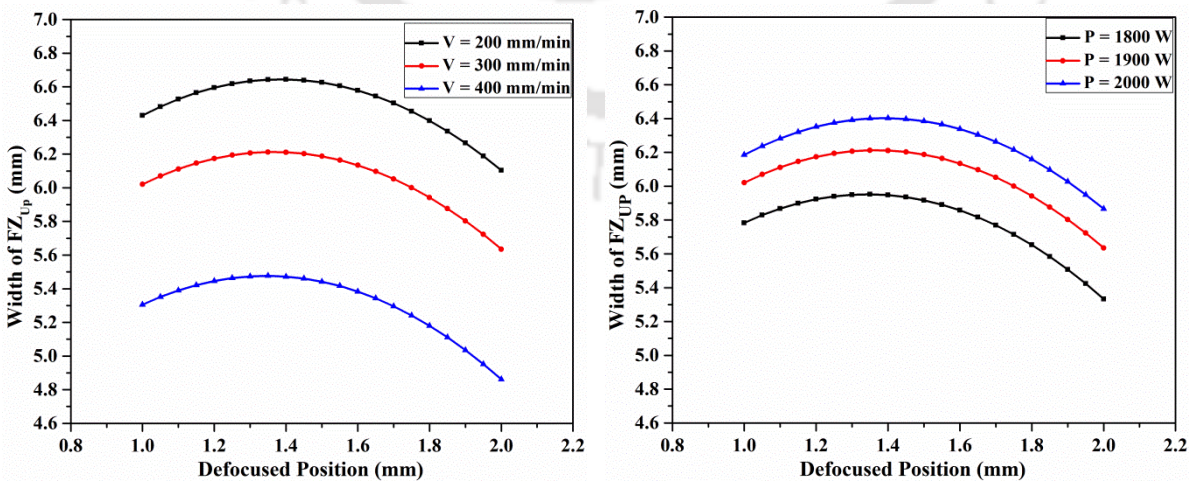

(a) (b)

Fig. 4.15 Effect of defocused position on the width of the fusion zone (FZ_{UP}) at different (a) welding speed and (b) LBW power

With increased defocused distance, laser beam spot area irradiated on the facade side of the welding seam increases inducing increased molten metal. Hence, FZ_{UP} progressively increases and it reaches to a maximum value at 1.5 mm of defocused position. With further increase in defocused position beyond 1.5 mm the FZ_{UP} width starts decreasing. Beyond 1.5 mm, the defocused position might have surpassed the laser beam Rayleigh length which leads to the increased laser beam spot diameter. Hence, energy density decreases continuously and it doesn't have sufficient energy to melt the metal around the periphery of the spot area. As a result, a decrement in the width of the FZ_{UP} is observed. It is clear from Table 4.7 that % contribution of welding speed (60 %) is more than LBW power (7.3 %). Hence, it may be concluded that the effect of welding speed on width of FZ_{UP} is highly dominant over LBW power as observed in both Figs. 4.15(a) and (b). Similar effect is observed by Batahgy et al. (2011) during LBW of duplex stainless steel. They reported that penetration depth is primarily dependent on LBW power whereas FZ_{UP} width primarily depends on welding speed.

4.3.2 Size of heat affected zone i.e. HAZ_{UP}

The size of the heat affected zone (HAZ) is one of the most important output responses for defining mechanical properties and quality of the welded components. The objective during welding was to reduce its size. The HAZ is the area of the base metal, which is not melted, but its microstructure and mechanical properties are changed after welding. The line energy and interaction time and also thermal conductivity of the base material play important role on HAZ_{UP} size. The cooling rate of any material having low thermal conductivity is slow. Hence, HAZ size becomes relatively large. Alternatively, a high thermal conductivity leads to high cooling rate and it makes lower size of the HAZ. Ti-6Al-4V alloy has very low thermal conductivity (6.7 W/m K). As a result, the thermal energy in the molten zone remains restrained for longer duration of time in the same place before it is dispersed (Caiazzo et al., 2004). Hence, higher size of HAZ is observed in case of Ti-6Al-4V alloy as compared to steel. The effect of process parameters on the size of the HAZ_{UP} are discussed in the following subsections.

4.3.2.1 Effect of LBW power and welding speed

The net heat input during welding is directly related to the LBW power (P), welding speed (V) and welding efficiency (η). The net heat input can be calculated as

$$Net\ heat\ input = \eta P / V \quad (4.7)$$

The efficiency of any welding process remains constant for a fixed combination of workpiece material and welding process. When beam power is increased and / or welding speed is decreased, heat input increases and vice versa. Hence, heat input during welding can be adjusted by controlling both LBW power and welding speed for achieving full penetration. At lower welding speed (i.e. 200 mm/min), heat input becomes higher. Hence, full penetration occurs at even lower value of LBW power i.e. 1800 W. Figures 4.16(a) and (b) show the macrographs in the weld region for 200 and 400 mm/min welding speeds, respectively at 1800 W constant LBW power. From Fig. 4.16, it is observed that full penetration is attained at a lower welding speed of 200 mm/min (Fig. 4.16(a)). Although at higher welding speed of 400 mm/min full penetration is not achieved (Fig. 4.16(b)) due to lower heat input at minimum interaction time.

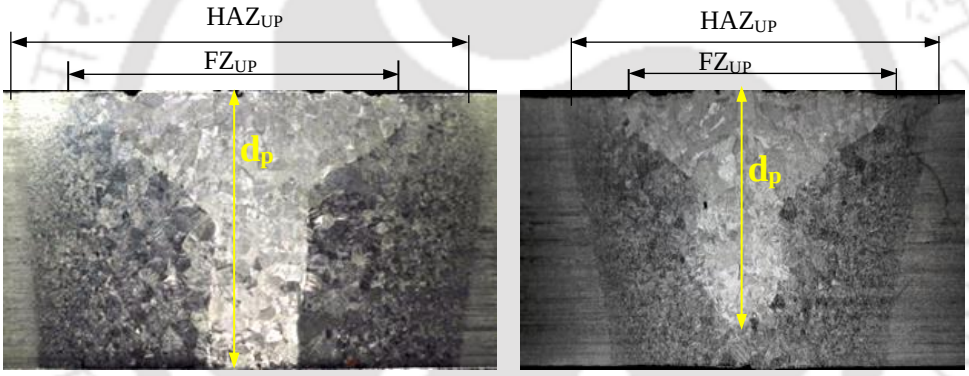

Fig. 4.16 Weld bead geometry at (a) 200 mm/min (b) 400 mm/min welding speeds at constant 1800 W LBW power and 1 mm defocused focus position (d_p is penetration depth)

Figure 4.17(a) shows the effect of LBW power on the size of the HAZ_{UP} at different welding speeds. From Fig. 4.17(a), it is observed that with increased LBW power, HAZ_{UP} increases continuously for lower welding speed of 200 mm/min. Since, full penetration is achieved at lower welding speed, further increase in welding power the heat input spreads laterally along width direction. Hence, HAZ_{UP} size increases. However, at higher welding speed (i.e. 300 and 400 mm/min), HAZ_{UP} size initially decreases up to 1870 W (for 300 mm/min speed) and up to 1950 W (for 400 mm/min speed) LBW power. Further increase in LBW power, the size of the HAZ_{UP} increases. It might be due to the combined effect of temperature dependent thermal conductivity of Ti-6Al-4V alloy, power density and heat input per unit length along the weld line.

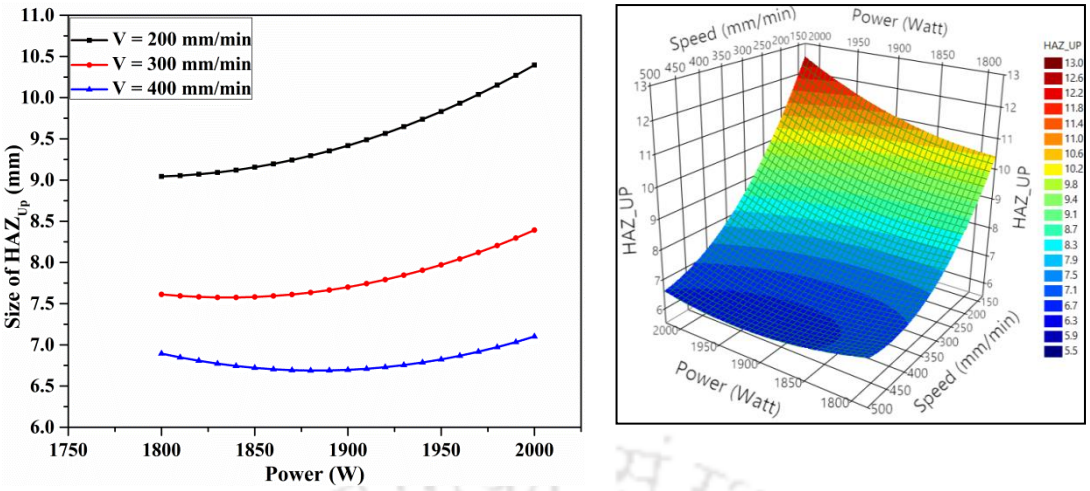

(a) (b)

Fig. 4.17 (a) Effect of LBW power on HAZ_{UP} size at different welding speeds; (b) 3D plot showing combined effect of LBW power and welding speed on HAZ_{UP} size

At lower range of LBW power (1800 to 1850 W) and higher range of welding speed (300 to 400 mm/min), the heat input is very low. Hence, full penetration does not occur as observed in the macrograph in Fig. 4.16(b). Initially, maximum amount of heat input is utilized to increase penetration depth and hence the size of the HAZ_{UP} decreases. When LBW power increases beyond threshold value for full penetration, the heat input spreads laterally along width direction. Thus the size of the HAZ_{UP} increases rapidly. However, the rate of increase in the size of the HAZ_{UP} is more at lower welding speed of 200 mm/min.

Fig. 4.17(b) shows 3D response surface plot of the combined effect of LBW power and welding speed on the size of the HAZ_{UP}. From Fig. 4.17(b), it is clearly observed that HAZ_{UP} size increases continuously with increased interaction time with reduced welding speed from 400 to 200 mm/min. At lower welding speed, the interaction time is very high and the heat energy in the FZ remains for longer duration of time. Hence, the heat energy is conducted from FZ to BMZ through HAZ and it makes wider size of HAZ_{UP}.

4.3.2.2 Effect of defocused position

Fig. 4.18(a) shows the effect of defocused position on the size of the HAZ_{UP} at different LBW power. Fig. 4.18(b) shows the effect of welding speed on the size of the HAZ_{UP} at different defocused positions of the beam at constant 1900 W beam power. The size of HAZ decreases with increasing value of welding speed due to the reduction in interaction time and heat input per unit length. Insignificant variation in the size of the HAZ_{UP} is observed for 1 and 1.5 mm defocussing positions.

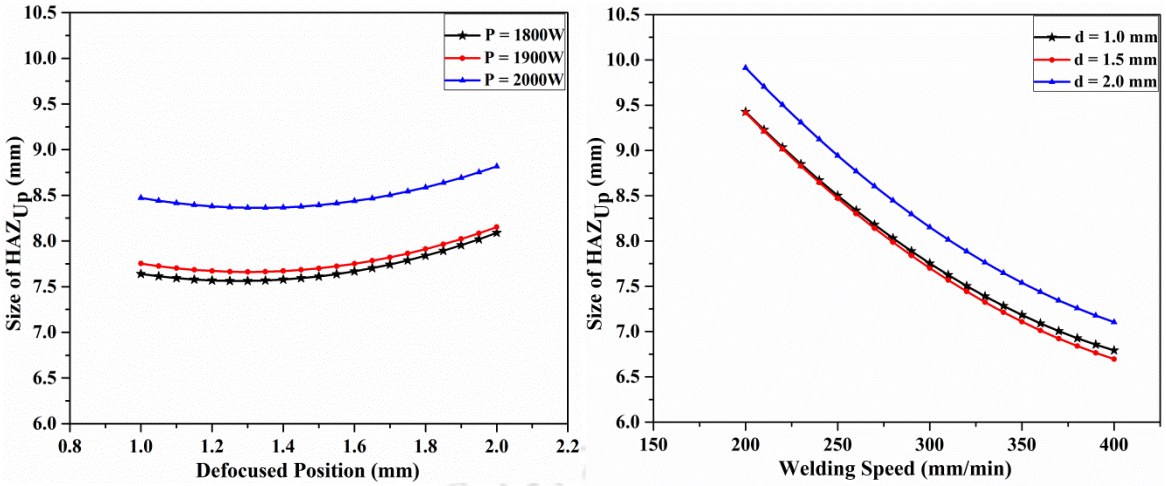

(a) (b)

Fig. 4.18 Effect of (a) defocused position and (b) welding speed on HAZ_{UP} size

The size of the HAZ_{UP} also depends on the diameter of the laser beam as it has negative impact on the power density. It is well known fact that the diameter of the laser beam varies little bit within Raleigh length. The defocused position in the present case may lie within the Raleigh length between 1 to 1.5 mm. Hence, negligible variation in the size of HAZ_{UP} is observed. Further increase in the defocused position beyond 1.5 mm, power density reduces on the metal surface. Hence, the generated temperature does not cross the melting point temperature of the Ti-6Al-4V alloy (i.e. 1690^0 C) across the cross section of laser spot. Thus the size of the HAZ_{UP} increases with increasing value of defocused position of the laser beam from 1.5 to 2 mm as observed in Figs. 4.18(a) and (b).

4.3.3 Fusion zone area i.e. FZ_{area}

The fusion zone area can be characterized as a mixture of molten base metal with high grade of homogeneity while the mixing is predominantly due to the convection of heat into melt pool. The main driving forces for convective heat flow and initiating the mixing of molten metal in the weld pool are buoyancy force, surface tension and electromagnetic force. Similar to the casting process, the microstructure in the FZ changes due to the melting and solidification of the base metal. The aim of the present study is to find out the optimum range of process parameters to achieve uniform microstructure and to reduce the fusion zone area (FZ_{area}) as discussed in the following subsections.

4.3.3.1 Effect of LBW power and welding speed

The laser beam power density plays a vital role during welding process. When power density exceeds beyond a certain limit, LBW mode changes from conduction to penetration

mode. At high welding speed, conduction mode of welding occurs and the weld pool becomes shallow. At low welding speed (provided LBW power density is high enough), deep penetration welding occurs and the weld pool becomes deep and narrow. With the increase in the welding speed to a higher value, non-uniform penetration occurs in the base plate. Figure 4.19(a) shows the effect of welding speed on fusion zone area (FZ_{area}) at different welding power and the combined effect of welding speed and LBW power is shown in Fig. 4.19(b) at a fixed 1.5 mm defocused position. It is observed from Fig. 4.19(a) that FZ_{area} continuously decreases with increased welding speed. As the welding speed increases, the interaction time of heat source with material decreases and also the heat input per unit length decreases which leads to less volume of base material being melted. Consequently, FZ_{area} decreases continuously.

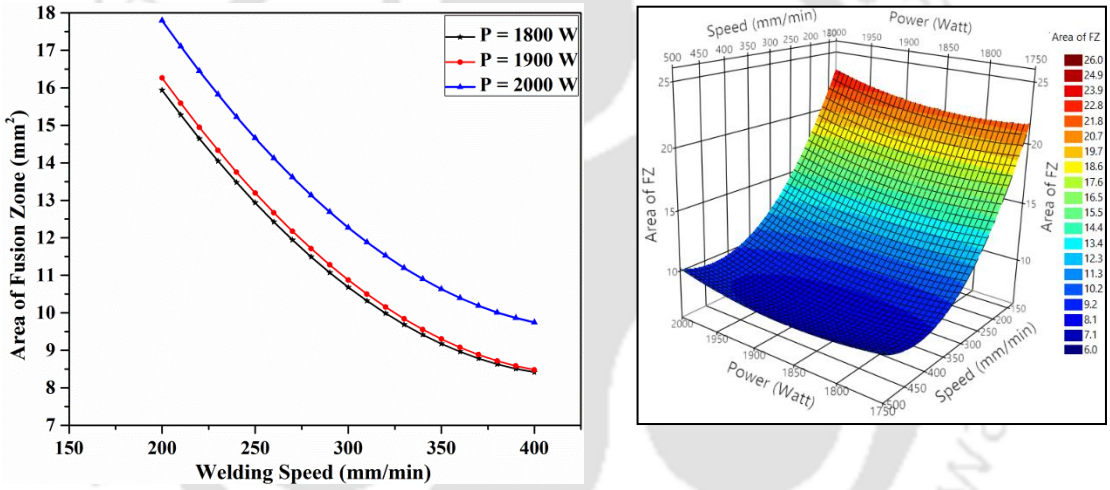

(a) (b)

Fig. 4.19 (a) Effect of welding speed at different LBW power and (b) combined effect of LBW power and welding speed on FZ_{area}

LBW power density primarily depends on LBW power for constant defocused position and welding speed. Higher LBW power means higher power density. Hence, larger volume of materials being melted. Therefore, increases with increased LBW power as observed in both Figs. 4.19(a) and (b). However, slight increment in the FZ_{area} is observed when LBW power increases from 1800 to 1900 W. When LBW power reaches to 2000 W, the power density is expected to exceed threshold value for the generation of keyhole. At this stage more prominent keyhole is generated and the energy is restrained inside weld pool due to multiple reflections of laser beam with keyhole wall. It leads to enlarged width of the fusion zone. As a result, the area of the fusion zone is drastically increased.

4.3.3.2 Effect of defocused position

Figure 4.20(a) shows the effect of defocused position and Fig. 4.20(b) shows the combined effect of defocused position and LBW power on FZ_{area} at 300 mm/min constant welding speed. In Fig. 4.20(a), insignificant variation in FZ_{area} is observed while increasing defocused positions for each LBW power. The % contribution of defocused position is very less (i.e. 0.08 % and insignificant) as compared to welding speed and LBW power (82.64% and 2.69%, respectively as per Table 4.9). Similar trend as in Fig. 4.20(a) is also observed by several researchers (Anawa et al., 2008a and Caiazzo et al., 2013). The effect of focal position on bead geometry is explained in details in section 4.3.1.2. The area of the fusion zone is predominantly dependent on overall bead geometry. Increasing defocused position from 1 to 1.5 mm, the laser beam enters into the keyhole and is converged gradually to the focus point. Hence, the power density is increased and also due to the multiple reflections of the beam with keyhole wall favours more melting and vaporization. It also transfers more energy towards the thickness direction and the weld bead becomes tapered. Hence, FZ_{area} slightly decreases. Figure 4.21 shows the macrograph of the weld bead for 1 mm defocused position at 1800 W beam power and 400 mm/min welding speed.

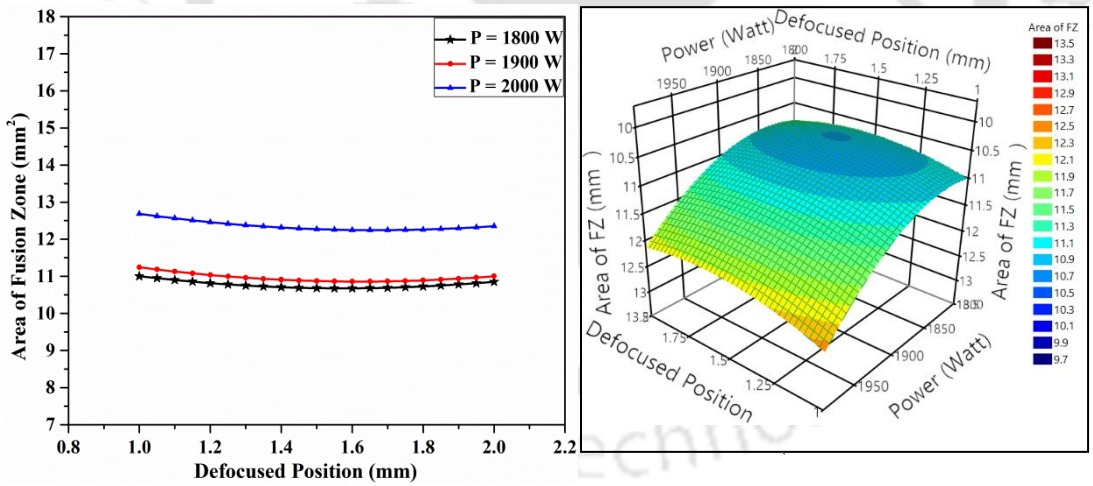

(a) (b)

Fig. 4.20 (a) Effect of defocused position at different LBW power and (b) combined effect of LBW power and defocused position on FZ_{area}

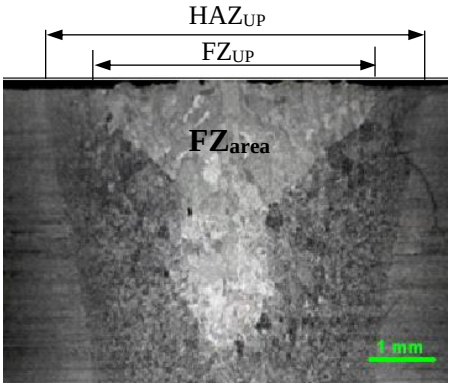

Fig. 4.21 Weld bead macrograph at 1 mm defocused position (P = 1800 W, V = 400 mm/min)

4.3.4 Microstructural analysis

During LBW process, heat source interacts with certain areas of the workpiece material. Hence, the welded region undergoes an excessive thermal gradient starting from weld pool to towards base material. It results in the generation of three distinct regions in the weldment namely FZ, HAZ and unaffected BMZ as shown in Fig. 4.22(a). Due to this spatial and temporal distribution of temperature, a non-uniform microstructure in the weldment is formed from FZ to BMZ. Among all three zones, HAZ experiences a temperature which is sufficient to produce only solid-state micro-structural changes without melting. The FZ experiences both melting and solidification. The microstructural development in the FZ depends on the solidification behavior of the weld pool which controls the shape and size of the grains and it affects the mechanical properties of the joint (Behler et al., 1998).

Figure 4.22 shows the optical and FESEM images of weld bead microstructures for Exp. 15 in Table 4.6. The optical macrograph with three different zones i.e. FZ, HAZ and unaffected BMZ of the weld bead is shown in Fig. 4.22(a). Figures 4.22(b) and (c) show the typical annealed microstructure (optical and FESEM micrograph, respectively) of the BM. In Fig. 4.22(c), the light and dark areas represent α and inter-granular β phase, respectively. The optical and FESEM micrographs of the fusion zone are shown in Figs. 4.22(d) and (e), respectively. It mainly consists of needle like α′ martensitic structure having acicular morphology. The acicular martensitic structure is formed by columnar α and β grains in the FZ and a mixture of martensitic α′, acicular α and primary α is formed in the HAZ. Similar microstructures in the FZ and HAZ in LBW of Ti-6Al-4V alloy are reported by several researchers (Cao and Jahazi, 2009, Caiazzo et al., 2013 and Balasubramanian et al., 2011). The reason for the formation of martensitic α′ phase is due to faster cooling rate involved during LBW process.

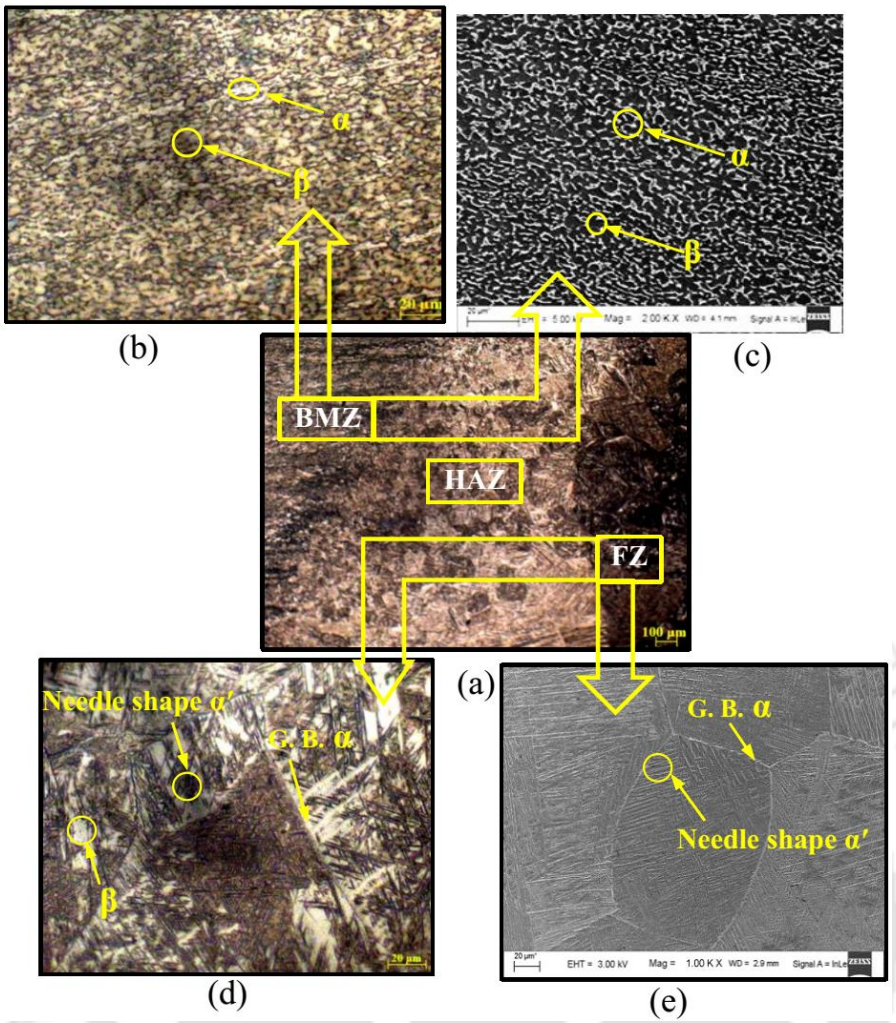

Fig. 4.22 Microstructure of the welded specimen (Exp. No. 15, Table 4.6) at different zones; (a) Optical image consisting three zones (BMZ, HAZ and FZ); (b) Optical image and (c) FESEM image of BMZ; (d) Optical image and (e) FESEM image of FZ

Cooling rate above 410 °C/s is required for (α + β) phase in the base metal of Ti-6Al-4V alloy to completely transform into martensitic α′ phase (Ahmad and Rack, 1998). This transformed microstructure exhibits high strength and hardness value at the expense of ductility and toughness. LBW promotes diffusionless transformation of the β phase into α′ martensitic microstructure due to its high self-quench rate. Some amount of β phase (Fig. 4.22(d)) may be retained within the martensitic matrix due to the presence of vanadium in the Ti-6Al-4V alloy which suppresses the formation of martensitic temperature below room temperature. In the present study, small amount of β phase is also observed in the FZ along with grain boundary (G. B) α phase. It indicates that the cooling rate is close to the required limit necessary for the formation of α′ martensite. When the FZ is fully martensitic they are highly prone to cracking as reported by some researcher (Huang et al., 2012). However, they did not observe any severe problem due to weld cracking. In the present study, such weld cracking is not observed in any experiments. It is mainly due to excellent crack resistance

property of Ti-6Al-4V alloy. The α′ martensite is a supersaturated non-equilibrium hexagonal α phase. The volume fraction of α′ martensite increases with increasing cooling rate.

A significant variation in the microstructure is observed while moving lateral direction from the weld line towards BMZ. The micrograph at different locations of the HAZ is shown in Fig. 4.23 (ii) (b). From microstructure near FZ (i.e. zone 3) it is observed that this region consists of almost 100% α′ martensite with a very small amount of α + β phases as shown in Figs. 4.23(i)(c) and 4.23(iii)(c) in optical and FESEM micrographs, respectively. The middle of the HAZ consists of a mixture of primary α and β phases with a little amount of α′ (Fig. 4.23(i)(b) and Fig. 4.23(iii)(b)). Away from the HAZ (close to BMZ i.e. zone 1), the region consists of α + β phase with very small amount of α′ (Fig. 4.23(i)(a) and Fig. 4.23(iii)(a)). The volume fraction of α′ decreases in HAZ from near FZ to close to BMZ. These variations of α′ martensite at different locations of weld bead affect hardness value at those regions as discussed in section 4.3.6.1.

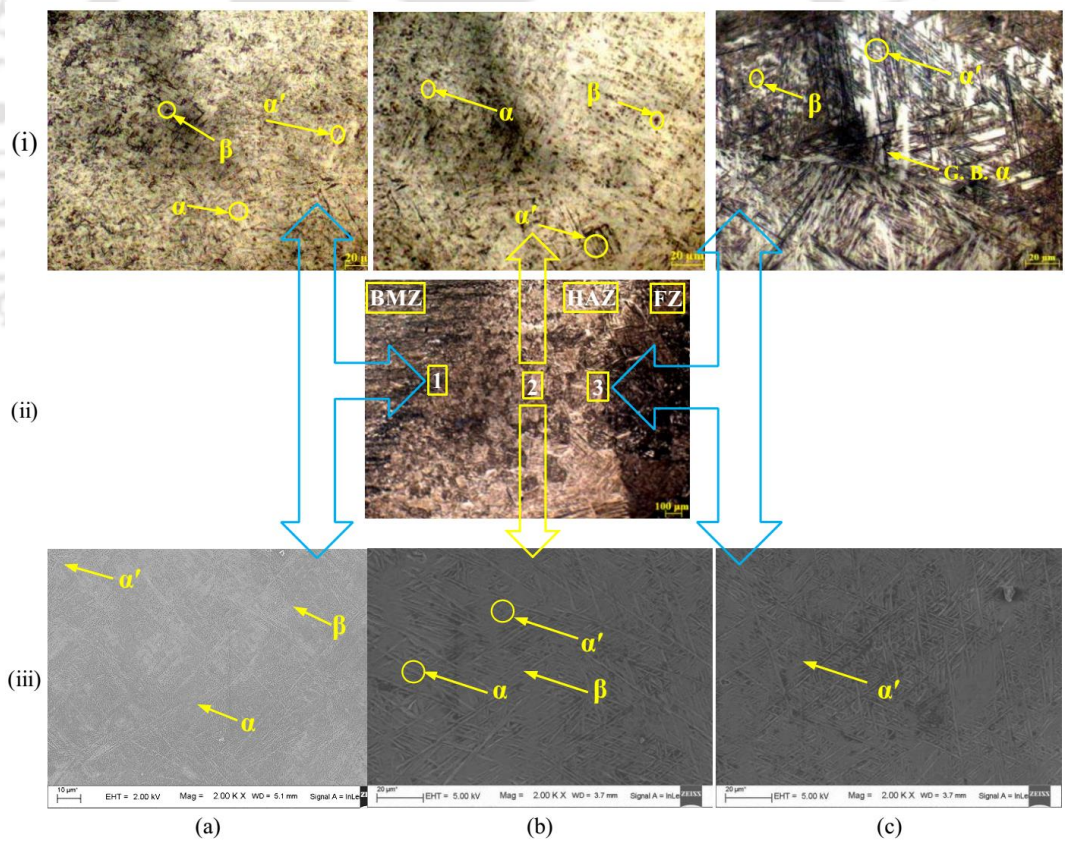

Fig. 4.23 Microstructure of HAZ at different locations (a) near BMZ, (b) middle of HAZ and (c) near FZ; (i, ii) Optical image and (iii) FESEM image of welded specimen for Exp. No. 15

Unlike FZ, each point in the HAZ experiences distinct temperature gradient in terms of both maximum temperature and cooling rate during welding. Thus, each point in the HAZ

has its own micro structural features. The microstructure in the HAZ is a mixture of α′ and primary α phases. Similar structure can be formed when Ti-6Al-4V is quenched below β transus temperature i.e. between 720 to 985 ˚C (Elmer et al., 2004). The percentage of α′ phase decreases from almost 100% in the FZ to approximately zero in the BMZ. It is obvious that the HAZ near FZ (i.e. zone 3) experiences higher temperature during welding than the HAZ near BMZ (i.e. zone 1). The zone 3 in HAZ is cooled from above-β-transus but below liquidus temperature and zone 1 is cooled from below-β-transus temperature (sufficient to change its microstructure).

4.3.5 Porosity

Porosity is one of the most common and undesirable welding defects which severely depreciates joint performance. Generally, two kinds of welding porosities i.e. metallurgical and characteristic pores are observed during deep penetration LBW of Ti-6Al-4V alloy. The pores can appear at various locations in the weld bead such as near the centerline of FZ, at the interface between FZ and HAZ or arbitrarily distributed in the FZ. The formation of the pores due to the trapped gases within the solidifying weld pool of Ti-6Al-4V alloy is reported in many literatures (Kabir et al., 2010, Cao and Jahazi, 2009 and Huang et al., 2012). In the present study, most of the welded samples are free from porosity as most of the welded samples are fully penetrated as observed in Table 4.6. However, in few samples small amount of pores are observed. In case of fully penetrated keyhole mode of welding, the top and bottom surfaces allows the bubbles to escape more effectively as compared to the partially penetrated samples. Caiazzo et al. (2013) also did not observe pores in their fully penetrated samples during LBW of Ti-6Al-4V alloy. Similar observations are also reported by Hilton et al. (2007) during LBW of 5 mm thick Ti-6Al-4V alloy. They reported that large amount of molten metal is produced in the lower part of weld bead due to the formation of keyhole inside melt pool. It promotes the escape of trapped shielding and evolved hydrogen gases from the weld pool.

In the present study, very small sized micro pores are observed as shown in optical micrograph in Fig. 4.24(a) in partially penetrated welded sample (Exp. 3, Table 4.6). In partially penetrated welded samples, the tendency for porosity formation is increased since the escape of gas porosity before solidification is accessible only from top surface. In Fig. 4.24(a), the shape of the pores is mostly spherical which indicates gas type porosity. It is usually caused by the absorbed hydrogen in the molten weld pool that cannot escape before solidification. For Exp. No. 15, although full penetration in keyhole mode of welding is

occurred. However, porosity is also observed (Fig. 4.24(b)) at the interface between FZ and HAZ. Here, porosity is formed due to the evolution of hydrogen gas at the solid / liquid interface. FESEM image of Fig. 4.24(b) indicates that the pores are round and smooth and their sizes are in between 25-36 µm. It satisfies the weld quality acceptance criteria as mentioned in European standard BS EN: 4678 (2011) where it is recommended that the size of the micro pores should be less than or equal to 0.40 mm. However, large sized pores are not observed in the weld pool area. It may be due to the presence of higher buoyancy force which favours the pores to escape out of the weld pool effectively.

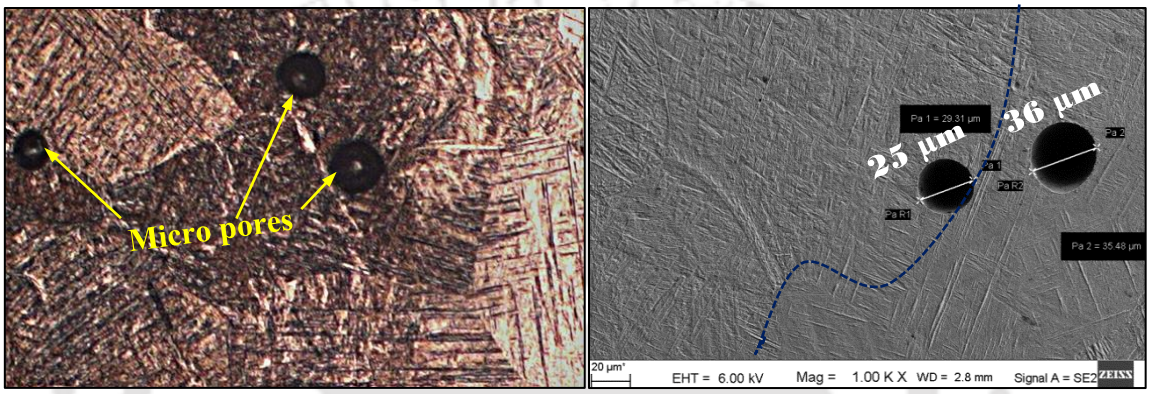

(a) (b)

Fig. 4.24 Micro pores appearance in weld bead (a) randomly scattered for Exp. 3 and (b) at solid liquid interface for Exp. 15 (Table 4.6)

4.3.6 Mechanical properties

The important mechanical properties like hardness and tensile strength of the welded samples are measured and are discussed in the following subsections.

4.3.6.1 Hardness

Hardness value of a material is not a unique property however a difference in hardness between two materials indicates that the materials are not alike. Among various mechanical tests performed to determine the characteristics of a material and its suitability for a given application, hardness testing is one of the most critical one. Hardness testing is often the best way of establishing component's survival and performance in their specific applications. The hardness value of the welded sample depends on the presence of different phases of the materials and developed microstructure during welding. The hardness value in the HAZ gives indications of its susceptibility to crack. Also, the hardness value in FZ is commonly used to find out the less ductile phases in that zone which may prone to cracking.

In the present study, Vickers microhardness of the welded specimens is measured in transverse direction to the weld line at different locations of upper and middle portion of bead cross sections for experiment No. 15 (Table 4.6) and its distribution is shown in Fig. 4.25(a). In Fig. 4.25(a), the lowest hardness value is observed in BMZ with average value between 305-315 HV. The hardness value increases from HAZ to the FZ. In the FZ its value ranges between 352-368 HV. The higher value of hardness is observed in both HAZ and FZ as compared to BMZ. It is mainly due to different microstructures developed across these regions during welding. The maximum hardness value in the FZ is due to the presence of α′ phase of martensitic structure due to high cooling rate in FZ which exhibits high hardness and strength at the expense of toughness and ductility. The percentage of α′ phase decreases approximately from 100% in the FZ to zero in the BMZ. Accordingly, hardness value also decreases from FZ to BMZ on both side of weld line as observed in Fig. 4.25(a). Similar phenomenon is also reported by Akman et al. (2009) during LBW of Ti-6Al-4V alloy. The relationship between hardness value and heat input per unit length i.e. line energy at 1 mm and 2 mm defocused positions is shown in Fig. 4.25(b).

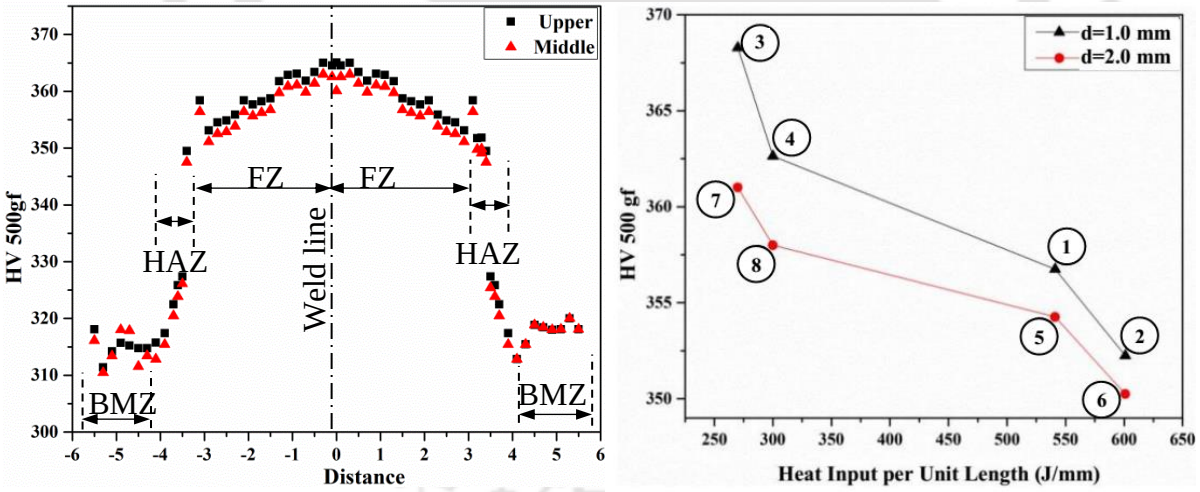

(a) (b)

Fig. 4.25 (a) Vickers microhardness profiles along transverse direction to weld line at upper and middle sections of the weld bead (Exp. No. 15, Table 4.6); (b) Average microhardness in FZ at different heat input per unit length for 1 and 2 mm defocused positions (The Exp. No. corresponding to welded samples in Table 4.6 are shown inside circles)

From Fig. 4.25(b), it is observed that for a certain defocused position, the hardness value decreases with increasing line energy in the FZ which affects cooling rate. When heat input per unit length decreases, cooling rate increases. Hence, more refined α′ phase is formed in the FZ and hardness is increased. It is also observed from Fig. 4.25(b) that the average hardness value in the FZ decreases with the increase in defocused position from 1 to 2 mm (Fig. 4.25(b)). It is also observed from Fig. 4.25(b) that the average value of hardness

in the FZ at 2 mm defocused position is lower than the hardness value for 1 mm defocused position. It is reported by several researchers that the grain size decreases with the increase in defocussing distance below workpiece surface (Caiazzo et al., 2013). The smaller the grain size the material becomes harder. But there is a critical range of grain size below which the hardness value decreases with decreasing grain size. In the present study at 2 mm defocussed position, the grain size may be decreased below the critical range of grain size. Hence, average hardness is decreased in the FZ.

4.3.6.2 Tensile strength

The tensile properties of the few welded samples are measured at room temperature and are given in Table 4.12. In all the tested samples fracture occurs in the HAZ. The percentage elongation and ultimate tensile strength after welding are degraded. It may be partly due to any one of the following reasons i.e. incomplete penetration, presence of microspores, excessive penetration and presence of brittle nature of martensitic phase. At lower welding speed, excessive penetration (dropout) occurs for Exp. 1 (Table 4.6) which produces underfill welding defects. Due to this reason tensile strength of the sample degraded.

Table 4.12 Tensile properties of the welded samples

Exp. No. (Table 4.6)	Yield strength (MPa)	Ultimate tensile strength (MPa)	Young's Modulus (GPa)	% elongation
1	763	872	87.86	3.74
3	774	887	84.27	4.16
15	697	918	86.74	3.26

Porosity as discussed in section 4.3.5 is one of the unwanted welding defects which reduces the joint strength. In case of Exp. 3 (Table 4.6) incomplete penetration occurs due to lower LBW power and high welding speed. As a result, randomly scattered porosities are formed in the partially penetrated weld bead of Exp. No. 3 as observed in the optical image shown in Fig. 4.24(a). However, such porosities are rarely observed for all fully penetrated welded samples for other experiments in Table 4.6. It indicates that proper balance between LBW power and welding speed is necessary to inhibit porosity. Porosity is also observed for Exp. 15 at the interface between FZ/HAZ (Fig. 4.24(b)). These defects (underfill and pores) act like a stress concentrator which leads to the initiation sites for fatigue cracks (Ahn et al., 2016). As a result, strength and % elongation (ductility) of few welded samples (Table 4.12) are decreased. The FZ having martensitic microstructure also leads to lower ductility of the

weldment. Both strength and ductility of the weldments may be improved by post heat treatment of the welded specimens.

4.4 Conclusions from design of experiment

In the present study, laser beam welding of 5 mm thick Ti-6Al-4V alloy in butt configuration is carried out using fiber laser at different welding conditions to understand the effect of process parameters on weld bead features i.e. FZ_{UP}, HAZ_{UP} and FZ_{area}. ANOVA is carried out to identify the most significant process parameters and their percentage contribution on output responses. Regression analysis is carried out to study individual and combined effect of process parameters. Later, few validation tests are conducted at few random points within the range of process parameters. Finally, optimization of the process parameters is carried out to minimize width of FZ_{UP}, size of HAZ_{UP} and FZ_{area} for achieving deep penetration.

Also, metallographic analysis of the welded joints using FESEM and optical micrographs are studied to find out the distribution of different phases within the matrix. The mechanical properties of the welded joints like tensile strength and hardness are studied and the change in mechanical properties are correlated with the developed microstructure in the FZ as well as in the HAZ. Smooth, uniform and shiny bead without spatter and crack having acceptable size of micro pores is formed. Full penetration in the weld bead is achieved at high power and low welding speed however undercuts, bead decay and excessive penetration are also observed. The weld pool is almost symmetrical about the centre line of FZ. Weld defects in the present study are reduced extensively under appropriate shielding gas environment with optimum selection of process parameters. From ANOVA, it is confirmed that welding speed has highest impact on the output response followed by LBW power and defocused position of laser beam. LBW power shows positive effect on the output responses whereas welding speed shows negative impact. However, defocused position of laser beam shows diverse effect on bead geometry. The FZ_{area} is not affected by the defocused position of the laser beam. The optimum welding parameters are effectively determined by using a optimization technique and their values are 1900 W beam power, 400 mm/min welding speed and 2 mm defocused position. From microstructural study of the weld bead, it is observed that α′ martensitic structure is formed in the FZ and near HAZ. The HAZ (near BMZ) consists of primary α, intergranular β and small amount of α′ phase. The amount of α′ phase in the HAZ decreases from approximately 100% in near FZ to almost zero in BMZ. Maximum hardness of the workpiece is observed in the FZ as well as near HAZ due to the

presence of large amount of α′ martensitic phase. The hardness values in the FZ for 2 mm defocused position is lower than 1 mm defocused position due to the decrement in grain size below a critical range. The ultimate tensile strength and % elongation of welded samples are degraded as compared to BM which can be improved by employing suitable post heat treatment.

Chapter 5
Experimental investigation of 2 mm thick Ti-6Al-4V plates

5.0 Introduction

The quality of weldments and its performance during service condition depends on different weld bead features such as size of FZ and HAZ, bead shape, flow behaviour of molten material during welding, developed microstructures in the weld bead and weld bead defects. The complexity of physical and metallurgical phenomenon which occurs during LBW process may result in subsequent failure of weldments in service condition. Around 45% cases, weld bead defects occur due to selection of inadequate welding process parameters. In fact, till date many welding fundamentals are not explored. Hence, it is important to anticipate and incorporate the effects of welding parameters. Also, significant amount of work is required to find out the most suitable welding conditions to produce consistently good quality of weldments. To investigate the weldability of 2 mm thick Ti-6Al-4V alloy plates two sets of welding experiments are conducted. In **1st set of welding experiments,** the individual effect of welding power and welding speed on output responses are discussed. The welding power and the welding speed are varied between 800 – 1200 W and 500 – 900 mm/min, respectively at constant defocused position on workpiece surface with 200 µm spot diameter. Line energy combines both welding power and welding speed as given in Eq. (4.2). Further, in **2nd set of welding experiments**, the comparison between bead shapes, line energy utilization factor, microstructures and mechanical properties of the weldments are analyzed at different line energies.

5.1 1st set of experiments: Effect of beam power and welding speed

In this section, different bead features such as width of upper (FZ_{UP}), middle (FZ_{Mid}) and lower (FZ_{Low}) fusion zone, fusion zone area (FZ_{area}), size of upper (HAZ_{UP}), middle (HAZ_{Mid}) and lower (HAZ_{Low}) heat affected zones are measured in optical microscope as shown in Fig. 5.1. The weld quality in terms of bead appearance, bead features, hardness of weldments, weld bead defects and its minimization techniques are discussed. Also, microstructural studies at different locations i.e. HAZ and FZ are carried out using FESEM as

well as optical microscope (OM). After that their morphologies are compared at different welding conditions using FESEM images. The experimental conditions are given in Table 5.1. Initially, beam power is varied between 800 – 1200 W at constant welding speed of 500 mm/min. Beyond 1200 W beam power, more cavities are formed along the weld line due to the evaporation of molten metal. Hence, further welding speed is varied between 500 – 900 mm/min keeping beam power fixed at 1200 W.

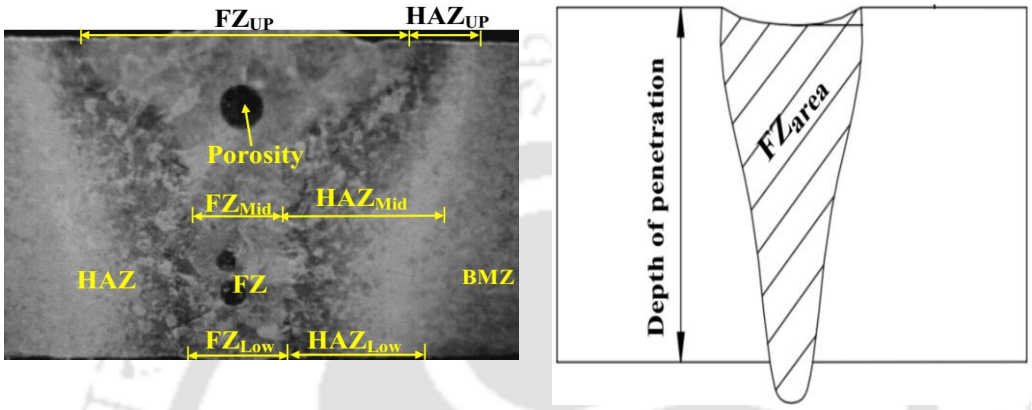

(a) (b)

Fig. 5.1 (a) Optical image of bead features and (b) schematic diagram showing depth of penetration and fusion zone area (FZ_{area})

Table 5.1 Experimental conditions and bead observations

Exp. No.	Process parameters			Response	Observations
	P (W)	V (mm/min)	H (J/mm)	DP (mm)	
1	800	500	96.04	1.28	DP* < 80%, USW
2	900	500	108.04	2	FP, SW
3	1000	500	119.90	2	FP, SW
4	1100	500	132.05	2	FP, SW
5	1200	500	144.06	2	EP, USW
6	1200	600	120.00	2	FP, SW
7	1200	700	102.83	2	FP, SW
8	1200	800	90.02	2	FP, SW
9	1200	900	80.00	1.42	DP < 80%, USW

**DP–Penetration depth, FP–Full penetration, EP–Excess penetration, USW–Unsuccessful weld, SW–successful weld*

5.1.1 Results and discussion

The experimental results at different welding conditions are discussed in details in the following subsections.

5.1.1.1 EDS analysis of weld bead

The concentration (wt. %) of alloying elements in base metal is confirmed by chemical analysis using EDS analysis as shown in Fig. 5.2(a). EDS analysis (Fig. 5.2(b)) is also conducted along the weld line of the welded samples to check formation of any metal oxide. The insignificant increase in O_2 concentration from 1.7 wt. % in the base metal (Fig. 5.2(a)) to 2.5 wt. % in the weldment (Fig. 5.2(b)) shows that the weld pool is efficiently protected by controlled flow rate of "Ar" shielding gas as explained in details in section 4.1.2.1.

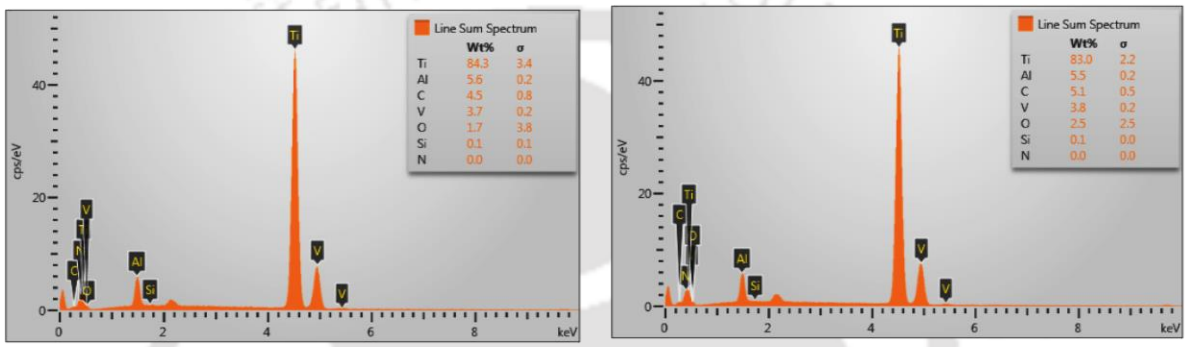

(a) (b)

Fig. 5.2 Concentration of alloying elements in Ti-6Al-4V using EDS (a) in base metal and (b) in welded sample along weld line

5.1.1.2 Bead appearance

The bead appearance on both top and bottom surfaces of weldments are shown in Table 5.2 at various welding conditions (Table 5.1). All the welded surfaces in Table 5.2 except Exp. No. 5 are bright, silvery and aesthetic in appearance which indicates good shielding of molten weld pool from environmental contaminations. These kinds of bead appearances are consistent with the results reported by Hong and Shin (2016) and Wang et al. (2014a). At higher beam power of 1200 W (at constant V = 500 mm/min), the color of top surface of specimen looks grey in powdery form (Exp. No. 5, Table 5.1). It indicates that the top surface of this weldment is highly contaminated by atmospheric air during solidification. Hence, this welding condition is not favorable to inhibit contamination in weld bead although the shielding gas is efficiently supplied. The most important finding during visual inspection is noticeable differences in the weld bead surface quality (Table 5.2) at different experimental conditions (Table 5.1). Smooth surface is observed at combination of lower welding power and higher welding speed. It is also observed that beyond 1000 W beam power, blowholes and cavities start appearing in the weldments.

Table 5.2 Weld bead appearance at different welding conditions (Table 5.1)

Exp. No.	Bead appearance: Top side	Bead appearance: Bottom side	Remarks
1			NC*, shiny bead, silver color, PP, SF
2			NC, shiny bead, golden color, FP, SF
3			NC, shiny bead, silver color, FP, US, HR
4	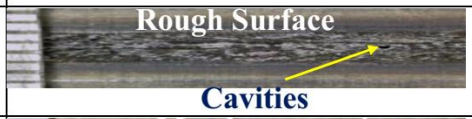		NC, shiny bead, silver color, FP, US, HR, ME, UW
5	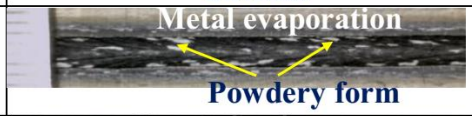		NC, shiny bead, silver color, FP, US, ME, UW
6			NC, shiny bead, golden color, FP
7			NC, shiny bead, golden color, FP
8	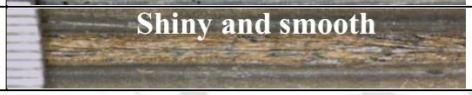		Shiny bead, NC, PP, US, spatter

**NC- No crack, FP- Full penetration, PP- Partial penetration, US- Uneven surface, SF- Smooth surface, HR- High roughness, ME- Metal evaporation, UW- Unsuccessfull weld*

It is mainly due to the presence of low boiling point alloying elements in Ti-6Al-4V BM which vaporizes inside molten metal at higher beam power. Hence, during solidification, sufficient liquid metal is not available for filling the cavities in the weld bead. Significant differences in weld bead appearance (Exp. 6 to Exp. 8, Table 5.2) are observed with increasing welding speed at a constant beam power. At lower welding speed (600 mm/min), the welded specimen has discontinuous and scraggy surface. Increasing welding speed, the specimen surface becomes continuous and uniform (Exp. 7, Table 5.2). Further increase in welding speed beyond 800 mm/min, spatter is generated due to higher welding speed and again the weld bead surface becomes irregular due to lower LE. Hence, a combination of higher beam power and intermediate welding speed is recommended for LBW of Ti-6Al-4V alloy.

5.1.1.3 Bead geometry

Figures 5.3(a) and (b) show bead geometries at different beam power and welding speed, respectively. Increasing beam power from 800 to 1100 W, the bead shapes gradually

change from U-shaped with elongated top to X-shaped (Fig. 5.3(a)). Finally, at 1200 W beam power, H-shaped weld bead is formed. At 1200 W beam power (Exp. 5, Fig. 5.3(a)), the power density is very high and welding speed is low (500 mm/min). Due to these reasons, evaporation of metal takes place and underfill weld defect is formed. However, the shape of the weld bead slowly changes from H-shaped (Fig. 5.3(a), Exp. 5) to T-shaped and FZ becomes shallower (Fig. 5.3(b)) with increased welding speed from 500 to 900 mm/min at a constant 1200 W welding power. From the macrographs of Fig. 5.3, it is observed that the weld bead is almost symmetrical about center line of FZ. However, at higher welding power, the beads in few cases (Exps. 4 & 5) become slightly asymmetric at the root side. It is mainly due to the combined effect of two opposite nature of forces i.e. electromagnetic force and surface tension acting in the weld pool as explained in section 4.1.2.2.

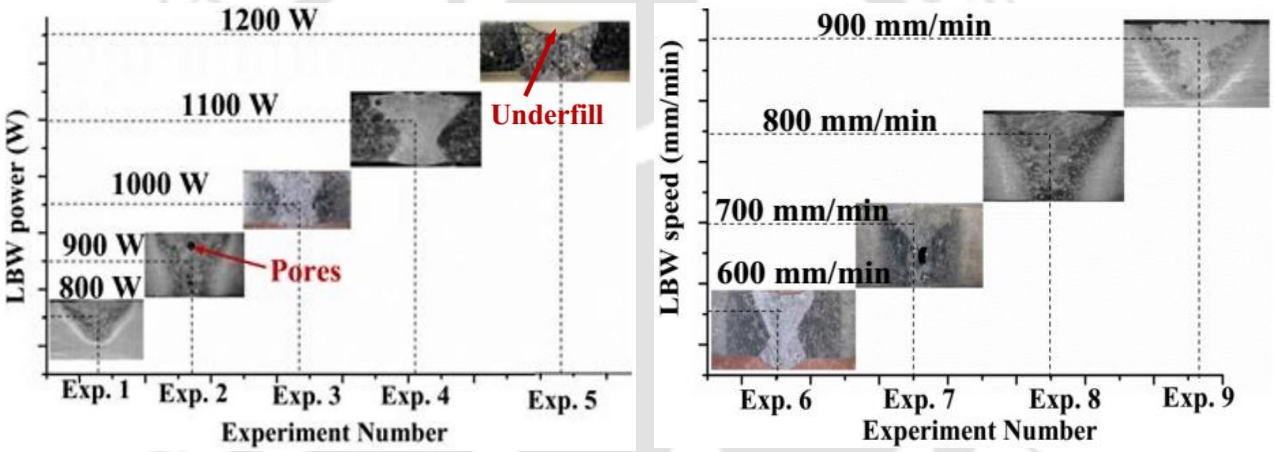

Fig. 5.3 Bead geometries at different (a) beam power and (b) welding speed

5.1.1.4 Penetration depth

In Exp. 1, 1.28 mm penetration depth is observed at 96.04 J/mm LE and 800 W LBW power. However, almost full penetration in Exp. 8 and higher penetration depth of 1.42 mm in Exp. 9 are observed at lower LE of 90.02 and 80 J/mm, respectively as compared to Exp. 1. However, in both these experiments, higher beam power of 1200 W is applied. These observations indicate that LBW power density (Eq. (4.1)) is the main controlling process parameter for penetration depth as compared to LE. Similar trends are also reported by Pakniat et al. (2016) for CW fiber LBW of 2 mm thick Hastelloy plates. From Exp. Nos. 8 and 9 (Table 5.1), it is observed that penetration depth is reduced from full penetration of 2 mm to 1.42 mm while increasing welding speed due to decreased LE with increased welding speed from 800 to 900 mm/min at a fixed 1200 W beam power.

5.1.1.5 Fusion zone widths and area (FZ_{area})

Figures 5.4(a) and (b) show the variation in FZ widths at different positions of weld bead cross-section (i.e. FZ_{UP}, FZ_{Mid} and FZ_{Low}) at different beam power (500 mm/min welding speed) and welding speed (1200 W beam power), respectively. From Figs. 5.4(a) and (b), it is found that FZ_{UP} is larger than both FZ_{Mid} and FZ_{Low} for all experiments in Table 5.1. It is mainly due to prominent flow of molten metal towards upper part of melt pool as compared to lower part which disrupts keyhole shape starting from bigger width at upper part to reduced one at lower part of weld bead.

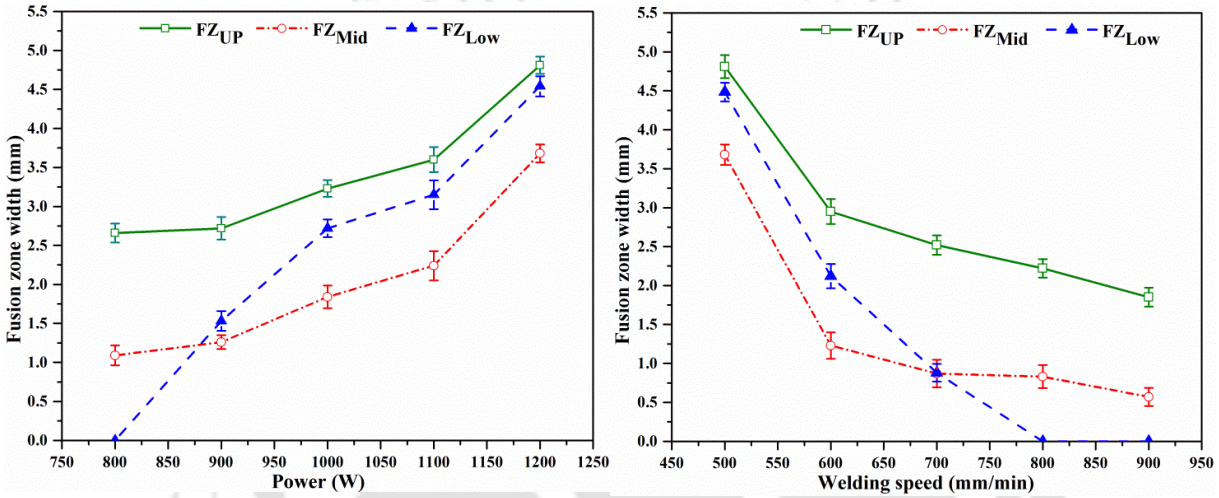

(a) (b)

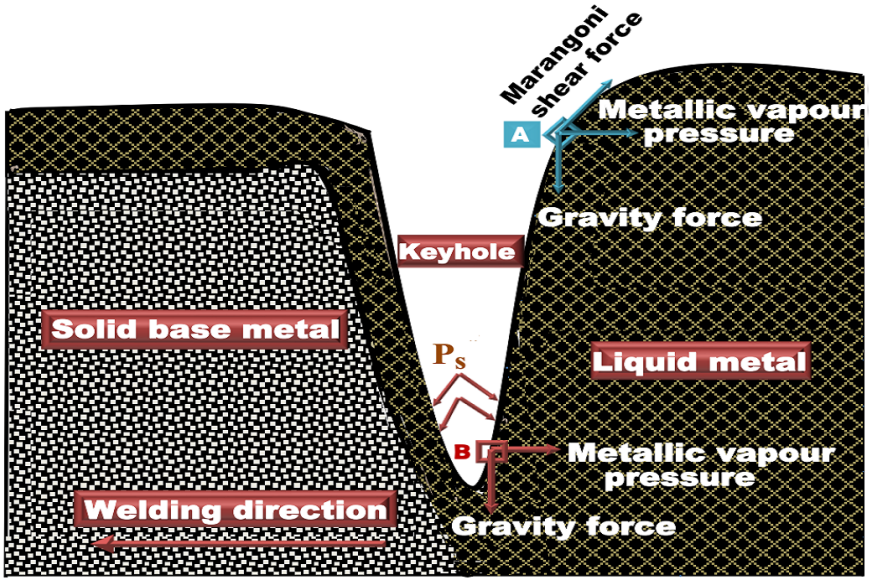

(c)

Fig. 5.4 Variation in FZ width at different (a) beam power (500 mm/min fixed welding speed) and (b) welding speed (fixed welding power of 1200 W); (c) Schematic diagram of forces acting inside keyhole (P_s= Surface tension force)

Initially, molten metal moves from the center of melt pool towards periphery of the keyhole due to Marangoni effect which is accelerated by the existing surface tension inside melt pool. At the top portion of keyhole (position "A" in Fig. 5.4(c)), Marangoni shear stress and vapour pressure are very strong as compared to gravitational force. Therefore, molten metal flows in outward direction. The accumulation of molten metal at weld bead center increases with increased beam power. It is gradually accelerated from the center towards periphery of melt pool (Mahrle et al., 2002 and Ai et al., 2017). As a result, the width of FZ_{UP} becomes larger than both FZ_{Mid} and FZ_{Low}. In addition to that, energy density at the upper surface of weld bead is higher as compared to bottom and middle section which enhances plasma absorption at upper most surfaces. The rate of plasma absorption on top surface of specimen increases by increasing of beam power. This absorbed plasma re-radiates the beam energy on the upper part of weld bead which leads to increased FZ_{UP}.

It is also observed from Figs. 5.4(a) and (b) that the width of FZ_{Low} is higher than FZ_{Mid} for fully penetrated samples due to the spreading of heat energy in the transverse direction to the weld line. At low welding power (Exp. 1, Table 5.1) and high welding speed (Exp. 9 Table 5.1), full penetration is not achieved due to insufficient heat supplied to the workpiece surface. Hence, FZ_{Low} is not formed in these experiments. Further increasing beam power or decreasing welding speed, full penetration occurs. Afterward, heat energy spreads in transverse direction. Consequently, width of FZ_{Low} rapidly increases. Moreover, inside keyhole at position "B" (Fig. 5.4(c)), both vapour pressure and Marangoni shear stress are weak. Therefore, due to gravitational effect, backfilling of molten metal occurs at weld bead's lower part. Hence, the width of FZ_{Low} is higher than FZ_{Mid} for fully penetrated samples. Also, the lower part of FZ is in contact with the atmosphere which accelerates solidification rate by spreading heat energy laterally. Hence, the width of FZ_{Low} becomes higher than FZ_{Mid}.

Figures 5.5(a) and (b) show the effects of beam power and welding speed, respectively on FZ_{area}. Power density increases with increased beam power. Therefore, larger volume of BM melts down. Consequently, FZ_{area} continuously increases as observed in Fig. 5.5(a). When beam power reaches beyond 1100 W, FZ_{area} drastically increases probably due to surpass power density from its threshold limit required for the formation of prominent keyhole in base plate. At this welding condition, more conspicuous and deeper keyhole is formed. Also, heat energy is trapped inside melt pool due to multiple reflections of beam energy with keyhole wall. Therefore, widening of FZ_{UP} takes place. As a result, FZ_{area} also drastically increases as observed in Fig. 5.5(a). From Fig. 5.5(b), it is found that FZ_{area}

continuously decreases with increased welding speed. As welding speed increases, the interaction time (Eq. (4.6)) of laser beam with workpiece material decreases. Hence, lesser volume of BM melts down which leads to continuous decrease in FZ_{area}.

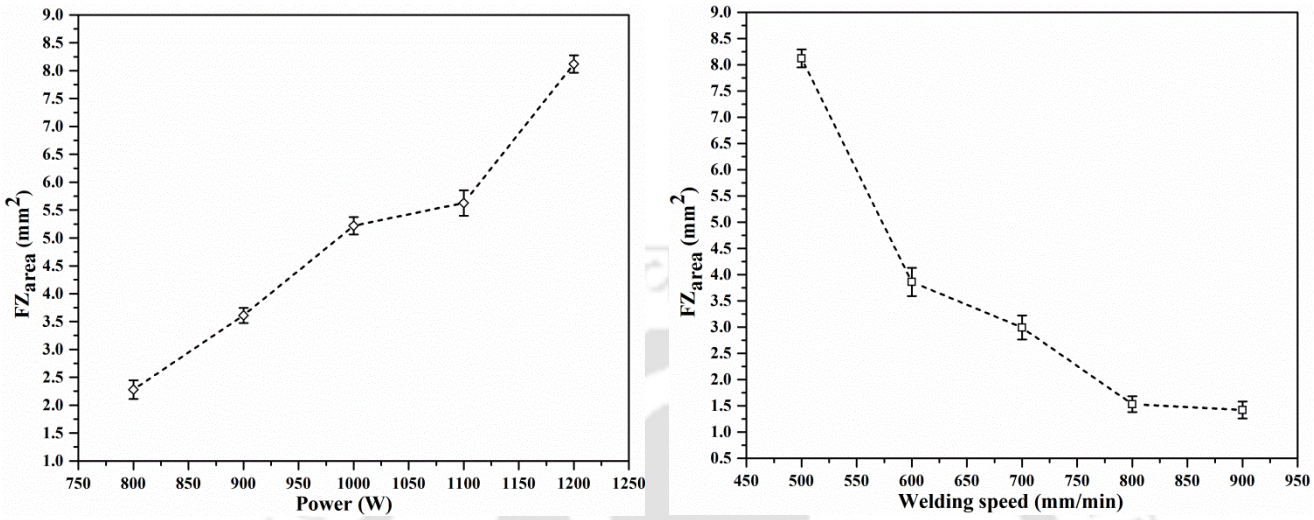

(a) (b)

Fig. 5.5 Variation in FZ_{area} at different welding (a) power (500 mm/min fixed welding speed) and (b) speed (1200 W fixed beam power)

5.1.1.6 Heat affected zone (HAZ) size

Size of HAZ predominantly depends on heat supplied to the workpiece surface, interaction time and conductivity of workpiece material. Figure 5.6(a) depicts the influence of beam power on HAZ size at different locations within HAZ at 500 mm/min constant welding speed. From Fig. 5.6(a), it is found that with increasing beam power, size of both HAZ_{UP} and HAZ_{Low} continuously increases due to increased power density with increased beam power. Initially, at lower beam power of 800 W (Exp. 1), incomplete penetration takes place in the base plate. Hence, heat is dissipated mostly from the keyhole mouth on the top face. Also, due to lower thermal conductivity (6.7 W/m K) of Ti-6Al-4V alloy, heat is restrained for a longer duration of time in the middle portion of weld bead. Therefore, higher size of HAZ_{Mid} is formed as compared to size of HAZ_{UP} and size of HAZ_{Low}. At 900 W welding power, most of the heat energy is consumed to increase penetration depth without spreading heat energy laterally. Because, at this welding condition, probably the heat energy just reaches to the threshold value for full penetration in base plate. Hence, lowest value of HAZ_{Mid} is observed. Further increase in welding power beyond 900 W, heat energy spreads laterally. Due to which, size of HAZ_{Mid} continuously increases. Figure 5.6(b) depicts the influence of welding speed on HAZ size at 1200 W constant beam power. Size of HAZ_{UP}, HAZ_{Mid} and HAZ_{Low}

continuously decrease with increasing welding speed due to continuously reduction in interaction time (Eq. (4.6)) with workpiece material with increased welding speed.

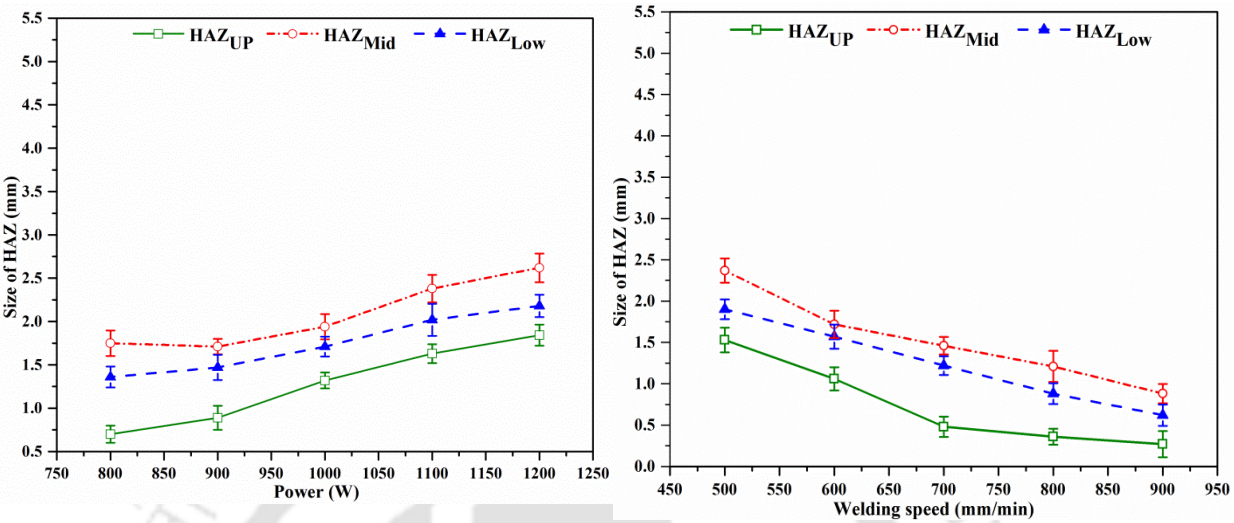

(a) (b)

Fig. 5.6 Variation in HAZ size at different (a) beam power (500 mm/min fixed welding speed) and (b) welding speed (fixed welding power of 1200 W)

5.1.2 Mechanism of phase transformation and bead characterization

Optical and FESEM microstructural images of Ti-6Al-4V alloy BM are presented in Figs. 5.7(a) and (b), respectively. BM microstructure primarily consists of two phases i.e. inter-granular β and globular α phases. β phase is dispersed in a dominant matrix of α phase. The light and dark areas in optical image (Fig. 5.7(a)) represent globular α and inter-granular β phases, respectively. In FESEM image (Fig. 5.7(b)), the dark gray color represents globular α and white regions represent inter-granular β phase. Bigger size of both α and β phases are observed in Fig. 5.7 as compared to 5 mm thick Ti-6Al-4V alloy BM (Fig. 4.8). It may be due to different annealing conditions adopted during heat treatment of BM by the manufacturer. However, in both Fig. 5.7 and Fig. 4.8, the size of both α and β phases are different. In the present study, the diameter of α and β grains are in the range of 7-16 μm and 4-6 μm, respectively as measured by line intercept method in optical microscope.

LBW process of Ti-6Al-4V alloy is completed in simultaneous heating and cooling steps followed by following sequence of transformations i.e.

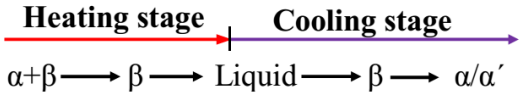

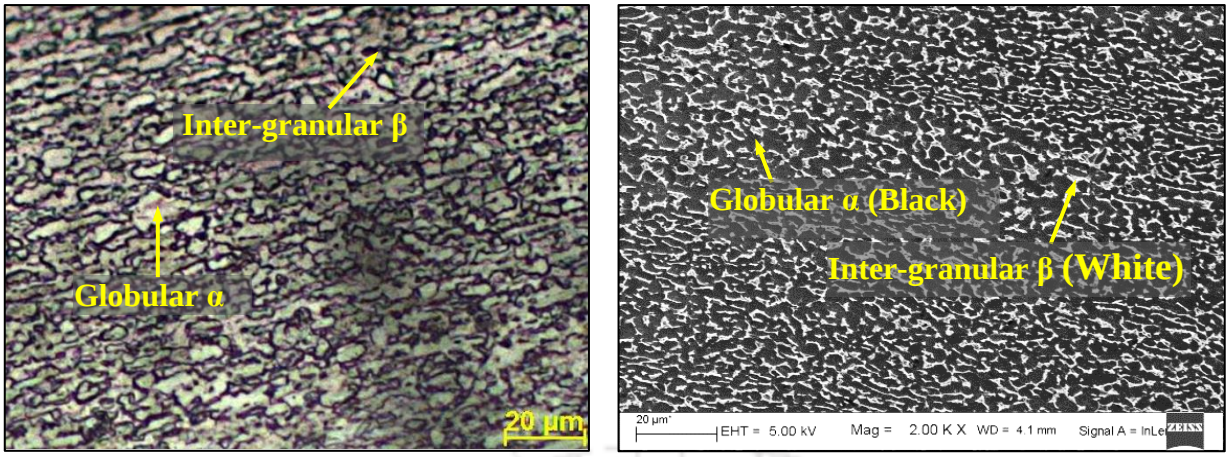

(a) (b)

Fig. 5.7 Microstructure of Ti-6Al-4V base metal; (a) Optical microscope and (b) FESEM image

During heating, vanadium diffuses out from dominant matrix of α phase. Hence, continuous growth of β phase takes place during heating process. Elmer et al. (2004) found that the volume fraction of β phase continuously increases during heating and it fully transforms into β phase at β transus temperature, T_β i.e. 975 °C. The stability of this β phase is observed up to solidus temperature (T_S) i.e. 1605 °C. The complete melting of FZ occurs beyond liquidus temperature, T_L i.e. 1655 °C. However, in the HAZ, homogenization of β phase prevails. It is very difficult to determine the microstructure of FZ as well as in HAZ for Ti-6Al-4V alloy because the microstructure that appears during heating is subsequently altered while cooling by diffusionless transformation in FZ and solid state phase transformation in HAZ.

The schematic diagram of phase transformation based on cooling rate i.e. continuous cooling transformation (CCT) diagram for Ti-6Al-4V alloy is shown in Fig. 5.8(a). The effect of line energy on cooling rate is provided in Fig. 5.8(b) where it is clearly seen that higher the line energy lower is the cooling rate and vice-versa. During cooling, both FZ and HAZ transform into either martensitic α′ or other morphology of martensitic α′ phase like massive α (α_m), transformed α (i.e. blocky α) or Widmanstatten α. The amount of martensitic α′ phase in FZ and HAZ depends on cooling rate below T_β temperature. Depending on cooling rate, different types of transformation mechanisms from β phase to α/α′ phase are perceived in LBW of Ti-6Al-4V alloy. At lower, medium and higher cooling rates, long range, short range (i.e. massive transformation, α_m) and diffusionless (i.e. martensitic α') transformations, respectively are observed (Ahmed and Rack, 1998).

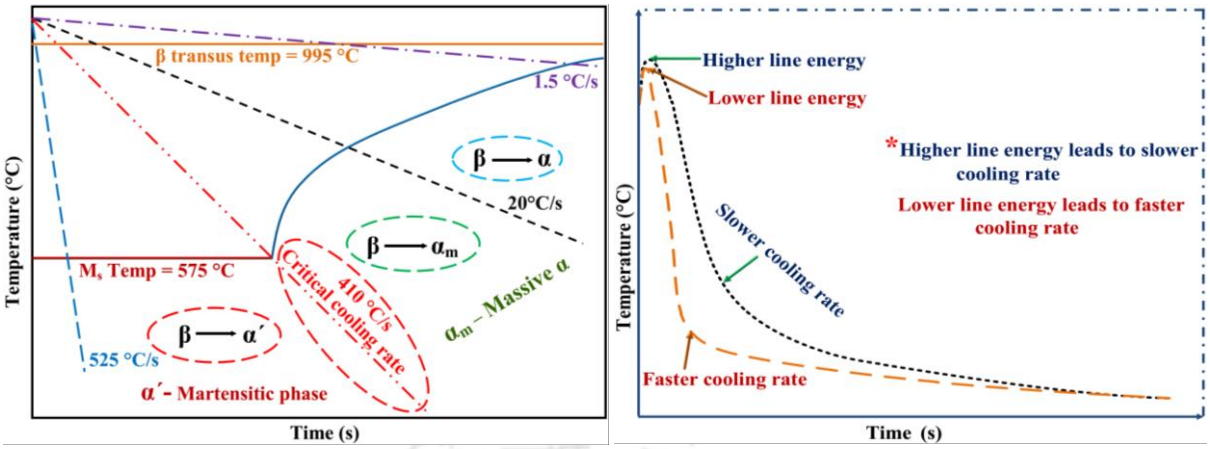

(a) (b)

Fig. 5.8 Schematic of (a) continuous cooling transformation (CCT) curve (Ahmed and Rack, 1998) and (b) effect of LE on cooling rate for Ti-6Al-4V alloy

By increasing line energy, the temperature of molten pool and BM around the melt pool is also increased. Hence, a reduction in temperature difference occurs between weld region and surrounding BM. Due to which the heat transfer rate decreases from melt pool towards BMZ. As a result, cooling rate is decreased in weld region. It is noticed from CCT curve (Fig. 5.8(a)) that for achieving fully hexagonal α′ martensitic microstructure, the cooling rate should be above 410 °C/s (known as critical cooling rate for martensitic structure). However, for cooling rate between 410-20 °C/s, partial transformation of β phase into α´ martensitic phase occurs along with massive α-plates i.e. a massive transformation (α_m). No transformation of β phase into α´ martensite occurs below 20 °C/s cooling rate where only Widmanstatten α is formed along with primary α and β phases. Cooling rate close to 20 °C/s in the range between 20 °C/s to 1.5 °C/s promotes the formation of basketweave microstructure, while at cooling rate close to 1.5 °C/s promotes the formation of larger sized α colonies (Ahmed and Rack, 1998).

The spot diameter of laser beam is very small (200 µm). Therefore, a very small area of workpiece interacts with the heat source. Hence, an excessive higher thermal gradient is generated in the welded specimen starting from weld pool to towards BMZ which leads to the formation of non-uniform microstructure staring from FZ to BMZ. As a result, it yields three separate zones in the weld bead i.e. BMZ, HAZ and FZ as shown in Fig. 5.9(a) (Exp. 6, Table 5.1). The boundary between HAZ and BMZ is clearly observed in Fig 5.9(b) and the boundary between FZ and HAZ is clearly visible in Fig. 5.9(c).

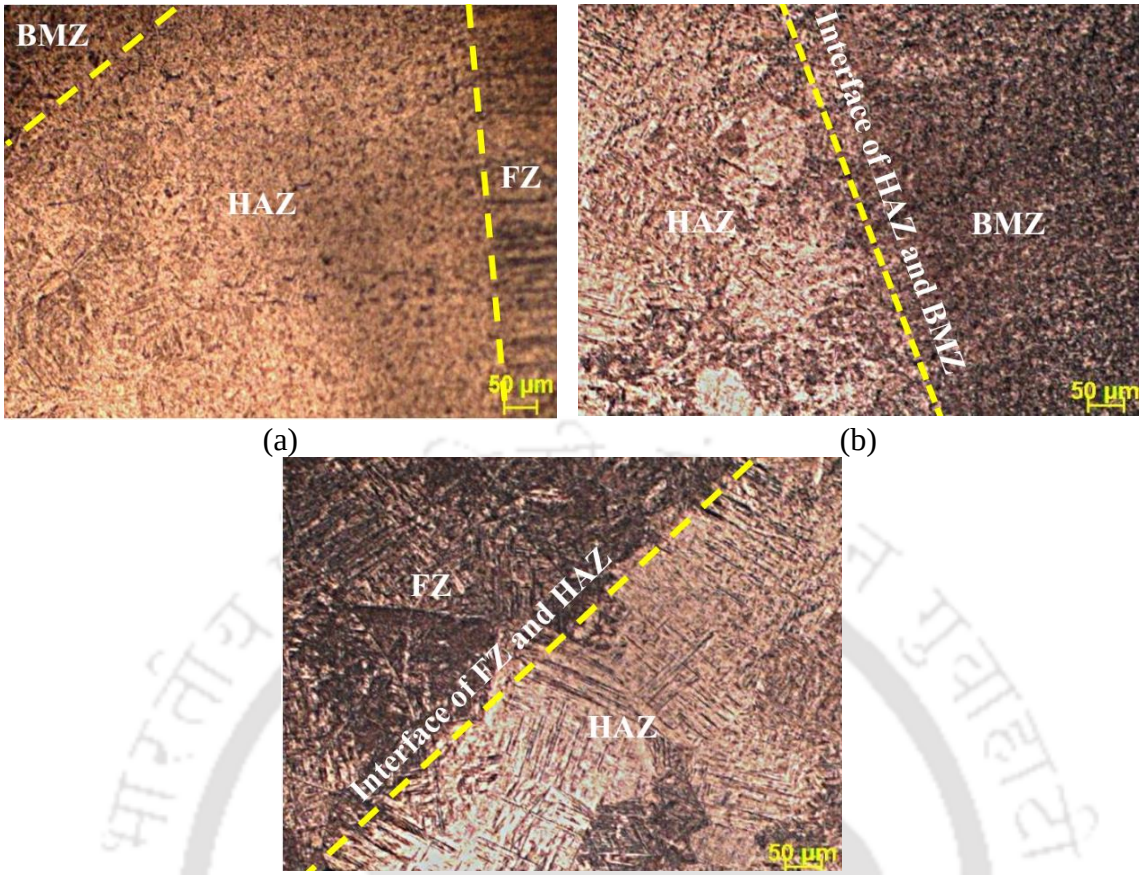

Fig. 5.9 Optical macrographs showing interface between (a) BMZ, HAZ and FZ, (b) HAZ and BMZ and (c) FZ and HAZ

5.1.2.1 Microstructural study in HAZ

Heat supplied to the surface of workpiece material is highly influenced by LBW power and welding speed which alters the microstructure in the welded region. The microstructural features in FZ as well as in HAZ highly depend on line energy. The change in microstructure depends on cooling rate and Ti-6Al-4V alloy's transformation kinetics. The distinct points within the HAZ from near FZ to near BMZ experience different temperatures. Therefore, each region cools down from different maximum temperature. Hence, a temperature gradient is developed. Due to which different microstructural features appear within various points in HAZ. Thus, every point within HAZ shows unique microstructural features which alter the mechanical behaviour of welded specimens. Hence, the study of the distribution of different phases within HAZ is more essential.

The optical and FESEM images of the microstructures at different locations in HAZ i.e. near FZ, middle of HAZ, far away from the FZ and near BMZ are shown in Figs. 5.10(a-d) for Exp. No. 6 (Table 5.1). From near FZ to near BMZ, each point in HAZ experiences different temperatures and subsequently cools down at different cooling rates. Due to which

different microstructural features are developed over the HAZ unlike FZ. In the HAZ which is nearer to FZ, a mixture of acicular α′ (martensitic phase) and small amount of blocky α (transformed α from prior β grain) phases are formed and these are clearly observed in optical micrographs in Fig. 5.10(a). These observations reflect that in this location maximum temperature reaches beyond β transus temperature i.e. T_β (995 °C for Ti-6Al-4V alloy) and remains below liquidus temperature i.e. T_L (1655 °C). The original α and β phases are not observed in near FZ. Hence, this region is termed as fully transformed HAZ region. The α′ martensitic phase is harder than original α and β phases as discussed in many literatures. Hence, it is expected that near the boundary between FZ and HAZ i.e. HAZ nearer to FZ may yield hardness comparable to FZ.

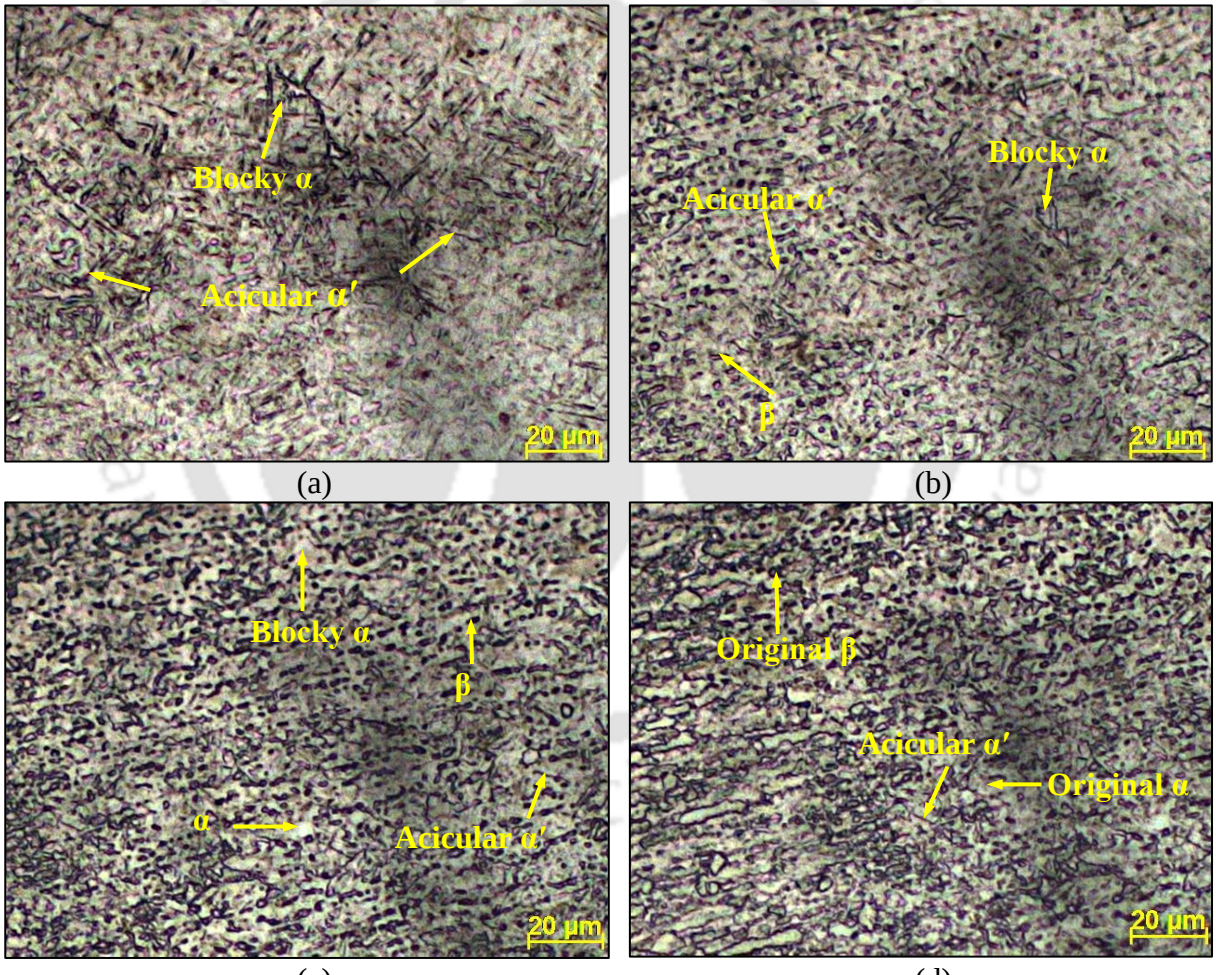

Fig. 5.10 Microstructure in HAZ (optical image) at various positions; (a) Near FZ, (b) Middle of HAZ, (c) Far away from FZ and (d) Near BMZ

In the middle position of the HAZ, a mixture of blocky α and martensitic α′ with a small amount of retained β phases are observed as shown in Fig. 5.10(b). Blocky α is transformed α from prior β grain, acicular α′ is martensitic phase. The fully transformed HAZ

is not observed in the middle part of the HAZ due to lesser peak temperature. In the HAZ, which is far away from FZ, a combination of blocky α, retained β and primary α with a small amount of α′ phases are observed (Figs. 5.10(c)). Similar microstructure is reported by Ahmed and Rack (1998) while quenching Ti-6Al-4V alloy below T_β and in between 720 to 985°C. This observation reflects that in this region, the maximum temperature reaches below T_β and greater than lowest temperature which is essential for microstructural changes. This minimum temperature in the far away to FZ is very challenging to define as it depends on transformation kinetics of molten pool (Short, 2009). The microstructural features in near BMZ (Fig. 5.10(d)) are fully different than the near FZ and middle of HAZ. In fact, this region is subjected to lower temperature than other regions of HAZ. Here, insignificant amount of α′ phase is found in the dominant matrix of original α and β phases. Due to the presence of original α and β phases, this region is termed as partially transformed region. This gradient in microstructure presented the typical appearance of that achieved by quenching from a temperature below T_β (Gao et al., 2014). As LBW process is itself recognized as a high self-quenching characteristic therefore, similar results are expected in the HAZ as well as FZ as observed by Ahmed and Rack (1998) while quenching Ti-6Al-4V alloy from different temperatures. Compared to the partially transformed HAZ, large amounts of α′ martensitic phases are found in fully transformed HAZ. The variation in developed microstructure within HAZ reflects that only solid-state micro-structural changes without melting occur in HAZ because this zone experiences sufficient temperature for microstructural changes and cooled below from liquidus temperature (T_L). From Figs. 5.10(a-d), it is also observed that the amount of martensitic α′ phase decreases from approximately 100% in near FZ to nearly zero in BMZ due to their differences in cooling rates. These variations in amount of martensitic α′ phase may affect the hardness values within the HAZ and will be discussed in details in subsection 5.1.3.

5.1.2.2 Microstructural study in FZ

Both melting and solidification process simultaneously occur in the FZ. Hence, microstructural change in the FZ is primarily influenced by the solidification behaviour of the melt pool which controls size and shape of newly developed grains in FZ. The developed microstructure in the FZ mainly depends on the cooling rate. The cooling rates (CR, °C/s) at all experimental conditions (Table 5.1) are calculated by using Eq. (3.1).

Microstructures in the FZ for fully penetrated welded specimens at different beam power from 900 to 1200 W for Exps. 2 to 5 (Table 5.1) are presented by optical images in

Figs. 5.11(a-d) and by FESEM images in Figs. 5.12(a-d). Depending on cooling rate and presence of micro constituents, the developed microstructures in the FZ are categorized into several types namely α′ martensite (i.e. acicular morphology), massive α_m, basketweave α, grain boundary α and primary/globular α. At lower beam power (900 W for Exp. 2 in Table 5.1), line energy (108.04 J/mm) is low which leads to higher cooling rate (CR = 424 °C/s) as discussed in Fig. 5.8(b). The calculated cooling rate for Exp. No. 2 is 424 °C/s which is close to critical cooling rate (410 °C/s) for the formation of fully α′ martensitic structure as per CCT curve in Fig. 5.8(b). Fully martensitic α′ (acicular α′) phase is formed due to the diffusionless transformation as shown in optical image in Fig. 5.11(a) and their morphology is shown in FESEM image in Fig. 5.12(a). Similar microstructure is reported by Ahmed and Rack (1998) while quenching Ti-6Al-4V alloy above T_β temperature. Also, the primary α phase is not observed in the developed microstructure in Fig. 5.11(a) and in FESEM image Fig. 5.12(a) in FZ.

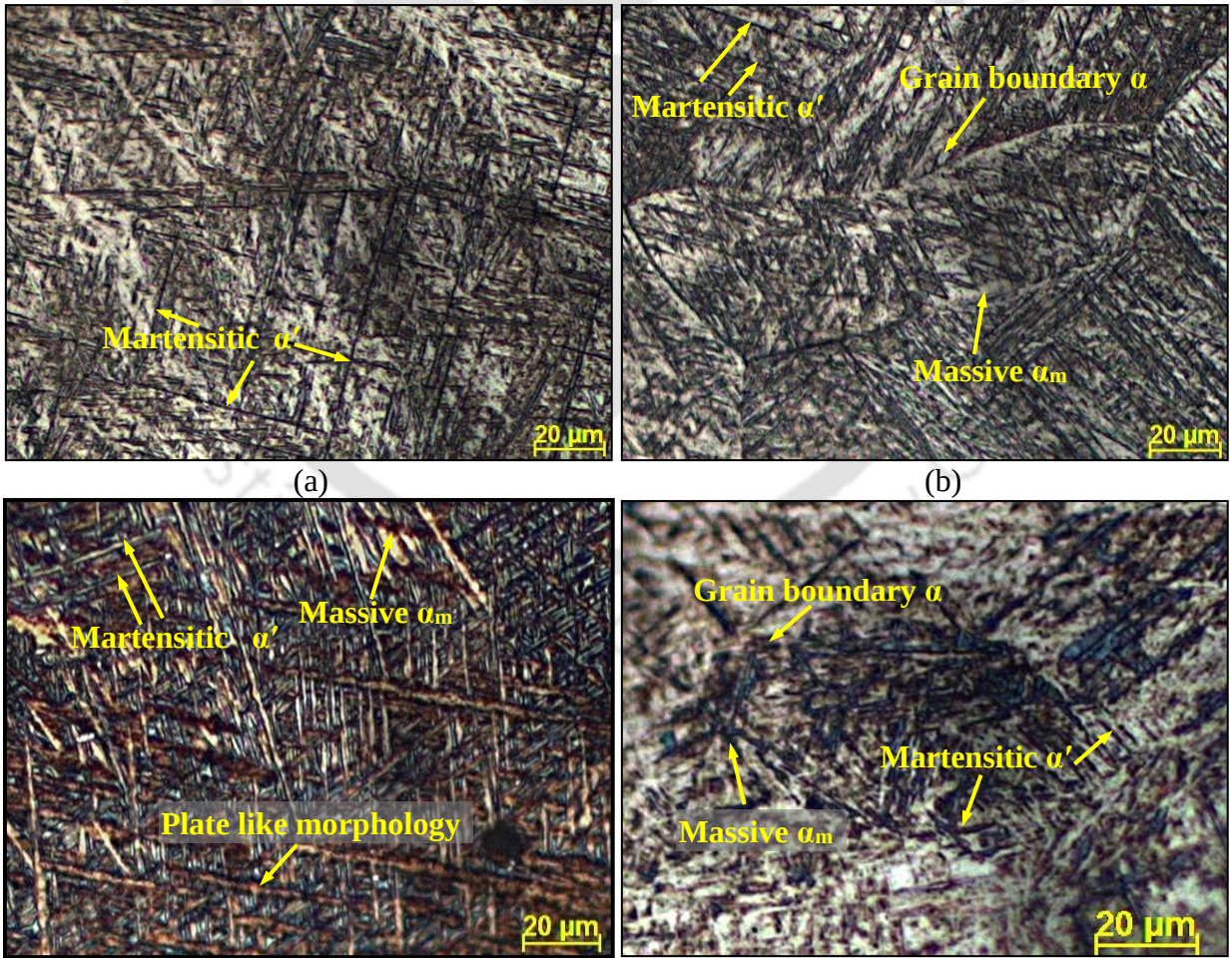

Fig. 5.11 Optical microscopic images of FZ microstructure for Exp. No. (a) 2, (b) 3, (c) 4 and (d) 5 in Table 5.1 with increasing beam power from 900 to 1200 W

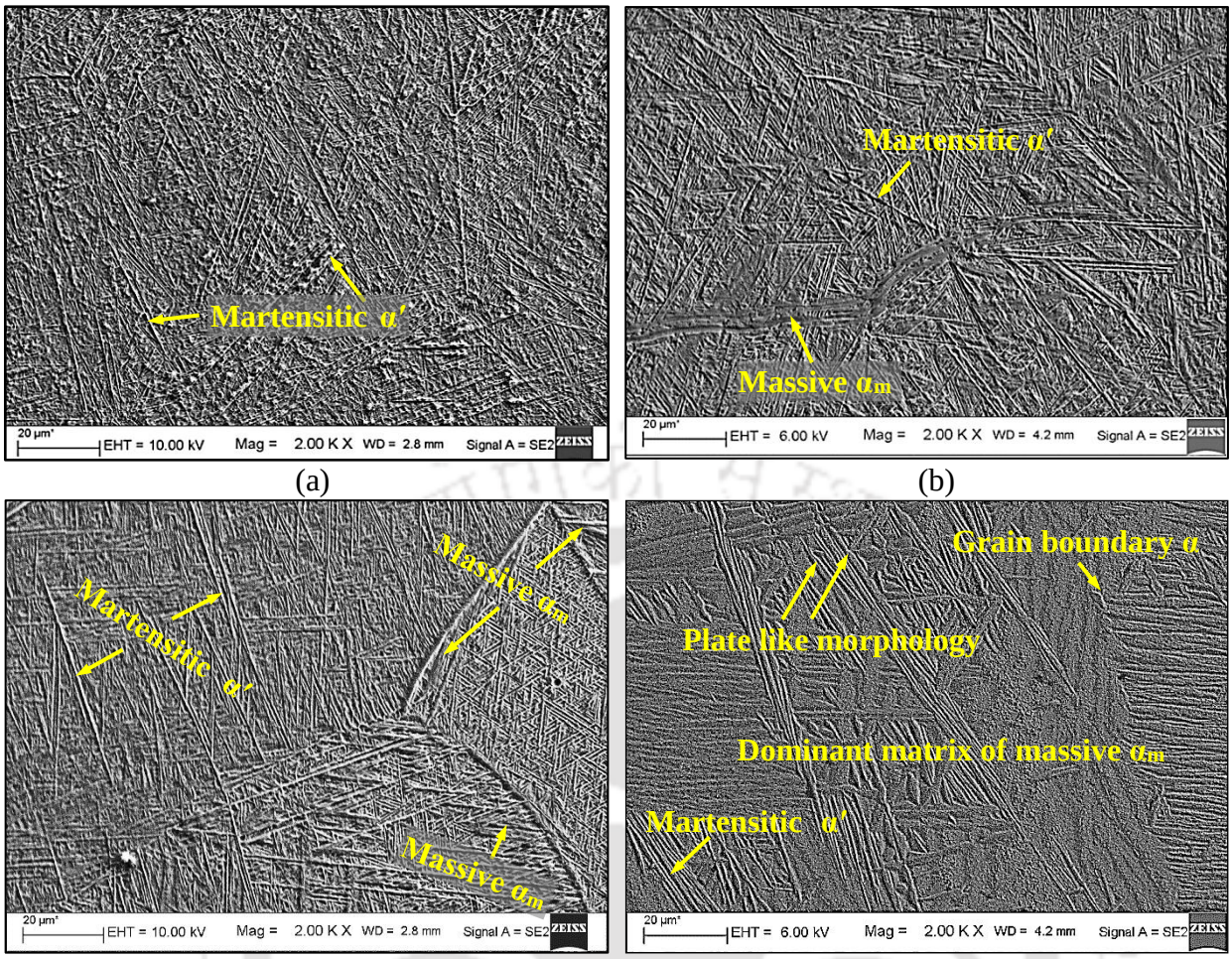

Fig. 5.12 FESEM images of FZ microstructure for Exp. No. (a) 2, (b) 3, (c) 4 and (d) 5 in Table 5.1 with increasing beam power from 900 to 1200 W

It indicates that at this welding condition the cooling rate is above the critical cooling rate of 410 °C/s for the formation of fully α′ martensitic structure. Hence, full transformation of β phase into needle like α′ martensitic phase occurs as clearly observed in Fig. 5.12(a). It is also found that with subsequent increase in LBW power from 900 W (Exp. 2) to 1200 W (Exp. 5), the needle shaped α′ martensitic phase is transformed into plate like morphology as observed in the FESEM images in Fig. 5.12(a-d). Similar observations are reported by Xu et al. (2014) in CO_2 LBW of Ti-6Al-4V alloy.

At 1000 W beam power (Exp. 3) the calculated cooling by using Eq. (3.1) is 344.53 °C/s which is little bit away from the critical cooling rate of 410 °C/s as per Fig. 5.8(a). From Fig. 5.8(a), this cooling rate of 344.53 °C/s falls in the range between 20 °C/s to 410 °C/s where mixed microstructure is formed. Hence, the fully martensitic structure is not observed in FZ for Exp. 3 as shown in OM image in Fig. 5.11(b) and FESEM image in Fig. 5.12(b). There is a combination of α′ martensite, grain boundary α and massive α is observed.

At 1100 W beam power (Exp. 4), the cooling rate becomes moderate (CR = 284.05 °C/s calculated from Eq. (3.1)) as compared to the specimens in Exp. 2 and Exp. 3 due to higher beam power. Hence, the second morphology of α′ martensitic phase i.e. massive α (α_m) is appeared in the FZ along with α′ martensitic phase as shown in the OM image in Fig. 5.11(c) and FESEM image in Fig. 5.12(c). This microstructure is consisting with the developed microstructure in FZ as explained Fig. 5.8(a). Due to massive transformation, fine wavy acicular structures are also appeared in FZ. It is entirely different than the fine lath like features formed by α′ martensitic transformation. Similar type of microstructure is reported by Ahmed and Rack (1998) while quenching Ti-6Al-4V alloy from slightly above T_β temperature at medium cooling rate. The nucleation rate of α_m phase prior to β grain boundaries continuously increases with increased LBW power (i.e. decreasing cooling rate). Also, broadening of α lamellas (grain boundary α) grows up. At higher LBW power (i.e. 1200 W, Exp. 5), the line energy is very high which further reduces the cooling rate (CR = 238.67 °C/s calculated from Eq. (3.1)). It promotes broadening of α lamellas. Also, more amount of massive α_m is formed along with little amount of α′ martensitic phase as clearly shown in the OM image in Fig. 5.11(d) and in FESEM image in Fig. 5.12(d).

Figures 5.13 (a-d) shows the optical images of the developed microstructures in the FZ for different welding speed from 500 to 800 mm/min for Exps. 5 to 8 (Table 5.1) and the microstructural features are compared using FESEM images as shown in Figs. 5.14(a-d). At 600 mm/min welding speed, small amount of grain boundary α and massive α_m phases at prior β grain boundaries are observed in a dominant matrix of α′ martensitic structure (Fig. 5.14(b)). The presence of massive α_m indicates that cooling rate at this welding condition is probably nearest to the lowest limit of the formation of α′ martensite in FZ. The cooling rate at this welding condition is 341.85 °C/s. These microstructural observations in Figs. 5.13(b) and 5.14(b) are consistent with CCT diagram Fig. 5.8(a) for Ti-6Al-4V alloy. From Figs 5.14(a-d), it is also observed that with increased welding speed, the thickness of the needle shaped α′ martensitic lamella decreases continuously. These observations are mainly related to the cooling rate of melt pool. With increasing welding speed, the cooling rate is also increased and it promotes the nucleation rate of α into the grain boundaries of β phase. As a result, at higher cooling rate beyond 410 °C/s, the transformation process becomes diffusionless forming fully α′ martensitic phase. Fully α′ martensitic structure is observed in samples for Exp. No. 7 & 8 (cooling rate (CR) for Exp. 7 and Exp. 8 are 476.08 and 611.22 °C/s, respectively) and these are presented in Figs. 5.14(c) & 5.14(d), respectively. However, the morphology of α′ phase becomes finer with increasing welding speed. At highest welding

speed of 800 mm/min, basketweave microstructure is observed in the FZ as shown in Fig. 5.14(d). During rapid cooling, nucleation of α phase occurs prior to β grain boundaries. Hence, there is a continuous formation of α layer along β grain boundaries. As a result, α colony is built and starts to grow till they meet other α colony. The thickness and length of α colony and individual α plates is reduced with increased cooling rate. At moderate to higher cooling rate, the nucleation of individual α plate also starts at the boundaries of the α colony and it grows perpendicular to the nucleation site and a basketweave microstructure is formed as shown in Figs. 5.13(d) and their morphology is clearly observed in FESEM image in Fig. 5.14(d).

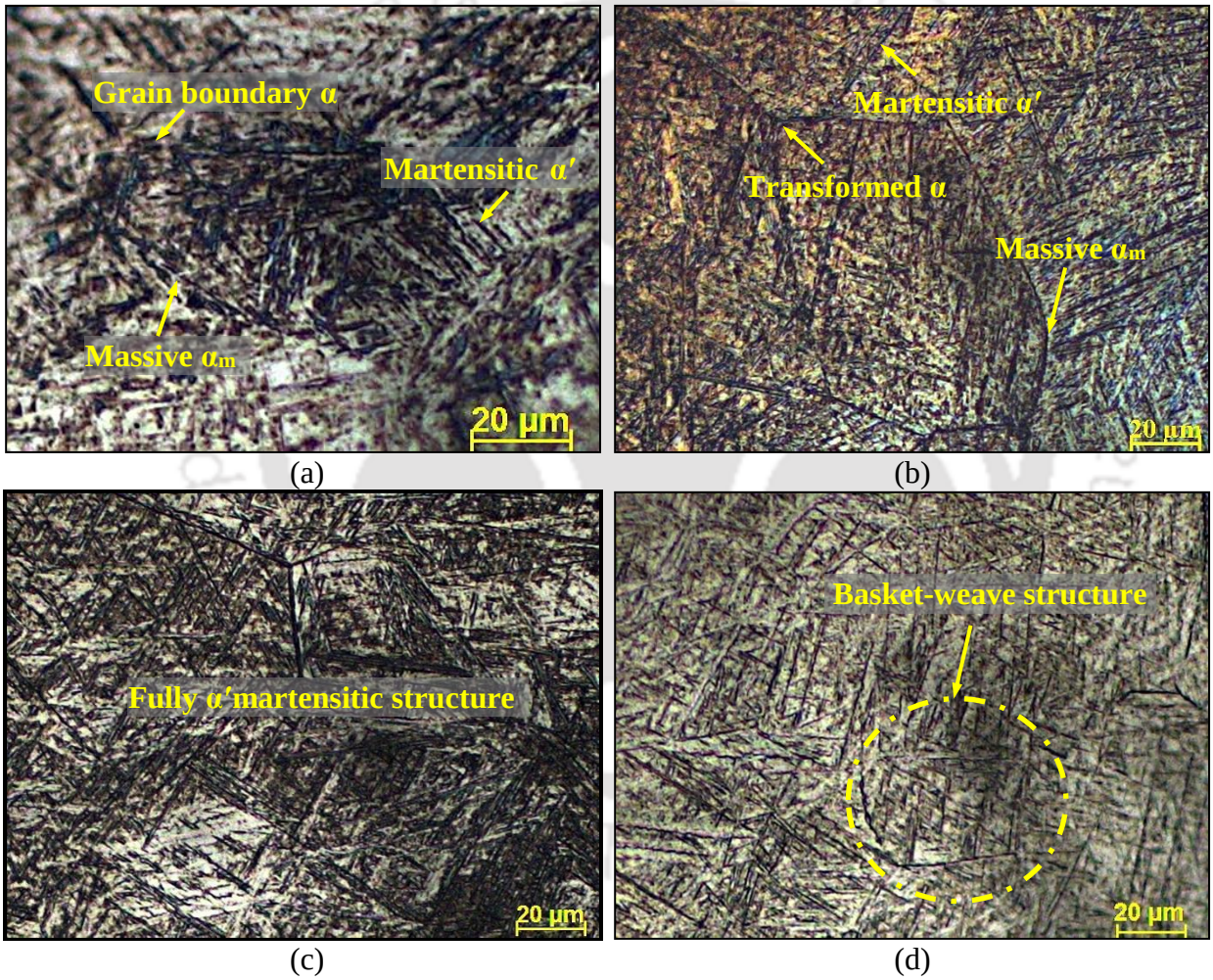

Fig. 5.13 Optical images of FZ microstructure for Exp. No. (a) 5, (b) 6, (c) 7 and (d) 8 in Table 5.1 with increasing welding speed from 500 to 800 mm/min

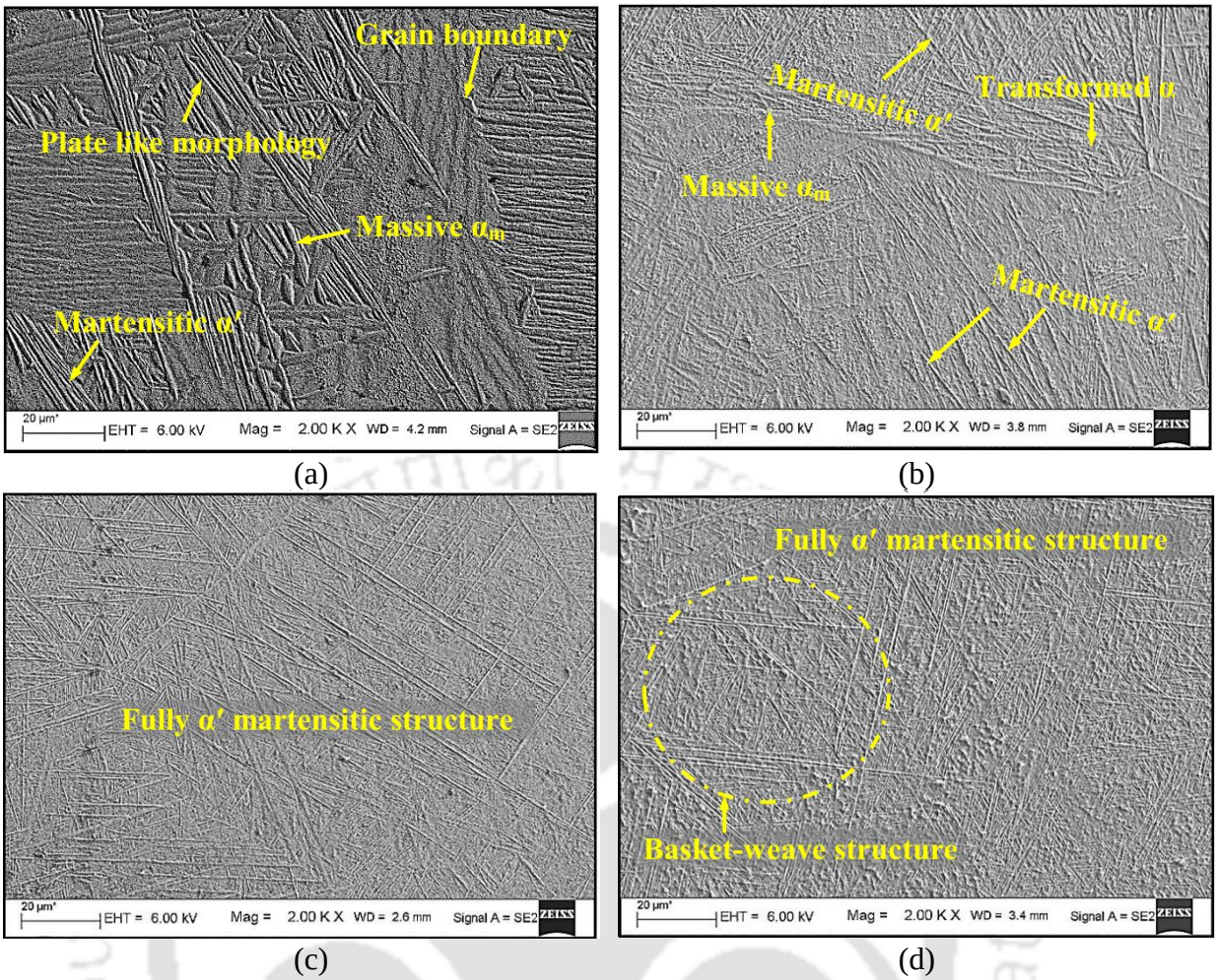

Fig. 5.14 FESEM images of FZ microstructure for Exp. No. (a) 5, (b) 6, (c) 7 and (d) 8 in Table 5.1 with increasing welding speed from 500 to 800 mm/min

5.1.3 Hardness

In the present study, hardness values are measured in the weld bead cross section across transverse direction of the center line of FZ at upper and middle portions of weld bead cross- section as shown in Fig. 5.15(a). The hardness distribution curves measured at upper and middle portions are shown in Fig. 5.15(b) for Exp. 6 (Table 5.1). In Fig. 5.15(b), continuous decrease in hardness value is observed from its maximum value in the FZ to a lowest value in the BMZ on both sides of the center line of FZ. It is mainly due to the decrease in the amount of α′ martensite from 100 % in the FZ to nearly zero in the BMZ as discussed in section 5.1.2.1 and these hardness variations within HAZ is consistent with observed microstructural characteristics in Figs. 5.10(a-d). Similar results are also reported by Akman et al. (2009) in laser welding of Ti-6Al-4V alloy. Higher self-quenching characteristics of LBW process promote the formation of α′ martensite in FZ which possesses high hardness and high tensile strength with reduced ductility. It is expected that at the middle portion of the weld bead, the size of α′ colonies becomes thicker and longer due to

slower cooling rate as compared to upper portion which is exposed to surrounding atmosphere. It may be the possible reason for decreased hardness in the middle section of the weld bead.

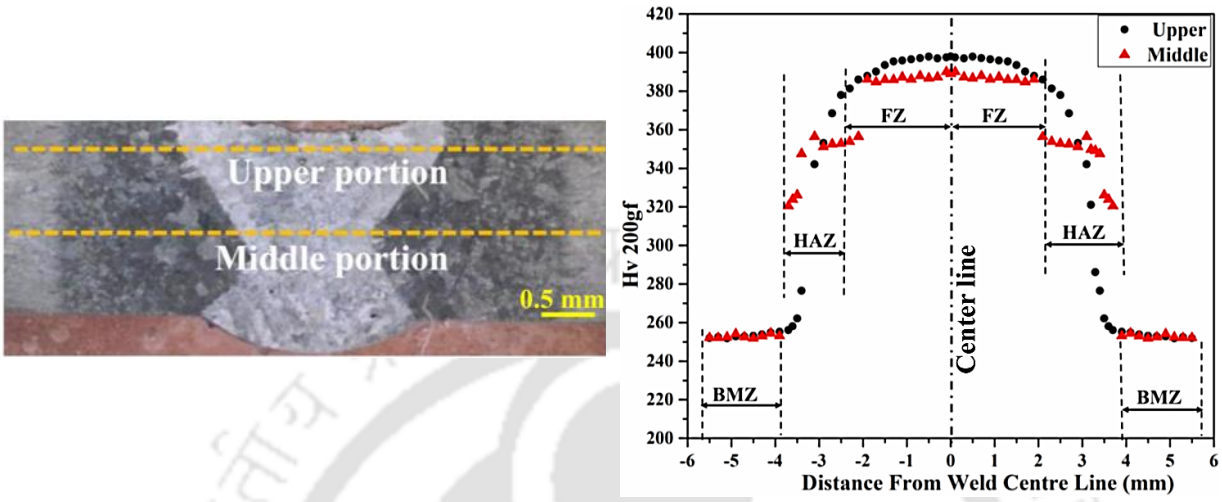

(a) (b)

Fig. 5.15 (a) Different positions of hardness measurement in weld bead cross section and (b) hardness distribution curve at upper and middle portions of bead cross-section for Exp. 6

The average hardness values for all the fully penetrated welded samples are measured in the FZ and it is compared at various beam power and welding speed in Figs. 5.16(a) and 5.16(b), respectively. From Fig. 5.16(a), it is found that average hardness of FZ is decreased with increasing beam power. The probable reason for decrease in hardness in the FZ is due to increased grain size at higher beam power. The line energy increases with increased beam power from 900 to 1200 W (Table 5.1) at 500 mm/min constant welding speed. Hence, temperature gradient as well as cooling rate are reduced in the FZ which lead to increased average grain size. The average grain size in weldments in Exp. 2, Exp. 3, Exp. 4 and Exp. 5 are 112.5 µm, 147 µm, 165 µm and 232.5 µm, respectively as measured by line intercept method in optical microscope. Similar phenomena are also reported by Akman et al. (2009) and Kumar et al. (2017b) while welding Ti-6Al-4V alloy.

Figure 5.16(b) shows the variation in average hardness values in the FZ at different welding speeds. It is observed that the hardness values in the FZ increase with increased welding speed. It is probably due to the difference in grain morphology of α′ martensitic structures as observed in Figs. 5.14(a-d). The microstructure and grain morphology strongly affect the hardness in weld bead. With increasing welding speed, the length and thickness of α′ lamellae are decreased as shown in optical image in Figs. 5.13(a-d) and in FESEM image in Figs. 5.14(a-d) and also explained in section 5.1.2.2 causing brittle α′ martensitic structure which leads to high hardness in FZ.

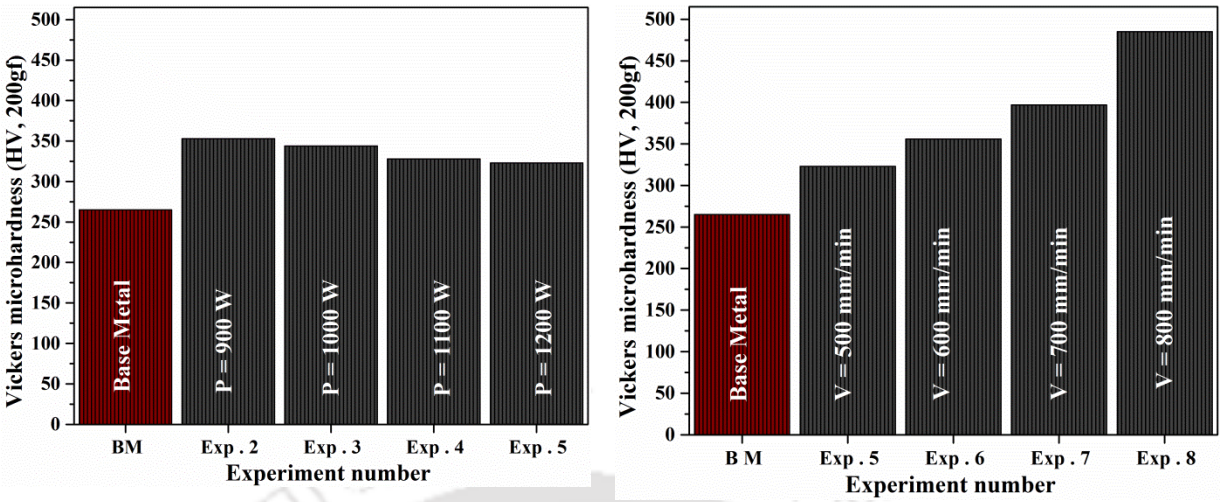

(a) (b)

Fig. 5.16 Comparison of average hardness value in FZ at different (a) beam power and (b) welding speed

5.1.4 Porosity

In the present study, most of the welded samples are defect free. However, in few welded samples small amount of underfill, excess penetration and porosity are observed in the weld beads. Underfill is a typical welding defect that arises in LBW of Ti-6Al-4V alloy. It works as a stress concentrator and reduce the tensile properties of welded specimens. In the present case, few underfill weld defects are observed at the top side of the bead. Lower underfill area (Figs. 5.3(a) and 5.3(b) for Exp. No. 5 and 6, respectively) are observed at a combined higher beam power and lower welding speed due to evaporation of the molten metal. However, at higher welding speed beyond 600 mm/min underfill weld defects are not observed. Therefore, higher welding speed is favored to reduce underfill defects.

Porosity is a major and severe weld defect which is frequently observed in deep penetration LBW process. It severely deteriorates the mechanical properties of the welded specimens. Ti-6Al-4V alloy are more susceptible to porosity formation during fusion welding and it is reported in many literature (Kabir et al., 2010, Gao et al., 2014b and Karimzadeh et al., 2005). The formation of porosity in keyhole mode of LBW is still not well understood. There is a discrepancy in the understanding of actual reason for the formation of porosity in the weld bead. The propensity of porosity formation in the present study is extensively minimized by providing shielding gas. However, porosities are still found in solidified weld bead of few welded samples. The reasons for porosity formation in partially penetrated welded samples are already discussed in section 4.3.5. Therefore, the reasons for porosity formation in the weld bead of fully penetrated weldments are only discussed here.

In the present study, the gas type micro pores are observed at the upper half of the FZ (Exps. 4 and 5, Figs. 5.17(a) and (b)), near FZ boundary along with some elongated pores along the center line of FZ as shown in Fig. 5.3(b) for Exp. 7. Micro pores having circular or pear-like shape with smooth walls as shown in FESEM images in Figs. 5.17(a) and (b) confirms the characteristics of gas type porosity.

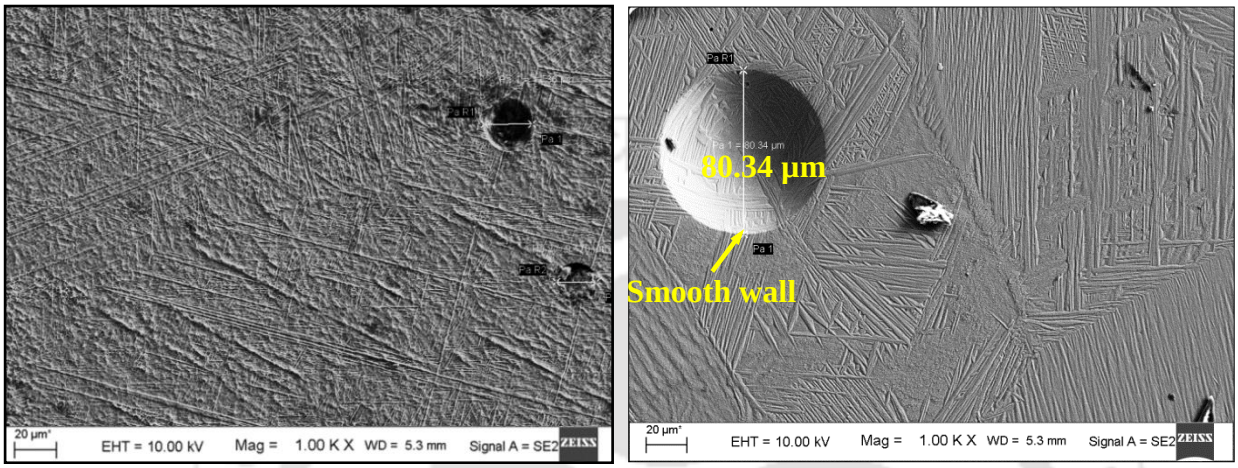

(a) (b)

Fig. 5.17 FESEM images showing morphology of gas type pores formed due to the trapping of gases in the FZ for welded samples in Exps. (a) 4 and (b) 5

Porosities of these types are generated because of entrapment of shielding gas as well as evolved hydrogen gas into the molten pool. The presence of hydrogen in the molten weld pool which can't get away at the onset of solidification of weld pool is the main source for the formation of micropores during LBW process. The hydrogen solubility is decreased continuously in both solid and liquid titanium alloy with increased temperature. Liquid titanium at melting point has higher hydrogen solubility than solid titanium. Heating during welding causes hydrogen precipitation due to the decrease in its solubility at higher temperature (Karimzadeh et al., 2005). Hence, porosities are formed by nucleation or direct diffusion into discontinuities or existing pores. In the weld pool, recirculation of liquid metal takes place. Hence, transportation of gas bubbles becomes complex. During welding, gas bubbles have a tendency to float in the liquid metal due to the density differences between bulk liquid metal and the bubbles. During rise, few small pores may meet together and the coalescence forms creating bigger pore. Figure 5.18 shows typical coalesced porosity of Exp. 7. It is also found that smaller sized but more number of pores are observed near FZ boundary as compared to weld center in Exp. 7 (Fig. 5.3(b)). The points near the weld center remain above the solidus temperature for a longer duration of time as compared to the points which are far away from the FZ boundary. It enhances the fluidity of molten metal close to weld

center. Also, due to lower melt pool temperature near FZ boundary, the solubility of the hydrogen gas is high in this zone. Therefore, hydrogen gas from the surrounding region like BMZ and weld center is most likely diffused near FZ boundary due to their differences in hydrogen solubility. The areas near FZ boundary solidify first than weld center. Hence, hydrogen gas bubbles don't get enough time to grow and get away from near FZ boundary. Also, the escape of the gas bubbles during weld pool solidification is obstructed due to higher hydrostatic pressure and lower melt pool fluidity in the FZ boundary. Therefore, gas bubbles are trapped in these locations as micropores.

Fig. 5.18 Coalescence of porosity in FZ for samples in Exp. 7

The morphology of the characteristics pores is shown in FESEM images in Figs. 5.19(a) and 5.19(b) for Exp. No. 2 and 3, respectively. The characteristics pores are formed due to collapsing and instability of the keyhole. There is a difference in diameter between upper and lower portion of the keyhole with a smaller diameter at the root. Due to which, higher surface tension and internal static pressure are developed at the root. Hence, higher vapor pressure is developed at the root as compared to the mouth of the keyhole to maintain equilibrium. As a result, the keyhole becomes unstable which enhances the propensity of the pore formation in the FZ. These pores are extremely irregular in shape with rough internal walls (Fig. 5.19) unlike gas type pores where smooth wall is observed (Fig. 5.17). However, the sizes of the pores formed in the present study are smaller in size having range between 30–82 µm. The pore size for both of gas and characteristics pores are in acceptable range as per European standard where the recommended size of micro pores for satisfactory weld quality should be less than or equal to 0.40 mm (BS EN 4678., 2011).

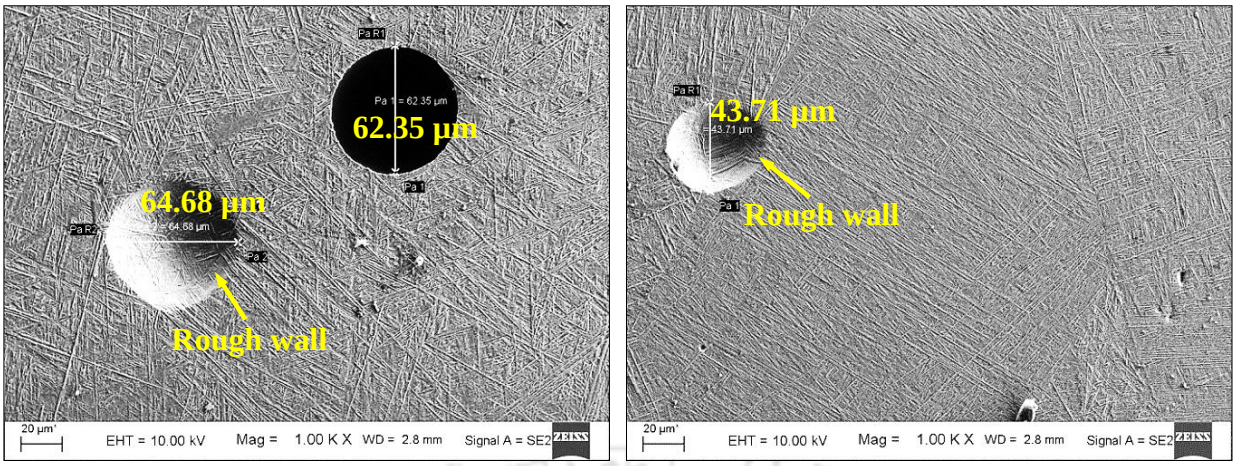

(a) (b)

Fig. 5.19 FESEM images showing morphology of characteristics pores for Exps. (a) 2 and (b) 3

5.1.5 Conclusions

In this experimental study, fibre laser beam is employed for conducting welding experiments at different welding power and speed on 2 mm thick Ti-6Al-4V plate. Argon gas efficiently protects the molten pool from environmental contamination as confirmed by EDS analysis. Crack free welds along with smooth, uniform, shiny bead having aesthetic appearance are formed. However, underfill and excess penetration are also observed in few welded samples. Weld bead is almost symmetrical about the centre line of fusion zone. Welding power shows direct effect on the bead features while welding speed shows inverse effect. Different morphologies of martensitic phase such as α′ martensite, massive α, transformed α and basketweave structures are observed in the FZ at different welding conditions because of differences in cooling rate. The amount of α′ martensite is decreased significantly from almost 100% in FZ to approximately zero near BMZ. However, a combination of α′ martensite, transformed α and primary α and β phases are observed in the different locations of HAZ. Maximum hardness is found in FZ due to the presence of higher volume of α′ martensite. Hardness in FZ decreases with increased welding power due to increased grain size. However, welding speed is the key factor for hardness enhancement in FZ as it reduces the thickness of α′ lamellae. Due to the entrapped shielding gas and instability of keyhole, two different types of micro pores are observed in the weld bead. However, its sizes are in acceptable range as per BS EN: 4678 European standards. The experimental results indicate that at a fixed 1200 W beam power, there is a certain range of welding speed (700 – 800 mm/min) which produces full penetration, narrower weld width, lesser HAZ, minimal weld defects and acceptable bead hardening.

5.2 2nd set of experiments: Effect of line energy on bead shape & features and mechanical properties

To achieve acceptable bead profile and mechanical properties, the control over weld bead shape is important because mechanical properties of weldments are highly influenced by the bead shape. Bead shape also affects weld metal solidification behaviour along with amount of line energy which imposes on workpiece surface. Therefore, it is essential to study the effect of line energy on bead morphology as well as to identify the sources of welding defects. Also, it will be beneficial to identify the range of welding parameters which can produce high quality weldments and minimize weld bead defects.

In this experimental study, the comparison of bead shape, bead features such as fusion zone width at upper (FZ_{UP}), middle (FZ_{Mid}) and lower (FZ_{Low}) position, size of the upper, middle and lower heat affected zone (HAZ_{UP}, HAZ_{Mid} & HAZ_{Low}) and fusion zone area (FZ_{area}), microstructure and mechanical properties of fiber laser beam welding of 2 mm thick plates of Ti-6Al-4V alloy are carried out at different line energies. Microstructural studies at different locations in HAZ and also in FZ are carried out using FESEM as well as optical microscope (OM) to characterize weld quality. After that their morphologies are compared at different welding conditions. The mechanical properties like Vickers microhardness and tensile properties are also measured for fully penetrated welded specimens and their differences are explained briefly with the help of their developed microstructure in both FZ and HAZ. Further, fracture surfaces are analyzed using FESEM images to confirm the mode of fracture failure i.e. ductile or brittle fracture mode. The LBW experimental conditions with experimental observations are shown in Table 5.3.

Table 5.3 Fiber LBW experimental conditions and observations

Exp. No.	Process parameters P (W)	V (mm/min)	LE (J/mm)	Observations
1	800	650	73.87	DP* < 75%
2	800	550	87.33	DP < 75%
3	1000	650	92.34	DP > 75%
4	1000	550	109.17	FP, SW, T-shaped bead
5	1200	650	110.80	FP, SW, T-shaped bead
6	1200	550	131	FP, SW, X-shaped bead

*****DP- Penetration depth, FP- full penetration, SW- successful weld, P-welding power, V-welding speed, LE-line energy*

5.2.1 Effect of process parameters

The experimental results of effect of line energy on output responses at different welding conditions are discussed in the following subsections. The line energy (J/mm) correlates both welding power and speed as discussed in Eq. (4.2). Also, a new parameter called line energy utilization factor (LEUF) for fiber LBW process is introduced in the present study by correlating FZ area with line energy as

$$\textit{Line energy utilization factor}\ (LEUF) = \frac{\textit{Fusion zone area}}{\textit{Line energy}} \tag{5.1}$$

which measures amount of energy spent to yield FZ in the welded specimens.

5.2.1.1 Bead appearance

The appearances of top surface of welded samples at different welding conditions are presented in Fig. 5.20. In the present study, all the welded surfaces are bright, silvery and aesthetic in appearance and these appearances are consistent with the results reported by Hong and Shin (2016) and Wang et al. (2014a) as discussed section 4.1.2.2. The most important finding in the present visual inspection is the significant differences in the appearance of bead surface at different line energies. As shown in Fig. 5.20 (f), at higher line energy i.e. 131 J/mm (Exp. 6, Table 5.3), blowholes are formed at the upper surface of the welded specimen. It is mainly due to the evaporation of low boiling point alloying elements from the surface of the Ti-6Al-4V alloy. Due to the lack of sufficient molten metal at higher line energy, it is not fully filled during solidification. It causes cavities on the weld surface. Hence, lower value of line energy is beneficial to achieve minimal weld defects while welding Ti-6Al-4V alloy.

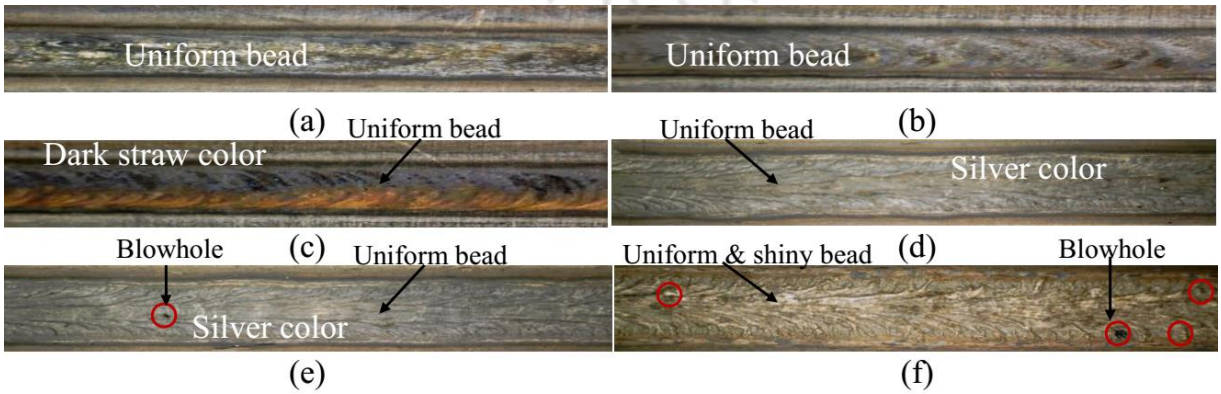

Fig. 5.20 Weld bead appearance of top surface of welded specimens for Exp. No. (a) 1, (b) 2, (c) 3, (d) 4, (e) 5 and (f) 6 in Table 5.3

5.2.1.2 Bead shape

The penetration depth in the base plate for different line energies are presented in Table 5.3. From Table 5.3, it is observed that full penetration is attained with line energy ranging between 109.17 to 131 J/mm. However, lack of penetration occurs between 73.87 to 92.34 J/mm line energies for selected welding conditions. Therefore, the welded samples with line energy below 109.17 J/mm are not further investigated in the present study. There are two different weld bead shapes i.e. T-shaped and X-shaped is observed for fully penetrated welded samples at different line energies as shown in Fig. 5.21. At lower line energies i.e. 109.17 and 110.80 J/mm (Table 5.3), T-shaped weld beads are formed in Exps. 4 & 5 (Fig. 5.21(a)) and 5.21(b)), respectively. Whereas, at higher line energy (131 J/mm, Exp. 6), X-shaped weld bead partially elongated towards top surface is formed (Fig. 5.21(c)). It is mainly due to the difference in flow pattern of molten metal which produces different keyhole shapes inside melt pool. Open keyhole (Fig. 5.22(a)) is formed at higher line energy (131 J/mm) whereas slightly blind keyhole is formed at lower line energies (109.17 and 110.80 J/mm) as shown in schematic diagram in Fig. 5.22(b).

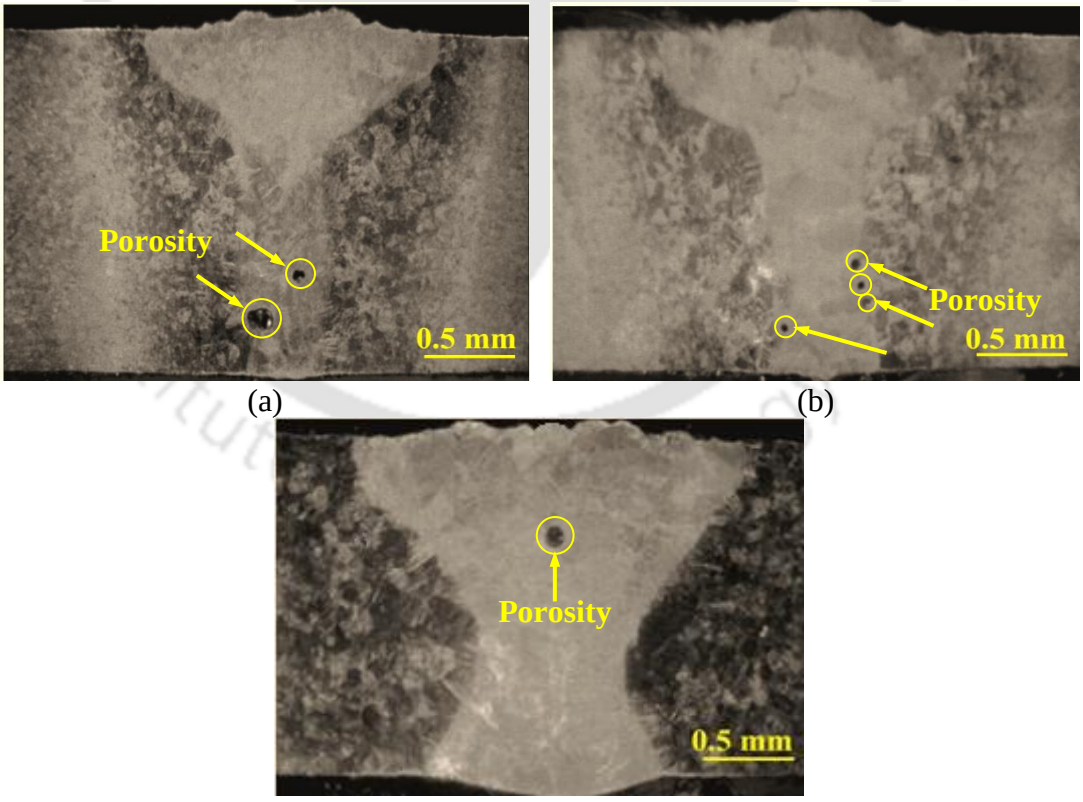

Fig. 5.21 Optical image (2X magnification) of bead shape at (a) 109.17 J/mm (T-shaped), (b) 110.80 J/mm (T-shaped) and (c) 131 J/mm (X-shaped) line energy

At the starting of the LBW process, the keyhole formation is initiated due to the vaporization of molten metal from top surface of weld bead. The flow pattern of liquid metal depends on gravity force, recoil pressure and the difference in surface tension between upper and lower halves of weld bead. The keyhole is stabilized by recoil pressure and it is counterbalanced by surface tension and gravity force (Chen et al., 2013 and Kim and Ahn, 2012). The amount of recoil pressure depends on effective beam intensity which strikes with keyhole wall. The effective beam intensity is influenced by laser beam's multiple reflections inside keyhole. In case of keyhole mode of LBW process, non-uniform distribution of beam energy occurs along the vertical direction of keyhole. Hence, non-homogeneous distribution of recoil pressure takes place along the keyhole depth.

Also, the temperature of melt pool at lower half is higher than the top surface due to multiple reflections of laser beam inside keyhole wall. At higher melt pool temperature, the surface tension is reduced at lower half of weld bead. Due to the difference in surface tensions and prominent non-uniform recoil pressure along keyhole depth, a clockwise vortex is developed in the melt pool. It leads to increased size of lower-half area of melt pool. Therefore, the reflected laser beam escapes out from both upper and lower part of weld bead. Hence, both top and bottom weld pool areas are elongated and the keyhole opens at the root side as shown schematically in Fig. 5.22(a). This is known as open keyhole. Therefore, after solidification of the melt pool, X-shaped weld bead is formed as shown in Fig. 5.21(c). However, at lower line energies (109.17 and 110.80 J/mm), the beam intensity is lower with respect to higher line energy. Because of this, the intensity of reflected laser beam within keyhole is weaker. Therefore, the size of the keyhole at the lower half is not enlarged much as found at higher line energy, explained earlier. Hence, at lower half of melt pool, the surface tension is almost counterbalanced by recoil pressure. Due to which the root of keyhole becomes slightly closed during solidification of molten metal which is known as blind (or, closed) keyhole as shown in schematic diagram in Fig. 5.22(b). As a result, T-shaped weld bead is formed after solidification of melt pool as shown in Figs. 5.21(a) and (b).

It is also observed from the macrograph of the fully penetrated weld bead (Fig. 5.21) that the weld bead is almost symmetrical about center line of FZ and the lack of symmetricity is observed only in the root side of the weld bead. The probable reasons for this phenomenon are already discussed in section 4.1.2.2. No bulk cracks are found in the FZ as well as in HAZ. It is probably due to extremely high crack resisting properties of Ti-6Al-4V BM and the welding conditions at which experiments are conducted.

(a) (b)

Fig. 5.22 Schematic diagram of different keyhole modes of welding (a) open and (b) blind keyhole

5.2.1.3 Width of FZ and its area (FZ_{area})

Figures 5.23(a) and (b) show the variation in FZ width (i.e. FZ_{UP}, FZ_{Mid} and FZ_{Low}) and FZ_{area}, respectively at different line energies. From Fig. 5.23(a), it is clearly seen that the FZ width continuously increases with increased line energy because of imposed higher energy on the work piece surface as already explained in section 5.1.1.5. Similar observations between FZ width and line energy is reported by Squillace et al. (2012). In Fig. 5.23(b), with the increase in line energy larger volume of material is melt down which leads to continuous increase in FZ_{area}.

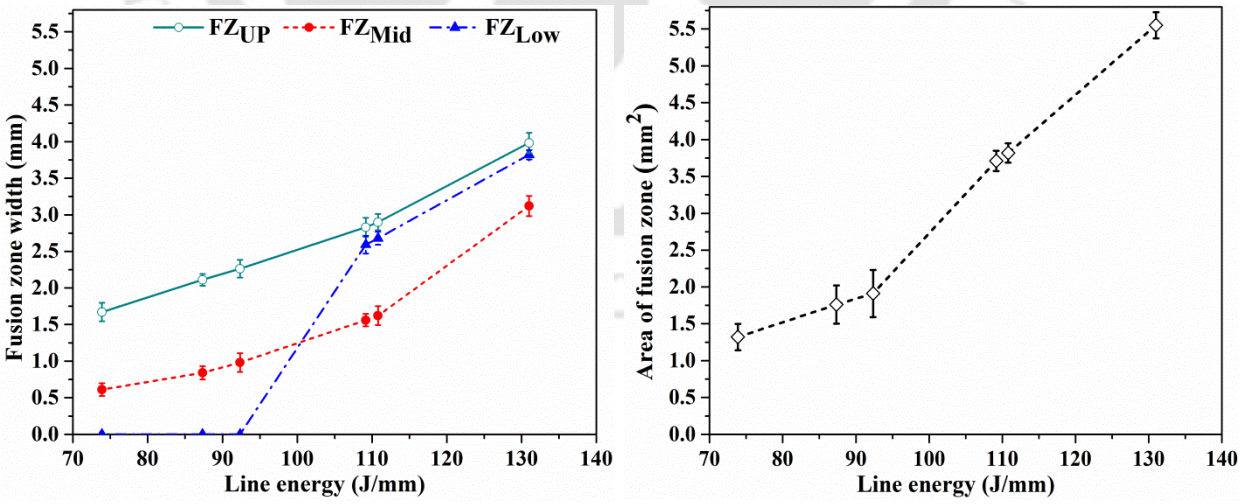

(a) (b)

Fig. 5.23 Effect of line energy on (a) width of FZ and (b) FZ area (FZ_{area})

Almost linear trend between FZ_{UP} and line energy is observed in the present study. Also, the upper width of FZ_{UP} is larger than both FZ_{Mid} and FZ_{Low} for all specimens mentioned in Table 5.3. It is mainly due to the prominent flow of molten metal towards the

upper part of melt pool as compared to lower part by the combined effect of Marangoni effect, vapour pressure and existing surface tension force which disrupts the keyhole shape starting from bigger width at upper part to reduced width at weld pool's lower part as explained briefly in section 5.1.1.5. Also, inside keyhole at position "B" (Fig. 5.4(c)), both vapour pressure and Marangoni shear stress are weak. Therefore, due to gravitational effect, backfilling of molten metal occurs at weld bead's lower part. Hence, the width of FZ_{Low} is higher than FZ_{Mid} for fully penetrated samples. Also, the lower part of FZ is in contact with the atmosphere which accelerates solidification rate by spreading heat energy laterally. Hence, the width of FZ_{Low} is higher than the FZ_{Mid}. In Fig. 5.23(a), at 73.87 J/mm (Exp. 1), 87.33 J/mm (Exp. 2) and 92.34 J/mm (Exp. 3) line energies, the width of FZ_{Low} is zero due to partial penetration in BM as mentioned in Table 5.3.

5.2.1.4 Size of heat affected zone (HAZ)

Figure 5.24 depicts the effect of line energy on HAZ size at different locations in the weld bead. It is observed that increasing line energy, HAZ_{UP} and HAZ_{Low} continuously increase due to the imposed higher heat energy on the workpiece surface. However, the maximum and minimum value of HAZ_{Mid} are obtained at 131 J/mm (Exp. 6) and 73.87 J/mm (Exp. 1) line energies, respectively (Fig. 5.24).

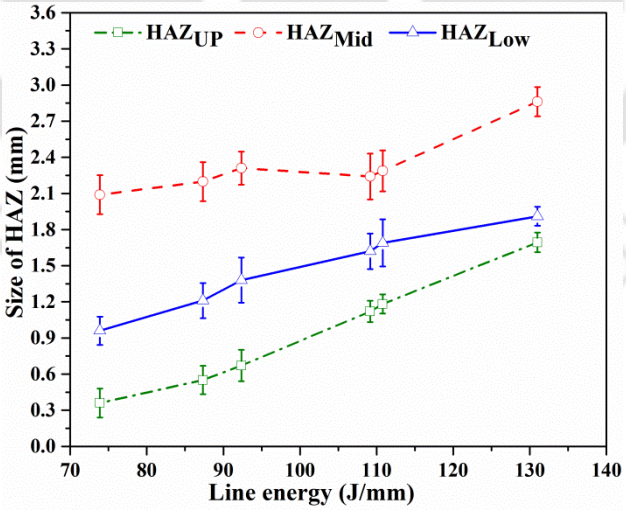

Fig. 5.24 Effect of line energy on HAZ size

Initially, at 73.87 to 92.34 J/mm line energy, incomplete penetration takes place. Therefore, heat energy is mostly dissipated from weld bead's upper surface. Hence, the heat is restrained for a longer duration of time at the same place in the middle portion of the weld bead before it is dispersed due to poor thermal conductivity of Ti-6Al-4V alloy. As a result,

HAZ_{Mid} size continuously increases from 73.87 to 92.34 J/mm line energies. Further increase in line energy at 109.17 J/mm, larger fraction of beam energy is consumed to increase the penetration depth before dispersing towards transverse direction. Hence, at higher line energy (i.e. 109.17 J/mm, Exp. 4), prominent keyhole is formed and full penetration is achieved. Therefore, the size of HAZ_{Mid} is reduced at 109.17 J/mm (Exp. 4) than in 92.34 J/mm (Exp. 3) as shown in Fig. 5.24. Further increase in line energy beyond 109.17 J/mm when full penetration is achieved, the heat energy is distributed again towards transverse direction of weld line. Hence, HAZ_{Mid} size continuously increases. In present study, almost linear relationship between HAZ_{UP} and HAZ_{Low} with line energy is observed irrespective of penetration depth in the base plate. However, in transition from partial to full penetration in the base plate, the size of HAZ_{Mid} is slightly reduced and further linearly increases with increased line energy.

5.2.1.5 Line energy utilization factor (LEUF)

The line energy utilization factor (LEUF) of the welded specimens is calculated from Eq. (5.1). Table 5.4 shows the values of LEUF having T-shaped (Exps. 4 & 5) and X-shaped weld bead (Exp. 6) cross section. From Table 5.4, it is observed that LEUF for T-shaped bead is higher than X-shaped bead.

Table 5.4 Line energy utilization factor (LEUF) for different bead shape

Exp. No.	P (W)	V (mm/min)	LE* (J/mm)	Bead shape	LEUF (mm^3/J)
4.	1000	550	109.17	T-shaped	0.033
5.	1200	650	110.80	T-shaped	0.034
6.	1200	550	131.00	X-shaped	0.028

***P-Welding power, V-welding speed, LE-line energy*

The probable reason for lesser value of LEUF for X-shaped bead is due to the loss of more amount of beam energy at higher line energy. At higher line energy with X-shaped bead (Exp. 6), excess penetration occurs in the base plate. Also, the evaporation of molten metal occurs from specimen's upper surface. Therefore, the heat energy is lost from both top and bottom surface of the specimen (due to larger diameter of top and bottom melt pool for X-shaped bead) without further increasing penetration depth in the base plate. Whereas, in case of T-shaped bead, the beam energy is mostly utilized to increase the FZ area. As, in case of X-shaped, the energy is dissipated from both top and bottom surfaces of the bead, therefore,

while considering LEUF for fully penetrated bead, the welding condition for T-shaped bead is favorable.

5.2.2 Microstructural analysis in HAZ

In the present study, the microstructures at different locations in HAZ i.e. near FZ, middle of HAZ, far away from FZ and near BMZ are discussed. A mixture of acicular α′ (i.e. martensitic phase) and small amount of blocky α (i.e. transformed α from prior β grain) phases are formed in HAZ which is nearer to FZ (near FZ). It is clearly observed in optical as well as FESEM micrographs in Figs. 5.25(a) and 5.26(a), respectively.

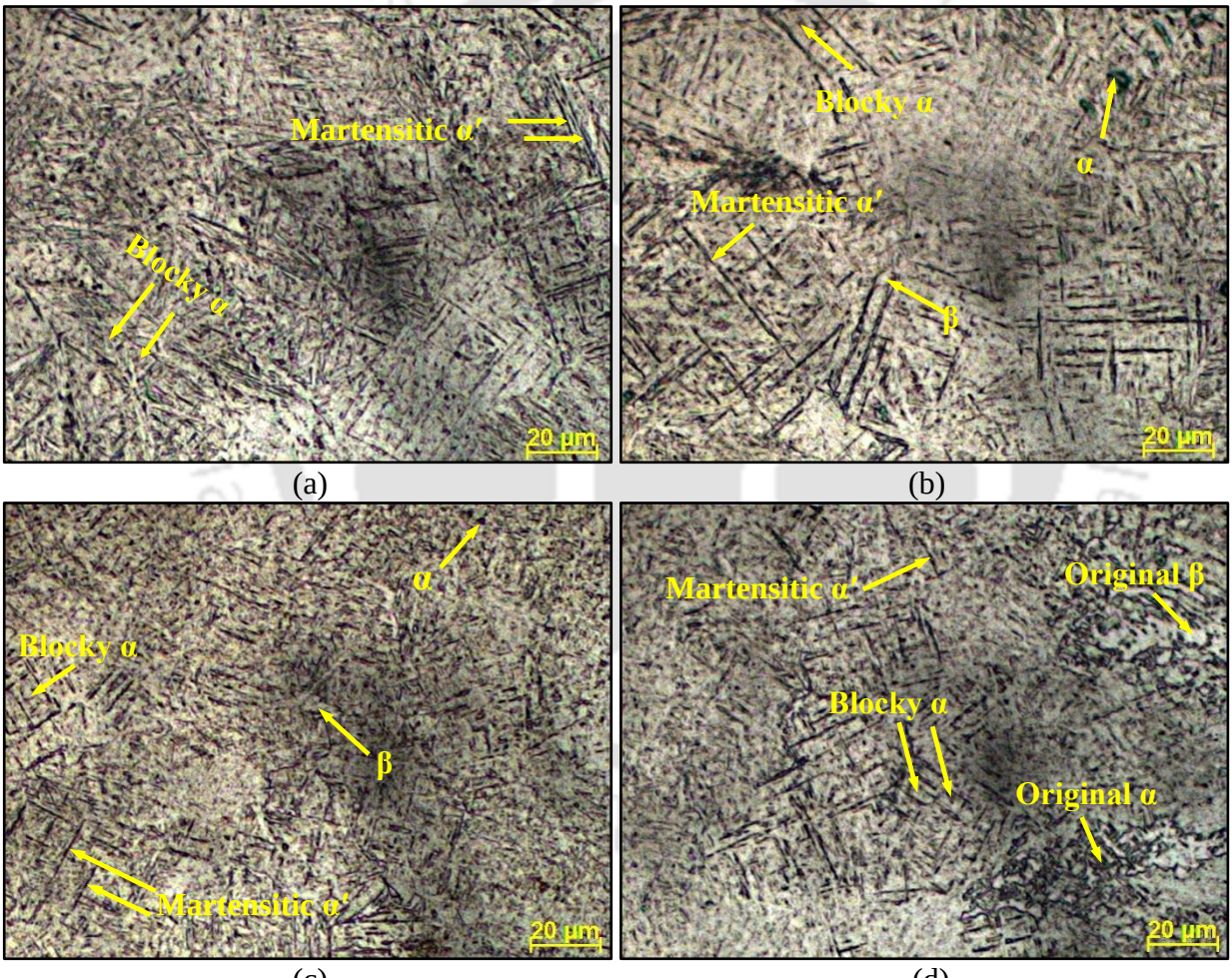

Fig. 5.25 Optical images of microstructure within HAZ at different positions in weld bead; (a) Near FZ, (b) middle part of HAZ, (c) far away from FZ and (d) near BMZ for Exp. 4 (Table 5.3)

Slightly lower amount of martensitic α′ phase and a combination of blocky α and primary β phases are observed in the middle of HAZ as shown in Figs. 5.25(b) and 5.26(b), in optical and FESEM images, respectively. The HAZ which is far away from FZ comprises of

a combination of blocky α phase, primary α phase and primary β phase with a small amount of α′ phase (Figs. 5.25(c) and 5.26(c)). The maximum temperature in this region is below T_β, however, sufficient enough for microstructural changes. This temperature in far away HAZ is very difficult to determine due to the dependency on transformation kinetics. Similar observations are discussed in details in section 5.1.2.1.

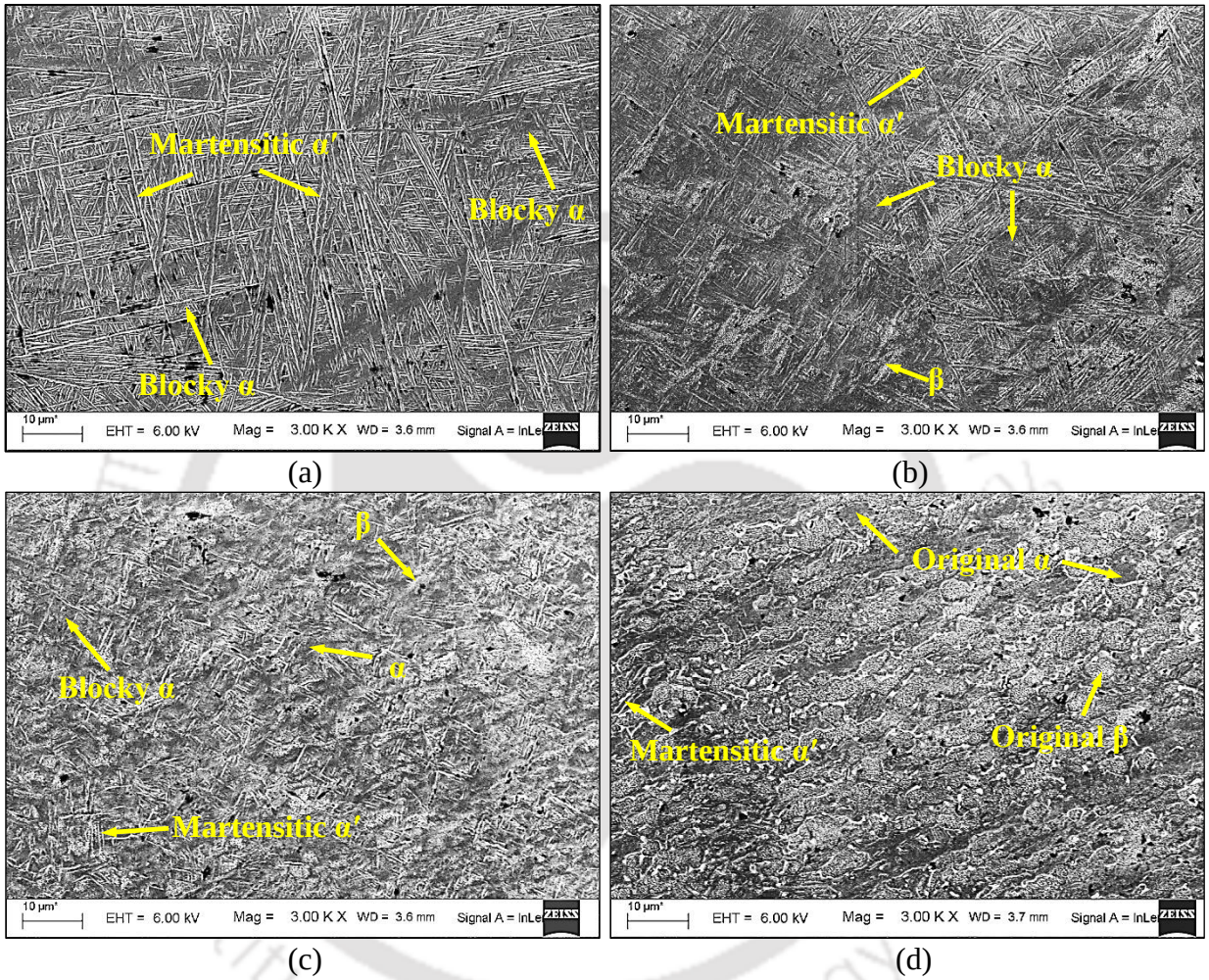

Fig. 5.26 FESEM images of microstructure in HAZ at different positions; (a) Near FZ, (b) middle of HAZ, (c) far away from FZ and (d) near BMZ for Exp. 4 (Table 5.3)

5.2.3 Microstructural analysis in FZ

In Fig. 5.8(b), the effect of line energy on cooling rate is presented where at higher line energy, slower cooling rate and at lower line energy faster cooling rate of molten pool occurs. Cooling rate is also affected by the thickness of the weld metal and thermo-physical material properties of the specimens. However, in the present case, specimen thickness of Ti-6Al-4V alloy is kept fixed as 2 mm. Hence, the cooling rate is mainly affected by the line energy. The dependency of cooling rate on line energy is already explained in section 5.1.2 and in Fig. 5.8(b). Due to the differences in line energy which affects cooling rate, different

types of microstructural features are developed in FZ as shown in Fig. 5.8(a). The optical and FESEM microstructural images of FZ are shown in Figs. 5.27(a-c) and 5.28(a-c), respectively with increasing line energy at three different weldments for Exp. 4, Exp. 5 and Exp. 6 (Table 5.3). At three different line energies, noticeable microstructural variations are observed in the FZ. From micrographs in Figs. 5.27(a-c) and Figs. 5.28(a-c), it is seen that α′ martensite is formed in FZ due to diffusionless transformation of β phases into the dominant matrix of α′ martensitic phase (acicular α′) which is promoted by high self-quenching rate of LBW process.

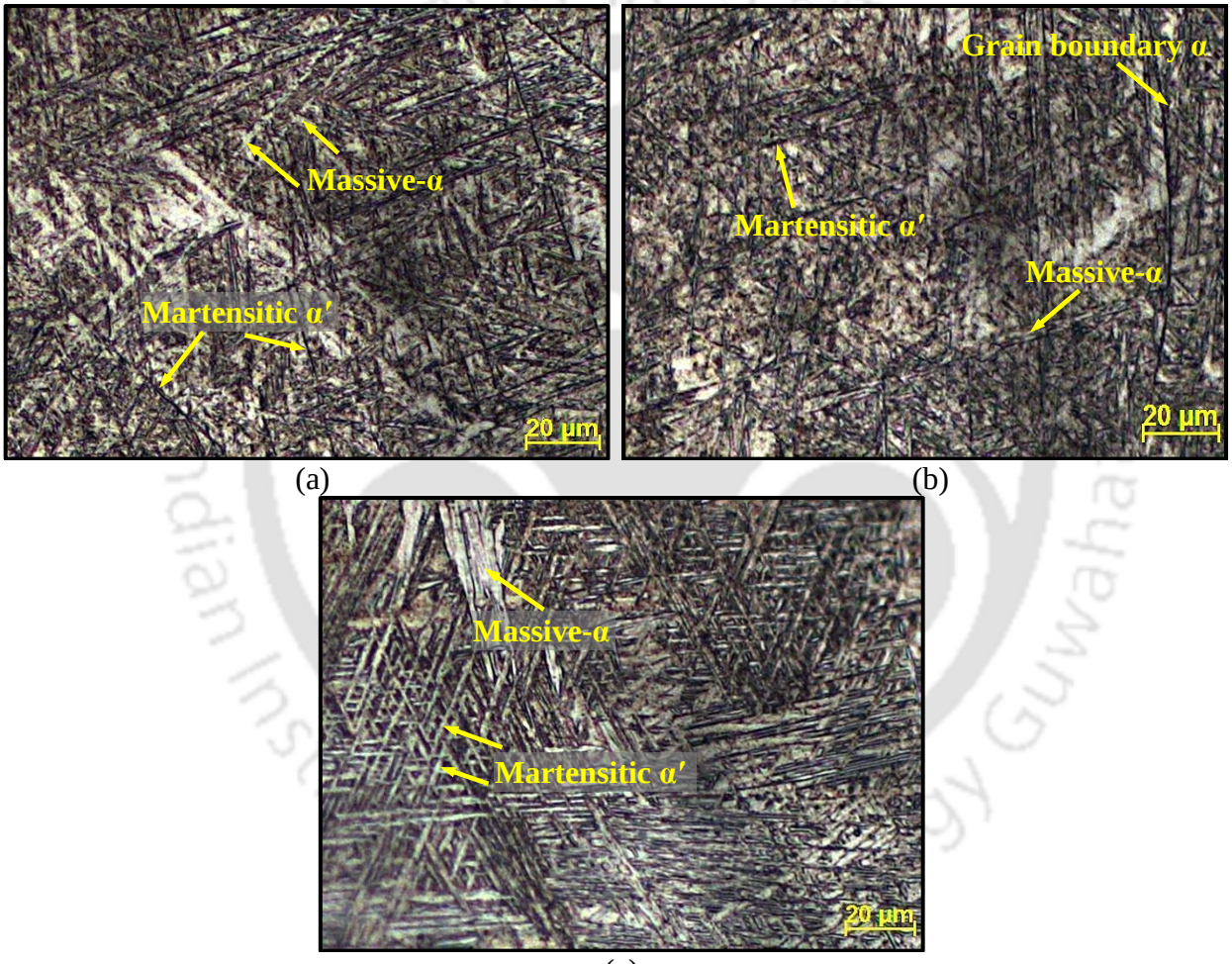

Fig. 5.27 Optical images of FZ microstructure for Exp. No. (a) 4 (109.17 J/mm), (b) 5 (110.80 J/mm) and (c) 6 (131 J/mm) with increasing line energy

When the weld region cools down from a higher temperature, large amount of β phase is transformed into martensitic α′, blocky α and massive-α (α_m) phases depending on the cooling rate. It is observed from Figs. 5.27(a & b) and 5.28(a & b), that at lower line energies i.e. 109.17 and 110.80 J/mm, dominant matrix of martensitic α′ phase along with grain boundary α (Fig. 5.28(b)) and massive α are formed due to higher cooling rates in FZ. The

presence of massive α in the dominant matrix of α′martensitic phase indicates that the cooling rate of FZ in the present welding condition is closer to the critical cooling rate (410 °C/s) needed for the development of fully α′ martensitic structure in FZ. At higher line energy of 131 J/mm, the cooling rate is calculated as 288 °C/s. It promotes broadening of α lamellas. Slightly higher amount of massive α_m phases are observed in Fig. 5.27(c) and Fig. 5.28(c) at prior β-grain boundaries in the dominant matrix of α′ martensitic phase.

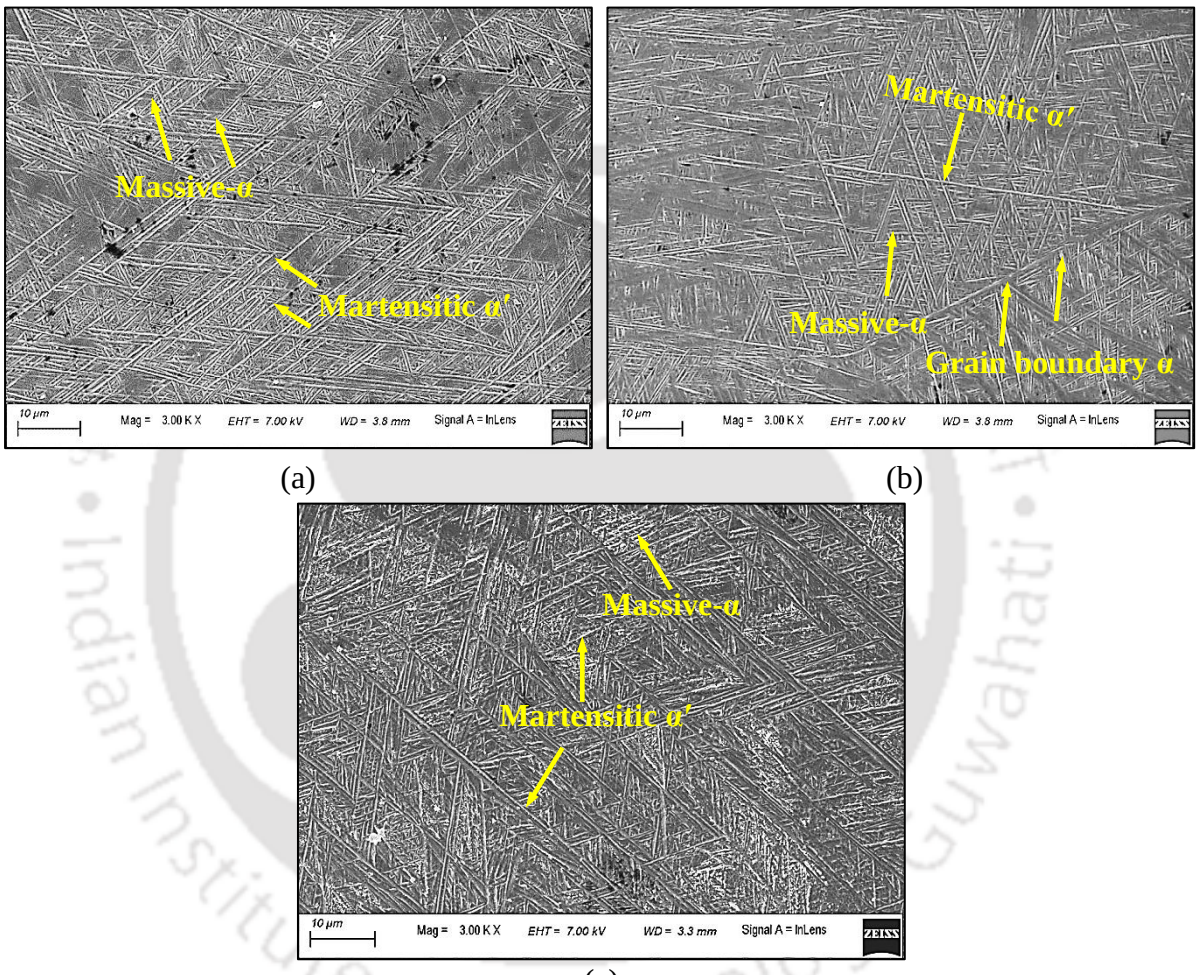

Fig. 5.28 FESEM images of FZ microstructure for Exp. No. (a) 4 (109.17 J/mm), (b) 5 (110.80 J/mm) and (c) 6 (131 J/mm) with increasing line energy

It is observed from Figs. 5.27(a-c) and 5.28(a-c) that the morphology of martensitic α′ phase changes from needle shape to plate like morphology with increased line energy. Both the length and thickness of α′ lamellae's increases with increasing line energy. The average length of needle shaped α′ lamellae's in the FZ is increased from 80 μm to120 μm from line energy of 109.17 (Exp. 4) to 131 J/mm (Exp. 6) as measured in optical microscope. It indicates that with increasing line energy, the prior β grain size in FZ increases due to the sufficiently longer time period available for grain coarsening. In general, the grain boundary

α quickly starts to form at locations where temperature drops below β transus temperature. Also, the amount and thickness of grain boundary α continuously decrease with higher cooling rate. However, in the present case the grain boundary α is only observed in the FZ for moderate line energy (110.80 J/mm) in Exp. 5. It is mainly due to adequate cooling rate (CR = 403 °C/s) of weld bead at line energy of 110.80 J/mm.

5.2.4 Porosity

In the present study, two different types of micro-pores i.e. intrinsic or gas type and characteristic pores are formed. Although, the number of pores are insignificant. However, in the present study, for fully penetrated welded specimens at lower line energies i.e. 109.17 J/mm (Exp. 4) and 110.80 J/mm (Exp. 5), the pores are observed at lower half of weld bead in FZ (Fig. 5.21(a)) and near FZ boundary (Fig. 5.21(b)), respectively. However, at higher line energy i.e. 131 J/mm, the micro-pores appear at the top of the weld bead near center line of FZ (Fig. 5.21(c), Exp. 6). By comparing the weld beads in Figs. 5.21(a-c), it is observed that more number of micro-pores are observed at lower half in FZ and near FZ boundary at lower line energies of 109.17 and 110.80 J/mm, respectively as compared to higher line energy (131 J/mm) where micro-pores are observed near weld center line only at upper half of FZ. The weld center achieves maximum temperature during LBW process and its value continuously decreases towards boundary between FZ and HAZ. Therefore, the temperature near weld center line remains above solidus temperature for a longer period of time as compared to the points which are at the boundary of FZ. It enhances the fluidity of the molten metal close to weld center.

Also, due to lower melt pool temperature near FZ boundary, the solubility of hydrogen gas is high at this location. In general in case of titanium alloy the hydrogen gas solubility decreases in liquid with increased temperature up to the melting point (T_m) of titanium alloy. Also, at melting point, the hydrogen solubility in liquid titanium suddenly increases and further increase of temperature beyond T_m again its solubility decreases (Karimzadeh et al., 2005). Therefore, hydrogen gas from the surrounding region like from BMZ and weld center most likely diffuses at the locations near FZ boundary due to their differences in hydrogen gas solubility. The areas near FZ boundary solidifies at a faster rate than weld center. Hence, hydrogen gas bubbles don't get enough time to grow and get away from FZ boundary. Also, gas bubbles escaping during solidification of weld pool is hindered due to higher hydrostatic pressure and lower melt pool fluidity near FZ boundary at lower line energy and its corresponding higher cooling rate. Therefore, gas bubbles are easily

trapped near FZ boundary as micropores. The morphology of gas type porosity having circular shape with smooth wall is shown in FESEM images in Figs. 5.29(b) and 5.29(c). Hence, it can be concluded that the hydrogen is the main cause for the formation of gas type micropores in LBW of Ti-6Al-4V alloy.

Investigation in Fig. 5.21(a-c) shows clear trend of porosity position with bead shape. In T-shaped weld bead (Figs. 5.21(a) and (b), lower line energy), the pores appear at lower half of weld bead. Whereas, for X-shaped weld bead (Fig. 5.21(c), higher line energy), the pores appear at upper half of FZ. At higher line energy with X-shaped bead, both widths of FZ_{UP} and FZ_{Low} as well as FZ area are bigger as compared to T-shaped bead. Hence, the pores can escape out easily from both top and bottom surfaces of the bead. Also, due to lower cooling rate at higher line energy, the micro pores get sufficient time to escape out from the melt pool since gas bubbles have a tendency to float upward in the liquid metal due to their difference in density with bulk liquid metal. Due to which the pores are moved towards upper half of weld bead and it is trapped at upper half of FZ which cannot escape during solidification.

The formation of larger sized pores (Fig. 5.29(a)) is most likely associated with the collapsing and high instability of keyhole at lower welding speed due to the difference in diameter between top and bottom portion of keyhole as explained earlier in section 5.1.4. However, the welding experiments conducted at combination of high beam power and higher welding speed (Exp. 5), both upper and lower part of bead size is wider and larger melt pool is formed as compared to low power and lower welding speed (Exp. 4). The larger melt pool helps to escape out the bubbles from the FZ efficiently and also it has high tendency to resist interrupting force inside keyhole. Hence, the melt pool has less chance to flow in turbulent manner which helps to keep the keyhole stable as compared to combination of moderate welding power and lower welding speed (Exp. 4).

The morphology of characteristics pores is shown in FESEM images in Fig. 5.29(a). These pores are slightly larger in size and irregular in shape and have rough internal wall unlike gas type pores where small sized pores having smooth wall (Fig. 5.29(b)) is observed. However, the size of all kind of pores are in the range between 6.82–46.44 μm which comes under the well-established welding quality acceptance criteria as per European BS EN: 4678 (2011) standard.

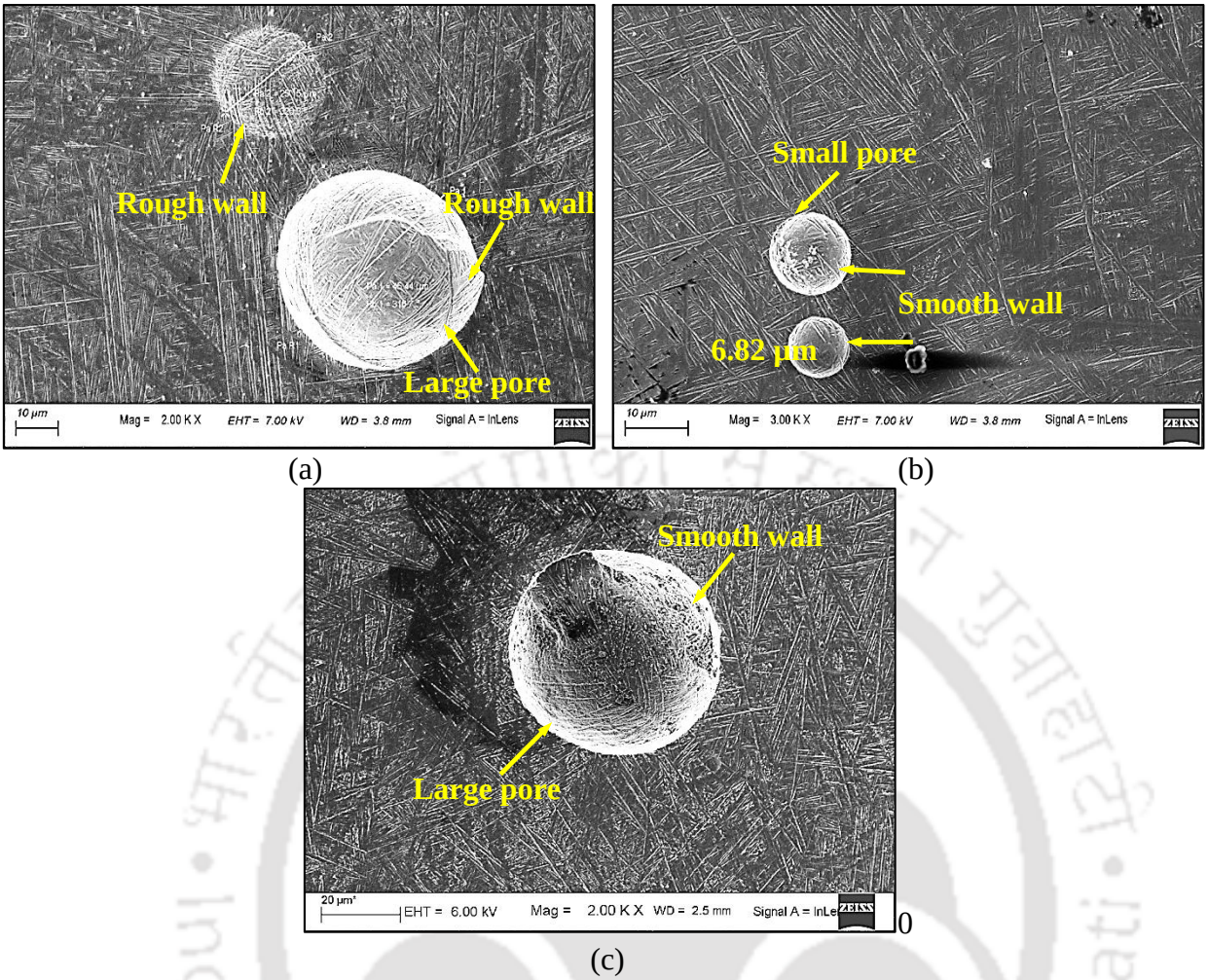

Fig. 5.29 FESEM images showing morphology of pores for T-shaped beads for (a) Exp. 4, (b) Exp. 5 and for X-shaped bead for (c) Exp. 6

5.2.5 Mechanical properties

The most essential mechanical properties namely Vickers microhardness and tensile properties are measured for both X and T-shaped weld beads as discussed in the following subsection.

5.2.5.1 Hardness

In the current study, hardness of laser beam welded specimens (Exps. 5 & 6, Table 5.3) are measured at different locations along transverse direction to weld line at top and middle portion of bead cross-section as shown in Figs. 5.30(a) and (b) for T and X-shaped weld beads, respectively. Figures 5.31(a) and (b) show the hardness distribution at upper and middle portion across weld bead for Exps. No. 5 and 6, respectively. Lowest value of hardness (256±10 HV) is perceived at BMZ and its value increases at HAZ. Maximum value of hardness (408.26 & 388.24 HV for Exps. No. 5 & 6, respectively) is observed in FZ. It is

mainly due to the formation of dominant matrix of α′ martensitic structure in FZ. The hardness distribution curves in Figs. 5.31(a) and (b) show similar trend as in Fig. 5.15(b). It is also observed that hardness values sharply decrease in HAZ in case of T-shaped bead (Figs. 5.31(a)) as compared to X-shaped bead (Figs. 5.31(b)) due to bigger sized HAZ in case of X-shaped bead. It is also observed that hardness in FZ is prominently higher (Fig. 5.31(a)) for lower line energy (110.8 J/mm, Exp. 5). Whereas, its value slightly lower (Fig. 5.31(b)) for higher line energy (131 J/mm, Exp. 6). It is primarily due to decreased cooling rate at higher line energy from Exp. No. 5 to 6 (CR = 403.46 and 288.62 °C/s, respectively).

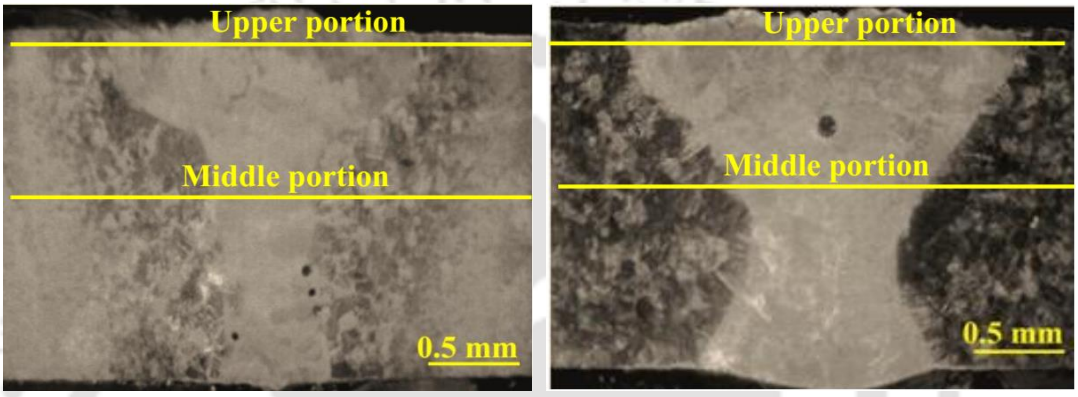

(a) (b)

Fig. 5.30 Position of hardness measurement on upper and middle portion of bead cross-section for (a) T-shaped (Exp. No. 5) and (b) X-shaped (Exp. No. 6) beads

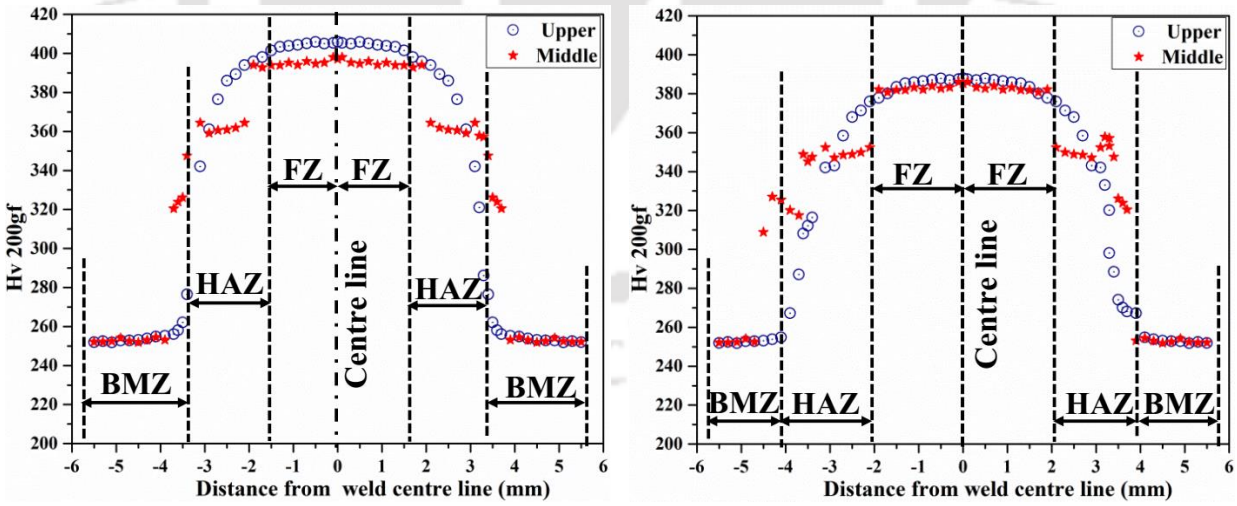

(a) (b)

Fig. 5.31 Hardness distribution along transverse direction to centre line of FZ for Exp. No. (a) 5 and (b) 6 at upper and middle portions of weld bead cross-section

Higher cooling rate promotes the formation of brittle nature of α′ martensitic phase and reduced thickness of α′ lamella which leads to higher hardness in Exp. 5 as compared to Exp. 6. The hardness value at the upper portion of weld bead is more than middle portion of

weld bead in both Figs. 5.31(a) and 5.31(b). It is mainly because of faster cooling rate at the upper portion of weld bead which is exposed to atmosphere as compared to middle region as explained in section 5.1.3.

5.2.5.2 Tensile properties and fractography

The tensile properties of BM of Ti-6Al-4V alloy and fully penetrated welded specimens are given in Table 5.5.

Table 5.5 Tensile properties of welded specimens

Exp. No. (Table 5.3)	YS* (MPa)	Avg. YS (MPa)	UTS (MPa)	Avg. UTS (MPa)	El (%)	Avg. El (%)
BM	912	892	981	981	14.58	13.89
	896		988		12.83	
	868		974		14.26	
4	864	868	943	948	6.47	6.18
	866		952		6.06	
	874		949		6.01	
5	862	860	944	942	7.38	6.84
	863		934		7.12	
	855		948		6.02	
6	873	872	958	957	9.68	8.86
	864		950		8.38	
	879		963		8.52	

**YS- Yield strength, UTS- Ultimate tensile strength, Avg.- average, El- elongation*

It is observed that the welded specimen's tensile properties are less than BM due to the formation of porosities in the weld bead region which acts as a stress concentrator and the cracks are initiated from the micropores. It is also observed that the tensile properties of the specimens having T-shaped weld bead are lower than X-shaped weld bead. However, failure occurs for both the welded specimens at the boundary between FZ and HAZ. It is probably due to non-uniform distribution of plastic strain during tensile tests. The material at the interface between HAZ and FZ is comparatively softer as compared to the adjacent regions in BM, HAZ and FZ where comparatively harder materials persist. It affects the higher rate of plastic deformation at the interface between HAZ and FZ. The size of HAZ is lesser for Exps. 4 and 5 at lower line energy as compared to higher line energy for Exp. 6. Due to which higher non-uniformity in plastic strain distribution occurs in T-shaped bead than X-shaped bead. Apart from these, due to the existence of more number of micro-pores at the boundaries between FZ and HAZ (Fig. 5.21(b), Exp. 5) and bigger size pores at the lower half of FZ (Fig. 5.21(a), Exp. 4) as discussed in section 5.1.4, the chances of crack initiation site

enhance. As a result, the strength of the welded specimens degrades in case of T-shaped bead as compared to X-shaped bead where lesser number of micro-pores are observed in FZ (Fig. 5.21(c), Exp. 6). Hence, the tensile and yield strength of T-shaped welded specimens are lesser than X-shaped bead.

The FESEM images of fractured surfaces for BM, T and X-shaped beads are shown in Figs. 5.32(a), (b & c) and (d), respectively. It is observed that more number of dimples are uniformly distributed over entire fractured surface of BM (Fig. 5.32(a)). It indicates the characteristics of higher ductility and ductile mode of fracture failure of BM. Micro voids are observed in the fractured region in both Exps. No. 4 and 5 welded specimens. In the fractured surface of the welded specimens a combination of non-uniform, shallow and elongated dimples are observed along with tearing ridges as shown in Figs. 5.32(b, c, d). The shallow dimples and tearing ridges found in the fractured area signifies the characteristics of ductile mode of failure of welded specimens (Wang et al., 2012b).

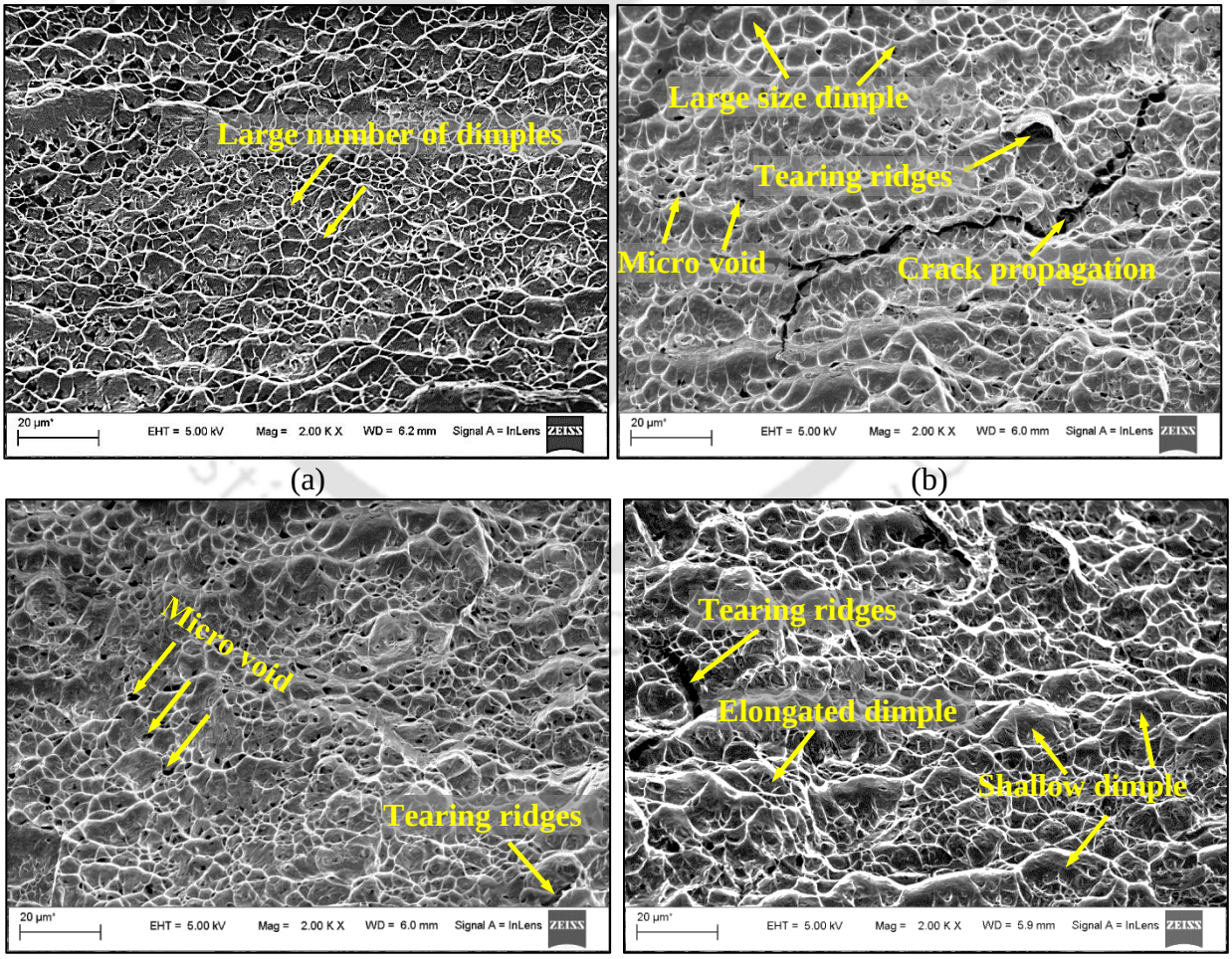

Fig. 5.32 FESEM micrographs of fractured surface of (a) BM, (b) T-shaped bead (Exp. 4), (c) T-shaped bead (Exp. 5) and (d) X-shaped bead (Exp. 6)

5.2.6 Conclusions

On the basis of the experimental results discussed above following conclusions are made:

- Line energy shows positive effect on width of fusion zone and fusion zone area. At higher line energy (131 J/mm), X-shaped weld bead is formed whereas lower line energies (109 and 111 J/mm) yield T-shaped bead.
- The microstructural analysis of weld bead reflects the evaluation of α′ martensitic phase along with massive-α in fusion zone whereas a combination of α′ martensite, transformed α and original α and β phases are observed in the HAZ which is nearer to base metal zone.
- The maximum hardness is observed in the FZ and its value continuously decreases towards base metal zone due to the reduction of α′ martensite.
- The tensile strength and % elongation of T-shaped bead are lower than X-shaped bead. However, fracture mechanism for both the weld beads are similar to ductile fracture mode. The percentage elongation of the welded specimens is lower than the base material owing to the presence of micro pores in the weld bead and brittle nature of α′ martensite.
- The T-shaped-bead welding condition is advantageous for achieving satisfactory weld quality in terms of bead appearance, full penetration with acceptable bead hardening and weld defects.

Chapter 6
Experimental investigation of 1.5 mm thick Ti-6Al-4V plates

6.0 Introduction

In the present study an experimental investigation of fiber LBW of 1.5 mm thick Ti-6Al-4V plates is carried out at different line energy to understand their effect on weld bead features i.e. penetration depth (d_p), fusion zone width at upper (FZ_{UP}), middle (FZ_{Mid}) and lower (FZ_{Low}) positions, size of upper, middle and lower heat affected zones (i.e. HAZ_{UP}, HAZ_{Mid} and HAZ_{Low}). To characterize the weld quality, the microstructural studies are carried out at various locations within HAZ and in FZ using FESEM and optical microscopy and their morphologies are compared at different welding conditions. The weld defects like underfill, porosity and its minimization techniques are discussed. The mechanical properties such as Vickers microhardness and tensile properties are also measured at different welding conditions and its variations are correlated with developed microstructure in FZ and HAZ. Further, the fractured surfaces are analyzed using FESEM to confirm different modes of fracture failure.

6.1 Experimentation

Laser beam welding experimental conditions and bead observations are given in Table 6.1.

Table 6.1 LBW experimental conditions and bead observations

Exp. No.	process parameters			Observations
	P (W)	V (mm/min)	LE (J/mm)	
1	700	600	70.00	FP*
2	700	800	52.51	PP, USW
3	700	1000	41.99	PP, USW
4	800	600	80.00	FP
5	800	800	60.01	FP
6	800	1000	47.99	FP
7	900	600	90.00	EP*, USW
8	900	800	67.52	FP
9	900	1000	53.98	FP

**LE = Line energy, P=Beam power, V=Welding speed, FP/PP=Full/Partial penetration, EP= Excess penetration, USW= Unsuccessful weld*

6.2 Results and discussion

The experimental results at different welding conditions are discussed in details in the following subsection.

6.2.1 EDS analysis and bead appearance

To confirm shielding gas effectiveness during welding, EDS analysis of BM and weldments along weld line are carried out as shown in Figs. 6.1(a) and (b). It is found that concentration of O_2 is little bit increased from 1.8 wt. % in BM to 2.5 wt. % along welding line because of the formation of TiO_2 during LBW process. It shows that in the present study, the weld pool is efficiently protected by delivering controlled flow rate of shielding gas (argon) as explained earlier in section 4.1.2.1. Further, to confirm the effectiveness of shielding gas, appearance of top surface of the welded samples is investigated at different welding conditions for fully penetrated samples of Exp. No. 4, 8, 5 and 6 with decreasing value of line energy as shown in Figs. 6.2(a-d). In the present study, the welded surfaces are bright, silvery and aesthetic in appearance which indicates excellent shielding of weld pool from environmental contaminations and these appearances are consistent with the results reported by Hong and Shin (2016) and Wang et al. (2014a) as discussed in section 4.1.2.2.

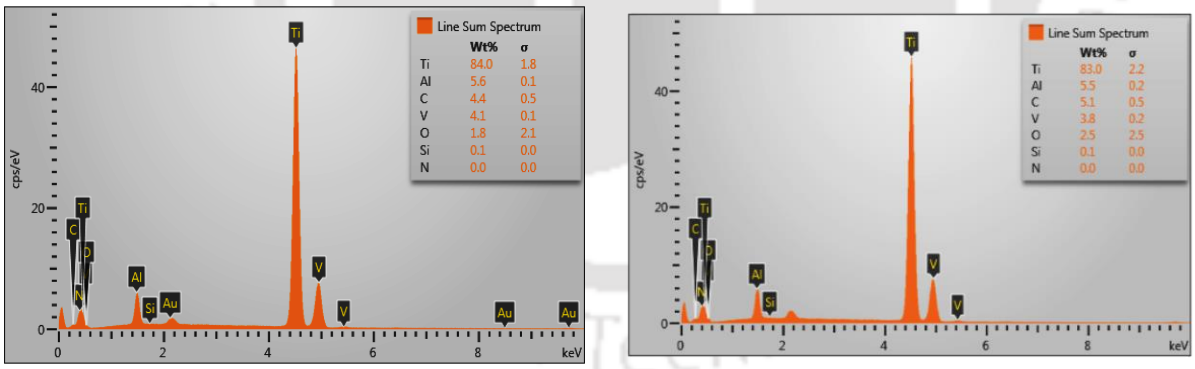

(a) (b)

Fig. 6.1 Chemical composition of Ti-6Al-4V specimen from EDS analysis in (a) BM and (b) welded specimen along weld line

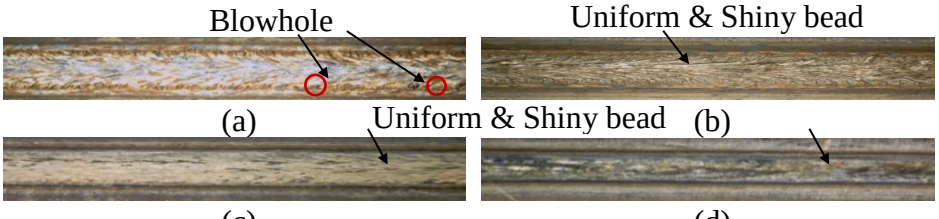

Fig. 6.2 Bead appearance on top surface of welded samples with decreasing line energy for Exp. (a) 4 (80 J/mm), (b) 8 (67.52 J/mm), (c) 5 (60.01 J/mm) and (d) 6 (47.99 J/mm)

6.2.2 Penetration depth

Penetration depth in the base plate for different line energies are presented in Table 6.1. From Table 6.1, it is found that full penetration is attained with line energy ranging between 53.98 to 90 J/mm irrespective of welding power and welding speed within selected range of process parameters. Moreover, from moderate welding speed of 800 mm/min (Exp. 2) to highest 1000 mm/min (Exp. 3) welding speed, full penetration is not observed at lowest beam power of 700 W as shown in the bead profiles in Figs. 6.3(b) and 6.3(a), respectively. However, full penetration is achieved at lower line energy of 47.99 J/mm (Exp. 6) at moderate beam power of 800 W as shown in Fig. 6.3(c). This observation indicates that power density is the main controlling parameter for penetration depth. It also contributes for achieving full penetration along with line energy. Similar trends are also observed while welding 2 mm thick plates of T-6Al-4V alloy as discussed in section 5.1.1.4 and also by Pakniat et al. (2016) during CW fiber LBW of 2 mm thick Hastelloy X plates.

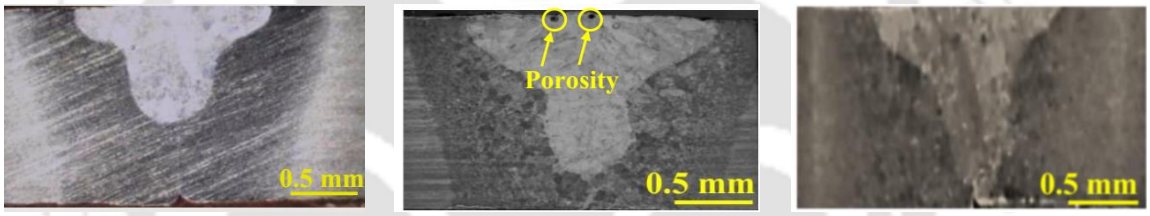

(a) (b) (c)

Fig. 6.3 Increase in penetration depth with increased line energy from (a) 41.99 J/mm (Exp. 3) to (b) 52.51 J/mm (Exp. 2) at 700 W beam power; (c) Full penetration at lower line energy of 47.99 J/mm (Exp. 6) with 800 W welding power

6.2.3 Width of FZ and HAZ size

Figures 6.4(a) and (b) show the variation in FZ width (i.e. FZ_{UP}, FZ_{Mid} and FZ_{Low}) and HAZ size (i.e. HAZ_{UP}, HAZ_{Mid} and HAZ_{Low}), respectively at different line energy. As observed in Fig. 6.4(a), FZ width continuously increases with increased line energy because of imposed higher energy on the work piece surface. In the present study, almost linear trend is observed between FZ_{UP} and line energy. These trends are in good agreement with the results discussed in section 5.2.1.3 for 2 mm thick Ti-6Al-4V plates. It is also observed from Fig. 6.4(a) that FZ_{UP} is larger than both FZ_{Mid} and FZ_{Low} for all specimens mentioned in Table 6.1. It is mainly due to the flow pattern of liquid metal which is prominent at the upper part of melt pool as compared to lower part, which produces gradually distinctive keyhole shape starting from bigger width at upper part to reduced width at the lower part of melt pool as explained in section 5.1.1.5. In Fig. 6.4(a), at 41.99 J/mm (Exp. 3) and 52.51 J/mm (Exp.

2) line energies, FZ_{Low} is zero due to partial penetration. It is also observed from Fig. 6.4(b) that the size of HAZ_{UP}, HAZ_{Mid} and HAZ_{Low} follows same trend with increasing of line energy similar to section 5.2.1.4 for 2 mm thick Ti-6Al-4V plates.

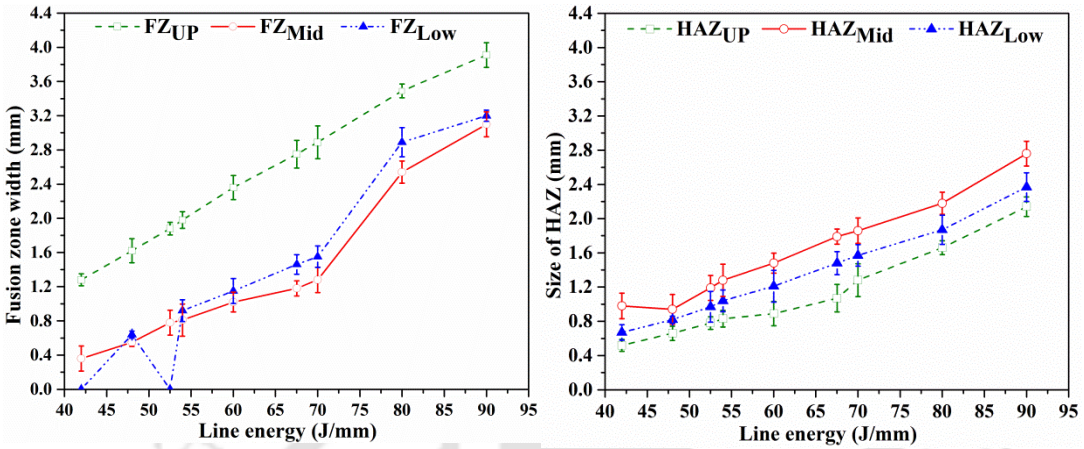

(a) (b)

Fig. 6.4 Effect of line energy on (a) width of FZ and (b) HAZ size

6.2.4 Microstructural analysis in HAZ

Figures 6.5(a) and (b) depict the optical and FESEM images, respectively of BM microstructure. It reveals that BM microstructure mainly comprises of inter-granular β and elongated α phases. The black and white areas in Fig. 6.5(b) represent elongated α and inter-granular β phases, respectively. The diameter of α and β grains are in the range of 6–10 µm and 2–5 µm, respectively as measured by line intercept method. The optical images of microstructures in the HAZ at various locations i.e. (a) close to FZ, (b) middle part of HAZ, (c) far away from FZ and (d) near BMZ are shown in Figs. 6.6(a-d) for Exp. 6. At these four locations inside HAZ different temperature gradients are developed across HAZ.

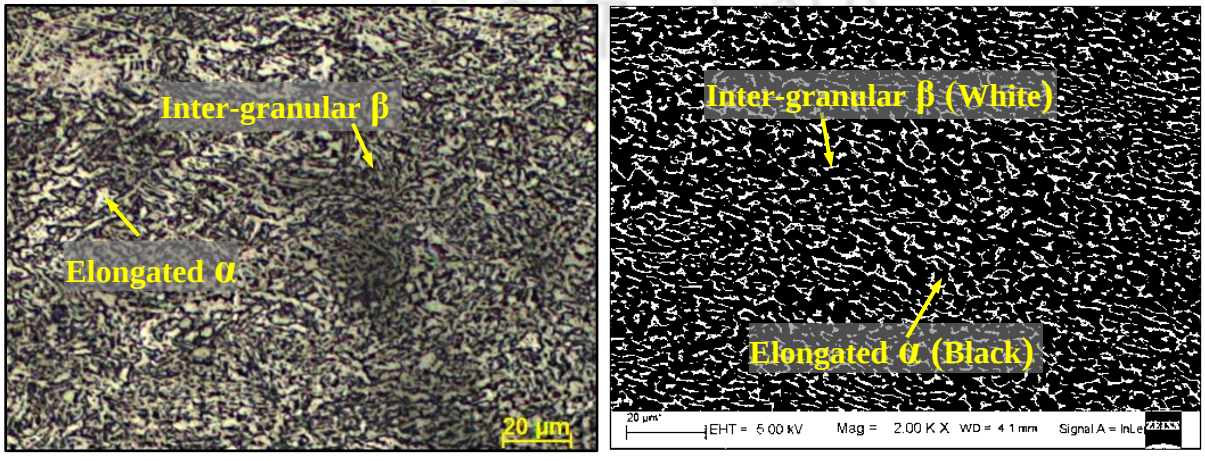

(a) (b)

Fig. 6.5 (a) Optical and (b) FESEM images of BM microstructure

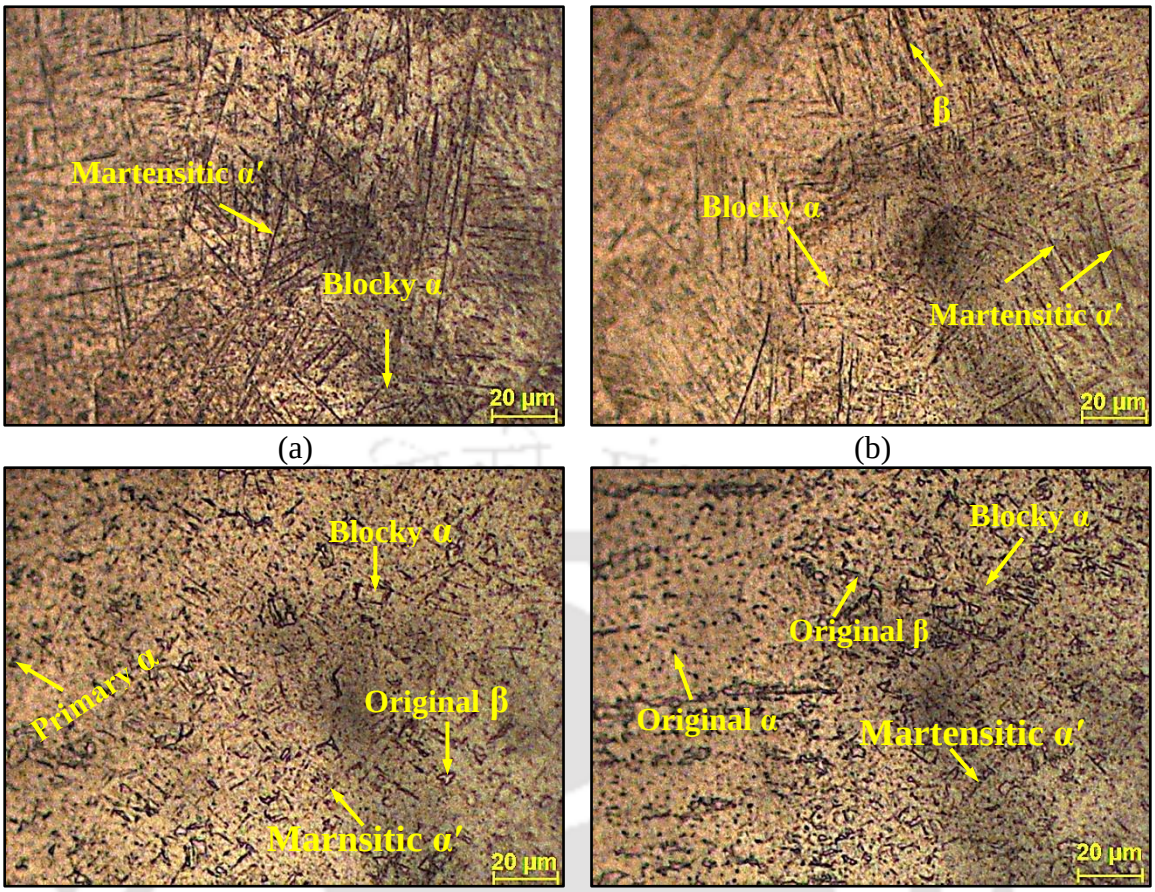

Fig. 6.6 Microstructures (optical image) at different locations in the HAZ; (a) close to FZ, (b) middle part of HAZ, (c) far away from FZ and (d) near BMZ

In the HAZ close to FZ, a mixture of α′ martensite and small amount of blocky α phases are observed as shown in optical micrographs in Fig. 6.6(a) and in FESEM image in Fig. 6.7(a). Due to the absence of original α and β phases, this region is termed as fully transformed HAZ. The middle part of HAZ comprises of combination of blocky α and primary β with small amount of martensitic α′ phase as observed in optical image in Fig. 6.6(b) and in FESEM image in Fig. 6.7(b). The region in the HAZ far away from the FZ comprises of blocky α, primary α and primary β phases with a lesser volume of α′ martensite as shown in optical image in Fig. 6.6(c) and FESEM image in Fig. 6.7(c). The microstructural features in the HAZ which is near to BMZ are totally different than near FZ and middle of HAZ as shown in the optical image in Fig. 6.6(d) and in FESEM image in Fig. 6.7(d). Due to the presence of original α and β phases along with very less amount of martensitic α′, this region is termed as partially transformed HAZ. Compared to partially transformed HAZ near BMZ, large amount of α′ martensite is observed in fully transformed HAZ i.e. close to FZ. The reasons behind the variation in HAZ microstructure are briefly discussed in section

5.1.2.1. Similar observations for 2 mm thick welded plates are discussed in section 5.1.2.1 which in turn affects the hardness distribution in the weld bead.

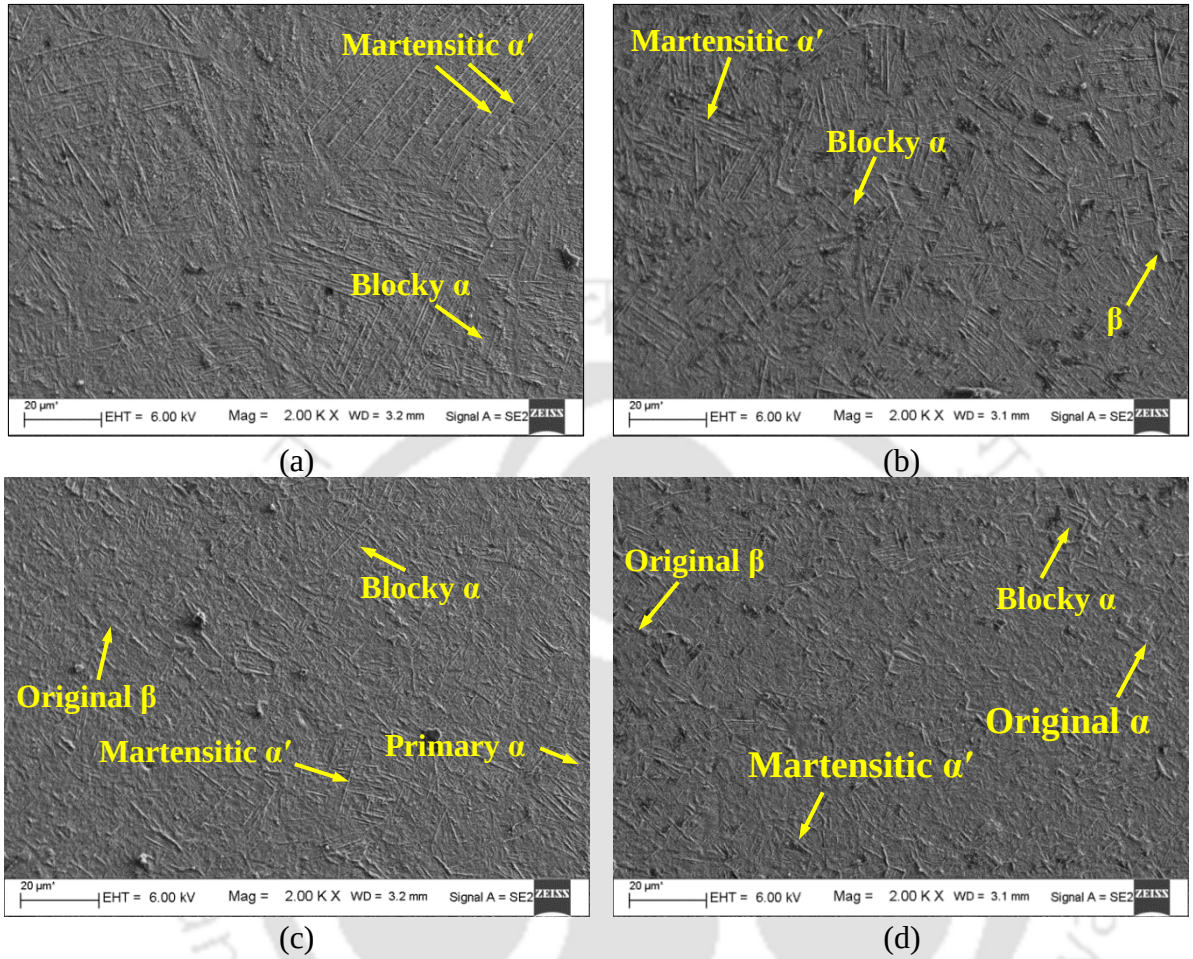

Fig. 6.7 FESEM images of the microstructures at different locations in the HAZ; (a) near FZ, (b) middle of HAZ, (c) far away from FZ and (d) near BMZ

6.2.5 Microstructural analysis in FZ

The change in microstructure in the FZ and HAZ depends on cooling rate and transformation kinetics of Ti-6Al-4V alloy. Different cooling rates prompt to the formation of distinct microstructural features as discussed in section 5.1.2. Also, the dependency of cooling rate on line energy is discussed and shown in Fig. 5.8(b). Also, the morphology of different phases formed in the FZ is explained briefly in section 5.1.2.

The FZ microstructure with decreasing line energies (LE) for fully penetrated welded samples are shown in optical micrographs in Figs. 6.8(a), (b), (c) and (d) for Exp. 4 (higher LE, 80 J/mm), Exp. 8 (intermediate LE, 67.52 J/mm), Exp. 5 (moderate LE, 60.01 J/mm) and Exp. 6 (lowest LE, 47.99 J/mm), respectively and their morphologies are shown in FESEM images in Fig. 6.9(a-d). Due to the differences in cooling rate associated with different line

energies in all these four samples, noticeable variations of the morphology of FZ microstructures are observed in Figs. 6.9(a-d)). The cooling rates in the FZ are calculated from Eq. (3.1) for 2 mm thick Ti-6Al-4V and are correlated with the FZ microstructures in section 5.1.2.2. Similarly, the cooling rates are also calculated for the present study for all the investigated samples and their calculated values go beyond critical cooling rate of 410 °C/s.

From Figs. 6.8, and Figs. 6.9, it is observed that in all four microstructural images original α, grain boundary α and blocky α phases are not found in the FZ. It indicates that the welding conditions for all these four samples reaches beyond critical cooling rate of 410 °C/s similar to calculated cooling rate as mentioned above which is required for fully martensitic transformation as per CCT curve shown in Fig. 5.8(a). The morphology of FZ microstructure at different line energies as shown in Figs. 6.9(a-d).

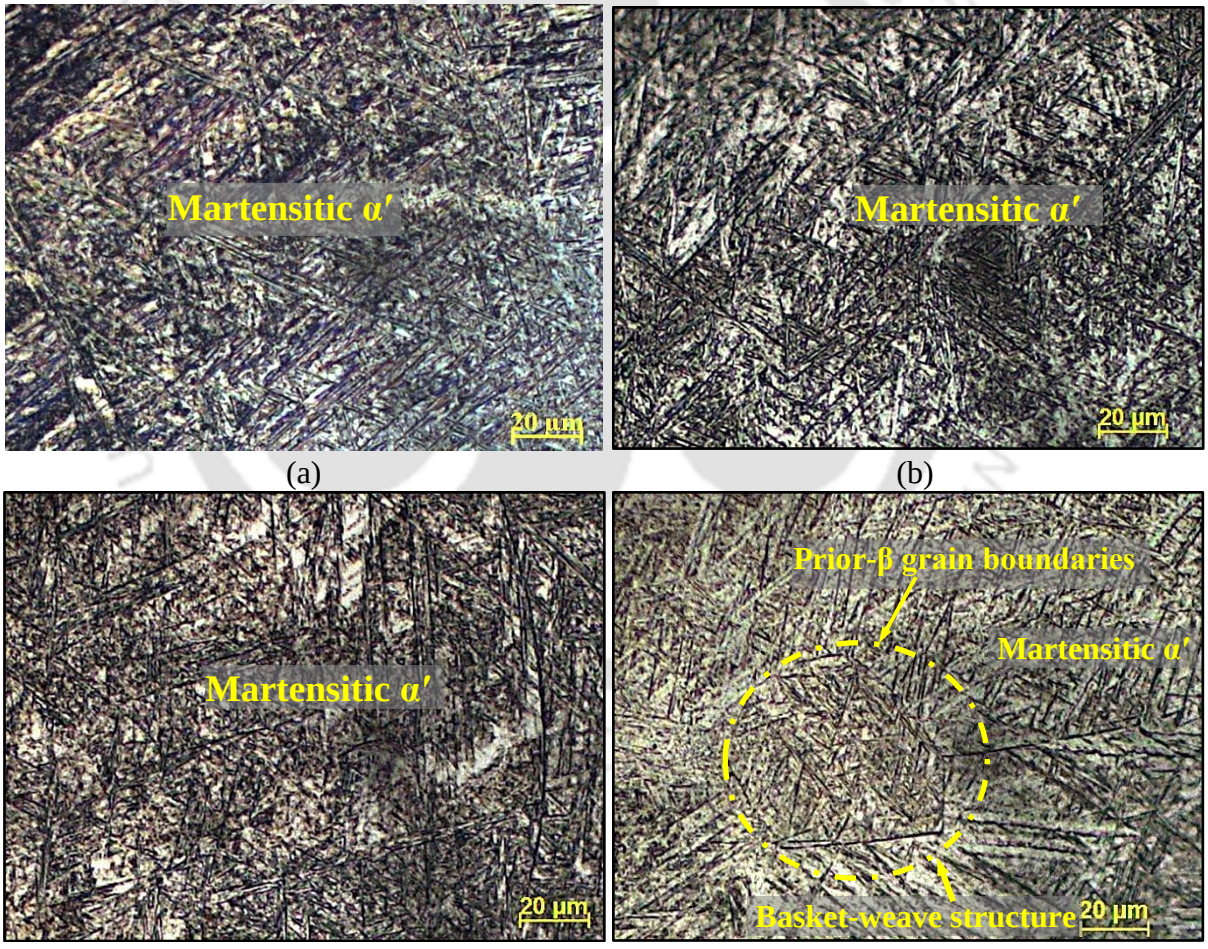

Fig. 6.8 Comparison of microstructures (optical image) in the FZ at different line energy for (a) Exp. 4 (80 J/mm), (b) Exp. 8 (67.52 J/mm), (c) Exp. 5 (60.01 J/mm) and (d) Exp. 6 (47.99 J/mm)

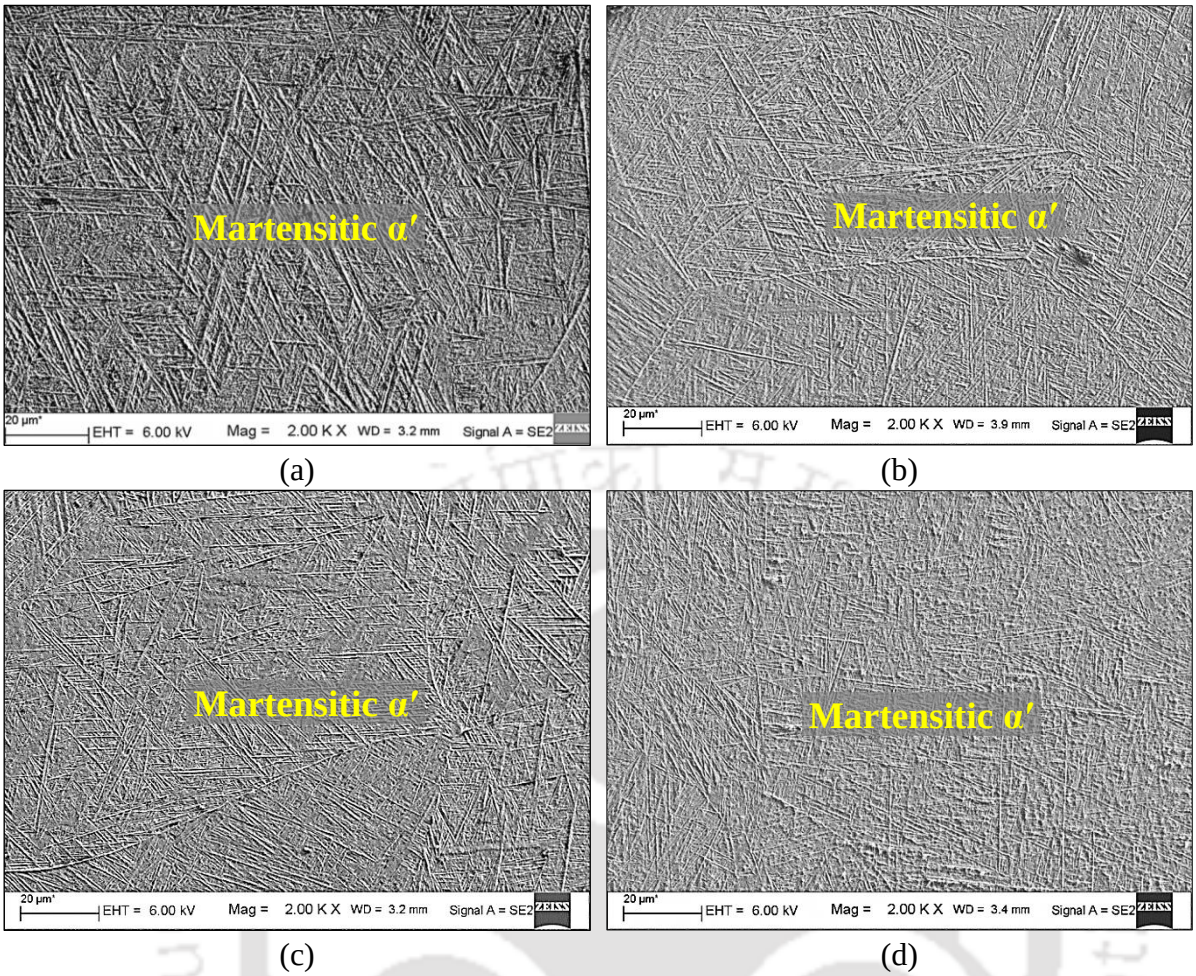

Fig. 6.9 Comparison of microstructures (FESEM image) in the FZ at different line energy for (a) Exp. 7 (80 J/mm), (b) Exp. 8 (67.52 J/mm), (c) Exp. 5 (60.01 J/mm) and (d) Exp. 6 (47.99 J/mm)

The fully α′ martensite having finer needle shaped morphology reveals the high self-quenching characteristics of LBW process. In Exp. 6, highest cooling rate occurs at lowest line energy (47.99 J/mm). Hence, at this cooling rate the nucleation of individual α plate also starts at the boundaries of α colony and it grows perpendicular to the nucleation site. As a result, a basketweave microstructure is formed within prior β grain boundaries as shown in OM image in Fig. 6.8(d) and in FESEM image in Fig. 6.9(d).

6.2.6 Weld defects

In the present study, most of the samples are defect free. However, in few samples small amount of underfill, excess penetration and porosity weld defects are observed. The underfill defects are found on the top side of fully penetrated welded specimens only at higher line energy of 90 J/mm (Exp. 7, unsuccessful weld due to excess penetration) and 80 J/mm (Exp. 4, Fig. 6.10(a)). It is mainly due to the evaporation of low boiling point element

from the specimen surface at higher line energy which causes depression that remains in the weld bead after solidification. Both underfill and excess penetration weld defects are not observed below 80 J/mm line energy in all welded specimens. Therefore, lower value of line energy is recommended to minimize excess penetration and underfill weld defects during LBW of Ti-6Al-4V alloy.

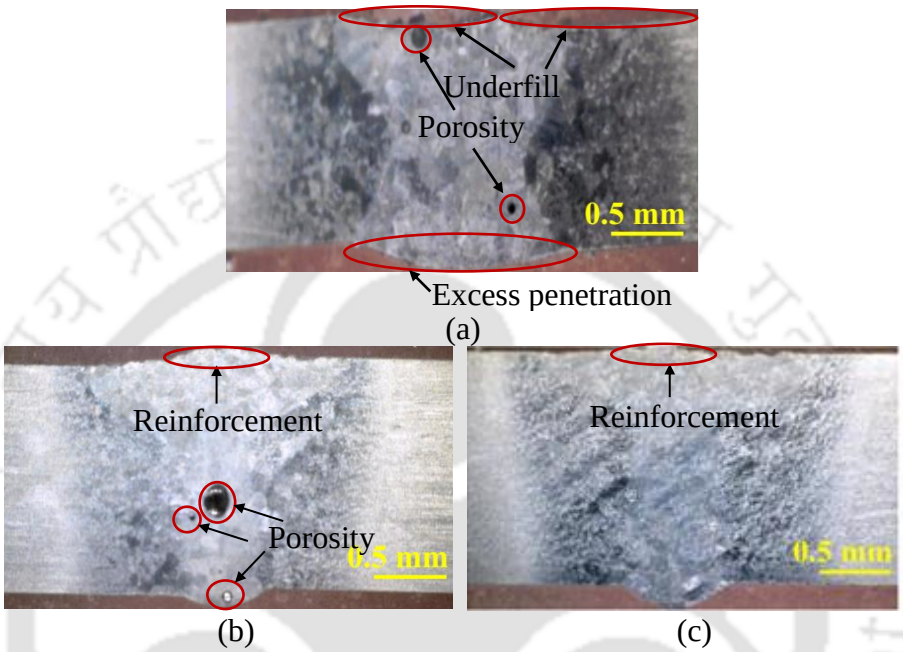

Fig. 6.10 (a) Underfill and excess penetration weld defects at higher line energy (80 J/mm) in Exp. 4; Reinforcement welding defects in weld bead at lower line energy for (b) Exp. 5 (60.01 J/mm) and (c) Exp. 8 (67.52 J/mm)

At lower line energy of 60.01 J/mm, Exp. 5 (Fig. 6.10(b)) and 67.52 J/mm, Exp. 8(Fig. 6.10(c)), a convex shape bead is formed at the top surface probably due to the collision of surface and ejected fluids inside melt pool. The flow of surface fluid is driven by thermal gradient and is induced by existing buoyancy force in the melt pool. The flow of ejected fluid occurs from bottom surface towards top along keyhole wall due to the recoil pressure. As a result, a collision between surface fluid and ejected fluid takes place and molten metal starts accumulating on the top surface forming convex shape weld bead. After solidification, it looks like reinforcement, similar to arc welding process.

6.2.6.1 Porosity

In the present investigation, porosity is observed in both partially penetrated and in few fully penetrated welded samples at different locations in the weld bead. Porosity is formed at the upper part of the FZ in partially penetrated samples (Exp. 2, Fig. 6.3(b) and in fully penetrated samples in Exp. 4, Fig. 6.10(a). It is mainly due to the entrapment of

hydrogen gas bubbles at this location since the absorbed hydrogen can only escape from the top side of bead in case of partial penetration. Porosity is also formed near centre line and at the lower half of the weld bead in Exp. 5 (Fig. 6.10(b)) probably due to the collapsing and instability of the keyhole (known as characteristic pores) inside melt pool at moderate welding power of 800 W and moderate welding speed of 800 mm/min. There is a difference in diameter between upper and lower portions of the keyhole with a smaller diameter at the root. Due to which, higher surface tension and internal static pressure are developed at the root. Hence, higher vapor pressure is developed at the root as compared to the mouth of the keyhole to maintain equilibrium. As a result, the keyhole becomes unstable which enhances the propensity of the pore formation in the FZ. The combination of higher welding power of 900 W and moderate welding speed (800 mm/min) and beyond it, porosity free weld bead is formed (Exp. 8, Fig. 6.10(c)). At higher beam power, the keyhole has larger opening and the large sized melt pool maintains the keyhole opening for longer duration of time. Hence, the pores get sufficient time to escape out of the weld bead. The morphology of the gas type porosities is shown in FESEM image in Fig. 6.11(a) whereas the morphology of characteristics pores is shown in Fig. 6.11(b).

In case of gas type porosity, the pores are round and smooth as shown in Fig. 6.11(a). Whereas, the characteristic pores in Fig. 6.11(b) are extremely irregular in shape with rough inner wall. However, the sizes of micro pores in all samples are below 0.40 mm. It satisfies the acceptance criteria (pore size ≤ 0.40 mm) of weld quality as per BS EN: 4678 (2011) standard. Bigger sized pores are not found in any welded samples. It is probably due to the presence of high intensity buoyancy force which helps to escape out the pores efficiently from the melt pool.

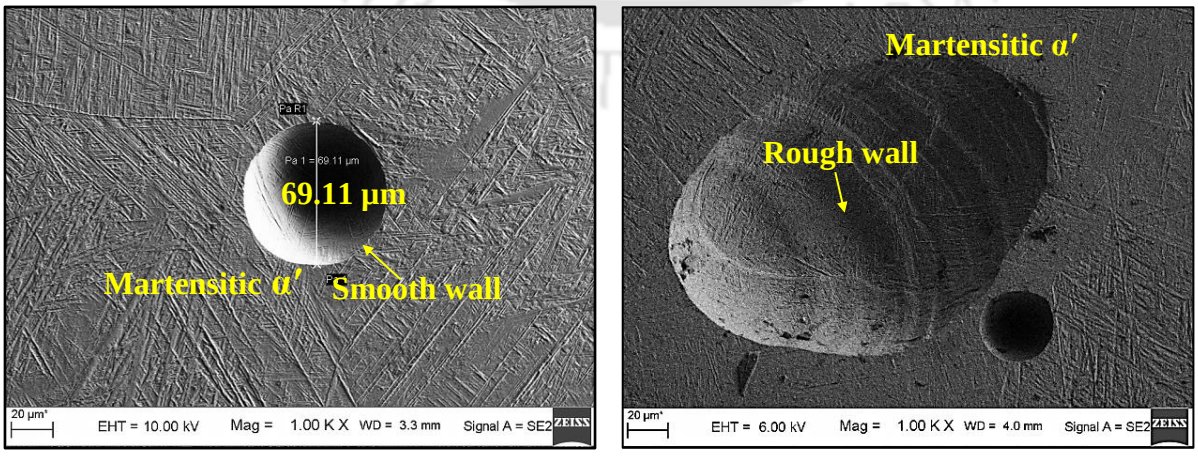

(a) (b)

Fig. 6.11 Morphology of pores at different locations (a) at the upper half of FZ for Exp. 2 and (b) near center line of FZ for Exp. 5

6.2.7 Mechanical properties

6.2.7.1 Hardness

The microhardness distribution curves at upper and middle portions of bead cross section across transverse direction on both sides of the weld line for Exp. 6 are presented in Fig. 6.12(a). Lowest hardness value of 320±10 HV is observed in BMZ. The hardness value continuously increases in the HAZ from near BMZ to near FZ. Later, the hardness value reaches to its maximum value of 424.84 ± 10 HV in the FZ due to the existence of harder α′ martensitic phase. In BMZ, there is no trace of α′ martensitic phase as observed in Fig. 6.5(a). However, within HAZ, the amount of α′ martensitic phase increases continuously from near BMZ (Fig. 6.7(d)) to near FZ (Fig. 6.7(a)). In the FZ, both α and β phases are converted into α′ martensitic phase. Hence, the amount of harder α′ martensitic phase increases from approximately zero percent in near BMZ (Fig. 6.7(d)) to almost 100 percent in FZ (Fig. 6.8). Subsequently, microhardness also decreases on both sides of weld bead centre line as observed in Fig. 6.12(a).

From Fig. 6.12(a), it can be seen that hardness at the top portion of the weld bead is higher than middle portion due to faster cooling of top portion as discussed in section 5.1.3. Further, the average hardness values in the FZ are compared in Fig. 6.12(b) with increasing line energy for four fully penetrated welded samples (Exps. 6, 5, 8 and 4). The highest and lowest average hardness in the FZ are observed at minimum and maximum line energy of 47.99 J/mm (Exp. 6) and 80 J/mm (Exp. 4), respectively.

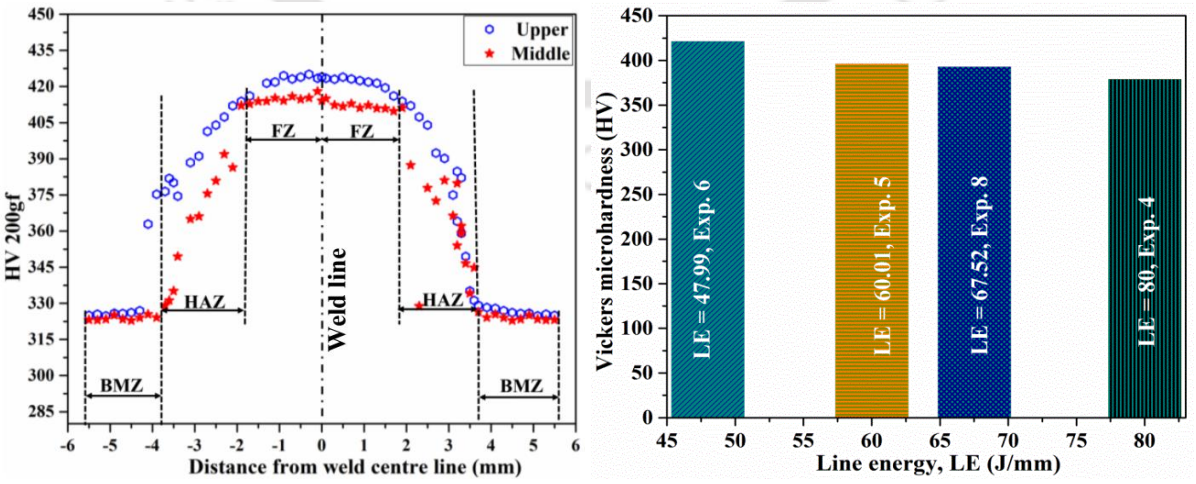

(a) (b)

Fig. 6.12 (a) Hardness distribution curve along transverse direction to the weld line for Exp. 6 at different portions of bead cross-section and (b) effect of LE on average hardness in FZ

It is mainly due to decreased cooling rate with increasing line energy which enhances the development of finer (Fig. 6.8(d) and Fig. 6.9(d) at 47.99 J/mm LE) to coarser α′ martensitic lamella (Fig. 6.8(a) and Fig. 6.9(a) at 80 J/mm LE). The finer α′ lamella is harder and brittle in nature. Therefore, highest hardness is observed at lowest LE of 47.99 J/mm. Hence, the hardness values change in the FZ depending on the microstructural variations in the FZ at different LE. Therefore, moderate line energy is recommended to minimize bead hardening.

6.2.7.2 Tensile properties and fractography

The tensile test results of BM and three welded specimens (Exps. 4, 8 and 6 with decreasing line energy) are provided in Table 6.2. It is observed that the tensile strength for Exps. 6 and 8 are comparable to the BM with reduced ductility. It is primarily due to the presence of finer lamella of martensitic α′ for samples in Exp. 6 (47.99 J/mm) and Exp. 8 (67.52 J/mm) at low line energy and also due to strengthening effect of α′ martensite in both FZ and HAZ. These samples are free from underfill and excess penetration weld defects. However, the tensile strength of Exp. 4 is lower than BM. It is probably due to underfill weld defects in sample of Exp. 4 and also due to the presence of micro pores in FZ as observed in Fig. 6.10(a). The porosity and underfill area act as a stress concentrator which enhances the chances of crack initiation site. From Table 6.2, it is also observed that the tensile strength increases with decreased line energy for Exp. 4 (LE = 80 J/mm), Exp. 8 (LE = 67.52 J/mm) and Exp. 6 (LE = 47.99 J/mm) although the measured percentage elongations are lower than BM. It is mostly due to the formation of coarser to finer α′ lamella of martensitic phase in the FZ as explained in section 6.2.5.

Table 6.2 Tensile properties of BM and few welded specimens

Exp. No.	YS* (MPa)	Avg. YS (MPa)	UTS (MPa)	Avg. UTS (MPa)	% elongation	Avg. % elongation	Fracture position
Base metal	892	886	972	962	15.30	14.55	BMZ
	877		964		12.25		
	889		952		16.12		
4	854	843	887	882	8.76	8.28	FZ
	836		878		8.20		
	841		881		7.88		
8	894	891	954	957	10.12	10.56	HAZ
	892		961		11.72		
	889		956		9.84		
6	906	903	974	971	10.42	10.30	HAZ/BMZ
	909		966		10.38		
	894		973		10.22		

**YS–Yield strength, UTS– Ultimate tensile strength*

The fracture surface morphologies of BM and few welded specimens are presented in Fig. 6.13. From Fig. 6.13(a), it is found that almost equi-axed dimples are uniformly distributed over entire fracture surface of BM. It indicates the characteristics of higher ductility and ductile mode of failure of BM. The fracture surface morphologies of fully penetrated welded specimens of Exps. 4, 8 and 6 are presented in Figs. 6.13(b), (c) and (d), respectively with decreased line energy. Micro voids are observed in fractured area for all three welded specimens. It is also observed that in tensile test non-uniform, shallow dimples and few tearing ridges appear in fracture area as show in Figs. 6.13(b), (c) and (d) for above three welded samples. The dimples observed in the fracture area of FZ and HAZ (Figs. 6.13(b), (c) and (d)) differ in size. However, equiaxed and uniform sized dimples are observed in BM (Fig. 6.13(a)). The shallow dimples and tear ridges found in fractured area signify the characteristics of ductile mode of failure of the investigated welded samples.

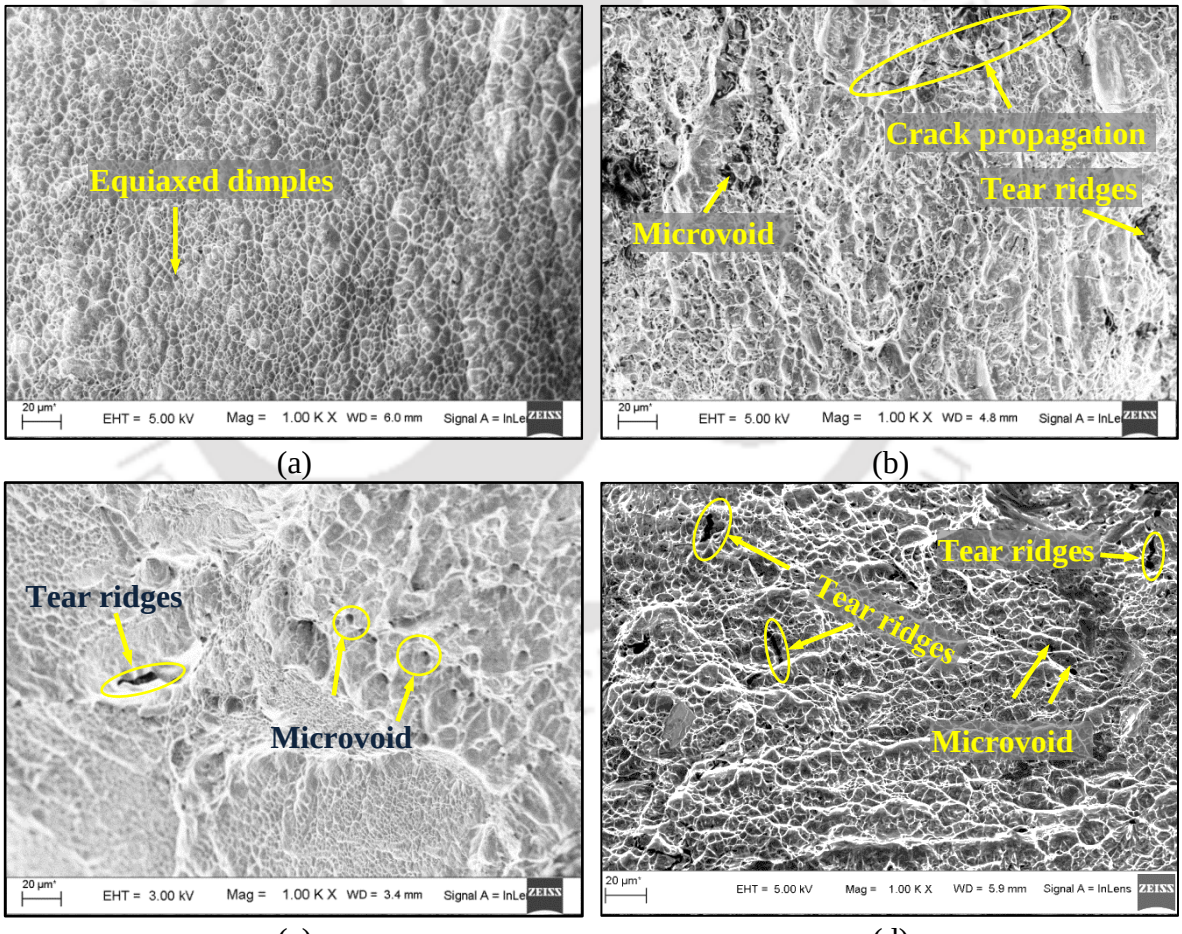

Fig. 6.13 FESEM micrographs of the fractured surface of (a) BM, (b) Exp. 4, LE = 80 J/mm, (c) Exp. 8, LE = 67.52 J/mm and (d) Exp. 6, LE = 47.99 J/mm

6.3 Comparative study between different thicknesses of Ti-6Al-4V alloy plates

In the present study, three different thickness of Ti-6Al-4V alloy are welded by using 2 kW fiber laser at various welding conditions. There are significant differences in the weldments are observed. Microstructure of the BM consists of equi-axed α with inter-granular β (Figure 4.4). The dark regions are inter-granular β and bright regions are equi-axed α. This microstructure is a typical mill-annealed structure of Ti-6Al-4V alloy in all of three different thicknesses of Ti-6Al-4V alloy plates. However, the size of α and intergranular β is varied in the BM. It may be due to different annealing conditions adopted during heat treatment of BM by the manufacturer. The specially designed workpiece fixture with shielding gas delivery system is suitable for holding the workpiece materials and efficiently protects the melt pool from environmental contamination for all different thickness of the workpieces. EDS analysis and bead appearance confirms the effective of shielding gas for all cases. This ascertains the robustness of the present laser welding technique for Ti-6Al-4V alloy.

Experimentally, it is observed that the total heat input per unit length (line energy) for achieving full penetration in the base plate for 5 mm thick Ti-6Al-4V alloy is higher than the heat input required for full penetration in 2 mm and 1.5 mm thick plates. Hence, the size of FZ, FZ area and HAZ sizes are comparatively smaller in case of 2 mm and 1.5 mm than 5 mm thick plates. For achieving deep penetration and smaller grain size in FZ the defocussed position of laser beam should be kept below from the workpiece surface in case of 5 mm thick plates. Moreover, it is not essential for lower thickness of 2 and 1.5 mm thick plates. For higher range of welding power and lower range of welding speed the line energy is the main controlling process parameters for penetration depth whereas for lower range of beam power and moderate welding speed the power density is the main controlling parameters for penetration depth in the base plate. However, FZ width and size of heat affected zone is mostly controlled by line energy for all of different thickness of Ti-6Al-4V alloy.

From microstructural analysis it is observed that the at lower line energy (cooling rate beyond 400°C/s) the fully α′ martensitic structure is formed in the FZ for all cases. However, more refined α′ martensitic needle is observed in lower thickness i.e. 1.5 mm thick Ti-6Al-4V plates. The similar type of variation in amount of α′ martensite is observed in all three different thick Ti-6Al-4V alloy plates i.e. varied from its maximum amount in FZ to approximately zero in BMZ. Also, the similar type of variation in Vickers microhardness is

observed from its maximum value in FZ to its minimum value in BMZ for all 5 mm, 2 mm and 1.5 mm thick plates. The tensile strength is increased with decreasing of line energy for all the cases. However, the maximum tensile strength is observed for 1.5 mm thick plates due the faster cooling rates of melt pool which is also enhanced with lower thickness of material. The % elongation of weldments is reduced for all the cases. In lower range of welding speed and welding power which is employed in 1.5 mm and 2 mm thick plates the both the gas type porosity and characteristic pores are formed in the FZ. However, characteristic pores are not found in higher thickness of 5 mm thick plates due to the formation of stable keyhole inside melt pool. From the comparative analysis it is observed that the T-shaped welding condition is favorable for achieving smaller sizes of FZ, HAZ and FZ area.

6.4 Conclusions

In the current study, fiber laser welding experiments are successfully conducted on 1.5 mm thick Ti-6Al-4V plates at different welding conditions. The proposed method of welding is very effective for improving weld quality of Ti-6Al-4V alloy. The key findings are summarized below:

- The specially designed shielding gas delivery system with workpiece fixture efficiently protects the weld bead from environmental contamination as per EDS analysis and bead appearance study.
- Penetration depth is primarily controlled by power density. However, FZ width and HAZ size depends on line energy.
- The martensitic α′ and blocky α phases are observed at the boundary between FZ and HAZ. However, the needle shaped fully martensitic α′ phase is observed in FZ. It is responsible for the increase in hardness in FZ and HAZ and also for the tensile strength of welded specimens.
- The most of the welded specimens are defect free. However, few welding defects like underfill and porosities are found in some specimens although size of micro pores are within acceptable range.
- The tensile strength of welded specimens is increased with decreasing line energy due to the formation of coarser to finer lamella of α′martensite with decreasing line energy.
- The elongation of the welded specimens is lower than the base metal owing to the presence of micro pores in the weld bead and brittle nature of α′ martensite in fusion zone.

- At beam power of 900 W, there is a critical range of welding speed from 800 to 1000 mm/min which produces deep penetration in keyhole mode, narrower weld width and small heat affected zone having high weld quality and acceptable mechanical properties.

Chapter 7
Weldability of 3 mm thick plates of austenitic stainless steel of grade 316L

7.0 Introduction

In the present study, autogenous fiber laser beam welding of 3 mm thick austenitic stainless steel of grade 316L in butt configuration is conducted at various welding conditions to find out their effect on bead features such as, fusion zone (FZ) width, fusion zone area (FZ_{area}) and ultimate tensile strength (UTS) of welded specimens. Statistical design of experiments based on RSM technique is carried to achieve satisfactory weld joint. Analysis of variance (ANOVA) is carried out to identify individual and combined parametric effect and their percentage contribution on output responses. The influence of each parameters and their interaction effect are studied regression analysis. Further an optimization study is carried out to find out optimum value of the process parameters. The variation in tensile strength of weldments at different experimental conditions and Vickers microhardness at different cross section of weld bead are studied. To characterize the quality of weld bead, microstructural analysis in the FZ are carried out using FESEM as well as optical microscopy. After that their morphologies are compared at different welding conditions. Further, fractured surfaces are analyzed using FESEM images to confirm the mode of fracture failure.

7.1 Design of experiments (DOE)

Central composite rotatable design (CCRD) methodology of RSM is employed to investigate the influence of input parameters on output responses within their investigated range. The range of input process parameters i.e. welding power (P), welding speed (V) and defocused position (d) are given in Table 7.1. The experimental design matrix and their measured responses along with bead observations are given in Table 7.2. It is to be noted that no weld solidification cracking is observed in any of the welds.

Table 7.1 Welding parameters and their range

Parameters	Unit	Levels		
		-1	**0**	**1**
Power (P)	Watt	1500	1650	1800
Speed (V)	mm/min	400	300	1200
Defocused position (d)	mm	-1*	0	+1

** + and - means focal position kept above and below workpiece surface*

Table 7.2 Design matrix, output responses and bead observations

Exp. No.	Input variables			Output responses			Observations
	P (W)	V (mm/min)	d (mm)	FZ (mm)	FZ_{area} (mm^2)	UTS (MPa)	
1	1500	400	-1	2.88	4.45	513.82	FP*, Porosity
2	1800	400	-1	3.42	5.92	526.23	FP, Underfill
3	1500	1200	-1	1.24	1.83	498.08	PP
4	1800	1200	-1	1.58	2.46	518.42	DP > 80%
5	1500	400	+1	1.72	3.84	437.82	FP, Porosity
6	1800	400	+1	2.18	4.89	455.55	FP, Dropout
7	1500	1200	+1	0.94	1.54	378.635	PP
8	1800	1200	+1	1.18	2.12	425.846	DP > 80%
9	1500	800	0	1.38	2.24	504.93	DP > 80%
10	1800	800	0	1.86	3.42	541.04	FP, SW
11	1650	400	0	2.46	4.52	521.14	Dropout
12	1650	1200	0	1.22	2.14	505.78	DP > 80%
13	1650	800	-1	2.01	3.27	572.24	FP, SW
14	1650	800	+1	1.33	2.36	481.69	DP > 80%
15	1650	800	0	1.56	2.56	552.79	FP, SW
16	1650	800	0	1.49	2.42	555.62	FP, SW
17	1650	800	0	1.51	2.49	558.73	FP, SW
18	1650	800	0	1.54	2.62	548.61	FP, SW
19	1650	800	0	1.47	2.47	551.69	FP, SW
20	1650	800	0	1.44	2.76	541.6	FP, SW

**SW- Successful weld, DP- penetration depth, FP/PP - full/partial penetration*

7.2 Analysis of variance

ANOVA tables for width of FZ, FZ_{area} and ultimate tensile strength (UTS) along with % contribution (F/ΣF) of each parameter and their interaction terms are presented in Table 7.3, Table 7.4 and Table 7.5, respectively for 95% confidence level. It is found from Tables 7.3 to 7.5 that welding speed has highest contribution on FZ width (63.40%) and FZ_{area} (79.13 %). Whereas, defocused position of laser beam is most significant parameter with contribution of 65.56 % on UTS of weldments. However, FZ_{area} is least affected by the defocused position. Quadratic model of regression equations is given in Eqs. (7.1), (7.2) and (7.3) for width of FZ, FZ_{area} and UTS, respectively.

Table 7.3 ANOVA for FZ width

Source	Sum of Squares	DOF	Mean Square	F-Value	p- value	% Contribution
Model	7.02	9	0.78	183.04	< **0.0001***	
P	0.42	1	0.42	99.59	< **0.0001***	6.37
V	4.23	1	4.23	991.53	< **0.0001***	63.40
d	1.43	1	1.43	335.32	< **0.0001***	21.44
PV	0.022	1	0.022	5.17	**0.0462***	0.33
Pd	4.05×10^{-3}	1	4.05×10^{-3}	0.95	0.3526**	0.06
Vd	0.36	1	0.36	84.78	< **0.0001***	5.42
P^2	3.028×10^{-3}	1	3.028×10^{-3}	0.71	0.4190**	0.05
V^2	0.18	1	0.18	41.37	< **0.0001***	2.65
d^2	0.019	1	0.019	4.47	**0.**0607**	0.29
Lack of Fit	0.033	5	6.546×10^{-3}	3.31	0.1074**	

**Significant,* ***Non-significant,* $R^2 = 0.99$

$$FZ\ width = 4.44 - 2.79\times10^{-3}P - 2.71\times10^{-3}V - 0.56d - 8.75\times10^{-7}PV - 1.50\times10^{-4}Pd + 5.31\times10^{-4}Vd + 1.47\times10^{-6}P^2 + 1.58\times10^{-6}V^2 + 0.083d^2 \quad (7.1)$$

Table 7.4 ANOVA for fusion zone area (FZ_{area})

Source	Sum of Squares	DOF	Mean Square	F-Value	p- value	% contribution
Model	24.69	9	3.47	82.04	< **0.0001***	
P	2.41	1	2.41	72.09	< **0.0001***	10.42
V	18.31	1	18.31	547.40	< **0.0001***	79.13
d	1.01	1	1.01	30.24	**0.0003***	4.37
PV	0.21	1	0.21	6.41	**0.0297***	0.93
Pd	0.028	1	0.028	0.83	0.3849**	0.12
Vd	0.13	1	0.13	3.81	0.0794**	0.55
P^2	0.027	1	0.027	0.81	0.3879**	0.12
V^2	0.99	1	0.99	29.56	**0.0003***	4.27
d^2	0.020	1	0.020	0.59	0.4610**	0.09
Lack of Fit	0.26	5	0.052	3.40	0.1025**	

**Significant,* ***Non-significant,* $R^2 = 0.99$

$$FZ_{area} = 10.77 - 9.14\times10^{-3}P - 4.87\times10^{-3}V + 0.08d - 2.73\times10^{-6}PV - 3.92\times10^{-4}Pd + 3.16\times10^{-4}Vd + 4.42\times10^{-6}P^2 + 3.75\times10^{-6}V^2 + 0.08d^2 \quad (7.2)$$

Table 7.5 ANOVA for ultimate tensile strength (UTS)

Source	Sum of Squares	DOF	Mean Square	F-Value	p- value	% contribution
Model	48930.24	9	5436.69	139.43	< **0.0001***	
P	1790.27	1	1790.27	45.91	< **0.0001***	5.82
V	1633.26	1	1633.26	41.89	< **0.0001***	5.31
d	20182.47	1	20182.47	517.60	< **0.0001***	65.56
PV	174.95	1	174.95	4.49	0.0602**	0.57
Pd	129.53	1	129.53	3.32	0.0984**	0.42
Vd	533.65	1	533.65	13.69	**0.0041***	1.73
P^2	1758.03	1	1758.03	45.09	< **0.0001***	5.71
V^2	3332.09	1	3332.09	85.46	< **0.0001***	10.83
d^2	1248.12	1	1248.12	32.01	**0.0002***	4.05
Lack of Fit	212.61	5	42.52	1.20	0.4235**	

**Significant,* ***Non-significant,* $R^2 = 0.99$

$$UTS = -2667.14 + 3.73P + 0.19V - 72.85d + 7.79\times10^{-5}PV + 0.03Pd - 0.02Vd - 1.12\times10^{-3}P^2 - 2.18\times10^{-4}V^2 - 21.30d^2 \quad (7.3)$$

7.3 Confirmation tests

To verify the developed models, confirmation tests are performed arbitrarily at different welding conditions within the range of process parameters as given in Table 7.6. The output responses are measured experimentally from three repeated confirmation tests and an average is considered. The estimated responses are obtained from regression models (Eqs. (7.1–7.3)). After that, the percentage error between the measured and estimated responses is compared. From Table 7.6, it is observed that there is a reasonable agreement between the experimentally measured and estimated responses having error below 5% at all three experimental conditions.

Table 7.6 Confirmation tests and comparison between experimentally measured and predicted responses

Exp. No.	Process parameters				Responses		
	P (W)	V (mm/min)	d (mm)	Results from	FZ (mm)	FZ_{area} (mm^2)	UTS (MPa)
1	1650	650	-1	Measured	2.42	3.72	577.25
				Regression Eq.	2.36	3.67	570.66
				Error (%)	**2.48**	**1.34**	**1.14**
2	1700	700	0	Measured	1.87	3.27	558.25
				Regression Eq.	1.80	3.19	552.48
				Error (%)	**3.74**	**2.45**	**1.03**
3	1750	800	+1	Measured	1.42	2.78	491.87
				Regression Eq.	1.38	2.72	484.34
				Error (%)	**2.82**	**2.16**	**1.53**

7.4 Optimization study

The desirability function technique developed by Derringer and Suich (1980) is used in the present study to optimize the process parameters for yielding high quality of weldments in terms of narrow FZ width, minimal FZ_{area} and higher UTS. The criteria for numerical optimization are given in Table 7.7. The optimum values of the process parameters based on highest desirability of the solutions are shown in Table 7.8. A final experiment is conducted at optimum parameter condition. In Table 7.8, the values of FZ width, FZ_{area} and UTS are experimentally measured and predicted from regression equations (Eqs. (7.1–7.3)). Figure 7.1 shows the optical image of the weld bead macrograph at optimum welding condition.

Table 7.7 Criteria for optimization study

Parameters	Goal
P (W)	In the range
V (mm/min)	In the range
d (mm)	In the range
FZ width (mm)	Minimize
FZ area (mm^2)	Minimize
UTS (MPa)	Maximize

Table 7.8 Optimal combinations of process parameters and predicted/measured responses

Exp. No.	Process parameters			Responses				
	P (W)	V (mm/min)	d (mm)	Results from	FZ (mm)	FZ_{area} (mm^2)	UTS (MPa)	Desirability
1	1610	1050	-0.4	Regression Eq.	1.29	2.02	540.16	0.86
				Measured	1.32	2.08	547.28	

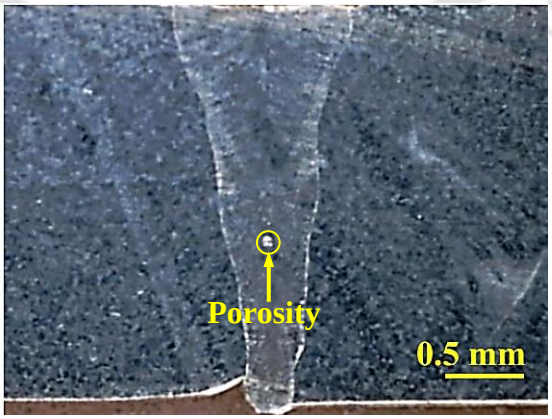

Fig. 7.1 Weld bead at optimal welding condition as given in Table 7.8

7.5 Results and discussion

The influence of individual and combined effect of welding process parameters on FZ width, FZ_{area} and ultimate tensile strength (UTS) of weldments are briefly discussed based on results obtained from regression equations (Eqs. (7.1–7.3)) within the selected range of process parameters.

7.5.1 Fusion zone width and area

In the following sections the effect welding speed (V), welding power (P) and defocused position of laser beam (d) on FZ width and FZ_{area} are discussed in details.

7.5.1.2 Effect of beam power and welding speed

Figure 7.2(a) shows the effect of beam power on FZ width at different welding speed and constant defocused position (d = 0 mm). From Fig. 7.2(a), it is observed that FZ width increases with increasing beam power almost linearly irrespective of welding speed. It is mainly due to the effect of line energy (LE) as discussed in Eq. (4.2). LE increases with increasing beam power or decreasing welding speed as defined in Eq. (4.2). However, the slope of each curve in Fig. 7.2(a) primarily depends on welding speed. Figure 7.2(b) shows the effect of welding speed on FZ width at various beam power and constant defocused position (d = 0 mm). Highest influence of welding speed on FZ width (63.40% contribution, Table 7.5) is observed as it affects both dimension and shape of the weld bead. The progressive decrease of FZ width in Fig. 7.2(b) with increased welding speed might be elucidated with the support of LE and interaction time. The interaction time of laser beam with workpiece material decreases with increased welding speed as interaction time is inversely proportional to the welding speed as per Eq. (4.6). Therefore, heat energy is exposed to the workpiece material for short period of time. Hence, lesser amount of BM melts down which yields narrower FZ width. The 3D plot in Fig. 7.2(c) shows combined effect of beam power and welding speed on FZ width where higher influence of welding speed than beam power is observed. Figure 7.3(a) shows the effect of beam power on FZ area (FZ_{area}) at different welding speed. The combined effect of beam power and welding speed on FZ_{area} is shown in 3D surface plot in Fig. 7.3(b).

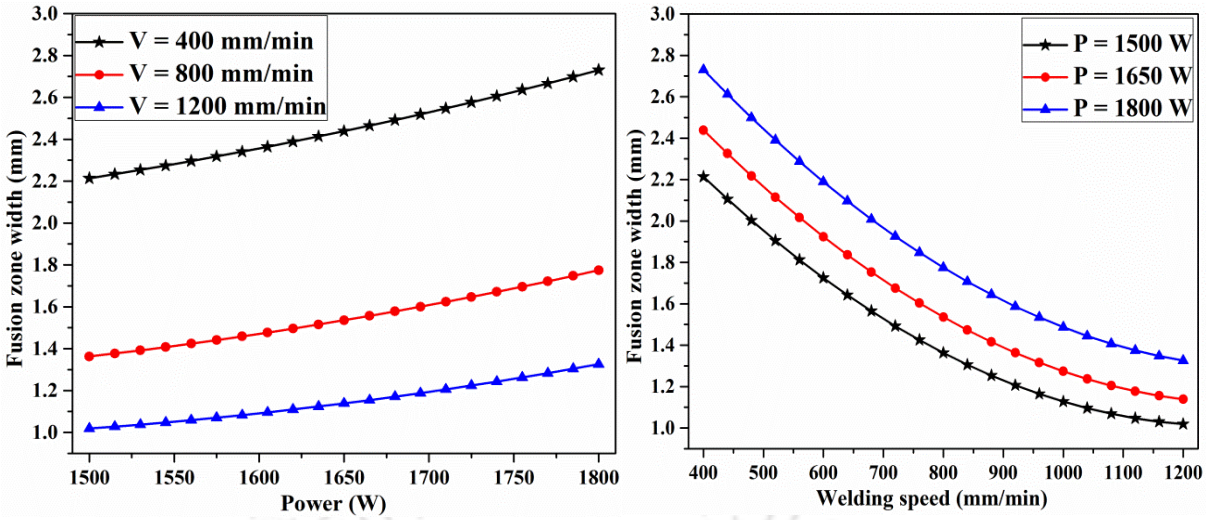

(a) (b)

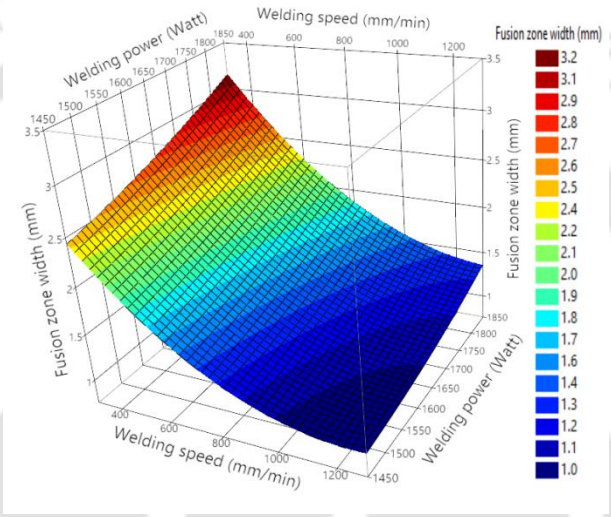

(c)

Fig. 7.2 (a) Effect of welding power on the FZ width at different welding speed, (b) variation of FZ width with respect to welding speed at different beam power and (c) 3D surface plot showing combined effect of beam power and welding speed on FZ width

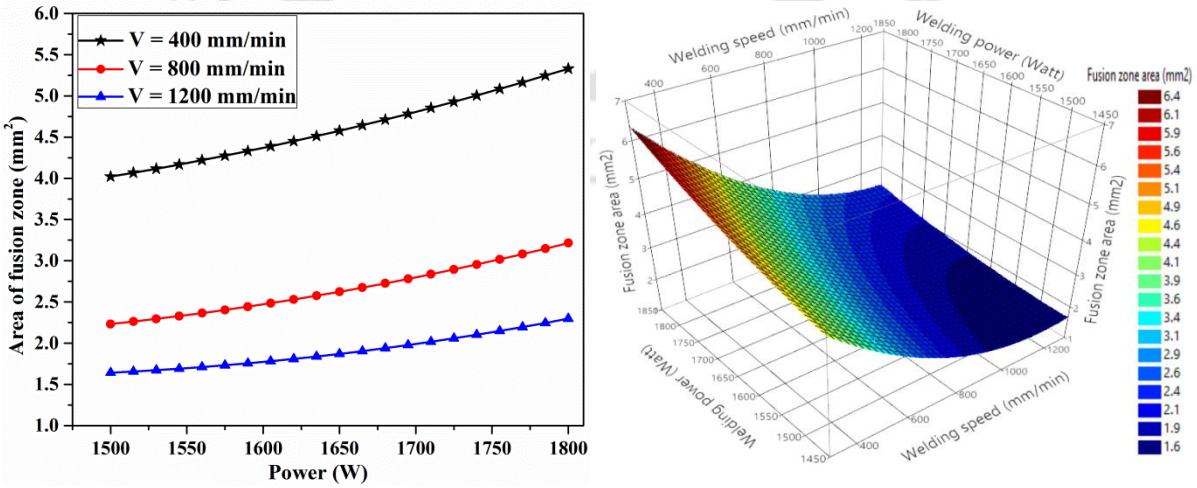

(a) (b)

Fig. 7.3 (a) Effect of welding power on FZ area (FZ_{area}) at different welding speed and (b) 3D surface plot presenting combined effect of welding speed and beam power on FZ_{area}

7.5.1.3 Effect of defocused position

Energy density primarily depends on both beam power and laser beam spot area as defined in Eq. (4.1). The diameter of the laser beam spot varies by changing defocused position (Kuryntsev and Gilmutdinov, 2015). Beam spot diameter progressively increases by changing defocused position either along the top or bottom direction with reference to workpiece surface. Figure 7.4(a) shows the effect of defocused position on FZ width at different welding speed. The 3D surface plot in Fig. 7.4(b) shows combined effect of beam power and defocused position on FZ width. From Figs. 7.4(a) and (b) it is found that maximum FZ width is achieved at -1 mm defocused position (i.e. 1 mm below workpiece surface). Further changing defocused position from -1 mm to 0 mm, FZ width continuously decreases. It is most likely due to multiple reflections of laser beam with keyhole wall as discussed in section 4.3.1.2. By keeping down defocused position below from workpiece surface i.e. from 0 to -1 mm laser beam converges gradually to the focal point enforcing higher energy density to the focal point as compared to the workpiece surface. It helps to transmit the beam energy into larger depth. Thus penetration depth goes deeper. Increasing defocused position from 0 mm up to -1 mm, the beam spot diameter continuously increases on the workpiece surface. However, within this range of defocused position (i.e. 0 mm up to -1 mm), the beam has sufficient energy density to melt down the BM. Hence, irradiated area on the front side of the weld bead increases inducing bigger molten area. Hence, FZ width reaches to a higher value at -1 mm of defocused position.

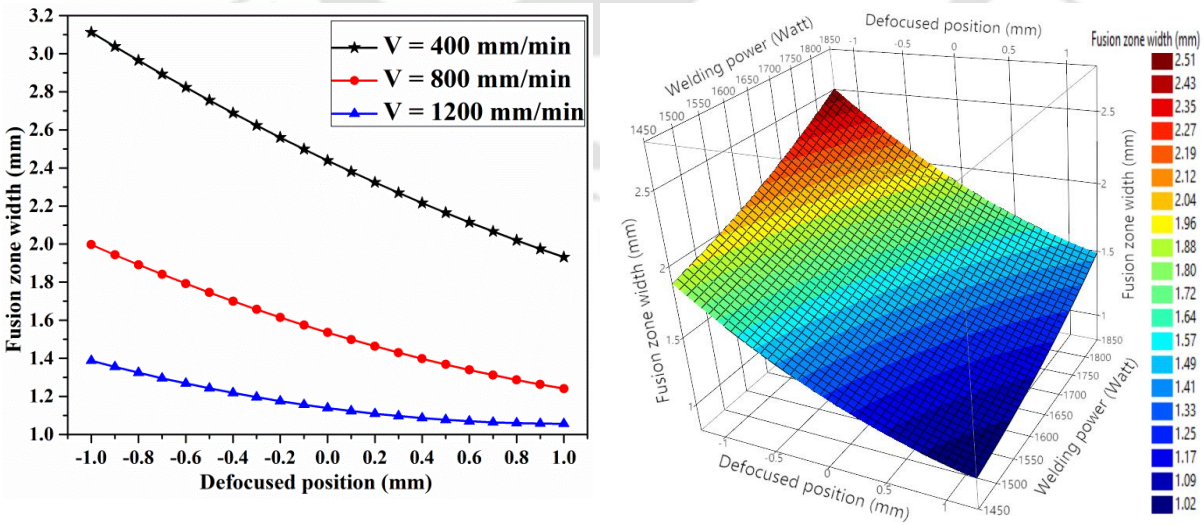

(a) (b)

Fig.7.4 (a) Effect of defocused position on FZ width at different welding speed and (b) 3D surface plot showing combined effect of beam power and defocused position on FZ width

It is evidently known that the lowest spot diameter of the laser beam is achieved at the focal point. Decreasing defocused position from -1 mm to 0 mm, the spot diameter on the workpiece surface also continuously decreases. Hence, bead width continuously decreases. Further increasing defocused position from 0 mm to +1 mm above workpiece surface, the laser beam gradually diverges away from the focal position on the workpiece surface. It induces decreased power density on the workpiece surface which induces reduced FZ width.

The effect of defocused position on FZ area is shown in Fig 7.5(a) at various welding speed. Whereas 3D response surface plot in Fig. 7.5(b) depicts interaction effect of defocused position and beam power on FZ_{area} keeping other parameters fixed at centre level (Table 7.1). In Figs. 7.5(a) and (b) insignificant variation in FZ_{area} is observed by changing defocused position. The % contribution of defocused position on FZ_{area} is insignificant (4.37%) as compared to welding speed and beam power (79.13% and 10.42%, respectively) as observed in Table 7.5.

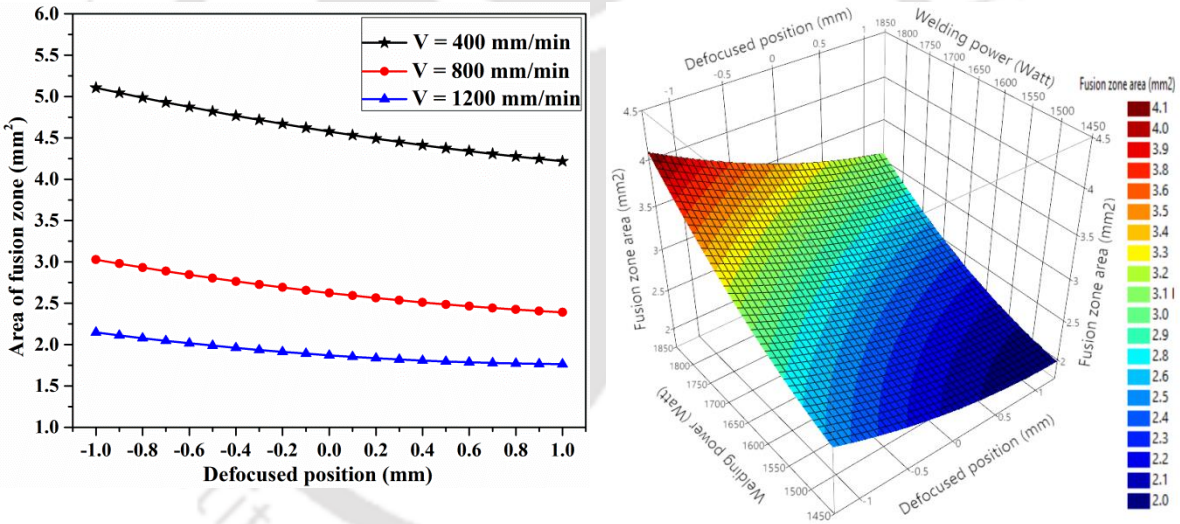

(a) (b)

Fig.7.5 (a) Effect of defocused position on FZ area (FZ_{area}) at different welding speed and (b) 3D surface plot showing combined effect of beam power and defocused position on FZ_{area}

7.5.2. Ultimate tensile strength (UTS)

Figure 7.6(a) shows the effect of beam power on UTS of weldments at different welding speed keeping other parameters constant at center level (Table 7.1). Also, 3D response surface plot in Fig. 7.6(b), shows combined effect of beam power and welding speed on UTS. From Fig. 7.6(a), it is observed that lower joint strength is obtained at lower beam power and it increases with increased beam power up to a threshold point and after that it starts decreasing with increased beam power. At lower beam power, the energy density is low

due to which lower penetration depth and poor mixing of molten material occur. Hence, weak bond is formed. However, excellent bond is formed at higher beam power which leads to higher tensile strength. Beyond threshold beam power, UTS starts decreasing irrespective of welding speed since the elements of base metal starts decomposing as it reaches to the critical temperature of decomposition. Also, excessive higher beam power or higher LE causes the degradation and evaporation of BM. It enhances the weld defects such as, underfill and excess penetration. These defects act as a stress concentrator and severely depreciate the joint strength.

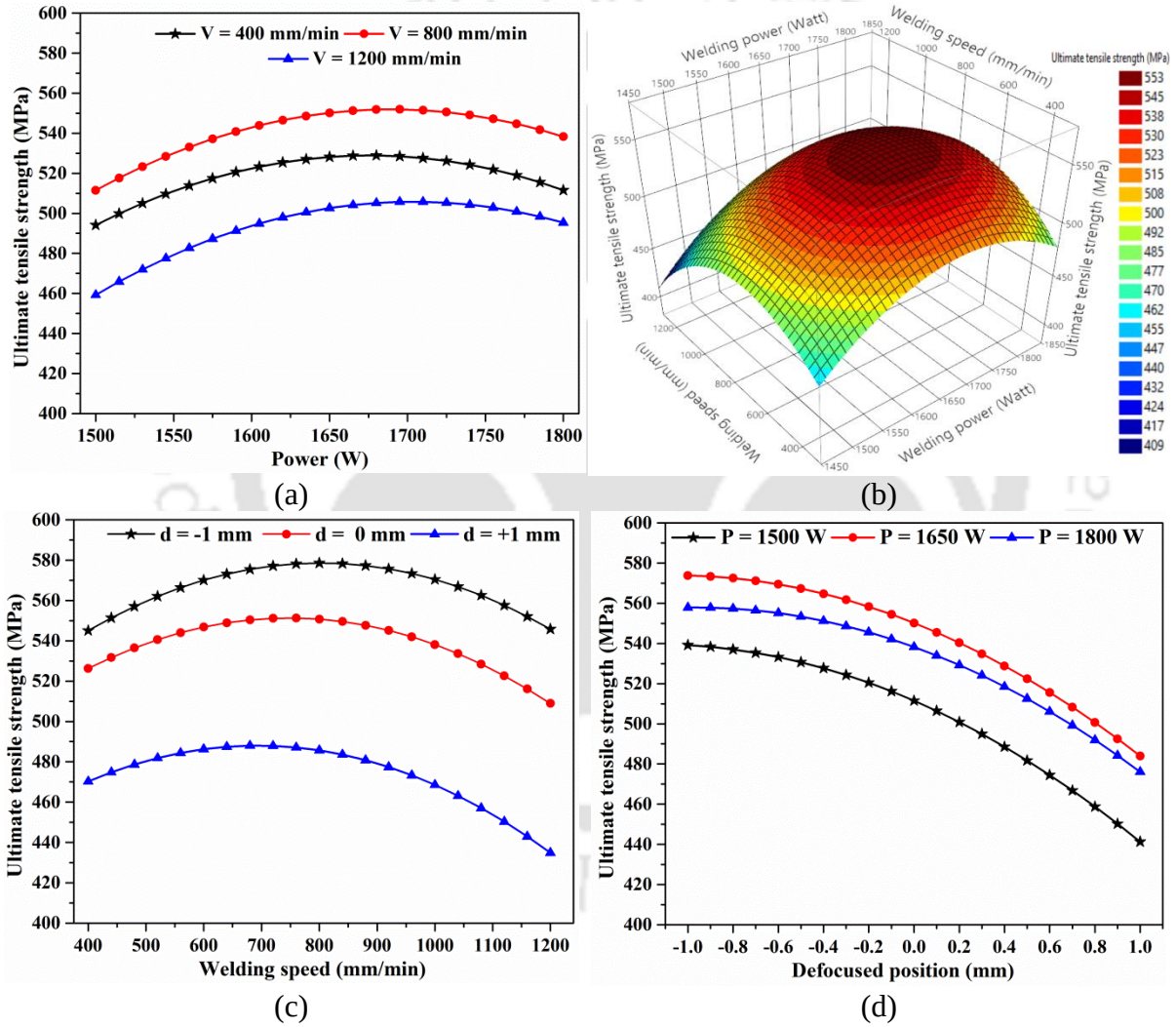

Fig. 7.6 (a) Effect of beam power on UTS of weldments at different welding speed, (b) 3D surface plot showing combined effect of beam power and welding speed on UTS, (c) effect of welding speed on UTS at different defocused positions and (d) effect of defocused position on UTS at different beam power

From Fig. 7.6(a) it is also found that UTS for 400 mm/min welding speed is lower than intermediate welding speed of 800 mm/min. It is probably due to the instability of keyhole for a combined lower welding speed (400 mm/min) and lower beam power between

1500 to 1650 W. At lower welding speed due to the instability of the keyhole, porosities are formed within weld bead which reduces joint strength. The porosities formed at lower welding speed and lower beam power is shown in Figs. 7.7(a) and (b) for Exp.1 and 11, respectively. Also, at a combination of higher beam power (1650− 1800 W) and lower welding speed (400 mm/min), higher line energy is generated which leads to evaporation of molten material from the top surface of weld bead. Due to which excessive penetration and underfill weld defects are formed which reduces UTS. The underfill weld defect is shown in Fig. 7.7(c) for Exp. No. 2. However, for a combination of moderate welding speed (800 mm/min) and higher beam power (1650 −1800 W), both upper and lower part of bead widths are wider and larger melt pool is formed as compared to bead width generated at a combination of lower beam power and welding speed. The wider melt pool helps to escape out the bubbles from the FZ efficiently and has higher tendency to resist counteracting forces inside keyhole (as discussed in 5.1.4), inducing higher UTS.

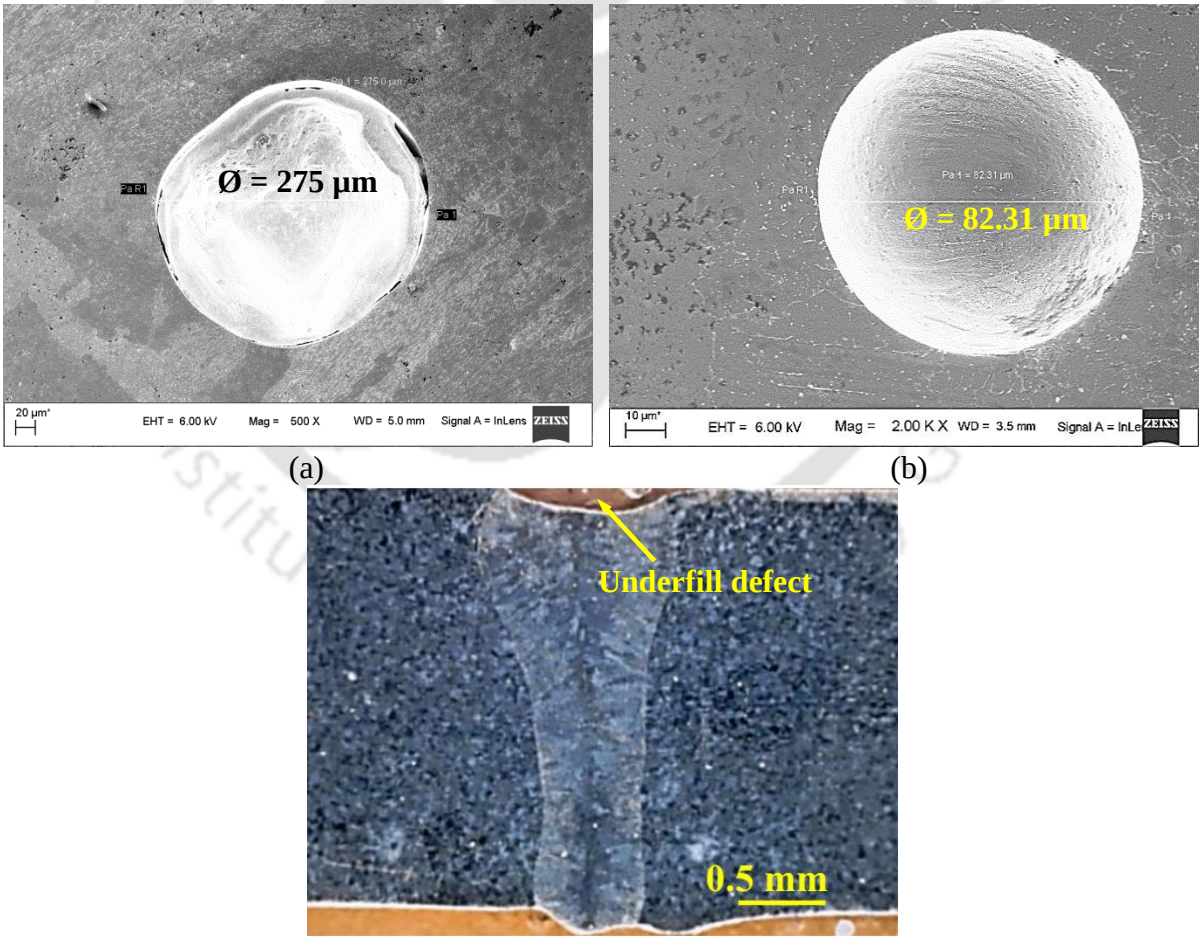

(a) (b)

(c)

Fig. 7.7 Porosity in FZ for Experiment No. (a) 1 and (b) 11; (c) Underfill defects in weld bead for Exp. 2

From Fig. 7.6(c), it is observed that tensile strength increases with increased welding speed up to 800 mm/min, after that it starts declining. It is probably due to different microstructures which are developed in the FZ at various welding speeds. Finer dendritic microstructure is formed while increasing welding speed from 400 to 800 mm/min due to increased cooling rate at higher welding speed. As welding speed increases, line energy is reduced which leads to higher cooling rate. The dependency of cooling rate on line energy is discussed in section 5.1.2 (Fig. 5.8(b)). Faster cooling rate at higher welding speed leads to finer microstructure in the FZ enhancing higher tensile strength (UTS) and vice versa. Above 800 mm/min welding speed, line energy becomes too low. Hence, full penetration does not occur in the base plate which leads to reduced joint strength.

Figure 7.6(d) shows the effect of defocused positions on joint strength at different beam power. From Fig. 7.6(d) it is observed that UTS of weldment is maximum at -1 mm defocused position and it decreases with decreasing defocused position from -1 to 0 mm. At -1 mm defocused position, deeper penetration occurs in the base plate due to multiple reflection of laser beam with keyhole wall as explained earlier. Also, the average grain size and average dendrite thickness becomes smaller when the defocused position kept below workpiece surface. Hence, maximum UTS is observed at -1 mm defocused position provided full penetration is achieved in the base plate. Further changing defocused position beyond 0 mm (above workpiece surface), UTS continuously decreases. When the defocused position is kept above workpiece surface, the laser beam slowly diverges away from the focal position and spot diameter of laser beam becomes larger. It leads to decreased power density on the workpiece surface. Hence, penetration depth continuously decreases with increasing defocused positions causing reduced UTS.

7.5.3 Microstructural analysis

Figure 7.8(a) shows the weld bead cross section for Exp. 13 (P = 1650 W, V = 800 mm/min and d = -1 mm). Due to non-uniform temperature gradient in the workpiece material, three different zones are observed in the weld bead i.e. BMZ, HAZ and FZ as seen in Fig. 7.8(a). The optical image in Fig. 7.8(b) shows BM microstructure of SS-316L. Small amount of dendritic ferrite is found in the dominant matrix of austenitic phase. The dark lines represent grain boundaries and the spot represents either inclusions or carbide particles. The average grain size of austenite in BM is around 72 µm as measured using line intercept method in optical microscope. Figure 7.8(c) shows the interface between BMZ and HAZ. Whereas Fig. 7.8(d) shows the interface between HAZ and FZ.

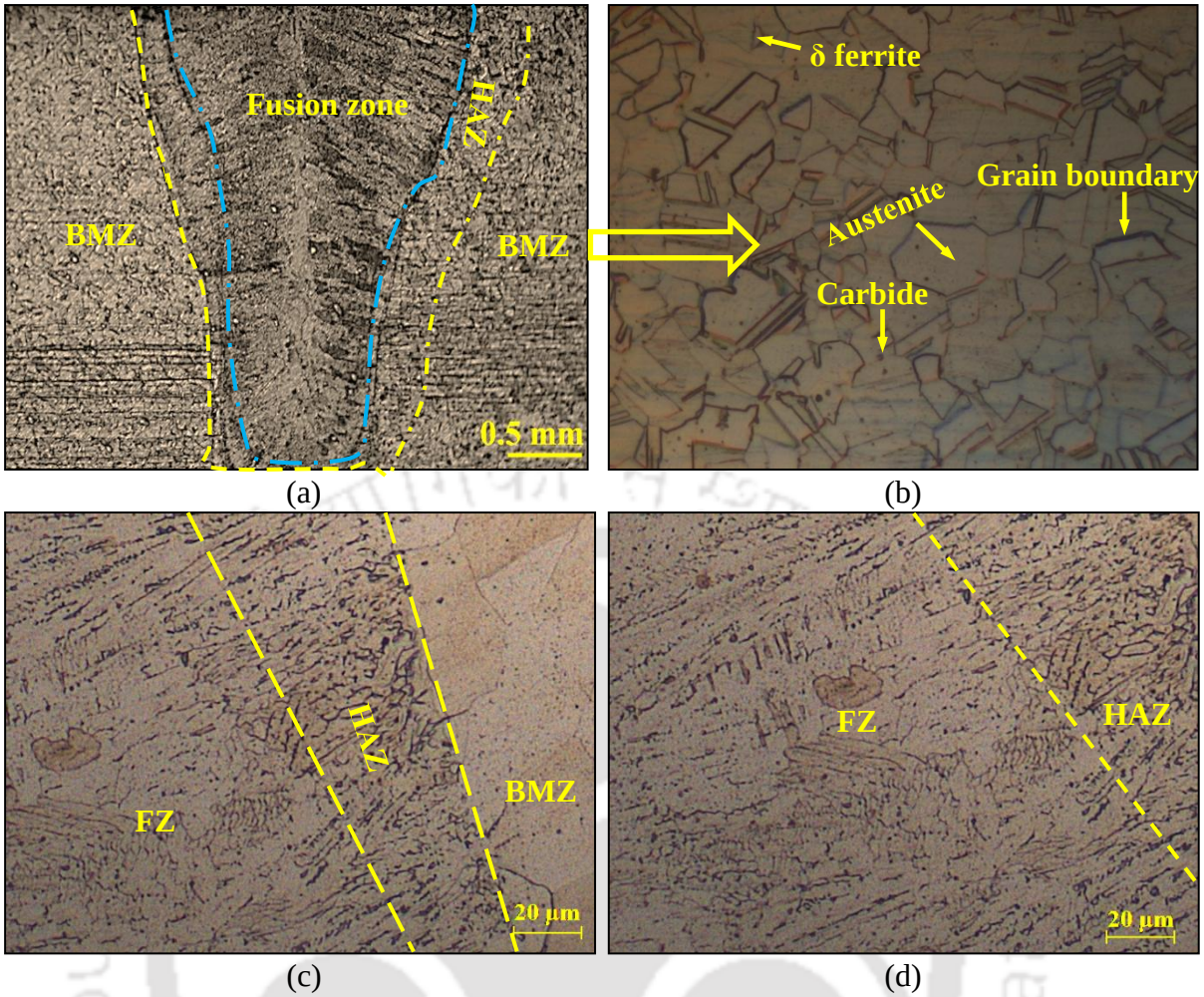

Fig. 7.8 Optical image of (a) weld bead macrograph, (b) BM microstructure, (c) interface between FZ, HAZ and BMZ and (d) interface between FZ and HAZ

The FZ microstructure at three different defocused positions (-1, 0 and +1 mm) are shown in Figs. 7.9(a-c) for Exp. Nos. 13, 15 and 14, respectively at constant 1650 W beam power and 800 mm/min welding speed. Finest sized dendritic microstructure having relatively lower interdendritic spacing is observed in the FZ at -1 mm defocused position as compared to 0 and +1 mm defocused positions. Not much microstructural variation is observed between -1 and 0 mm defocused positions due to similar nature of solidification and cooling rate. However, at highest defocused position (i.e. +1 mm), the size of the dendritic arm and interdendritic spacing are increased. It is probably due to slower cooling rate in the FZ. At higher defocused position of +1 mm, the spot diameter is bigger as compared to 0 mm defocused position. Hence, the beam energy spreads on larger area due to which the cooling rate is reduced and coarser grain is formed as shown in Fig. 7.9(c).

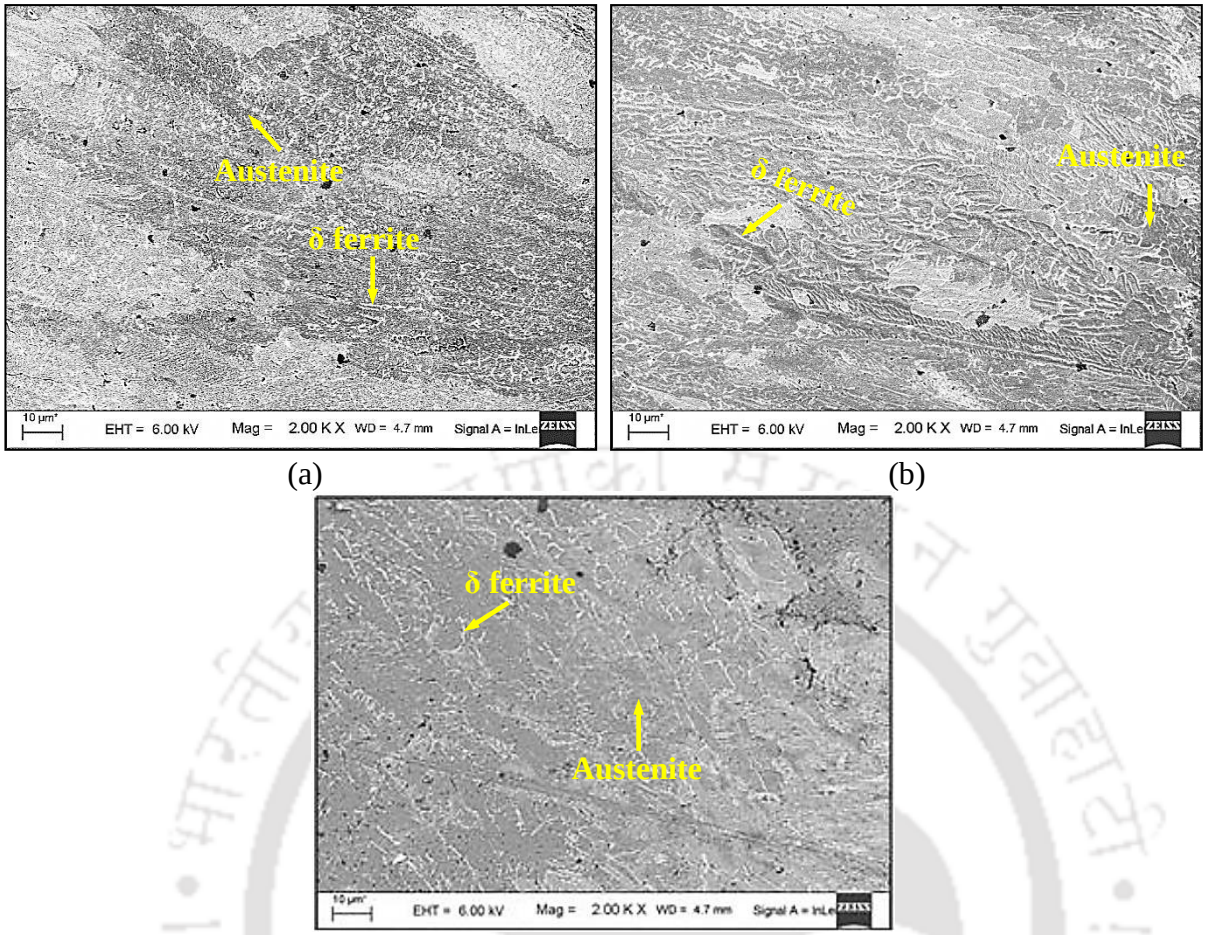

Fig. 7.9 FESEM images of FZ microstructure at different defocused positions (a) -1 mm, (b) 0 mm and (c) +1 mm

7.5.4 Fractography analysis

The FESEM images in Figs. 7.10(a) and (b) show the fracture surface of SS-316L BM and weldment for Exp. 13 (Table 7.2), respectively after tensile tests. The UTS and % elongation of the welded sample (Exp. 13) is comparable to the BM with reduced ductility as observed in Table 7.9. Cup shaped dimples of different sizes (Fig. 7.10 (a)) are observed in the fracture area of BM and its large density reflects ductile mode of fracture failure. Dimples of similar nature having relatively larger size with lesser density and with few tearing ridges are observed in the fracture surface of weldment as shown in Fig 7.10(b). It follows the characteristics of ductile mode of fracture failure of weldment.

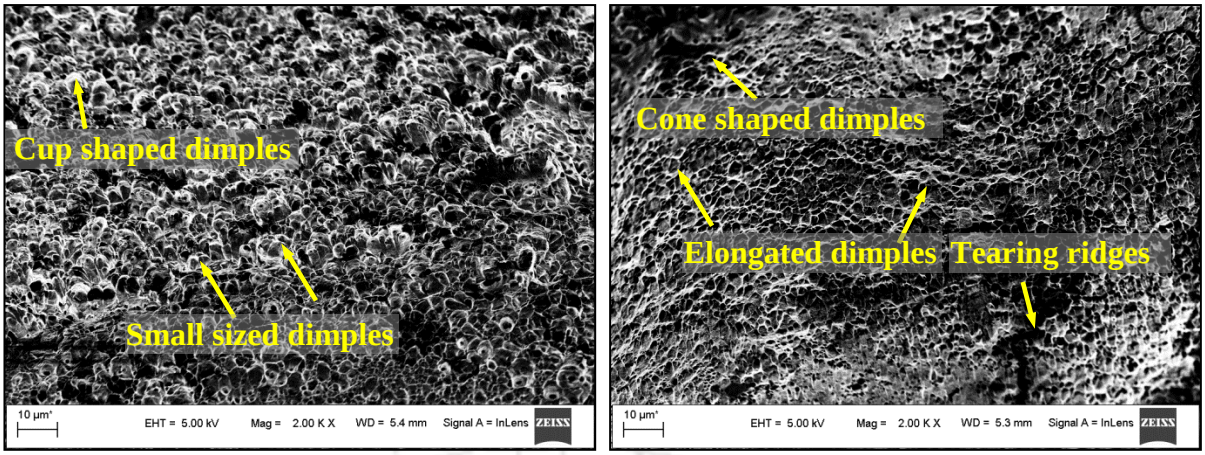

(a) (b)

Fig. 7.10 Fracture surface morphology of (a) BM and (b) weldment for Exp. 13 (Table. 7.2)

Table 7.9 Mechanical properties of BM and weldment at room temperature

Sample specification	Yield strength (MPa)	Ultimate tensile strength (MPa)	% elongation
BM	351.24	602.18	47.22
Exp. 13	324.52	572.24	34.54

7.5.5 Hardness

Vickers microhardness tests are carried out at the middle portion of the weld bead cross section across transverse direction to the FZ center line for experiment No. 13 (Table 7.2). The hardness distribution at both sides of the FZ center line is shown in Fig. 7.11(a). Minimum hardness value (200−212 HV) is observed in the BMZ and its value gradually increases towards FZ as seen in Fig. 7.11(a). In the FZ, its value is found in between 252 − 261 HV. The maximum hardness in the FZ is due to the formation of finest equiaxed dendritic structure because of higher cooling rate in the FZ which promotes reduced grain size. The hardness in the FZ at three different defocused position i.e. -1 mm, 0 mm, +1 mm (fixed beam power of 1650 W and 800 mm/min welding speed) as well as in BM are shown in Fig. 7.11(b). From Fig. 7.11(b), it is found that at all defocused positions, the FZ hardness is higher than BM. Maximum value of hardness is observed for -1 mm defocused position due to the formation of finest grains (Fig. 7.9(a)) which possess higher hardness as compared to coarser grain as discussed in section 7.5.3. However, at +1 mm defocused position coarser grain along with increased size of interdendritic spacing (Fig.7.9(c)) is formed in the FZ which reduces FZ hardness as observed in Fig. 7.11(b).

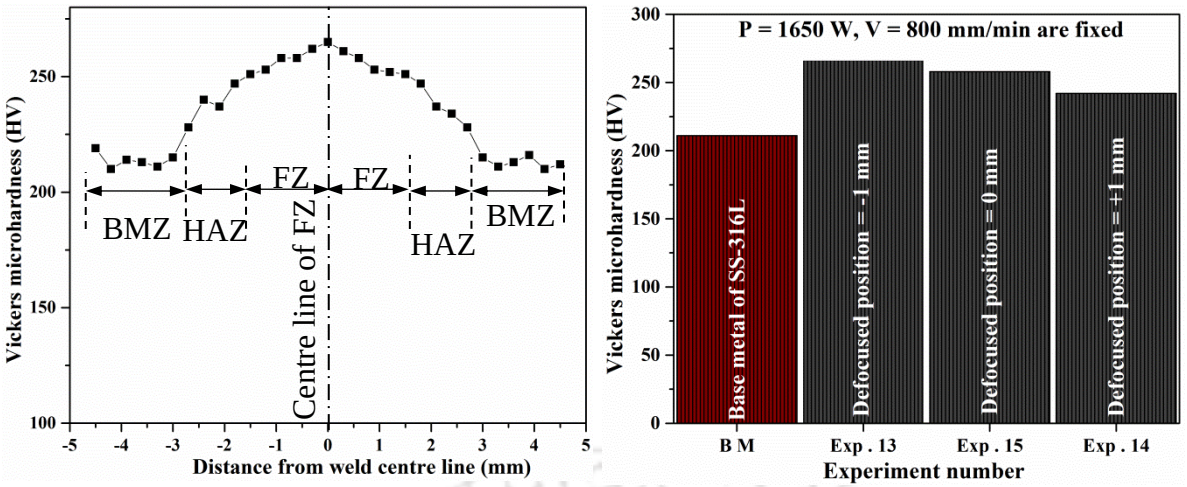

(a) (b)

Fig. 7.11 (a) Hardness distribution in weld bead cross section across transverse direction to the centre line of FZ for Exp. 13 (Table 7.2) and (b) comparison between FZ hardness at different defocused positions and BM

7.6 Conclusions

In this chapter, 3 mm thick austenitic stainless steel plates of grade 316L are welded using fibre laser to investigate the influence of beam power, welding speed and defocused position on bead features, microstructure and mechanical properties. Based on present experimental study, following conclusions are drawn.

- Welding power directly affects the FZ width and its area although inverse effect by welding speed is observed due to the variation in line energy. Insignificant variation in FZ area is observed at different defocused positions.
- Tensile strength of weldment is increased with increased beam power and welding speed up to certain threshold level, beyond that it starts decreasing due to different FZ microstructure which is developed at reduced line energy and higher cooling at increased welding speed.
- Finer microstructure is developed in the FZ when the defocused position is kept -1 mm below workpiece surface. However, coarser microstructure is formed when defocused position is kept on or above the workpiece surface.
- High hardness is observed in the FZ due to the presence of dendritic structure. For a fixed beam power and welding speed, highest hardness in FZ is observed at -1 mm defocused position due to the formation of finest dendritic structure.
- Ductile mode of fracture failure is observed in both BM as well in the welded specimen.

Chapter 8
Numerical simulation of laser welding of Ti-6Al-4V alloy

8.0 Introduction

LBW is a complex process since large number of process parameters are involved which must be controlled for better functioning of the process. Also, due to the stochastic nature of LBW process, achieving optimum process parameters by doing experiments using trial-and-error method is difficult. During LBW, non-uniform temperature distribution takes place throughout the workpiece. The temperature distribution depends on several factors such as heat input, temperature depended material properties, latent heat of fusion and rate of convective heat flow in the FZ. The temperature dependent thermo-physical properties of Ti-6Al-4V alloy are given in Table 8.1.

Table 8.1 Thermo-physical properties of Ti-6Al-4V alloy (Yang et al. 2010)

Temperature (^{0}C)	Thermal Conductivity (W/mK)	Specific heat (J/kg K)	Density (kg/m^3)	Emissivity
25	7.0	546	4420	----
100	7.45	562	4406	----
200	8.75	584	4395	0.67
300	10.15	606	4381	----
400	11.35	629	4366	0.47
500	12.6	651	4350	----
600	14.2	673	4336	0.43
700	15.5	694	4324	----
800	17.8	714	4309	0.50
900	20.2	734	4294	----
995	19.3	641	4282	----
1000	----	----	----	0.60
1100	21	660	4267	----
1200	22.9	678	4252	----
1300	23.7	696	4240	----
1400	24.6	714	4225	----
1500	25.8	732	4205	----
1600	27	750	4198	----
1650	28.4	759	4189	----
Uncertainty	± 10%	± 3%	± 3%	----

The heat loss to the surrounding takes place by convection and radiation. Due to these large numbers of variables, the experimental determination of effect of all input parameters is very difficult and time consuming for achieving satisfactory welding performance. Hence, the demand for finite element method (FEM) based numerical simulation is progressively increasing. In this chapter, the methodologies for the modeling and simulation of LBW process using FEM are described. A heat transfer based FEM model is developed to determine transient temperature profile and to study the effect of laser beam power and welding speed on weld bead geometry and fusion zone size.

8.1 FEM simulation of LBW process

FEM is mostly used to simulate transient thermal, structural as well as heat transfer phenomena in LBW process. The finite element modeling procedure consists of following steps as shown in Fig. 8.1.

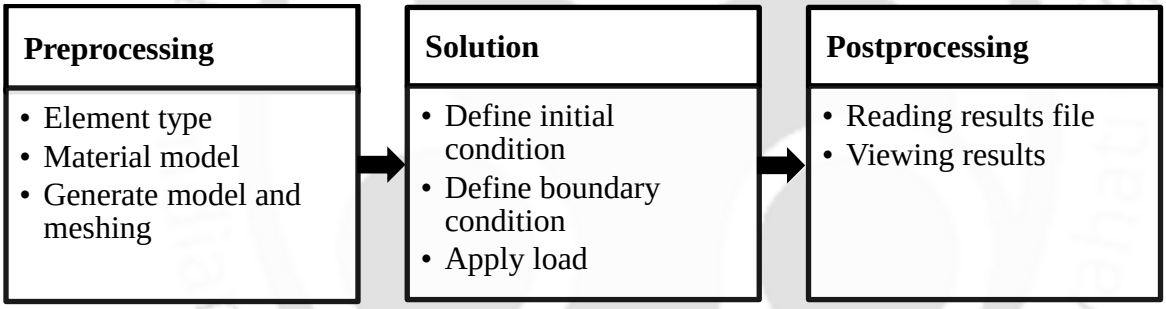

Fig. 8.1 Finite element modeling procedure

In the preprocessing step, solid modeling of workpiece geometry is designed. Ansys® 14.5 provides an option of creating solid model of the workpiece on its GUI or it may be imported from any CAD software. After that the whole domain of the workpiece is divided into a number of small elements. Ansys®14.5 library contains large number of different elements.

8.1.1 Element type and material properties

The size and type of the element are crucial to obtain higher accuracy of the result. For the present thermal analysis, element type of 'solid 70' is selected. It is an eight-noded element having single degree of freedom (Shanmugam et al., 2012). Ti-6Al-4V alloy of Grade 5 is selected as workpiece material. The melting point of Ti-6Al-4V is 1690^0 C. The dimension of the workpiece is considered as 30 × 30 × t mm^3. The two different workpiece

thickness ‘t’ of 2 and 3 mm are considered. The temperature dependent material properties (i.e. thermal conductivity, enthalpy, density, specific heat and emissivity) of Ti-6Al-4V alloy are assumed to be isotropic and homogeneous (Yang et al., 2010).

8.1.2 Meshing

The accuracy and convergency of the FEM results depend on type of element and the mesh size at different zones. In the present study, the geometry of the workpiece is meshed with a fine meshing near weld line and coarser meshing away from the weld line as shown in Fig. 8.2(a). Also, convergency tests are carried out for selecting suitable number of elements particularly around the weld line and along thickness direction. It is observed that five and six elements (as shown in Fig. 8.2(b)) along the thickness direction give reasonable convergency with less solution time and good accuracy for 2 and 3 mm thick plates, respectively.

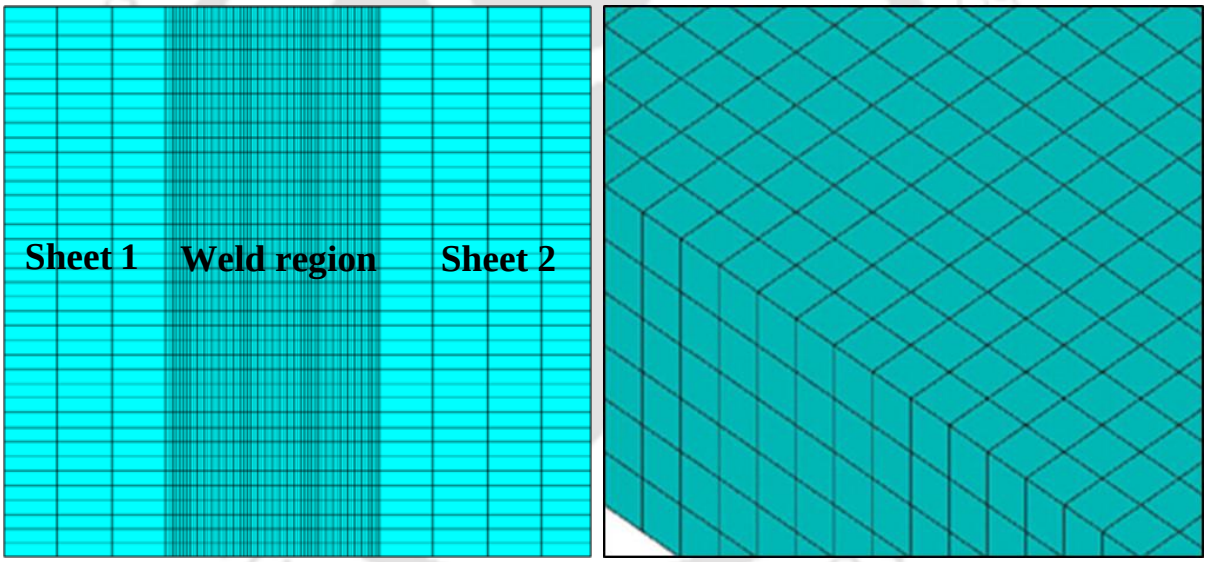

(a) (b)

Fig. 8.2 (a) Finite element non-uniform meshing of the workpiece and (b) number of elements along thickness direction

8.1.3 Solution procedure

In the solution module of Ansys14.5®, the applied load (i.e. heat source), initial condition and boundary conditions are specified. The boundary conditions may be absolute, natural or a function of time. The absolute boundary conditions define the values of primary variables at the boundary, whereas, the natural boundary conditions define the gradients of the primary variables (Ansys® 14.5 manual). In LBW process, the natural boundary condition is specified by the application of heat flux on the elements. The ambient temperature of 27°C is set as initial condition. In post processing of LBW process, transient temperature profile,

shape of the molten zone and weld bead profile are obtained. From both temperature and weld bead profiles, the size of FZ and penetration depth are measured. The shape of the molten pool is determined from the melting and vaporization isotherms.

8.2 Governing equation and boundary conditions

The 3-D transient non-linear heat transfer equation for LBW process can be written as

$$\rho c\left[\frac{\partial T}{\partial t}+(-v)\frac{\partial T}{\partial y}\right]=K\left[\frac{\partial}{\partial x}\left(\frac{\partial T}{\partial x}\right)+\frac{\partial}{\partial y}\left(\frac{\partial T}{\partial y}\right)+\frac{\partial}{\partial z}\left(\frac{\partial T}{\partial z}\right)\right]+Q(x,y,z) \quad (8.1)$$

where, $Q(x,y,z)$ is volumetric heat source and it varies with beam power, beam incident angle, beam exposure time and welding speed. *K*, c, ρ and *v* are the thermal conductivity, specific heat, density of the workpiece and the velocity of the laser heat source, respectively. The initial condition at time *t*=0 is given as (Akbari et. al., 2014)

$$T(x,y,z,0)=T_0(x,y,z) \quad (8.2)$$

The top surface of the plate is subjected to heat flux produced by laser beam and the remaining surfaces of the plate are subjected to heat losses by convection and radiation only. The natural boundary condition is given as

$$K_n(\partial T/\partial n)-\mathrm{q}+\mathrm{h}(\mathrm{T}-T_o)+\sigma\varepsilon\left(T^4-T_o^{\,4}\right)=0 \quad (8.3)$$

where, K_n is thermal conductivity, *q* is heat flux (W/m^2 K), σ is Stefan-Boltzmann constant, ε is emissivity, *h* is heat transfer coefficient and T_o is the ambient temperature. It is observed that with the addition of radiative boundary condition in the model, solution time increases. Hence, a lumped heat transfer coefficient i.e. Vinokurov empirical relationship is used in the present analysis which combines both radiative and convective heat transfer phenomena (Frewin and Scott, 1999). It is given as

$$h_{lump}=2.4\times10^{-3}\varepsilon T^{1.61} \quad (8.4)$$

where, h_{lump} is lumped heat transfer coefficient. Equation (8.3) can be modified by combining it with Eq. (8.4) and it is given as

$$K_n(\partial T/\partial n) - q + h_{lump}(T - T_o) = 0 \quad (8.5)$$

During welding, the temperature in the fusion zone reaches beyond boiling point of the material. Hence, a phase change phenomenon during welding is implemented in FE simulation by considering enthalpy as a function of temperature as

$$E = \int \rho c dT \quad (8.6)$$

The initial temperature of the workpiece is considered as 27°C. Following assumptions are considered for FE simulation.

- Thermo-physical material properties are temperature dependent.
- Heat source moves during welding and workpiece is kept fixed.
- Forced convection due to the shielding gas is neglected.
- The physical phenomena like viscous force, buoyancy force, convective melt flow and Marangoni effect are neglected.

The simulation is performed in two steps. In the first step, both heat flux and heat generation are applied on workpiece top surface. In the second step, the heat flux and heat generation are removed and the heat is dissipated from all workpiece boundaries by convection and radiation.

8.3 Heat source models

Two different heat source models i.e. double ellipsoidal and conical heat source are considered as discussed below.

8.3.1 Double-ellipsoidal heat source

The double-ellipsoidal Gaussian-distribution of volumetric heat source model is most suitable for the simulation of fusion welding process and is mostly used in present time. It is a combination of two ellipsoids which have same intersection in a plane given by source

location and vertical to welding direction. Schematic illustration of a double-ellipsoid model is shown in Fig. 8.3. The double-ellipsoidal model is described by two equations, individually for each ellipsoid. The front and the rear part of this heat source model are given in Eqs. (8.7) and (8.8), respectively.

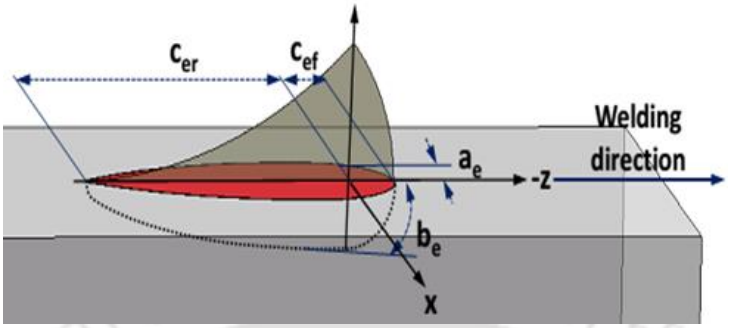

Fig. 8.3 Double-ellipsoidal heat source model (Lundback and Runnemalm, 2005)

$$q_{ef}(x,y,z) = \frac{6\sqrt{3} f_{ef} Q}{a_e b_e c_{ef} \pi^{3/2}} \exp\left\{-\left(\frac{kx^2}{a_e^2} + \frac{ly^2}{b_e^2} + \frac{mz^2}{c_{ef}^2}\right)\right\} \tag{8.7}$$

$$q_{er}(x,y,z) = \frac{6\sqrt{3} f_{er} Q}{a_e b_e c_{er} \pi^{3/2}} \exp\left\{-\left(\frac{kx^2}{a_e^2} + \frac{ly^2}{b_e^2} + \frac{mz^2}{c_{er}^2}\right)\right\} \tag{8.8}$$

The parameters f_{ef} and f_{er} are the fractions between the front and rear quadrants in the ellipsoid. To obtain continuity between front and rear quadrants of the functions, they must obey following relationships.

$$f_{ef} + f_{er} = 2 \tag{8.9}$$

$$f_{ef} = \frac{2c_{ef}}{c_{ef} + c_{er}} \tag{8.10}$$

The parameters f_{ef} and f_{er} decide about how much of overall heat produced by source goes to individual ellipsoids. These are invariables influencing energy flow intensity distribution to the material which to a certain degree are able to compensate the influence of a welding torch curl. It is a common practice to point 60% and 40% of total energy to the front and rear ellipsoid, respectively. While using double-ellipsoid model, it is necessary to know the size of

the fusion zone parameters i.e. a_e, b_e, c_{ef} and c_{er} as shown in Fig. 8.3. These parameters can be determined on the basis of experimental results and it is taken from the macrographs of weld bead. Presently, a modified version of double-ellipsoid heat source model is commonly used. Modification and calibration consist of changing the values of the parameters *k*, *l* and *m* in exponents (Eqs. (8.7) and (8.8)). This way the modified and calibrated heat source models can be used for the majority of fusion welding process such as, laser, plasma and electron beam welding. It is very difficult to find out the optimum length of the front and rear part of the double-ellipsoidal volumetric heat source model. Till date, the lengths of these parameters are taken arbitrary. Yadaiah and Bag (2012) suggested an optimum value of ratio of front and rear length of a double ellipsoidal heat source model over a wide range of welding current and velocity in GTAW process. They reported that this ratio is a function of weld velocity. Integrated optimization algorithm was used to optimize the ratio of front and rear length. The values of the heat source parameters are given in Table 8.2. The total length of heat source and the length of front ellipsoid are considered as 2×10^{-3} m and 0.5×10^{-3} m, respectively.

Table 8.2 Values of heat source parameters

Parameter	a_e	b_e	c_{ef}	c_{er}
Value (mm)	1.7	0.2	0.2	3

8.3.2 Conical heat source

A 3-D cone-shaped, volumetric heat source model is considered for laser welding simulation of 2 mm thick Ti-6Al-4V plates. The conical heat source distribution consists of two parts, i.e. one is plane Gaussian heat source, which is distributed on the top surface of the workpiece. Another one is conical shape which is distributed along thickness direction of the workpiece. The maximum heat intensity is distributed on the top surface and the minimum is in the thickness direction of the workpiece. During simulation it is considered that 25% of beam power is absorbed by the top surface of the workpiece and remaining 75% is absorbed by keyhole wall. The conical Gaussian heat flux distribution is given as

$$Q(r,z) = Q_0 \exp(-\frac{3r^2}{r_0^2}) \tag{8.11}$$

where, Q_0 = maximum heat intensity of laser beam, r_0 = heat distribution parameter, r = radial coordinate of the interior point. Assuming that the laser beam maintains a constant

transverse electromagnetic mode (TEM_{00}), the conical Gaussian heat flux distribution given in Eq. (8.11) can be written in terms of x and y coordinates as

$$q(x,y) = \frac{3Q_{surf}}{\pi R^2} \exp(-3(x^2 + y^2)) \tag{8.12}$$

where, Q_{surf} is the plane heat source and it is considered 25% for the present analysis. The heat source radius (R) is calculated from focal length of the focusing lens and it is written as

$$R = \frac{2M_0{}^2 \lambda f}{\pi D_0} \tag{8.13}$$

where, M_0^2 is the value of beam quality, λ is the wavelength of the laser source. λ=1.08 μm is considered for present fiber laser. The value of M_0^2 is assumed as 1.0 for an ideal Gaussian beam. In Eq. (8.13), f is the focal length of the focusing lens and D_0 is the minimum diameter of the laser beam (0.4 mm for present case). Assuming conical shape of the keyhole, the Gaussian distribution of heat flux along thickness direction is written as

$$q(z) = \frac{Q_{keyhole}}{\pi r_e^2 H} \tag{8.14}$$

Where, $Q_{keyhole}$ is the absorbed laser beam power (75%), r_e is the average keyhole radius, H is the plate thickness. The total heat input to the model is computed from the summation of surface and volume heat source. It is given as

$$Q_v(r,z) = q(x,y) + q(z) \tag{8.15}$$

8.4 Results and discussion

8.4.1 Thermal analysis of 3 mm thick plate

The transient thermal analysis is performed in commercial FE package Ansys® 14.5 considering double ellipsoid heat source model. Simulations are performed at 500, 1000 and 1500W laser beam power to study its effect on workpiece temperature profiles at a constant welding speed of 312 mm/min and 90° beam incident angle. Laser spot welding simulation is

also performed at 500, 1000 and 1500 W beam power. 25 ms time duration is considered for laser spot welding.

The transient temperature profiles for laser welded Ti-6Al-4V workpieces are shown in Figs. 8.4(a), (b) and (c) for 500, 1000 and 1500 W beam power, respectively. From Figs. 8.4(a), (b) and (c), it is observed that the temperature profile around the laser heat source increase rapidly from ambient temperature of 27 °C to peak temperature of around 2593 °C, 3205 °C and 5946 °C at beam power of 500 W, 1000 W and 1500 W, respectively for 0 to 3s time interval.

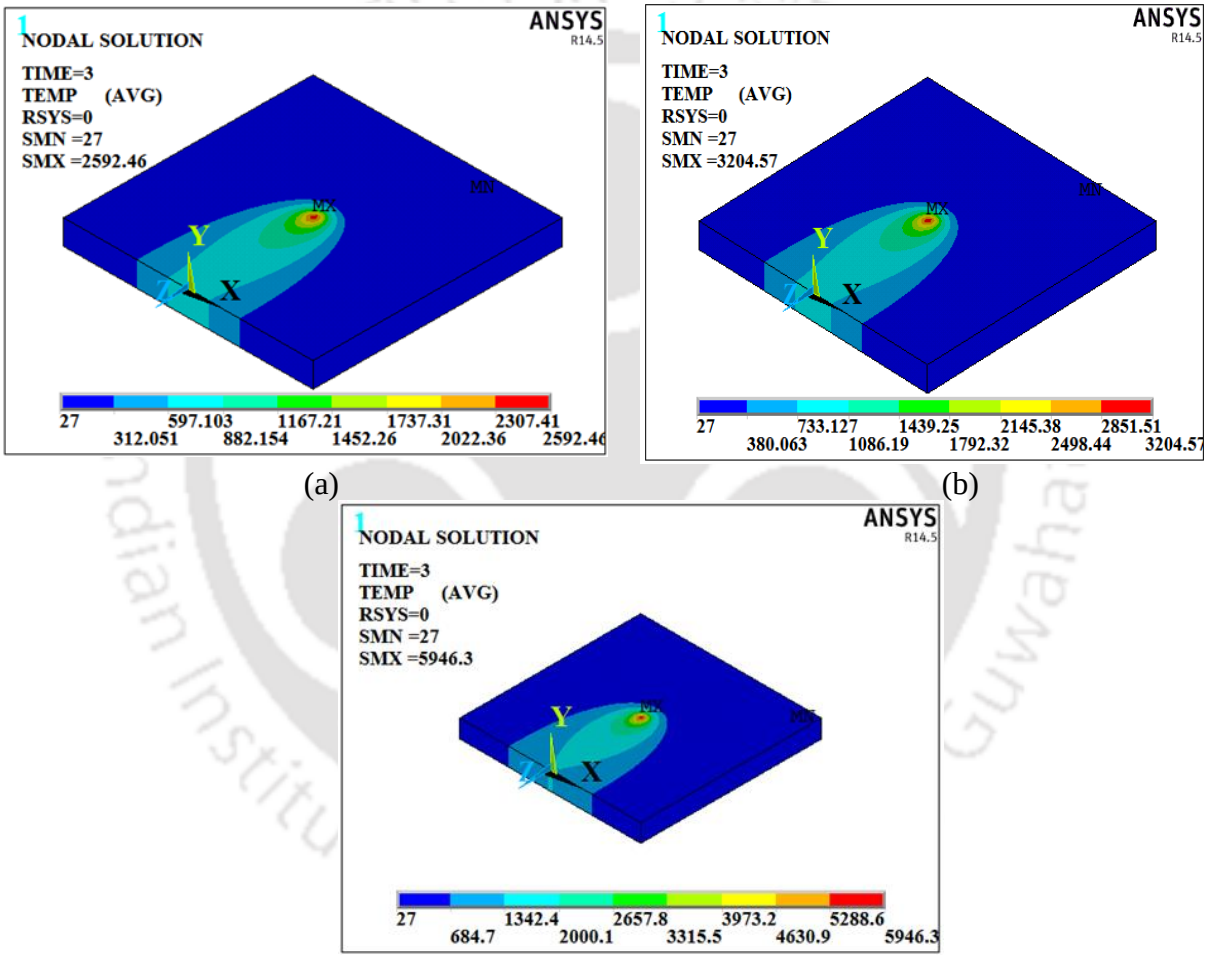

Fig. 8.4 Temperature distribution at 3s for (a) 500 W, (b) 1000 W and (c) 1500 W beam power

At the end of 3s, the position of the heat source reaches approximately to the middle of the workpiece. During this time period, the temperature gradient at the front of the heat source is comparatively lesser than the rear part of the heat source. At this stage, the workpiece is subjected to three modes of heat transfer i.e. conduction, convection and radiation. It is observed that both peak temperature and the temperature gradient increase while increasing beam power from 500 W to 1500 W. It can be attributed to the fact that at higher beam

power, the laser beam power density is highly concentrated over a small area (~0.4 mm spot diameter). The size of the weld bead also increases with the increase in the laser beam power. It can be attributed to the facts that with the increase in the laser beam power, the power density distribution widely spreaded over the top surface of the workpiece. Therefore, a slight increment in bead geometry is observed.

Figures 8.5 (a), (b) and (c) show the temperature distribution on the top surface of the workpiece for 0 to 6s time interval at 500, 1000 and 1500 W beam power, respectively. At the end of 6s, the position of the heat source reaches at the end of the workpiece. Comparing Figs. 8.4 and 8.5, it is observed that the temperature in the fusion zone at 6s falls down to 1667 ˚C, 2030 ˚C and 3684 ˚C (Fig. 8.5 (a), (b) and (c), respectively) from its peak temperature of 2592 ˚C, 3204 ˚C and 5946 ˚C at 3s (Fig. 8.4 (a), (b) and (c), respectively) for 500, 1000 and 1500 W beam power, respectively. At the edge of workpiece after 6s, temperature decreases since the heat source is turned off and the temperature profiles are influenced only by the convective and radiative boundary conditions.

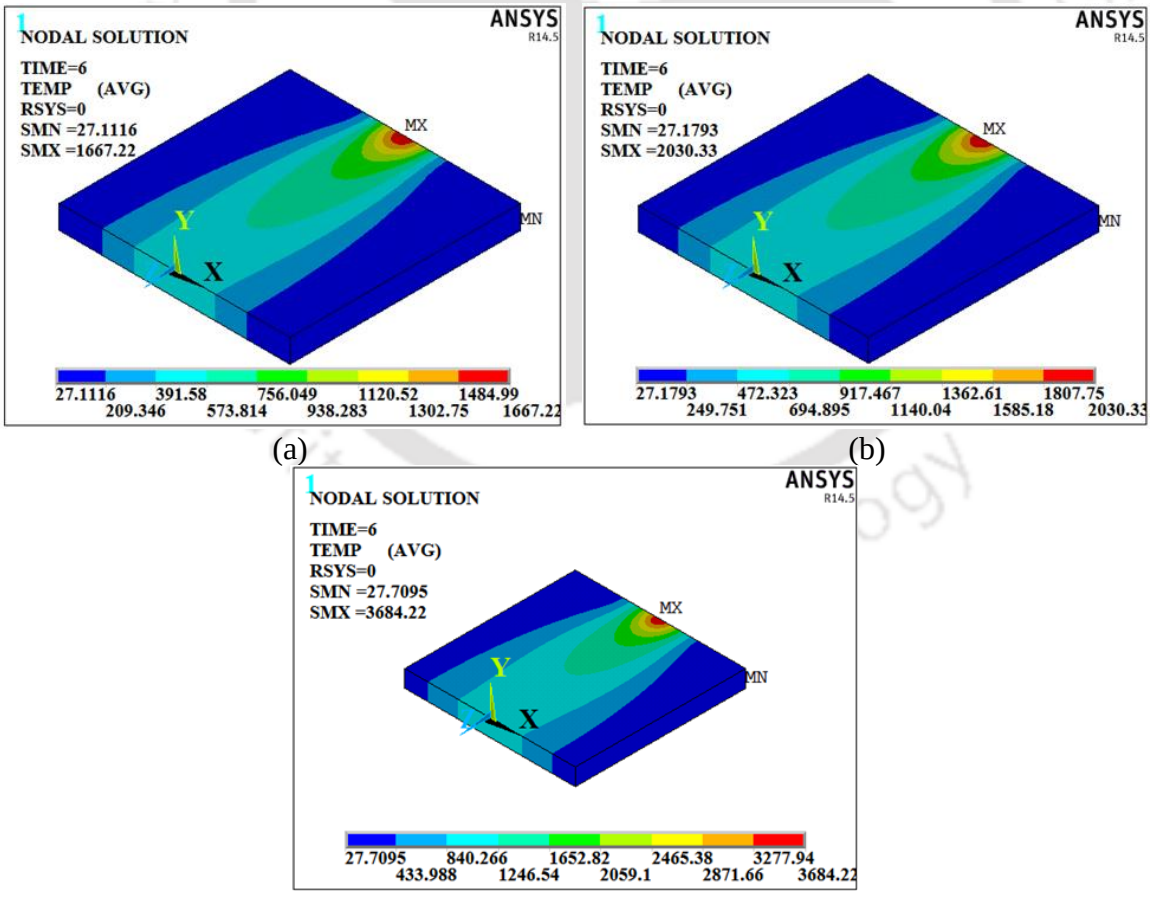

Fig. 8.5 Temperature distribution at 6s for (a) 500 W, (b) 1000 W and (c) 1500 W beam power

Figs 8.6(a), (b) and (c) show the distribution of temperature along workpiece cross section for laser spot welding at 500, 1000 and 1500 W beam power, respectively after heating for 20 ms. From Fig. 8.6, it is observed that the temperature in the fusion zone increases from ambient temperature to peak temperature of 2492 ˚C, 3047 ˚C and 5548 ˚C for 500, 1000 and 1500 W beam power, respectively.

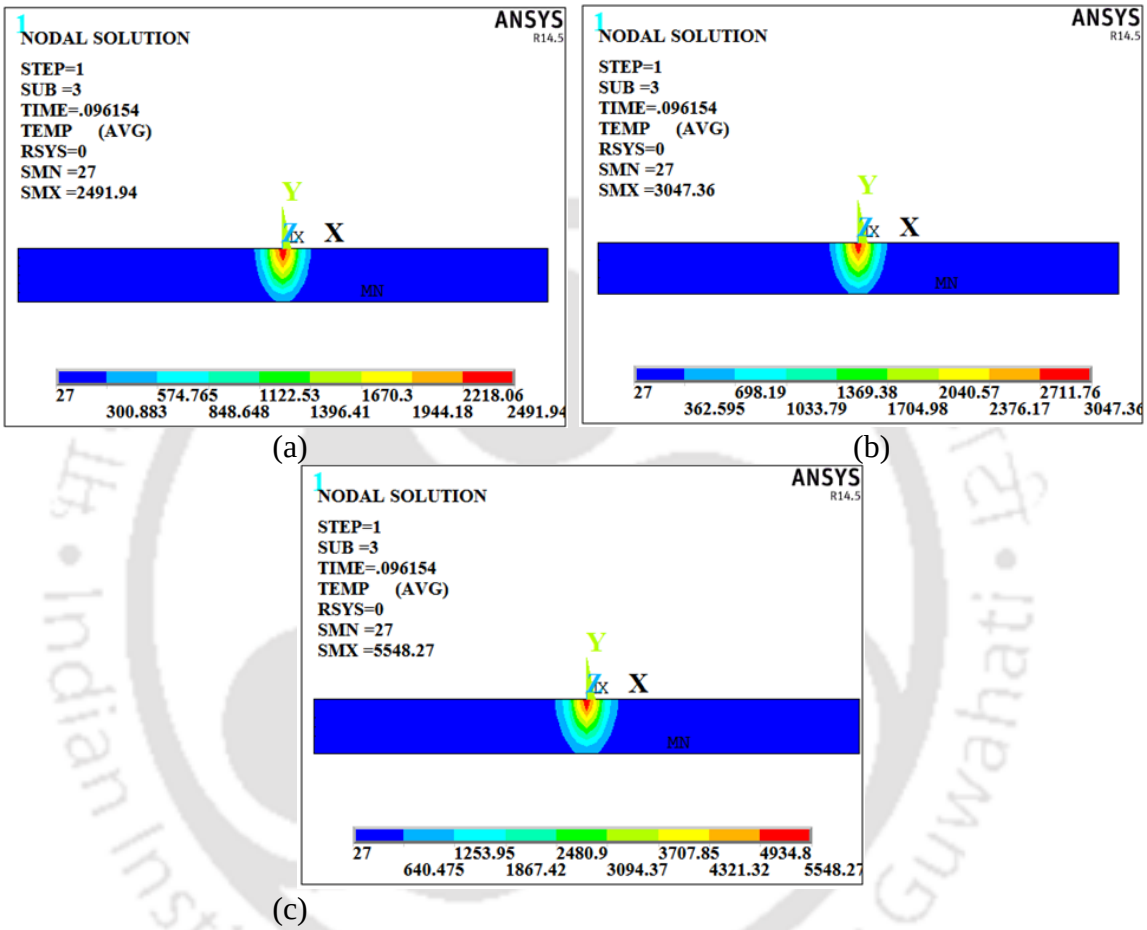

Fig. 8.6 Temperature distribution plot after 20 ms at (a) 500 W (b) 1000 W and (c) 1500 W beam power

The transient temperature profiles at a particular node along the weld line are shown in Fig. 8.7 for 500, 1000 and 1500 W beam power. It is observed that when heat source is applied on workpiece surface, temperature in the fusion zone increases rapidly and reaches to the melting point at around 0.9s. Also, the temperature at a particular node in fusion zone increases from ambient temperature to peak temperature of 2492 ˚C, 3047 ˚C and 5548 ˚C for 500, 1000 and 1500 W beam power, respectively after that temperature decreases continuously. It is also noticed that the cooling rate is relatively smaller than the heating rate. A non-linear relationship between the peak temperature and the laser beam power is noticed as shown in Fig. 8.7. The possible reason is due to the variation of absorption coefficient of the Ti-6Al-4V alloy with temperature. The absorptivity plays an important role on the

thermal field since it controls the heat input to the workpiece. Also, absorptivity is a function of surface temperature.

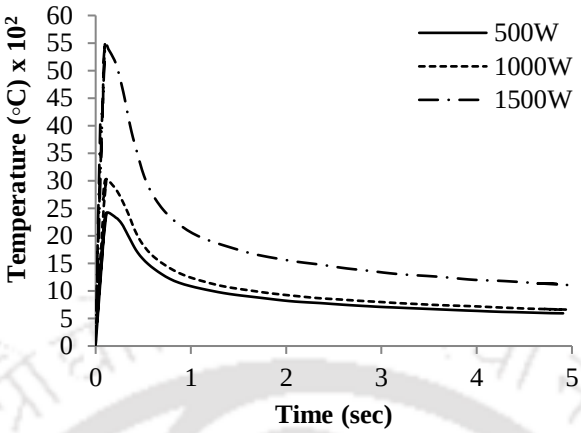

Fig. 8.7 Comparison between transient temperature histories at a node along weld line at different laser beam power

8.4.2 Thermal analysis of 2 mm thick plate

In order to study the effect of LBW process parameters on transient temperature profile, FE simulations are performed on 2 mm thick Ti-6Al-4V plate using conical heat source.

8.4.2.1 Effect of welding time

Figures 8.8 (a), (b), (c) and (d) show transient temperature profiles of laser welded Ti-6Al-4V work pieces at 1, 2.5, 3.5 and 7.5 s time intervals, respectively at 800 W beam power, 400 mm/min welding speed and 90° beam incident angle. From Fig. 8.8(a), it is observed that the temperature profile around laser heat source increases rapidly from 27 °C ambient temperature to around 3550 °C peak temperature for 0 to 1s time interval. It is also observed that peak temperature continuously increases during 1 to 7.5s time interval and reaches up to 4677 °C (Fig. 8.8(d)). The time interval between 0 to 1s is called as initial transient stage.

It is observed from Fig. 8.8 that the shape of the molten pool is elliptical in nature as shown by red color. Similar trend of Fig. 8.8 is observed for laser beam power of 1000 W and 1200 W at a constant welding speed of 400 mm/min as shown in Figs. 8.9 and 8.10, respectively. It is observed from the temperature profiles that some portion of surface area attains a temperature above 1700 °C and it starts to melt and forms the molten pool. The melting point Ti-6Al-4V is around 1700 °C. Hence, the width of the bead is measured as the intercept of 1700 °C isotherm from temperature distribution profile along the width direction.

Similarly, the depth of penetration of molten pool is obtained from the temperature distribution profile along the thickness direction.

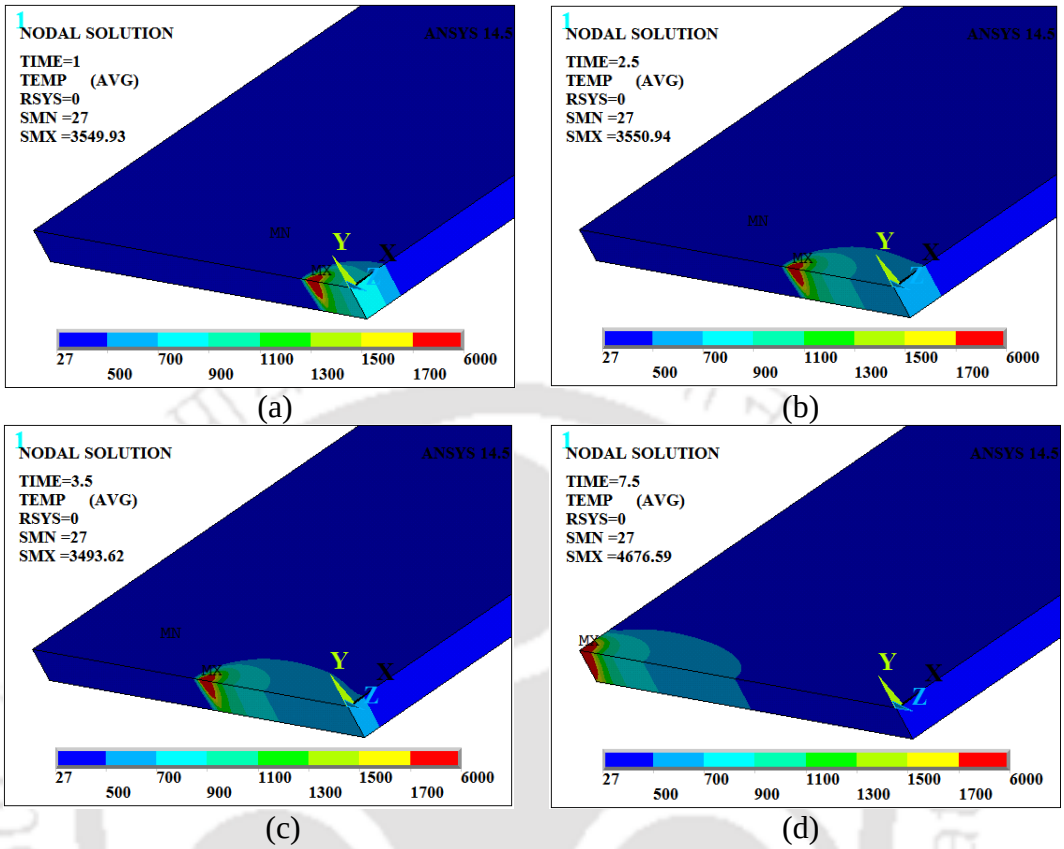

Fig. 8.8 Temperature distribution at (a) 1, (b) 2.5, (c) 3.5 and (d) 7.5 s time interval for 800 W beam power and 400 mm/min welding speed

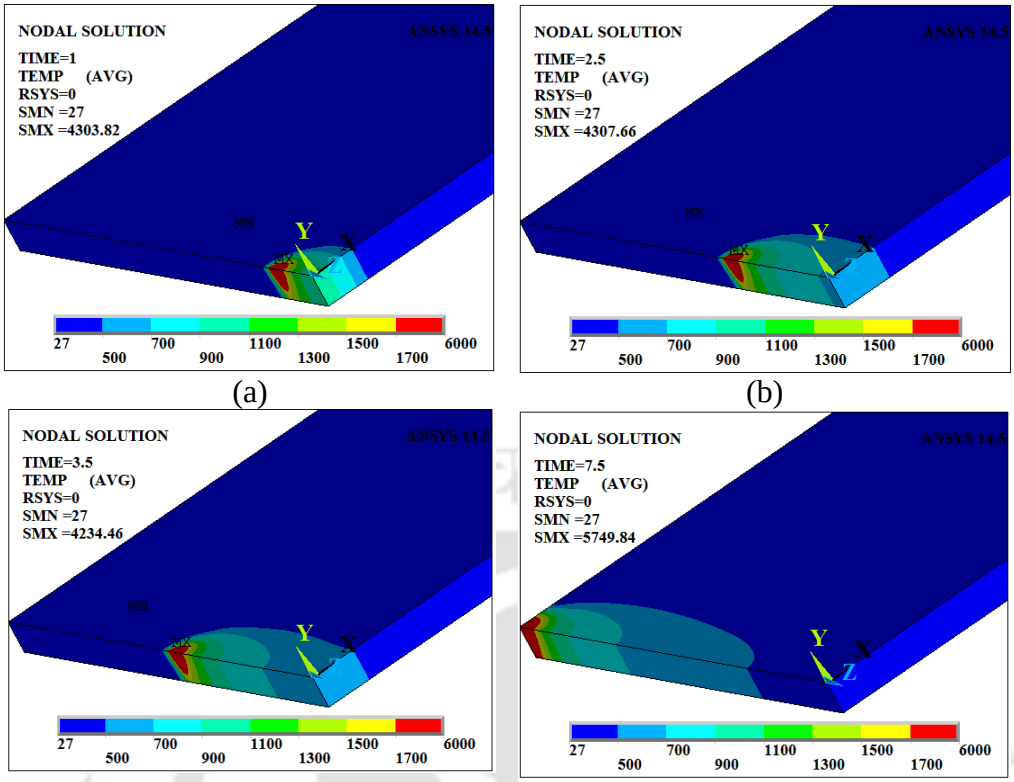

(a) (b)

(c) (d)

Fig. 8.9 Temperature distribution at (a) 1, (b) 2.5, (c) 3.5 and (d) 7.5 s time interval for 1000 W beam power and 400 mm/min welding speed

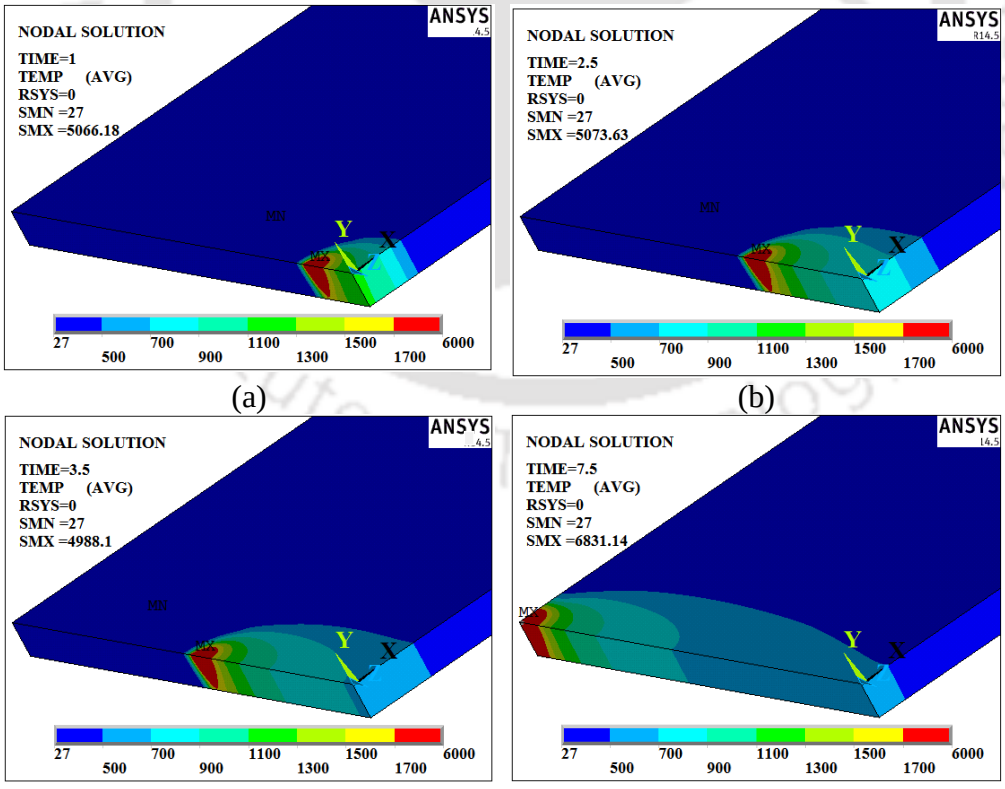

(a) (b)

(c) (d)

Fig. 8.10 Temperature distribution at (a) 1, (b) 2.5, (c) 3.5 and (d) 7.5 s time interval for 1200 W beam power and 400 mm/min welding speed

8.4.2.2 Effect of beam power

Figures 8.11(a), (b) and (c) show weld bead geometries at 800, 1000 and 1200 W beam power, respectively for a fixed 400 mm/min welding speed, 90° beam angle and 0.4 mm spot diameter. It is noticed from Fig. 8.11 that bead dimension changes with increasing beam power. A marked increase in penetration depth approximately 1.36 mm at 800 W to 1.96 mm at 1200 W beam power is noticed. Similarly, slight increment in bead width from 0.62 mm at 800 W to 1.38 mm at 1200 W is observed. It can be attributed to the fact that when beam power increases the power density is distributed widespread over top surface of the workpiece. Therefore, a slight increment in bead width is observed.

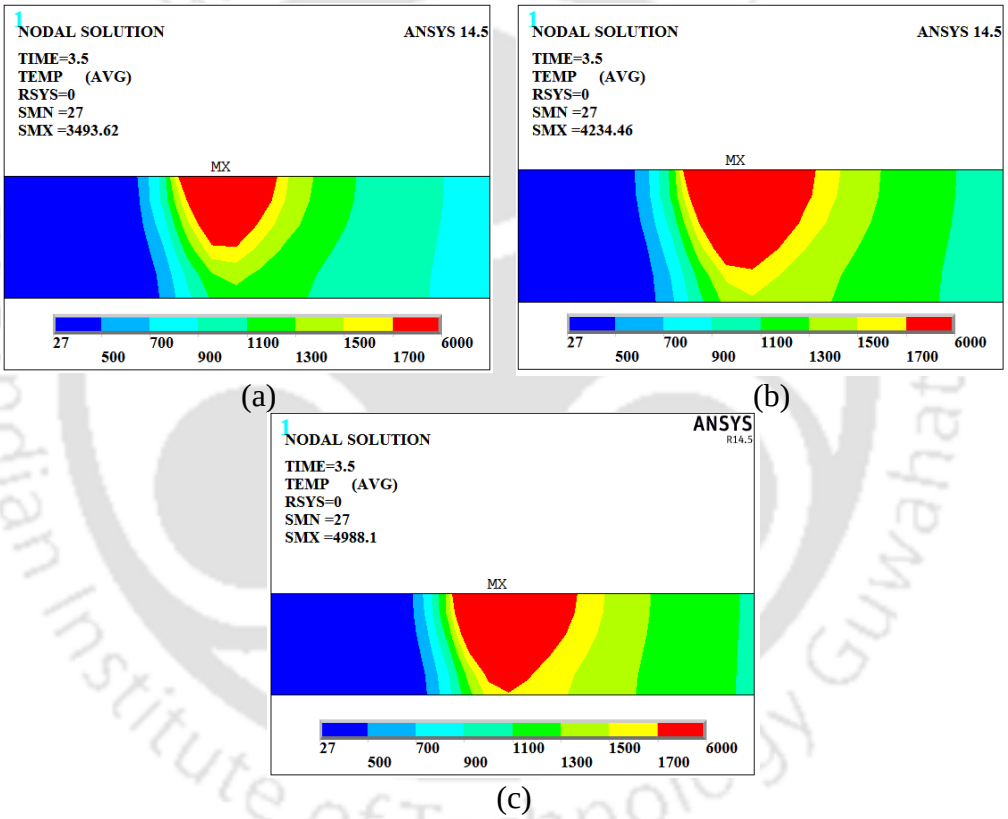

Fig. 8.11 Weld bead geometries at (a) 800, (b) 1000 and (c) 1200 W beam power for a fixed 400 mm/min welding speed

8.4.2.3 Effect of welding speed

The effect welding speed from 400 to 1200 mm/min is shown in Fig. 8.12 for a fixed 1200 W beam power, 90° beam angle and 0.4 mm spot diameter. From Fig. 8.12, it is observed that penetration depth decreases with increasing welding speed at a constant beam power. Full penetration into the base plate is obtained at 400 mm/min welding speed and 1200 W beam power as shown in Fig. 8.12(a). Also, there is considerable reduction in bead width at highest welding speed as shown in Fig. 8.12(c). It can be attributed to the fact that at

very high welding speed, the interaction time of the laser beam to the base material reduces which leads to lesser penetration depth.

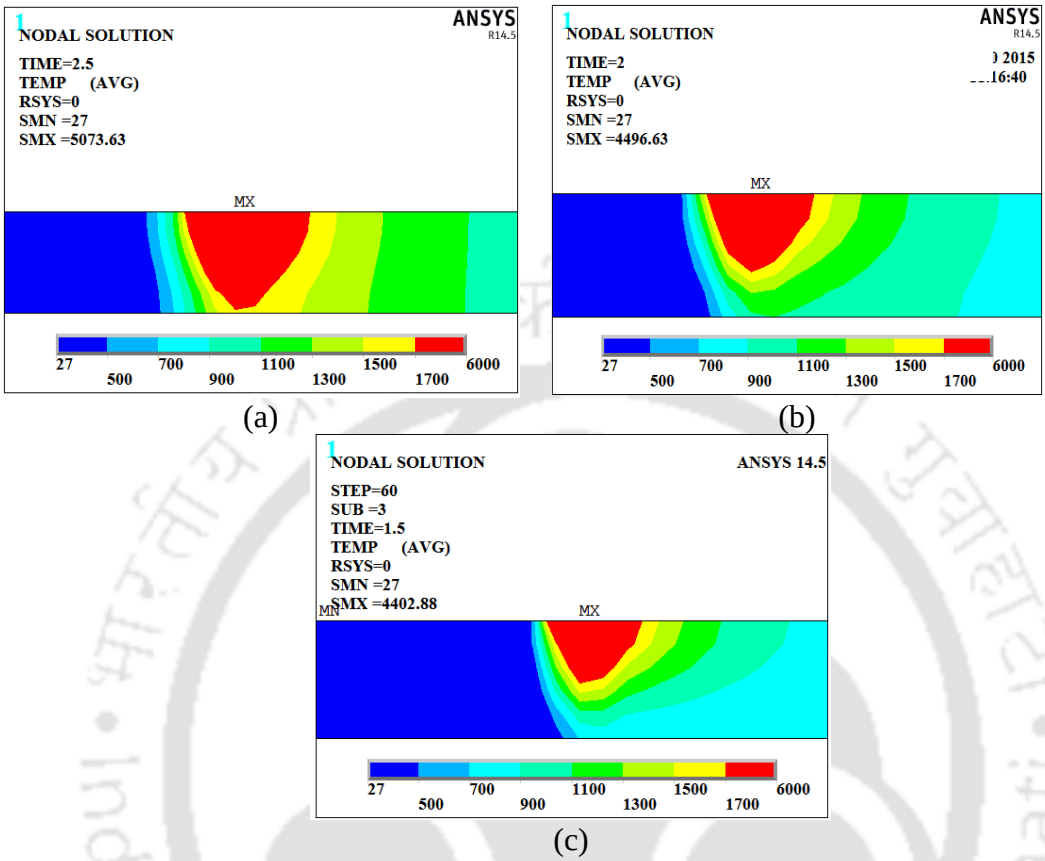

Fig. 8.12 Weld bead geometries at (a) 400, (b) 800 and (c) 1200 mm/min welding speed for a fixed 1200 W beam power

8.4.2.4 Distribution of peak temperature

Figure 8.13 shows the effect of laser beam power on temperature distribution on a particular node along (a) weld line and (b) transverse direction to weld line for 800 W, 1000 W and 1200 W beam power at 400 mm/min constant welding speed. It is observed that both peak temperature and temperature gradient increase as beam power increases due to highly concentrated power density over a very small area of spot. A non-linear relationship between the peak temperature and the beam power is noticed as shown in Figs. 8.13(a) and (b).

Figure 8.14 shows the effect of welding speed on peak temperature at a particular node along (a) weld line and (b) transverse direction to the weld line for 400, 800 and 1200 mm/min welding speed and constant 1200 W beam power. From Figs. 8.13 & 8.14, it is observed that the peak temperature along the weld line is very high and decreases continuously in transverse direction away from the weld line. In the welded zone, the peak temperature rises beyond the melting point temperature of Ti-6Al-4V alloy.

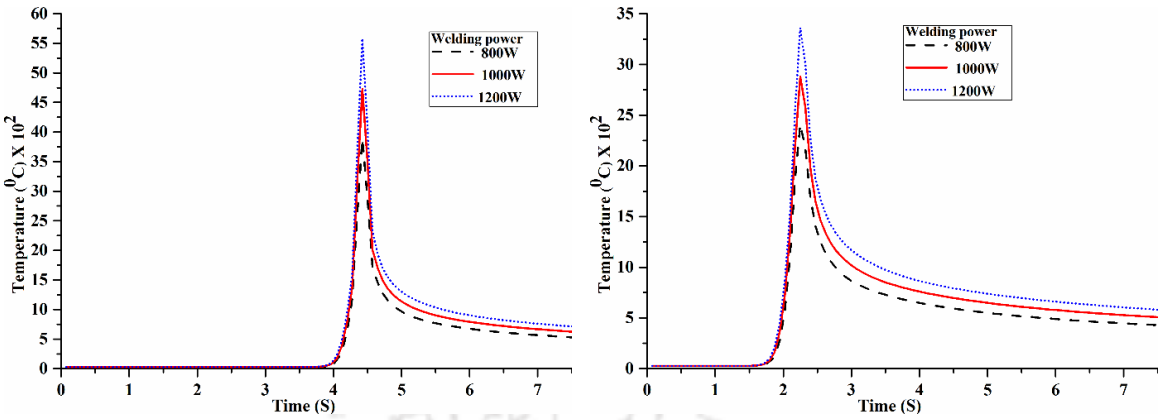

Fig. 8.13 Distribution of peak temperature at a node along the (a) weld line and (b) transverse direction to the weld line at different beam power and 400 mm/min constant welding speed

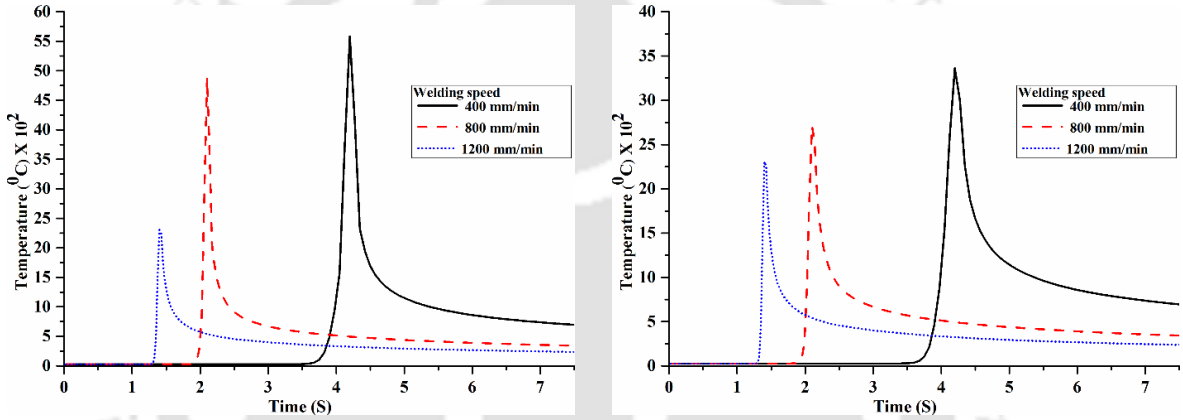

Fig. 8.14 Distribution of peak temperature at a node along the (a) weld line and (b) transverse direction to the weld line at different welding speed for 1200 W constant beam power

8.5 Conclusions

In the present study, a FEM based simulation of LBW process of Ti-6Al-4V workpiece is carried out for both spot welding and moving heat source. Also, two different heat sources i.e. double ellipsoidal and conical heat source are considered. The non-uniform finite element mesh save solution time during simulation and yields better results with reasonable convergency. The temperature dependent thermos-physical material properties play an important role in thermal analysis of LBW process. It is observed from the transient temperature profiles that the peak temperature increases with increasing laser beam power at a constant welding speed. A nonlinear relationship between laser beam power and peak temperature of the welded samples is observed. Also, weld bead geometry is affected by the beam power and both bead width and penetration depth increase with increasing beam power. It is observed that the peak temperature along the weld line is very high and decreases

continuously in transverse direction away from the weld line. The present model will be useful to reduce number of trial experiments before performing the actual experiment which helps in reducing experimental costs.

Chapter 9
Conclusions and scope for future work

9.1 Conclusions

In the present study, fiber laser heat source is successfully employed for conducting welding experiments in butt configuration on three different thicknesses (i.e. 5 mm, 2 mm and 1.5 mm) of Ti-6Al-4V alloy and 3 mm thick SS-316L plates at different welding conditions. The main objectives of the present study are to better understand the beam-material interaction phenomenon and to find out the relationship between weld bead geometry, microstructural features and mechanical properties of the welded samples under different welding conditions. A specially designed workpiece fixture with shielding gas delivery system is fabricated to minimize the distortion and movement of workpieces during welding. A FEM based numerical simulation is also carried out for laser beam welding of Ti-6Al-4V alloy. The main conclusions from experimental and simulation study are as follows

- The specially designed workpiece fixture with shielding gas delivery system efficiently protects the melt pool from environmental contaminations and the controlled flow rate of shielding gas efficiently reduces the oxidation issues in the weldments for both Ti-6Al-4V alloy and SS-316L workpieces.
- Crack and spatter free welds along with smooth, uniform, shiny beads having aesthetic bead appearance are observed in most of the cases. However, underfill, bead decay and excess penetration are also observed in few weldments due to imposed higher heat energy on the workpiece surface. The weld bead is almost symmetrical about the centre line of fusion zone. Moreover, lack of symmetricity is only observed at higher beam power at root side of weld bead.
- From experimental analysis it is observed that penetration depth in base plate is primarily controlled by power density on workpiece surface. However, width of fusion zone and size of heat affected zones depend on line energy. In present study, almost linear relationship between FZ_{UP}, HAZ_{UP} and HAZ_{Low} with line energy is observed irrespective of penetration depth in the base plate. However, in transition from partial to full penetration in the base plate, the size of HAZ_{Mid} is slightly reduced and further increases linearly with increased line energy. Also, the upper width of FZ_{UP} is larger than both FZ_{Mid} and FZ_{Low} for all cases. It is mainly due to the prominent flow of molten metal towards the upper part of melt pool as compared to

lower part which disrupts the keyhole shape starting from bigger width at upper part to reduced width at weld pool's lower part.

- Laser beam welding power shows positive effect on bead features whereas welding speed shows inverse effect on it. However, defocused position of laser beam shows diverse effect on bead geometry. The fusion zone area is not affected by the defocused position of laser beam in case of 5 mm thick plates of Ti-6Al-4V alloy. However, it shows diverse effect on bead features in case of SS-316L plates due to reduced power density with increased spot diameter on workpiece surface.
- Line energy is a very important parameter in laser welding process. When line energy is too low, lack of penetration occurs in the base plate. While at high line energy, excessive penetration and underfill weld defects are generated in the weld bead.
- Heat input per unit length for achieving full penetration in the base plate for 5 mm thick Ti-6Al-4V alloy is higher than the heat input required for full penetration in 2 mm and 1.5 mm thick plates. Hence, the size of FZ, FZ area and HAZ sizes are comparatively smaller in case of 2 mm and 1.5 mm than 5 mm thick plates. For achieving deep penetration and smaller grain size in FZ the defocussed position of laser beam should be kept below from the workpiece surface in case of 5 mm thick plates. Moreover, it is not essential for lower thickness of 2 and 1.5 mm thick plates of Ti-6Al-4V alloy.
- To achieve an acceptable bead profile and mechanical properties, the control over weld bead shape is important. The mechanical properties of weldments are highly influenced by bead shape. The weld bead shape also affects the weld metal solidification behaviour along with line energy which imposes on the workpiece surface. From the experimental study of 2 mm thick Ti-6Al-4V alloy plates it is observed that the higher line energy yields X-shaped weld bead whereas lower line energy yields T-shaped weld bead. From the comparative analysis it is observed that T-shaped welding condition is favourable for achieving smaller sized FZ, HAZ, FZ area and acceptable bead hardening.
- Non-uniform microstructural variations are observed from FZ towards BMZ in weld bead due to the change in cooling rate. During cooling, both FZ and HAZ transform into either martensitic α′ or other morphology of martensitic α′ phase like massive α (α_m), transformed α (i.e. blocky α) or Widmanstatten α. The amount of martensitic α′ phase in FZ and HAZ depends on cooling rate below T_β temperature. At all welding

conditions, microstructural evaluation in FZ are consistent with the continuous cooling transformation curve of Ti-6Al-4V alloy.

- The microstructural analysis of weld bead reflects the evaluation of α′ martensitic phase in the fusion zone of Ti-6Al-4V alloy. It reflects the high self-quenching characteristics of laser beam welding process. Whereas a combination of α′ martensite, transformed α, original α and β phases are observed in the HAZ which is near to BMZ. The shape of α′ martensite looks like needle shaped. However, its shape changes from needle shaped to plate like morphology with increasing line energy. The length and thickness of α′ lamella depends on cooling rate. Lower cooling rate promotes the broadening of α′ lamella whereas faster cooling rate yields basket-weave structure in the FZ.
- In the present study, most of the welded samples are defect free. Although, in few welded samples small amount of underfill, excess penetration and porosity are observed in the weld bead. Porosity is a major and severe weld defect which is frequently observed in deep penetration LBW process. It severely deteriorates the mechanical properties of the welded specimens. Ti-6Al-4V alloys are more susceptible to porosity formation during fusion welding. The formation of porosity in keyhole mode of LBW is still not well understood. There is a discrepancy in the understanding of actual reason for the formation of porosity in the weld bead. The propensity of porosity formation in the present study is extensively minimized by providing shielding gas. However, porosities are still found in solidified weld bead of few welded samples. Two different kind of welding porosities i.e. metallurgical and characteristic pores are observed during deep penetration LBW of Ti-6Al-4V alloy. The metallurgical pores are formed due to the trapping of shielding as well as hydrogen gas in the solidified melt pool and the characteristic pores are formed due to the instability of the keyhole at combination of higher beam power and lower welding speed. However, their sizes are within acceptable range (< 0.4 mm) as per BS EN: 4678:2011 European standards. It is observed that the keyhole stability is very critical issue to obtain consistently high quality of weldment.
- Maximum hardness is observed in the fusion zone for Ti-6Al-4V alloy and its value continuously decreases towards BMZ due to the reduction of amount α′ martensite from almost 100 % in the FZ to nearly zero in near BMZ. The microhardness values in the FZ are increased with decreasing line energy for all cases due to the formation of higher amount of α′ martensite and reduced size of α′ lamella.

- The tensile strength of the welded samples is lower than Ti-6Al-4V alloy BM for most of the welding conditions due to the presence of micropores in the weld bead. However, in few cases, the tensile strength of weldments is comparable to the Ti-6Al-4V alloy base metal. Moreover, it is well in accordance with the relationship between microstructure and mechanical properties of the weldments. The percentage elongation of the welded specimens is lower in all the cases than the base metal owing to the presence of brittle nature of α′ martensitic phase in FZ. However, ductile mode of fracture failure is observed in both the base metal as well as in welded specimen. The suitable heat treatment procedure must be employed to enhance the ductility of welded specimens.
- Central composite rotatable design of RSM is successfully employed to obtain the relationship between input variables and output responses in case of 5 mm thick Ti-6Al-4V alloy and 3 mm thick SS-316L plates. Further, the process parameters are efficiently optimized to enhance the weld quality.
- The finer microstructure having more amounts of austenite and a lesser quantity of ferrite is developed in FZ when the defocused position kept below the workpiece surface. However, coarser microstructure is formed when defocused position kept on or above the workpiece surface in case of SS-316L plates.
- In case of SS-316L plates, the tensile strength is increased with increased beam power and welding speed up to center level afterward it starts decreasing due to the differences in developed microstructure in fusion zone. However, ductile mode of fracture failure is observed in both the base metal as well as welded specimen.
- A FEM based numerical simulation of LBW process is carried out for transient thermal analysis of Ti-6Al-4V workpiece by employing double ellipsoidal and 3-D cone-shaped volumetric heat source models. There is a non-linear relationship between peak temperature and laser beam power is noticed, possibly due to the variation of Ti-6Al-4V alloy's absorption coefficient with temperature. The present model can be useful to reduce the number of trial experiments before performing the actual experiment which helps in reducing experimental cost.

9.2 Scope for future work

In the present study, different thicknesses of Ti-6Al-4V alloy and 3 mm thick SS-316L plates are welded and studied with special attention to the microstructural changes and mechanical properties. Different bead features and mechanical properties are tested and compared at different welding conditions to identify the optimum value of the welding parameters to minimize the size of HAZ, FZ width and area and to maximize the mechanical properties. However, more studies are needed in the aspect of joining technology on the Ti-6Al-4V alloy and SS-316L.

- Thicker workpiece may be considered for further experimental investigation using fibre laser.
- More variations in defocusing distances may be studied.
- Other mechanical properties such as fatigue, impact and creep may be considered.
- Suitable heat treatment process after welding may be employed to enhance the ductility of the weldments.
- Experimental investigation of fibre laser welding of dissimilar materials Ti-6Al-4V and SS-316L may be studied.

References

1. Acherjee, B., Kuar, A. S., Mitra, S., Misra, D., Acharyya, S., 2012. Experimental investigation on laser transmission welding of PMMA to ABS via response surface modeling. Opt. Laser Technol. 44, 1372–1383.
2. Adams, C. M. Jr.,1958. Cooling rates and peak temperatures in fusion welding. Weld. J. 37, 210s–215s.
3. Ahmed, T., Rack, H. J., 1998. Phase transformations during cooling in α+β titanium alloys. Mater. Sci. Eng. A 243, 206–211.
4. Ahn, J., Chen, L., Davies, C.M., Dear, J.P., 2016. Parametric optimisation and microstructural analysis on high power Yb-fibre laser welding of Ti–6Al–4V. Opt. Lasers Eng. 86, 156–171.
5. Ai, Y., Jiang, P., Shao, X., Li, P., Wang, C., 2017. A three-dimensional numerical simulation model for weld characteristics analysis in fiber laser keyhole welding. Int. J. Heat Mass Transf. 108, 614–626.
6. Akbari, M., Saedodin, S., Toghraie, D., Razavi, R. K., 2014. Experimental and numerical investigation of temperature distribution and melt pool geometry during pulsed laser welding of Ti6Al4V alloy, Opt. Laser Technol. 59, 52-59.
7. Akman, E., Demir, A., Canel, T., Sınmazcelik, T., 2009. Laser welding of Ti6Al4V titanium alloys. J. Mater. Process. Technol. 209, 3705–3713.
8. Alcock, J. A., Baufeld, B., 2017. Diode laser welding of stainless steel 304L. J. Mater. Process. Technol. 240, 138–144.
9. Aleksander, L., 2012. Laser welding of titanium alloy Ti6Al4V using a disk laser. Int. Virtual J. Mach. Technol. Mater. 7, 53–56.
10. Anawa, E. M., Olabi A. G., 2008a. Using Taguchi method to optimize welding pool of dissimilar laser-welded components. Opt. Laser Technol. 40:379–388.
11. Anawa, E. M., Olabi, A. G., 2008b. Optimization of tensile strength of ferritic/austenitic laser-welded components. Opt. Lasers Eng. 46, 571–577.
12. AnsysTM 14.5 Manual.
13. Asibu, E. K., 2009. Principles of Laser Materials Processing. John Wiley & Sons, USA.
14. Assuncao, E., Quintino, L., Miranda, R., 2010. Comparative study of laser welding in tailor blanks for the automotive industry. Int. J. Adv. Manuf. Technol. 49, 123–131.
15. ASTM E 112-113: Standard Test Methods for Determining Average Grain Size.
16. ASTM E3: Standard Guide for Preparation of Metallographic Specimens, 2011.

17. ASTM E8/E8M, Standard Test Methods for Tension Testing of Metallic Materials. 2013. ASTM International, West Conshohocken.
18. Baeslack, W. A., Banas, C. M., 1981. A Comparative evaluation of LBW and GTAW in high temperature titanium alloys. Welding Research Supplement, 60, 121-130.
19. Bag, S., De, A., 2010. Probing reliability of transport phenomena based heat transfer and fluid flow analysis in autogeneous fusion welding process, Metall. Mater. Trans. A 41, 2337–2347.
20. Baghjari, S. H., Akbari Mousavi, S. A. A., 2013. Effects of pulsed Nd:YAG laser welding parameters and subsequent post-weld heat treatment on microstructure and hardness of AISI 420 stainless steel. Mater. Des. 43, 1–9.
21. Balasubramanian, K. R., Buvanashekaran, G., Sankaranarayanasamy, K., 2007. Mathematical and ANN modeling of Nd: YAG laser welding of thin SS sheets. J. Manuf. Eng. 6, 56-60.
22. Balasubramanian, K. R., Shanmugam, S., Buvanashekaran, G., Sankaranarayanasamy, K., 2008. Numerical and experimental investigation of laser beam welding of AISI 304 stainless steel sheet. Adv. Prod. Eng. Manag. 3, 93–105.
23. Balasubramanian, T. S., Balasubramanian, V., Manickam, M. A. M., 2011. Fatigue crack growth behaviour of gas tungsten arc, electron beam and laser beam welded Ti- 6Al-4V alloy. Mater. Des. 32, 4509–4520.
24. Banas, C. M., 1971. 11th IEEE Symposium on Electron ion laser beam technology. UARL Report, 125.
25. Baruah, M., Bag, S., 2016. Influence of heat input in micro welding of titanium alloy by micro plasma arc. J. Mater. Process. Technol. 231, 100–112.
26. Batahgy, A. M. El., Khourshid A. F., Sharef T., 2011. Effect of laser beam welding parameters on microstructure and properties of duplex stainless steel. Mater. Sci. Appl. 2, 1443–1451.
27. Behler, K., Berkmanns, J., Ehrhardt, A. U., Frohn, W., 1998. Laser beam welding of low weight materials and structures. Mater. Des.18, 261–267.
28. Benjamin J., Katherasan, D., Sathiya, P., Srinivasa, M. C. V., 2012. Weld metal characterization of 316L(N) austenitic stainless steel by electron beam welding process. Int. J. Engg. Sci. Technol. 4,169-176.
29. Benyounis, K.Y., Olabi, A. G., Hashmi, M. S. J., 2005. Effect of laser welding parameters on the heat input and weld-bead profile. J. Mater. Process. Technol. 164–165, 978–985.

30. Bhargava, P., Paul, C. P., Mundra, G., Premsingh, C. H., Mishra, S. K., Nagpure, D., Kumar, A., Kukreja, L. M., 2014. Study on weld bead surface profile and angular distortion in 6mm thick butt weld joints of SS304 using fiber laser. Opt. Lasers Eng. 53, 152–157.
31. Biswas, P., Mahapatra, M. M., Mandal, N. R., 2010. Numerical and experimental study on prediction of thermal history and residual deformation of double-sided fillet welding. Proc. Inst. Mech. Eng. Part B J. Eng. Manuf. 224, 125–134.
32. Boyer, H. E., Collings, E.W., Welsch, G., 1994. Materials Properties Handbook: Titanium Alloys. ASM International, OH.
33. Brewer, W. D., Bird, R. K., Wallace, T. A., 1998. Titanium alloys and processing for high speed aircraft. Mater. Sci. Eng. A 243, 299–304.
34. British Standards Institution., 1997. BS EN 1321 Destructive Tests on Welds in Metallic Materials : Macroscopic and Microscopic Examination of Welds.
35. Brock, C., Hohenstein, R., Schmidt, M., 2014 Mechanisms of vapour plume formation in laser deep penetration welding. Opt Lasers Eng. 58, 93-101.
36. BS:EN: 4678:2011 Standard, Aerospace series. Weldments and Brazements for Aerospace Structures. Joints of Metallic Materials by Laser Beam Welding. Quality of Weldments.
37. Caiazzo, F., Alfieri, V., Corrado, G., Cardaropoli, F., Sergi, V., 2013. Investigation and optimization of laser welding of Ti-6Al-4V titanium alloy plates. J. Manuf. Sci. Eng. 135, 610121–8.
38. Caiazzo, F., Cardaropoli, F., Alfieri, V., Sergi, V., Argenio, P., Barbieri, G., 2017. Disk-laser Welding of Ti-6Al-4V titanium alloy plates in T-joint configuration. Procedia Eng. 183, 219–226.
39. Caiazzo, F., Curcio, F., Daurelio, G., Memola Capece Minutolo, F., 2004. Ti6Al4V sheets lap and butt joints carried out by CO2 laser: mechanical and morphological characterization. J. Mater. Process. Technol. 149, 546–552.
40. Campanelli, S. L., Casalino, G., Mortello, M., Angelastro, A., Ludovico, A. D., 2015. Microstructural characteristics and mechanical properties of Ti6Al4V alloy fiber laser welds. Procedia CIRP 33, 428–433.
41. Cao, X., Jahazi, M., 2009. Effect of welding speed on butt joint quality of Ti–6Al–4V alloy welded using a high-power Nd:YAG laser. Opt. Lasers Eng. 47, 1231–1241.

42. Casalino, G., Curcio, F., Memola, F., Minutolo, C., 2005. Investigation on Ti6Al4V laser welding using statistical and Taguchi approaches. J. Mater. Process. Technol. 167, 422–428.
43. Casalino, G., Mortello, M., Campanelli, S. L., 2015. Ytterbium fiber laser welding of Ti6Al4V alloy. J. Manuf. Process. 20, 250–256.
44. Chen, G., Zhang, M., Zhao, Z., Zhang, Y., Li, S., 2013. Measurements of laser-induced plasma temperature field in deep penetration laser welding. Opt. Laser Technol. 45, 551–557.
45. Chen, H. C., Pinkerton, A. J., Li, L., Liu, Z., Mistry, A. T., 2011a. Gap-free fibre laser welding of Zn-coated steel on Al alloy for light-weight automotive applications. Mater. Des. 32, 495–504.
46. Chen, H. C., Pinkerton, A.J., Li, L., 2011b. Fibre laser welding of dissimilar alloys of Ti-6Al-4V and Inconel 718 for aerospace applications. Int. J. Adv. Manuf. Technol. 52, 977–987.
47. Chen, W., Ackerson, P., Molian, P., 2009. CO2 laser welding of galvanized steel sheets using vent holes. Mater. Des. 30, 245–251.
48. Cheng, Y., Jin, X., Li, S., Zeng, L., 2012. Fresnel absorption and inverse bremsstrahlung absorption in an actual 3D keyhole during deep penetration CO2 laser welding of aluminum 6016. Opt. Laser Technol. 44, 1426–1436.
49. Cho, W. I., Na, S. J., Thomy, C., Vollertsen, F., 2012. Numerical simulation of molten pool dynamics in high power disk laser welding. J. Mater. Process. Technol. 212, 262–275.
50. Chung, B. G., Rhee, S., Lee, C. H., 1999. The effect of shielding gas types on CO2 laser tailored blank weldability of low carbon automotive galvanized steel. Mater. Sci. Eng. A, 272(2), 357-362.
51. Costa, A., Miranda, R., Quintino, L., Yapp, D., 2007. Analysis of beam material interaction in welding of titanium with fiber lasers. Mater. Manuf. Process. 22, 798–803.
52. Dawes, C., 1992. Laser welding. McGraw-Hill, Inc, NY.
53. Deng, D., Murakawa, H., 2006. Numerical simulation of temperature field and residual stress in multi-pass welds in stainless steel pipe and comparison with experimental measurements, Comput. Mater. Sci. 37, 269–277.
54. Derringer, G., 1980. Simultaneous optimization of several response variables. J. Qual. Technol. 12, 214–219.
55. Donachie, M. J., 2000. 2nd Edition, Titanium : A Technical Guide. ASM International.

56. Dowden, J., Davis, M., Kapadia, P., 1983. Some aspects of the fluid dynamics of laser welding. J. Fluid Mech. 126, 123.
57. Ducharme, R. F., Kapadia, P., Dowdene, J., 1992. A mathematical model of the defocusing of the laser light above a workpiece in laser material processing. Proceeding ICALEO, 187.
58. Duley, W.W., 1998. Laser welding. Wiley-Interscience.
59. Elmer, J. W., Palmer, T. A., Babu, S. S., Zhang, W., DebRoy, T., 2004. Phase transformation dynamics during welding of Ti–6Al–4V. J. Appl. Phys. 95, 8327–8339.
60. Filip, R., Kubiak, K., Ziaja, W., Sieniawski, J., 2003. The effect of microstructure on the mechanical properties of two-phase titanium alloys. J. Mater. Process. Technol. 133, 84–89.
61. Frewin, M. R., Scott, D. A., 1999. Finite element model of pulsed laser welding, Welding Research Supplement, 78, 15-22.
62. Gao, X. L., Zhang, L. J., Liu, J., Zhang, J. X., 2014a. Effects of weld cross-section profiles and microstructure on properties of pulsed Nd:YAG laser welding of Ti6Al4V sheet. Int. J. Adv. Manuf. Technol. 72, 895–903.
63. Gao, X. L., Zhang, L. J., Liu, J., Zhang, J. X., 2014b. Porosity and microstructure in pulsed Nd:YAG laser welded Ti6Al4V sheet. J. Mater. Process. Technol. 214, 1316–1325.
64. Gaspar, B., 2012. Microstructural characterization of Ti-6Al-4V and its relationship to sample geometry PhD Thesis, Materials Engineering Dept., Cal Poly – San Luis Obispo.
65. Goldak, J., Chakravarti, A., Bibby, M., 1984. A new finite element model for welding heat sources, Metallurgical Transactions B, 15, 299-305.
66. Gu, H., Yin, G., Shulkin, B., 2011. Laser beam welding of nitride steel components. Phys. Procedia 12, 40–45.
67. Hanson, F., Duley, W., 1994. Attenuation of laser radiation by particles during laser material processing. J. Laser Appl. 6: 137.
68. Hao, K., Li, G., Gao, M., Zeng, X., 2015. Weld formation mechanism of fiber laser oscillating welding of austenitic stainless steel. J. Mater. Process. Technol. 225, 77–83.
69. Hayajneh, M. T., Al-Dwairi, A. F., Obeidat, S. F., 2018. Optimization and control of bending distortion of submerged arc welding I-beams. J. Constr. Steel Res. 142, 78–85.
70. Heidecker, E., Schafer, J. H., Uhlenbusch, J., Viol, W., 1988. Time-resolved study of a laser-induced surface plasma by means of a beam-deflection technique. J. Appl. Phys. 64: 2291.

71. Hilton P, Blackburn J, Chong P. Welding of Ti–6Al–4V with fibre delivered laser beams. 2007. In: Proceedings of the 26th international congress on applications of lasers and electro-optics. Orlando, FL: Laser Institute of America, 887–895.
72. Hong, K. M., Shin, Y.C., 2016. Analysis of microstructure and mechanical properties change in laser welding of Ti6Al4V with a multiphysics prediction model. J. Mater. Process. Technol. 237, 420–429.
73. Hongping, G., Yin, G., Shulkin, B., 2011. Laser beam welding of nitride steel components. Physics Procedia, 12, 40-45.
74. Huang, J. L., Warnken, N., Gebelin, J. C., Strangwood, M., Reed, R. C., 2012. On the mechanism of porosity formation during welding of titanium alloys. Acta Mater. 60, 3215–3225.
75. Huiqiang, W., Jicai, F., Jingshan, H., 2004. Microstructure evolution and fracture behaviour for electron beam welding of Ti–6Al–4V. Bull. Mater. Sci 27, 387–392.
76. ISBN: 978-1118-14692-7.
77. Jin, X., Li, L., 2004. An experimental study on the keyhole shapes in laser deep penetration welding. Opt. Lasers Eng. 41, 779–790.
78. Joshi, V. A., 2006. Titanium Alloys: An Atlas of Structures and Fracture Features. Taylor & Francis, NY.
79. Kabir, A. S. H., Cao, X., Medraj, M., Wanjara, P., Cuddy, J., Birur, A., 2010. Effect of welding speed and defocusing distance on the quality of laser welded Ti-6Al-4V. Mater. Sci. Technol. 2787–2797.
80. Kaflan, A. F. H., Wiklund, G., 2009. Advanced welding analysis methods applied to heavy section welding with a 15 kW fiber laser. Welding in the World, 53: 295-300.
81. Karimzadeh, F. M., Salehi, A., Saatchi, M., 2005. Effect of micro plasma arc welding process parameters on grain growth and porosity distribution of thin sheet Ti6Al4V alloy weldment, Mater. Manuf. Process. 20, 205–219.
82. Kashaev, N., Ventzke, V., Fomichev, V., Fomin, F., Riekehr, S., 2016. Effect of Nd:YAG laser beam welding on weld morphology and mechanical properties of Ti–6Al–4V butt joints and T-joints. Opt. Lasers Eng. 86, 172–180.
83. Katayama, S., Kawahito, Y., Mizutani, M., 2010. Elucidation of laser welding phenomena and factors affecting weld penetration and welding defects. Phys. Procedia 5, 9–17.
84. Katayama, S., Nagayama, H., Mizutani, M., Kawahito, Y., 2009. Fibre laser welding of aluminium alloy. Weld. Int. 23, 744–752.

85. Kawahito, Y., Kinoshita, K., Matsumoto, N., Mizutani, M., Katayama, S., 2007a. Interaction between laser beam and plasma/plume induced in welding of stainless steel with ultra-high power density fiber laser. Q. J. Japan Weld. Soc. 25, 461–467.
86. Kawahito, Y., Kinoshita, K., Matsumoto, N., Mizutani, M., Katayama, S., 2007b. High-speed observation and spectroscopic analysis of laser-induced plume in high-power fiber laser welding of stainless steel. Q. J. Japan Weld. Soc. 25, 455–460.
87. Kawahito, Y., Mizutani, M., Katayama, S., 2009. High quality welding of stainless steel with 10 kW high power fibre laser. Sci. Technol. Weld. Join. 14, 288–294.
88. Khaled, T., 1994. An investigation of pore cracking in titanium welds. J. Mater. Eng. Perform. 3, 21–36.
89. Khan, M.M.A., Romoli, L., Fiaschi, M., Dini, G., Sarri, F., 2012. Laser beam welding of dissimilar stainless steels in a fillet joint configuration. J. Mater. Process. Technol. 212, 856–867.
90. Khorram, A., Ghoreishi, M., Reza, M., Yazdi, S., Moradi, M., 2011. Optimization of bead geometry in CO2 laser welding of Ti6Al4V using response surface methodology. Engineering 3, 708-712.
91. Khorram, A., Soleymani Yazdi, M.R., Ghoreishi, M., Moradi, M., 2010. Using ANN approach to investigate the weld geometry of Ti6Al4V titanium alloy. Int. J. Eng. Technol. 2, 491–498.
92. Ki, H., Mohanty, P. S., Mazumder, J., 2002. Multiple reflection and its influence on keyhole evolution. J. Laser Appl. 14, 39–45.
93. Kim, C. H., Ahn, D.C., 2012. Coaxial monitoring of keyhole during Yb:YAG laser welding. Opt. Laser Technol. 44, 1874–1880.
94. Kou, S., 2002. Welding Metallurgy. 2nd Edition John Wiley & Sons, Hoboken, New Jersey.
95. Kuhlman, G. W., Chakravorty, A. K., Yu, T. L., Pishko, R., Terlinde, G., 1987. Effect of microstructure on fracture toughness and fatigue crack growth rates in titanium alloys TMS-AIME annual symposium, 171-192.
96. Kumar, C., Das, M., Paul, C. P., Singh, B., 2017c. Experimental investigation and metallographic characterization of fiber laser beam welding of Ti-6Al-4V alloy using response surface method. Opt. Lasers Eng. 95, 52–68.
97. Kumar, N., Mukherjee, M., Bandyopadhyay, A., 2017a. Study on laser welding of austenitic stainless steel by varying incident angle of pulsed laser beam. Opt. Laser Technol. 94, 296–309. Kuryntsev S. V, Morushkin A. E, Gilmutdinov A. K. Fiber laser

welding of austenitic steel and commercially pure copper butt joint. Opt. Lasers Eng. 2017;90:101-109.

98. Kumar, N., Mukherjee, M., Bandyopadhyay, A., 2017b. Comparative study of pulsed Nd:YAG laser welding of AISI 304 and AISI 316 stainless steels. Opt. Laser Technol. 88, 24–39.
99. Kuryntsev, S. V., Gilmutdinov, A. K., 2015. Welding of stainless steel using defocused laser beam. J. Constr. Steel Res. 114, 305–313.
100. Larson, N. E., Meredish W. F., 1990. Shielding gas selection manual, Union Carbide Industry Gases Technology Corp: 10.
101. Leyens, C., Peters, M., 2003. Titanium and Titanium Alloys: Fundamentals and Applications. Wiley-VCH Verlag GmbH & Co. KGaA, Weinheim, FRG.
102. Li, C., Ding-Yong, H., Fu, G., Xiao-Yan, L., Jian-Min, J., 2010. Effect of fiber laser–MIG hybrid process parameters on weld bead shape and tensile properties of commercially pure titanium. Mater. Manuf. Process. 25, 1309–1316.
103. Li, C., Muneharua, K., Takao, S., Kouji, H., 2009. Fiber laser-GMA hybrid welding of commercially pure titanium. Mater. Des. 30, 109–114. Li, Z., Gobbi, S.L., Norris, I., Zolotovsky,
104. Li, Z., Gobbi, S.L., Norris, I., Zolotovsky, S., Richter, K.H., 1997. Laser welding techniques for titanium alloy sheet. J. Mater. Process. Technol. 65, 203–208.
105. Lifang, M., Dongbing, Y., Jiming, Y., Chen, G., Hong, G. Xiao., 2013. Comparative analysis on overlap welding properties of fiber laser and CO_2 laser for body-in-white sheets. Mater. Des. 49, 905–912.
106. Lima, M. S. F., 2005. Laser beam welding of titanium nitride coated titanium using pulse shaping. Mater. Res. 8, 323-328.
107. Lisiecki, A., 2012a. Laser welding of titanium alloy Ti6Al4V using a disk laser. Int. Virtual J. Mach. Technol. Mater. 7, 53–56.
108. Lisiecki, A., 2012b. Welding of titanium alloy by different types of lasers. Arch. Mater. Sci. Eng. 58, 209–218.
109. Liu, X. B., Pang M., Zhang, Z. G., Ning, W. J., Zheng, C. Y,, Yu, G., 2007. Characteristics of deep penetration laser welding of dissimilar metal Ni-based cast super alloy K418 and alloy steel 42CrMo. Opt. Lasers Eng. 45, 929-934.
110. Lundback, A., Runnemalm, H., 2005. Validation of three-dimensional finite element model for electron beam welding of inconel 718, Sci. Technol. Weld. Join. 10, 717-724.

111. Mahrle, A., Schmidt, J., 2002. The influence of fluid flow phenomena on the laser beam welding process. Int. J. Heat Fluid Flow 23, 288–297.
112. Manonmani, K., Murugan, N., Buvanasekaran, G., 2007. Effects of process parameters on the bead geometry of laser beam butt welded stainless steel sheets. Int. J. Adv. Manuf. Technol. 32, 1125–1133.
113. Masoumi, M., Marashi, S. P. H., Pouranvari, M., 2010. Metallurgical and mechanical characterization of laser spot welded low carbon steel sheets. Steel Res. Int. 81, 1144–1151.
114. Mastrocinque E., Corrado G., Caiazzo F., Pasquino N., Sergi V., 2012. Effect of defocusing on bead-on-plate of Ti6Al4V by Yb:YAG disk laser. Adv. Mater Res. 383-390, 6258-6264.
115. Matsunawa, A., 1990. Physical Phenomena and their interpretation in laser material processing. Proceeding ICALEO 90, SPIE 1601: 313.
116. Matsunawa, A., Kim, J. D., Seto, N., Mizutani, M., Katayama, S., 1998. Dynamics of keyhole and molten pool in laser welding. J. Laser Appl. 10, 247–254.
117. Miranda, R., Costa, A., Quintino, L., Yapp, D., Iordachescu, D., 2009. Characterization of fiber laser welds in X100 pipeline steel. Mater. Des. 30: 2701-2707.
118. Mohandas, T., Banerjee, D., Kutumba Rao, V. V., 1999. Fusion zone microstructure and porosity in electron beam welds of an α+β titanium alloy. Metall. Mater. Trans. A 30, 789–798.
119. Mohandas, T., Banerjee, D., Kutumba Rao, V.., 1998. Observations on impact toughness of electron beam welds of an α+β titanium alloy. Mater. Sci. Eng. A 254, 147–154.
120. Montgomery, D. C., 2012. Design and Analysis of Experiments. John Wiley & Sons, Inc. 8th
121. Mukherjee, M., Saha, S., Pal, T.K., Kanjilal, P., 2015. Influence of modes of metal transfer on grain structure and direction of grain growth in low nickel austenitic stainless steel weld metals. Mater. Charact. 102, 9–18.
122. Na, S. J., Lee, S. Y., 1987. A Study on the three-dimensional analysis of the transient temperature distribution in gas tungsten arc welding. Proc. Inst. Mech. Eng. Part B Manag. Eng. Manuf. 201, 149–156.
123. Nath, A. K., Sridhar, R., Ganesh, P., Kaul, R., 2002. Laser power coupling efficiency in conduction and keyhole welding of austenitic stainless steel. Sadhana 27, 383–392.

124. Nguyen, N. T., Mai, Y. W., Simpson, S., Ohta, A., 2004. Analytical approximate solution for double ellipsoidal heat source in finite thick plate. Welding Journal, 82 -93.
125. Nirsanametla, Y., Bag, S., Paul, C. P., Kukreja, L. M., 2014. Efficient finite element modeling of fiber laser welding process under conduction regime on 316 stainless steel plate. Int. J. Curr. Eng. Technol. 31–36.
126. Nirsanametla, Y., Bag, S., Paul, C. P., Kukreja, L. M., 2015. Fiber laser welding in a controlled Inert gas atmosphere: an experimental and numerical investigation, in: Lasers Based manufacturing: Topics in Mining, Metallurgy and Materials Engineering. Springer, New Delhi. doi:10.1007/978-81-322-2352-8_20.
127. Olabi, A.G., Casalino, G., Benyounis, K.Y., Rotondo, A., 2007. Minimisation of the residual stress in the heat affected zone by means of numerical methods 28, 2295–2302.
128. Pakniat, M., Ghaini, F.M., Torkamany, M.J., 2016. Hot cracking in laser welding of Hastelloy X with pulsed Nd:YAG and continuous wave fiber lasers. Mater. Des. 106, 177–183.
129. Pal, S., Pal, S.K., Samantaray, A.K., 2008. Artificial neural network modeling of weld joint strength prediction of a pulsed metal inert gas welding process using arc signals. J. Mater. Process. Technol. 202, 464–474.
130. Pan, L.K., Wang, C.C., Wei, S.L., Sher, H.F., 2007. Optimizing multiple quality characteristics via Taguchi method-based Grey analysis. J. Mater. Process. Technol. 182, 107–116.
131. Panwisawas, C., Perumal, B., Ward, R. M., Turner, N., Turner, R. P., Brooks, J. W., Basoalto, H. C., 2017. Keyhole formation and thermal fluid flow-induced porosity during laser fusion welding in titanium alloys: Experimental and modelling. Acta Mater. 126, 251–263.
132. Pengfei, H., Yang, L., Yang, L. Z., 2011. Numerical simulation of the temperature filed in fixed TIG welding pool. International Conference on Modeling Simulation and Control IPCSIT, 10: 74-78.
133. Quintino, L., Costa, A., Miranda, R., Yapp, D., Kumar, V., Kong, C. J., 2007. Welding with high power fiber lasers-A preliminary study. Mater. Des. 28: 1231-1237.
134. Rahman Chukkan, J., Vasudevan, M., Muthukumaran, S., Ravi Kumar, R., Chandrasekhar, N., 2015. Simulation of laser butt welding of AISI 316L stainless steel sheet using various heat sources and experimental validation. J. Mater. Process. Technol. 219, 48–59.

135. Rai, R., Elmer, J.W., Palmer, T.A., DebRoy, T., 2007. Heat transfer and fluid flow during keyhole mode laser welding of tantalum, Ti–6Al–4V, 304L stainless steel and vanadium. J. Phys. D. Appl. Phys. 40, 5753–5766.
136. Rajakumar, S., Balasubramanian, V., 2012. Predicting grain size and tensile strength of friction stir welded joints of AA7075-T6 aluminium alloy. Mater. Manuf. Process. 27, 78–83.
137. Ranjbarnodeh, E., Serajzadeh, S., Kokabi, A.H., Fischer, A., 2011. Prediction of temperature distribution in dissimilar arc welding of stainless steel to carbon steel. J. Eng. Manuf. 226, 117–125.
138. Rao, K. P., Angamuthu, K., Srinivasan, P. B., 2008. Fracture toughness of electron beam welded Ti6Al4V. J. Mater. Process. Technol. 199, 185–192.
139. Ready, J. F. 2001. LIA Hanbook of Laser Material Processing,; Laser Institute of America, USA.
140. Richter, K., Behr, W., Reisgen, U., 2007. Low heat welding of titanium materials with a pulsed Nd:YAG laser. Mater. Sci. Engg. Tech. 38, 51–56.
141. Richter, S., K. H., 1997. Laser welding techniques for titanium alloy sheet. J. Mater. Process. Technol. 65, 203–208.
142. Rong, Y., Huang, Y., Zhang, G., Mi, G., Shao, W., 2017. Laser beam welding of 316L T-joint: microstructure, microhardness, distortion, and residual stress. Int. J. Adv. Manuf. Technol. 90, 2263–2270.
143. Rosenthal, D., 1946. The theory of moving source of heat and its application to metal treatment, Transactions ASME, 68, 849–866.
144. Sakagawa, T., Nakashiba, S., Hiejima, H., 2011. Laser micro welding system and its application to seam welding of rechargeable battery. Phys. Procedia 12, 6–10.
145. Sathiya, P., Abdul Jaleel, M.Y., Katherasan, D., Shanmugarajan, B., 2011. Optimization of laser butt welding parameters with multiple performance characteristics. Opt. Laser Technol. 43, 660–673.
146. Sathiya, P., Panneerselvam, K., Abdul, J. M. Y., 2012. Optimization of laser welding process parameters for super austenitic stainless steel using artificial neural networks and genetic algorithm. Mater. Des. 36, 490–498.
147. Shanmugam, N. S., Buvanashekaran, G., Sankaranarayanasamy, K., Manonmani, K., 2012. Some studies on temperature profiles in AISI 304 stainless steel sheet during laser beam welding using FE simulation. Int. J. Adv. Manuf. Technol. 43, 78–94.

148. Shanmugam, N. S., Buvanashekaran, G., Sankaranarayanasamy, K., Ramesh Kumar, S., 2010. A transient finite element simulation of the temperature and bead profiles of T-joint laser welds. Mater. Des. 31, 4528–4542.
149. Shanmugarajan., B. J. N., C., G., P., B., A., Albert, S. K., A. K., B., 2013. Studies on autogenous laser welding of type 304B4 borated stainless steel. Opt. Lasers Eng. 51, 1272–1277.
150. Short, A. B., 2009. Gas tungsten arc welding of α+β titanium alloys: A review, Mater. Sci. Technol. 25, 309–324.
151. Siva Shanmugam, N., Buvanashekaran, G., Sankaranarayanasamy, K., 2012. Some studies on weld bead geometries for laser spot welding process using finite element analysis. Mater. Des. 34, 412–426.
152. Sokolov, M., Salminen, A., Somonov, V., Kaplan, A. F. H., 2012. Laser welding of structural steels: Influence of the edge roughness level, Opt. Laser Technol. 44, 2054–2071.
153. Spina, R., Tricarico, L., Basile, G., Sibillano, T., 2007. Thermo-mechanical modeling of laser welding of AA5083 sheets. J. Mater. Process. Technol. 191, 215–219.
154. Squillace, A., Prisco, U., Ciliberto, S., Astarita, A., 2012. Effect of welding parameters on morphology and mechanical properties of Ti–6Al–4V laser beam welded butt joints. J. Mater. Process. Technol. 212, 427–436.
155. Steen, W. M., 2003. Laser Materials Processing. Springer-Verlag London Limited, London .
156. Suder, W. J., Williams, S., 2014. Power factor model for selection of welding parameters in CW laser welding. Opt. Laser Technol. 56, 223–229.
157. Sun, J., Liu, X., Tong, Y., Deng, D., 2014. A comparative study on welding temperature fields, residual stress distributions and deformations induced by laser beam welding and CO2 gas arc welding. Mater. Des. 63, 519–530.
158. Sun, Z., Pan, D., Zhang, W., 2002. Correlation between welding parameters and microstructures in TIG, plasma and laser welded Ti-6Al-4V, in Proceedings of the 6th International Conference Trends in Welding Research, Pine Mountain, USA, 760-767.
159. Suryanarayana, C., Norton, M. G., 1998 X-Ray Diffraction – A Practical Approach Plenum Press. New York, USA.
160. Tadamalle, A. P., Reddy, Y. P., Ramjee, E., Reddy, V., 2014. Evaluation of Nd: YAG Laser Welding Efficiencies for 304L Stainless Steel. Procedia Mater. Sci. 6, 1731–1739.

161. Tan, W., Shin, Y. C., 2015. Multi-scale modeling of solidification and microstructure development in laser keyhole welding process for austenitic stainless steel. Comput. Mater. Sci. 98, 446–458.
162. Tani, G., Ascari, A., Campana, G., Fortunato, A., 2007. A study on shielding gas contamination in laser welding of non-ferrous alloys. Appl. Surf. Sci. 254, 904–907.
163. Tenner, F., Brock, C., Klampfl, F., Schmidt, M., 2015. Analysis of the correlation between plasma plume and keyhole behavior in laser metal welding for the modeling of the keyhole geometry. Opt. Lasers Eng. 64, 32-41.
164. Tobar, M., Lamas, M., Yáñez, A., Sánchez-Amaya, J., Boukha, Z., Botana, F., 2010. Experimental and simulation studies on laser conduction welding of AA5083 aluminium alloys. Phys. Procedia 5, 299–308.
165. Torkamany, M. J., Malek Ghaini, F., Poursalehi, R., Kaplan, A. F. H., 2016. Combination of laser keyhole and conduction welding: Dissimilar laser welding of niobium and Ti-6Al-4V. Opt. Lasers Eng. 79, 9–15.
166. Tsirkas, S. A., Papanikos, P., Kermanidis, T., 2003. Numerical simulation of the laser welding process in butt-joint specimens, J. Mater. Process. Technol. 134, 59–69.
167. Wang, G., Wu, A., Zou, G., Zhao, Y., Chen, Q., Ren, J., 2009. Bending properties and fracture behavior of Ti-23AI-17Nb alloy laser beam welding joints. Tsinghua Sci. Technol. 14, 293–299.
168. Wang, H., Shi, Y., Gong, S., Duan, A., 2007. Effect of assist gas flow on the gas shielding during laser deep penetration welding. J. Mater. Process. Technol. 184, 379–385.
169. Wang, J., Wang, C., Meng, X., Hu, X., Yu, Y., Yu, S., 2012a. Study on the periodic oscillation of plasma/vapour induced during high power fibre laser penetration welding. Opt. Laser Technol. 44, 67–70.
170. Wang, S., Liao, Z., Liu, Y., Liu, W., 2014a. Influence of thermal oxidation temperature on the microstructural and tribological behavior of Ti6Al4V alloy. Surf. Coatings Technol. 240, 470–477.
171. Wang, S., Wei, M., Tsay, L., 2003. Tensile properties of LBW welds in Ti–6Al–4V alloy at evaluated temperatures below 450 °C. Mater. Lett. 57, 1815–1823.
172. Wang, S., Wu, X., 2012b. Investigation on the microstructure and mechanical properties of Ti–6Al–4V alloy joints with electron beam welding. Mater. Des. 36, 663–670.

173. Wang, W., Yang, X., Li, H., Cong, F., Liu, Y., 2014b. Effect of laser welding parameters on formation of NiTi shape memory alloy welds. Adv. Mater. Sci. Eng. 2014, 1–8.
174. Weldingh, J., Kristensen, K. J., 2001. Very deep penetration laser welding - techniques and limitations, Proc. 8th NOLAMP Conference, Copenhagen, Denmark.
175. Wu, A. P., Zou, G. S., Ren, J.L., Zhang, H. J., Wang, G. Q., Liu, X., Xie, M. R., 2002. Microstructures and mechanical properties of Ti–24Al–17Nb (at.%) laser beam welding joints. Intermetallics 10, 647–652.
176. Wu, B., Ding, D., Pan, Z., Cuiuri, D., Li, H., Han, J., Fei, Z., 2017. Effects of heat accumulation on the arc characteristics and metal transfer behavior in wire arc additive manufacturing of Ti6Al4V, J. Mater. Process. Technol. 250, 304–312.
177. Xu, P., Li, L., Zhang, C. (Sam), 2014. Microstructure characterization of laser welded Ti-6Al-4V fusion zones. Mater. Charact. 87, 179–185.
178. Yadaiah, N., Bag, S., 2012. Effect of Heat Source Parameters in Thermal and Mechanical Analysis of Linear GTA Welding Process. ISIJ Int. 52, 2069–2075.
179. Yadaiah, N., Bag, S., 2013. Role of Oxygen as Surface-Active Element in Linear GTA Welding Process. J. Mater. Eng. Perform. 22, 3199–3209.
180. Yadaiah, N., Bag, S., 2014. Development of egg-configuration heat source model in numerical simulation of autogenous fusion welding process. Int. J. Therm. Sci. 86, 125–138.
181. Yang, J., Sun, S., Brandt, M., Yan, W., 2010. Experimental investigation and 3D finite element prediction of the heat affected zone during laser assisted machining of Ti-6Al-4V alloy. J. Mater. Process. Technol. 210, 2215-2222.
182. Yousuke, K., Masami, M., Seiji, K., 2007. Investigation of high-power fiber laser welding phenomena of stainless steel. Trans. JWRI 36, 11–16.
183. Zhang, M., Chen, G., Zhou, Y., Liao, S., 2014. Optimization of deep penetration laser welding of thick stainless steel with a 10kW fiber laser. Mater. Des. 53, 568–576.
184. Zhou, J., Tsai, H. L., Wang, P. C., 2006. Transport phenomena and keyhole dynamics during pulsed laser welding. J. Heat Transfer 128, 680–690.
185. Zhou, W., Chew, K.., 2003. Effect of welding on impact toughness of butt-joints in a titanium alloy. Mater. Sci. Eng. A 347, 180–185.
186. Zhu, X. K., Chao, Y. J., 2004. Numerical simulation of transient temperature and residual stresses in friction stir welding of 304L stainless steel. J. Mater. Process. Technol. 146, 263–272.

List of publications

International Journals

1. **Chandan Kumar,** Manas Das, C. P. Paul, B. Singh, Experimental Investigation and Metallographic Characterization of Fiber Laser Beam Welding of Ti-6Al-4V Alloy Using Response Surface Method, Optics and Lasers in Engineering, 95 (2017) 52–68.
2. **Chandan Kumar,** Manas Das, C. P. Paul, K. S. Bindra, Bead Shape and Microstructural Comparison in Fiber Laser Beam Welding of Ti-6Al-4V alloy, Optics and Laser Technology, 105 (2018) 306-321.
3. **Chandan Kumar,** Manas Das, C. P. Paul, K. S. Bindra, Characteristics of Fiber Laser Weldments of Two Phases (α+β) Titanium Alloy, Under review.
4. **Chandan Kumar**, Manas Das, C. P. Paul, K. S. Bindra, Influence of Line Energy in Fiber Laser Beam Welding of Two Phases α+β Titanium Alloy, Submitted.
5. **Chandan Kumar,** Manas Das, C. P. Paul, K. S. Bindra, Experimental Investigation of Fiber Laser Beam Welding of Austenitic Stainless Steel Grade-316L, Submitted.

Book chapters

1. **Chandan Kumar,** Manas Das, P. Biswas, A 3-D Finite Element Analysis of Transient Temperature Profile of Laser Welded Ti-6Al-4V Alloy, Lasers Based Manufacturing, Topics in Mining, Metallurgy and Materials Engineering, Springer, Publisher- Springer, DOI: 10.1007/978-81-322-2352-8_21. (2015) 421-440.
2. **Chandan Kumar,** Manas Das, C. P. Paul, B. Singh, Experimental Study of Fiber Laser Weldments of 5 mm Thick Ti-6Al-4V Alloy, Application of Lasers in Manufacturing, Publisher- Springer, DOI: 10.1007/978-981-13-0556-6_3. (2018) 45-67.

International Conferences

1. **Chandan Kumar**, Manas Das, P. Biswas, A 3-D Finite Element Analysis of Transient Temperature Profile of Laser Welded Ti-6Al-4V Alloy, 5th International & 26th All India Manufacturing Technology, Design and Research Conference December 12–14, (2014), IIT Guwahati, Assam, India.
2. A. Barman, **C. Kumar,** M. Das, Analysis of Magnetic Field Assisted Finishing (MFAF) Process Parameters For Finishing Brass Workpiece Using Soft-Computing Technique, 5th

International & 26th All India Manufacturing Technology, Design and Research Conference December 12–14, (2014), IIT Guwahati, Assam, India.

3. **Chandan Kumar**, Manas Das, P. Bhargava, C. P. Paul, Finite Element Method Based Numerical Simulation of Laser Beam Welded Titanium Alloy (Ti-6Al-4V), International Conference on Precision, Meso, Micro and Nano Engineering December 10-12, (2015), IIT Bombay, Maharashtra, India.
4. **Chandan Kumar**, Manas Das, P. Bhargava, C. H. Premsingh, C. P. Paul, Effect of Process Parameters on Fiber Laser Welded Titanium Alloy, International Conference on Precision, Meso, Micro and Nano Engineering December 10-12, (2015), IIT Bombay, Maharashtra, India.
5. **Chandan Kumar**, Manas Das, C. Premsingh, C. P. Paul, B Singh, Effect of Heat Input and Defocussing Distance on The Weld Quality of Laser Beam Welded Ti-6Al-4V Alloy, 6th International & 27th All India Manufacturing Technology, Design and Research Conference December 16–18, (2016), College of Engineering Pune, India.
6. **Chandan Kumar** and Manas Das, Finite Element Method Based Transient Thermal Analysis of Laser Beam Welded Titanium (Ti-6Al-4V) Alloy, International Conference on Precision, Meso, Micro and Nano Engineering, December 07-09, (2017), IIT Madras, Tamilnadu, India.
7. **Chandan Kumar** and Manas Das, Microstructural Characterization and Its Effect on Mechanical Properties of Fiber Laser Beam Welded Ti-6Al-4V Alloy, International Conference on Precision, Meso, Micro and Nano Engineering, December 07-09, (2017), IIT Madras, Tamilnadu, India.
8. **Chandan Kumar** and Manas Das, Microstructural Analysis in Fiber Laser Weldments of Ti-6Al-4V Alloy, 7th International & 28th All India Manufacturing Technology, Design and Research Conference December 16–18, (2018), College of Engineering Guindy, Anna University, Chennai, India, (Submitted).